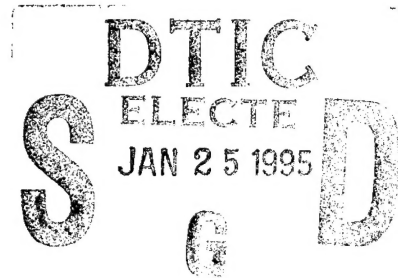# NUMERICAL EXPERIMENTS ON THE FLOW PAST A CIRCULAR CYLINDER AT SUB-CRITICAL REYNOLDS NUMBER

By
Patrick Beaudan and Parviz Moin

DTIC
S ELECTE D
JAN 2 5 1995
G

Report No. TF-62

Thermosciences Division
Department of Mechanical Engineering
Stanford University
Stanford, California 94305

December 1994

19950123 049

NUMERICAL EXPERIMENTS ON THE FLOW PAST A CIRCULAR CYLINDER AT SUB-CRITICAL REYNOLDS NUMBER

by

Patrick Beaudan and Parviz Moin

Accesion For		
NTIS CRA&I	X	
DTIC TAB	☐	
Unannounced	☐	
Justification		
By		
Distribution /		
Availability Codes		
Dist	Avail and / or Special	
A-1		

Report No. TF-62

Thermosciences Division
Department of Mechanical Engineering
Stanford University
Stanford, California 94305

December 1994

Abstract

The performance of the dynamic subgrid-scale eddy-viscosity model and the suitability of high-order accurate, upwind-biased numerical methods for large-eddy simulations of complex flows are investigated in the case of the turbulent wake behind a circular cylinder at Reynolds number 3,900, based on freestream velocity and cylinder diameter.

The numerical method consists of high-order upwind-biased finite difference techniques applied to the compressible Navier-Stokes equations written in generalized coordinates. Integration in time is done using a fully implicit, second-order accurate iterative technique. The results of three fifth-order accurate simulations performed on identical grids with the least-squares version of the dynamic model, the fixed-coefficient Smagorinsky model, and with no subgrid-scale model are compared in the first 10 diameters of the wake. The impact of three-dimensionality is also examined via two and three-dimensional calculations without a subgrid-scale model. The effect of numerical dissipation is investigated by comparing two simulations using upwind-biased schemes, the first being fifth-order, and the second seventh-order accurate.

It is found that the near-wake is highly three-dimensional at this Reynolds number. It contains pairs of counter-rotating streamwise vortices, the effect of which cannot be reproduced in two-dimensional calculations. Three-dimensional computations are essential for predicting flow statistics of engineering interest.

Amongst the three-dimensional simulations, although the overall results are comparable, the one which uses the dynamic subgrid-scale model predicts more accurate mean velocities and Reynolds stresses in the vortex-formation region, which includes the first four diameters of the wake. The fixed-coefficient model yields, overall, the

least accurate results in that region. The magnitude of the eddy-viscosity in the transitioning free shear layers and the near-wake is in better agreement with expectations based on the flow physics when computed using the dynamic model rather than the fixed-coefficient model. Differences between the three calculations are largest in the vortex-formation zone. In the near-wake between 4 and 10 diameters downstream of the cylinder, the extent and magnitude of the differences diminish due to numerical dissipation. Ten diameters downstream, the three simulations predict comparable mean velocities and Reynolds stresses.

In the near-wake where the mesh coarsens, numerical dissipation is found to significantly affect the small scales computed using the fifth-order accurate, upwind-biased scheme. The seventh-order accurate scheme predicts improved low-order statistics at the cylinder surface and in the near-wake. With the seventh-order accurate scheme, smaller-scale structures emerge in the wake, which are absent in the simulations with the fifth-order scheme. Velocity power spectra indicate a significant increase in energy content at higher frequencies relative to the fifth-order accurate calculations, reflecting the impact of reduced levels of numerical dissipation. Based on these calculations, we have concluded that even high order upwind-biased schemes are overly dissipative and ill-suited for large-eddy simulations.

Acknowledgements

Nomenclature

Roman Symbols

c	Speed of sound
$c_{1,\,2,\,3,\,4,\,5}$	Time-advancement scheme constants
$C(x, y, z)$	Turbulence model constant
$C_i(x, y, z)$	Turbulence model constant for q^2
C_D	Total drag coefficient
C_{D_p}	Form drag
C_{D_v}, C_f	Skin-friction coefficient
C_L	Total lift coefficient
C_{L_p}	Lift coefficient due to pressure
C_{L_v}	Lift coefficient due to drag
C_P	Pressure coefficient
C_{P_b}	Cylinder back pressure coefficient
D	Cylinder diameter
e	Total energy per unit volume
$E(t)$	Perturbation energy
$\vec{F}$	Flux vector
h	Channel height
H	Wake half-width
H_k	Heat flux at test filter level
I	Identity matrix
J	Jacobian of transformation to generalized coordinates

$k_{1,2,3}$	Geometric coefficients used in generalized coordinates
L	Length of the reversed flow region behind the cylinder
L_{ij}	Leonard stress tensor
L_z	Spanwise length of the computational domain
l_K	Kolmogorov length scale
M_∞	Mach number of incoming flow
N_x	Number of points in the streamwise direction
N_y	Number of points in the azimuthal direction
N_{y_w}	Number of azimuthal points in the wake
N_z	Number of points in the spanwise direction
p	Pressure
P	Rate of turbulent energy production
Pr	Prandtl number
Pr_t	Turbulent Prandtl number
q^2	Isotropic part of the subgrid-scale Reynolds-stress tensor
q_k	Subgrid-scale heat flux
$q_{1,2,3,4,5}$	Conservative variables
$\vec{Q}$	Vector of conservative variables
r	Radial distance
$R_{1,2}$	Locally one-dimensional Riemann invariants
R_c	Cylinder radius
R_D	Radius of the computational domain
Re	Reynolds number
R_{ii}	Two-point correlation of velocity component 'i'
r_{min}	Bubble minimum velocity location on symmetry axis
$\vec{S}_t$	Source flux arising from subgrid-scale terms
S_{ij}	Rate of strain tensor
St	Strouhal shedding frequency
t	Time
T	Temperature
T_{ij}	Test-filtered stress tensor

u	Streamwise velocity
u_c	Centerline streamwise velocity
u_d	Centerline streamwise velocity deficit
u_{min}	Minimum velocity on the symmetry axis of the recirculation zone
v	Vertical velocity
V_N	Normal velocity
V_t	Tangential velocity
w	Spanwise velocity
x	Streamwise direction
y	Vertical direction
z	Spanwise direction

Greek Symbols

δ_{ij}	Kronecker delta
Δ	Grid-filter width
Δt	Time step
η	Generalized coordinate
$\hat{\Delta}$	Test-filter width
γ	Specific-heats ratio
$\vec{\Gamma}$	Forcing flux in the channel flow calculation
Λ	Magnitude of the momentum forcing term in the channel calculation
Λ_i	Eigenvalues of the Euler fluxes
μ	Molecular viscosity
μ_t	Turbulent eddy viscosity
$\vec{\omega}$	Vorticity
Ω	Frequency
Ω_{St}	Vortex shedding frequency
Ω_{Z_0}	Wall spanwise vorticity
ρ	Density

τ{ij}	Subgrid-scale stress tensor
σ_{ij}	Resolved viscous stress tensor
ξ	Generalized coordinate
θ	Azimuthal angle
ϵ	Rate of energy dissipation

Abbreviations

CFL	Courant-Friedrichs-Lewy number
$sgn(.)$	Sign of (.)
RANS	Reynolds-averaged Navier-Stokes
LES	Large-eddy simulation
CDNS	Coarse direct numerical simulation
RSE	Reynolds-stress Equation model
ASM	Algebraic Stress Model
PIV	Particle Image Velocimetry

Superscripts and Subscripts

e	Euler flux
h	Heat flux
∞	Incoming free-stream conditions
n	Time level
w	Wall quantity
$'$	Resolved turbulent component
$\tilde{.}$	Periodic component
$\bar{.}$	Global averaging in time and span
v	Viscous flux
$\pm$	Split eigenvalues

Other symbols

$<.>$ Spanwise Averaging

$<.>_k$ Averaging at constant phase k

Contents

xv

List of Tables

List of Figures

xix

Chapter 1

Introduction

1.1 Review of Circular Cylinder Flow Regimes

For the past century the flow over a circular cylinder has been the subject of numerous investigations, of theoretical, experimental, and more recently numerical variety. Extensive reviews of the knowledge accumulated on this flow appear every decade (Morkovin 1964, Berger & Wille 1972, Norberg 1987), yet our understanding of the subjacent physics is incomplete. The relevant non-dimensional parameter in the flow is the Reynolds number, but because of sensitivity to experimental conditions, global statistics such as drag, pressure coefficient, and Strouhal frequency vary by as much as 25% from one experiment to the next at a fixed Reynolds number (Cantwell & Coles 1983). These variations indicate that in addition to the Reynolds number, several parameters arising from experimental set-ups are important in the cylinder flow. These include the blockage ratio, the free-stream turbulence intensity, the cylinder aspect ratio, and the end boundary conditions, each of which has been the subject of numerous studies.

A broad classification of the cylinder flow behavior in different regimes of Reynolds number is presented in table (1), which also lists some representative experiments for each flow regime. The table follows the descriptions of this flow presented by Morkovin (1964), Roshko (1954a,b, 1961, 1969), and Norberg (1987).

At Reynolds numbers less than approximately 40, the flow is laminar and steady.

1

The boundary layer on the cylinder surface separates at a Reynolds number of 3.2 (Nisi & Porter 1923) to 5 (Taneda 1956), and a pair of steady symmetric vortices form behind the cylinder. A large body of early experimental work has documented that range of Reynolds numbers, detailing the main features of the boundary layer and near-wake region (*e.g.* Tritton 1959, Coutanceau & Bouard 1977, Thom 1933, Taneda 1956, Acrivos *et al.* 1965). Between Reynolds numbers 10 and 40, the velocity profiles in the wake are self-similar past 10 diameters downstream of the cylinder, the length of the recirculation zone behind the cylinder grows linearly with Reynolds number, and the velocity distributions on the rear symmetry axis in the recirculation zone at different Reynolds numbers exhibit similarity (Nishioka & Sato 1974).

For Reynolds numbers higher than approximately 40, a characteristic frequency expressed in non-dimensional form as the Strouhal number is associated with the wake. Taneda (1956) puts the critical Reynolds number at which shedding first occurs at 30, whereas Homman (1936), Kovasznay (1949) and Roshko (1954b) find that shedding starts at Reynolds number 40. Local linear parallel stability theory applied to the cylinder wake (Monkewitz 1988) indicates that the flow becomes absolutely unstable at Reynolds number 25, approximately two-thirds the value at which a Karman vortex street develops experimentally, showing that the notion of absolute instability cannot by itself predict a precise Strouhal frequency even at the onset of vortex shedding. Chomaz, Huerre & Redekopp (1988) use the concept of global instability, and show that global oscillations of a shear flow will occur only once a critical sub-volume of the flow is absolutely unstable.

For Reynolds numbers up to 150, the flow remains laminar (Bloor 1964, Roshko 1954a), the shed vorticity decays as it convects downstream, and the Strouhal number increases with Reynolds number. A least-squares curve-fit of the Strouhal curve for Reynolds numbers between 50 and 180 is given by

$$St = A/Re + B + C\ Re \qquad (1)$$

where $A = -3.3265$, $B = 0.1816$ and $C = 1.6 \times 10^{-4}$ (Williamson 1991).

Transition to three-dimensionality in the near-wake occurs around $Re = 180$, and is signaled by two discontinuities in the Strouhal-Reynolds number relation. The first,

around $Re = 180$, arises from the generation of vortex loops evolving into pairs of counter-rotating streamwise vortices in the wake, the second comes from a transition to fine-scale streamwise vorticity at $Re = 230 \sim 260$.

At Reynolds numbers between 300 and 2×10^5, the sub-critical range, the flow around the entire periphery of the cylinder is laminar, and transition to turbulence occurs in the separated free shear layers (Cardell 1993). At the lowest Reynolds numbers in this range, the wake becomes fully turbulent in 40 to 50 cylinder diameters downstream (Uberoi 1969), after which distance the regular vortices have completely decayed. At the higher end of the Reynolds number range, transition occurs very near the wall surface, and the wake is fully turbulent close downstream of the cylinder (Cantwell & Coles 1983). For Reynolds numbers larger than 10^4, transition in the shear layers occurs very close to the separation points, and the base-pressure coefficient, drag coefficient and Strouhal number are approximately constant at values of -1.1, 1.2 and 0.2 respectively (Roshko & Fiszdon 1969).

In the past fifteen years, studies of the turbulence structure in plane wakes have attempted to delineate the contributions of the organized and random motions using a triple decomposition of the flow into a global mean, a phase-averaged mean and a random component (Perry & Lim 1978, Perry & Watmuff 1981, Hussain 1983, 1986, Hayakawa & Hussain 1989, Matsumura & Antonia 1993). Analyses of flow statistics using this technique link the production of random Reynolds shear stress to the stretching of streamwise vortices (or braids) between adjacent spanwise rollers (Kiya & Matsumura 1988, Antonia *et al.* 1987). Two representative experiments at low and high sub-critical Reynolds numbers investigated the properties of the coherent and random Reynolds stresses in the wake. Cantwell & Coles (1983) analyzed transport processes in the near-wake at Reynolds number 1.4×10^5. Matsumura & Antonia (1993) examined the intermediate wake, from 10 to 40 diameters downstream, at Reynolds number 5,830.

At a Reynolds number of 1.4×10^5, Cantwell & Coles found that in the first 8 diameters downstream of the cylinder, the coherent and random Reynolds stresses are of comparable magnitude. The peak values of the mean random shear and streamwise

Reynolds stresses are respectively 36% and 77% higher than their periodic counterparts. The coherent motion makes a more important contribution to the vertical velocity fluctuations, and the periodic vertical Reynolds stress peaks are 17% higher than the random component. As vortices are shed from both sides of the cylinder and turbulent convective mixing occurs in the base region, approximately 55% of the originally shed vorticity is lost, and the emerging vortices convect downstream with their centroids close to the wake centerline. In a frame of reference moving with a shed vortex, the flow can be described as a series of centers and saddle points. Near these saddles lie peaks in turbulent random shear stresses, and turbulence production results from the stretching of vorticity aligned with the separatrices defining the topology.

At the lower sub-critical Reynolds number of 5,830, Matsumura & Antonia describe the relative importance of the random and periodic components of the flow. As in the case of Cantwell & Coles at higher Reynolds number, the coherent motion contributes a large portion of the vertical Reynolds stresses. Ten diameters downstream, random stresses account for only 25% of the total vertical Reynolds stress, but for 70% of the streamwise Reynolds stress. The Reynolds shear stress at the same location is closely equi-partitioned between the periodic and random components, and its peak value occurs in the centers, not in the saddle points as is found at Reynolds number 1.4×10^5.

Much of the literature dealing with experiments on the cylinder documents phenomena in the sub-critical Reynolds number region. It has been known since the work of Gerrard in 1965 that the mean aerodynamic properties of the cylinder are particularly sensitive to free-stream disturbances in the sub-critical range of Reynolds number. These disturbances, as well as acoustic noise levels, cylinder vibrations, surface roughness, blockage ratio, and other geometric parameters which have not been carefully documented in most experiments, have been shown by Norberg (1987), amongst others, to influence transition to turbulence in the free shear layer, as well as mixing and entrainment in the wake region for sub-critical and critical Reynolds numbers up to 3×10^5. This may account for the lack of agreement in the literature on the near-wake properties of the flow. The influence of such perturbations is best illustrated by

the dependence of mean cylinder-surface statistics on surface roughness for Reynolds numbers larger than 10^5 (Shih, Wang, Coles & Roshko 1992). Surface roughness is quantified by a parameter representing the mean protrusion height (k) at the cylinder surface, normalized by the cylinder diameter (D). At a Reynolds number of 10^6, the mean drag and base-pressure coefficients of smooth cylinders are approximately 0.25 and -0.3 respectively. For $k/D = 0.0003$, the mean drag increases by a factor of 3 to 0.75, and the base-pressure coefficient drops to -0.8. As (k/D) further increases to 0.01, the drag rises to 1.1, while the base-pressure coefficient falls to -1.3. Experimental results of Achenbach (1971), Roshko (1961), and Shih, Wang, Coles & Roshko (1992) suggest that in the extreme case of very rough cylinders, some mean statistics, including the base-pressure coefficient, the pressure rise near separation, and the boundary layer separation angle, become Reynolds-number independent and vary only with surface roughness beyond a Reynolds number of 2×10^6.

The critical range of Reynolds numbers, between 2×10^5 and 3.5×10^6, displays two transitions in the drag coefficient, labeled the lower and upper transitions by Roshko (1961). In the lower transition range ($2 \times 10^5 \leq Re \leq 5 \times 10^5$), the drag coefficient drops abruptly from 1.2 to about 0.3 due to an increase in base pressure at a Reynolds number of approximately 3.6×10^5. A laminar separation of the boundary layer is followed by transition to turbulence, reattachment and a final turbulent separation. The separation point moves from the front to the downstream side of the cylinder, and the width of the near-wake decreases to less than 1 diameter. In the upper transition region ($5 \times 10^5 \leq Re \leq 3.5 \times 10^6$), the base-pressure coefficient decreases monotonically from approximately -0.2 to -0.5, while the drag coefficient increases from 0.3 to 0.7, and remains at that value for Reynolds numbers of up to 10^7. With increasing Reynolds number the separation point moves forward, but it remains on the downstream side of the cylinder, and the wake width increases but stays smaller than 1 diameter. The sensitivity of the flow to disturbances in the critical regime, in particular the non-zero mean lift which can develop around the cylinder, has been experimentally investigated by Schewe (1986).

In the post-critical regime, past Reynolds number 3.5×10^6, the boundary layer

on the cylinder surface transitions to turbulence before separating. The separation-reattachment bubble present in the critical region disappears. The base-pressure coefficient pursues its monotonic decrease started at Reynolds number 5×10^5, reaching -0.6 at Reynolds number 8×10^6; the drag coefficient is constant at around 0.7, and vortices are shed regularly at an approximately constant Strouhal frequency of 0.27 (Roshko 1961).

1.2 On Comparison with Experiments and the Case Selected for Simulations

The flow in the sub-critical Reynolds number range ($300 \leq Re \leq 2 \times 10^5$) features several challenging phenomena for large-eddy simulations: a laminar boundary layer including unsteady separations and reattachments, flow reversals at the cylinder surface and in the near-wake, adverse pressure gradients, transitioning free shear layers, and a turbulent wake with random and periodic Reynolds stresses of comparable magnitudes.

The selection of a particular Reynolds number represents a compromise between competing effects. At higher Reynolds numbers, random motions account for an increasingly larger share of the total Reynolds stresses close to the cylinder, but the laminar cylinder boundary layer and the transitioning separated shear layers become thinner. The resolution requirements of these layers increase with the Reynolds number, independently of whether the turbulent wake is simulated via direct or large-eddy simulations.

The choice of Reynolds number is also dependent on the available experimental data. Accurate measurements of velocities and stresses are difficult in low or reversed mean velocity regions where turbulence intensities are high, as well as in high flow-angle regions, which accounts for the dearth of complete, published experimental data in the near wake. A careful review of the literature reveals that despite the imposing volume of published work on the circular cylinder, most experiments concentrate on the mean and fluctuating properties at the cylinder surface (*e.g* Achenbach 1968,

Roshko 1954a, West 1990, Farell & Blessmann 1983, Schewe 1983, Norberg 1987), the intermediate wake region between 10 and 40 diameters downstream (*e.g.* Matsumura & Antonia 1993, Zhou & Antonia 1992, Hayakawa & Hussain 1989), or the small-deficit far-wake region extending from 50 to several hundred diameters downstream (*e.g* Townsend 1949, Antonia & Browne 1987, Wygnanski *et al.* 1986, Fabris 1979, Papailiou & Lykoudis 1974, Ferre *et al.* 1990).

Experiments detailing near-wake properties at sub-critical Reynolds numbers are few, and all but one provide inadequate or insufficient data for comparison with a numerical simulation. Bouard & Coutanceau (1980) study the time evolution of the near-wake velocity profiles at Reynolds numbers between 40 and 10^4, but provide no Reynolds-stress information. Bloor (1964), Wei & Smith (1986) and Kourta *et al.* (1987) concentrate on transitional waves in the separated shear layers and do not discuss other statistics. Bloor & Gerrard (1966) provide mean streamwise velocity profiles, at Reynolds numbers of $2,000$ and $16,000$, at different locations downstream of the recirculation region, but give no details on the Reynolds stresses, the mean vertical velocities, or the velocity distribution inside the bubble.

One experiment which provides detailed Reynolds stress and velocity information within the stagnation zone and in the near-wake region was performed by Cantwell and Coles (1983), at a Reynolds number of 1.4×10^5. Mean and phase-averaged velocity and Reynolds stress fields are documented within 8 diameters downstream of the cylinder, as well as mean and fluctuating quantities at the cylinder surface. At the lower Reynolds number of $3,900$, two separate experiments provide details on the velocity and Reynolds-stress distributions. Lourenco *et al.* (1993) used a Particle Image Velocimetry technique to compile mean and phase-averaged data within three diameters downstream of the cylinder. In the near-wake region, between the closure point of the recirculation bubble and 10 diameters downstream, single sensor measurements of the mean velocities and Reynolds stresses have been documented by Ong and Wallace (1994). The data at both Reynolds numbers of $3,900$ and 1.4×10^5 are adequate for comparison with large-eddy simulation results. On a structured mesh, and with the fifth-order spatially-accurate numerical method used in this work, the number of mesh points in the plane of mean motion required at the higher Reynolds

number is approximately one order of magnitude larger than at Reynolds number $3,900$, a point further discussed in chapter 4. For this reason, the lower Reynolds number is selected for comparison with large-eddy simulations.

1.3 On Computing the Flow Over Circular Cylinders

The many physical phenomena arising in the turbulent flow around circular cylinders (section 1.1) represent a difficult challenge for numerical prediction methods. At the 1980-1981 HTTM-Stanford Conference on Complex Turbulent Flows, the experiment of Cantwell & Coles (1983), documenting mean flow quantities in the near wake at Reynolds number 1.4×10^5, was suggested as a test case for numerical methods. Of the 52 participating computational groups, none attempted simulating this case, for reasons which were not documented. In recent years, the advent of more powerful computers and sophisticated numerical methods has led to new efforts to simulate the transitional and turbulent cylinder flow regimes. The features and principal conclusions of several representative calculations are discussed below.

In the transitional Reynolds number range ($150 \leq Re \leq 300$), two-dimensional simulations can accurately predict a restricted number of global parameters, such as mean drag on the cylinder and Strouhal number, without modeling three-dimensional effects. Braza, Chassaing & Ha Minh (1986) use a finite-volume method, second-order accurate in space and time, to discretize the two-dimensional Navier-Stokes equations written in logarithmic-polar coordinates. At Reynolds numbers of 100 and 200, the computed Strouhal frequency and mean drag coefficient are in good agreement with experimental measurements. Franke, Rodi & Schönung (1990) attempt to predict these coefficients at Reynolds numbers as high as $5,000$ with a spatially third-order accurate, first-order time-accurate, finite-volume method applied to the equations written in standard polar coordinates. Having confirmed the grid and time-step independence of their results, they noted that Strouhal frequency and drag coefficient could be accurately computed only for Reynolds numbers under 300. Past

this Reynolds number, in the sub-critical regime, the computed drag increases with Reynolds number, contrary to the experimental trend, which the authors surmise is a consequence of neglecting the three-dimensionality of the flow.

Visualization experiments (Bays-Muchmore & Ahmed 1992, Williamson 1989, 1991b) demonstrate the presence of counter-rotating streamwise vortices in the braid region between consecutive spanwise vortices, directly behind the cylinder, for Reynolds numbers higher than approximately 200. The importance of accounting for the consequent three-dimensionality is further corroborated by the results of Karniadakis & Triantafyllou (1992), who performed direct numerical simulations of the cylinder flow at Reynolds numbers between 175 and 500 with a mixed spectral/spectral-element technique. The time-trace of the velocity at a representative point in the near-wake, calculated from a two-dimensional simulation at Reynolds number 500, exhibits a quasi-periodic behavior. In the three-dimensional simulations however, the flow behavior alternates between apparently random and almost periodic states, which is in qualitative agreement with the experimental observations of Bloor (1964).

These low Reynolds number simulations investigated the onset of three-dimensional motions in the wake as well as the mechanisms involved in transition to turbulence. Three-dimensionality in the wake was found to arise from a secondary instability of the vortex street appearing in the computations between Reynolds numbers of 200 and 210, and was not accompanied by the hysteresis phenomenon documented experimentally by Williamson (1988). Transition to turbulence is analyzed from power spectra and three-dimensional phase portraits at locations in the near-wake. These indicate that a period-doubling bifurcation cascade may be responsible for transition to turbulence. However, time-averaged statistics at the cylinder surface and in the near-wake are not compared with experimental data, making it difficult to assess the accuracy of the computations.

Steady Reynolds-averaged computations at higher than transitional Reynolds numbers were undertaken by Majumdar & Rodi (1985), who used a $k - \epsilon$ model to compute sub-critical and post-critical cases, at Reynolds numbers of 1.4×10^5 and 3.6×10^6 respectively. Majumdar & Rodi sought to establish the level of inaccuracy

of predictions based on steady RANS simulations. Their method consisted of a finite-volume formulation, with a hybrid central/upwind scheme applied to the convective terms. Neither the mean forces acting on the cylinder, nor the near-wake mean flow were predicted accurately. At the sub-critical Reynolds number of 1.4×10^5, the solution was compared with the experiments of Achenbach (1968) and Cantwell & Coles (1983). The quantities which compared well with these experiments are the wall shear stress upstream of separation, and the wake spreading-rate downstream of the stagnation region. However most other relevant quantities were predicted incorrectly. The boundary-layer separation occured too far downstream, the base pressure was too high and the drag coefficient correspondingly too low. In the wake region, the maximum shear stress was 4 times smaller, and the recirculation bubble 80% longer than found experimentally. These results were qualitatively insensitive to the treatment of the eddy viscosity in the laminar and attached part of the cylinder boundary layer. Setting the eddy viscosity to zero in that region, or using a Van Driest damping function resulted in an improved wall shear stress distribution past the separation point. At the post-critical Reynolds number of 3.6×10^6, separation was predicted 11% too far downstream along the cylinder surface, the base pressure was too high although the minimum pressure coefficient compared fairly well with experimental measurements, and the wall shear stress was far too large, with a peak 2.8 times higher than found experimentally. Similar discrepancies were reported by Sugawanam & Wu (1982).

Seeking the cause of the difficulties encountered in these computations, Franke, Rodi & Schönung (1989) studied the phase-averaged experimental data of Cantwell & Coles at Reynolds number 1.4×10^5, in which they examined the validity of the $k - \epsilon$ formulation. Their principal finding was that the eddy viscosity is anisotropic, and is negative in regions where history and transport effects dominate over production of Reynolds stresses, indicating that in the case of the circular cylinder, the $k - \epsilon$ model is not adequate. Algebraic stress models have been applied to flows around square cylinders (Franke, Rodi & Schönung 1989, Franke & Rodi 1991, Murakami *et al.* 1991, Murakami 1990), but not to circular cylinders.

The difficulties encountered by Reynolds-averaged models have recently motivated the undertaking of three-dimensional simulations of the sub-critical and critical regimes. These efforts have been restricted to demonstrating improvements in the predictions of the mean and fluctuating forces acting on the cylinder when three-dimensionality is introduced in the simulations, and do not concentrate on the statistical description of the wake region. At Reynolds number 10^4, a finite-element large-eddy simulation was performed by Kato & Ikegawa (1991), using the standard Smagorinsky model and a linear wall-damping function. The computed mean drag coefficient (1.14), base-pressure coefficient (-1.08), Strouhal number (0.20) and fluctuating lift coefficient (0.27) are in good agreement with experimental values. In a similar effort to demonstrate the improvements in these coefficients when extracted from three-dimensional simulations, Tamura, Ohta & Kuwahara (1990) performed finite-difference calculations at Reynolds numbers of 10^4, 10^5 and 10^6 without turbulence models. The incompressible Navier-Stokes equations, written in generalized coordinates in the plane of mean motion, are discretized with an upwind, third-order accurate scheme for the convective terms, and marched in time with a semi-implicit first-order accurate method. The mean drag is in reasonable agreement with experimental results at the aforementioned Reynolds numbers, although the computed base-pressure coefficient, of -0.5 at Reynolds number 10^6, is far lower than the experimental value of -0.3.

The collective findings of the simulations described in this section are summarized in table (2). Two-dimensional, unsteady Navier-Stokes simulations can predict Strouhal numbers and drag coefficients at transitional Reynold numbers, but become unreliable in the sub-critical regime. Direct numerical simulations, performed to examine the physics of the transition to three-dimensionality and turbulence in the near-wake, have been limited to maximum Reynolds numbers of 500. Steady Reynolds-averaged (RANS) simulations using the $k - \epsilon$ model at sub-critical and post-critical Reynolds numbers predict inaccurate velocity and Reynolds stress distributions in the near-wake, while giving mixed results at the cylinder surface. Coarse direct simulations improve on the RANS calculations, predicting reasonable drag coefficients up to a critical Reynolds number of 10^6, providing further evidence that

11

resolving the three-dimensionality of the flow is of foremost importance past the transitional regime. A large-eddy simulation at the low sub-critical Reynolds number of 10^4 was able to predict both drag and wall-pressure coefficients in agreement with experiments, although an accurate resolution of the near-wake was not attempted.

1.4 Present Status of Large-Eddy Simulation

In large-eddy simulation the dynamically important large-scale motions are computed directly, while a subgrid-scale turbulence model represents the effect of the unresolved small scales on the large scales.

In the Smagorinsky subgrid-scale eddy-viscosity model, the eddy viscosity is locally proportional to the large-scale strain-rate tensor, and includes an adjustable coefficient. A brief review of the adjustments required in different flows is presented by Germano, Piomelli, Moin & Cabot (1991), who note that although specific complicating factors in a given flow may be accommodated by altering the model constant, no single coefficient performs well under arbitrary flow conditions. Further empiricism is introduced into the Smagorinsky model by the use of wall damping and intermittency functions, which ensure the proper asymptotic behavior of the subgrid-scale stresses near solid boundaries and in transitioning flows.

The mismatch between the premise that small scales tend to be more universal than large ones, and the degree of arbitrariness prevalent in early LES applications motivated the use of modern statistical turbulence theories in the search for more general models. A description of the models which subsequently emerged in the 1980's and early 1990's is given by Moin & Jimenez (1993). The model of Yakhot & Orszag (1986) based on renormalization group theory has incorrect limiting wall behavior; in a modified version developed by Piomelli *et al.* (1990), grid-independent results are found difficult to achieve. Chollet & Lesieur (1981), following Kraichnan's (1976) eddy viscosity model in spectral space, proposed a simplified model formulated in Fourier space. This model cannot be used in complex flow applications. A related model, developed by Metais & Lesieur (1992) to remedy this shortcoming and expressed in physical space, does not have the correct asymptotic behavior near walls and is nearly

12

identical to Smagorinsky's model.

The concept of dynamic subgrid-scale modeling, introduced by Germano, Piomelli, Moin & Cabot in 1991, is based on the scale-similarity ideas of Bardina *et al.* (1980), in which spectral information available from the resolved scales is used to model the small scales. When used in conjunction with the Smagorinsky formulation, the Smagorinsky coefficient becomes a function of space and time, dynamically computed from the resolved large-scale fields. The distinguishing properties of the dynamic eddy viscosity model are its correct asymptotic behaviors near solid surfaces, and its intrinsic ability to differentiate between laminar and turbulent regions of the flow, without *ad hoc* damping or intermittency functions.

The dynamic subgrid-scale model has been generalized to compressible flows and scalar transport by Moin, Squires, Cabot & Lee (1991) and Cabot & Moin (1991). The method for computing the coefficient of the model, initially restricted in applicability to flows statistically homogeneous in at least one direction, has been generalized by Ghosal, Lund & Moin (1992) to apply to inhomogeneous flows using a constrained optimization formulation. This model, tested in the decay of homogeneous isotropic turbulence and in channel flow, gives results in good agreement with the experimental data.

Various formulations of the dynamic model have been successfully tested against experimental and direct numerical simulation results in a variety of flows involving specific complications. These include transitional and fully developed turbulent channel flow (Germano, Piomelli, Moin & Cabot 1991), channel flow with passive scalars (Cabot & Moin 1991), isotropic turbulence decay (Moin, Squires, Cabot & Lee 1991, Ghosal, Lund & Moin 1992), planetary boundary layer (Bohnert & Ferziger 1993), three-dimensional channel flow (Cabot 1993), channel flow with system rotation (Squires & Piomelli 1993 and Cabot 1993), boundary layers with imbedded streamwise vortices (Liu & Piomelli 1993), flow over a backward-facing step (Akselvoll & Moin 1993a,b) and driven cavity flows (Zang, Street & Koseff 1993). The quality of the results achieved in these simulations suggests that the dynamic procedure is highly successful for the simulation of flows in which a variety of physical phenomena are present in different sub-regions.

1.5 Objectives and Overview

The first objective of this study is to evaluate the performance of the dynamic subgrid-scale eddy model in a complex flow where Reynolds-averaged turbulence models have faced difficulties. One of the most challenging applications of dynamic models to date has been the computation of the flow over a backward-facing step by Akselvoll & Moin (1993a,b). The turbulent wake behind a circular cylinder is the first application of dynamic models to external flows. It involves unsteady separation and reattachment, laminar sub-regions and transition to turbulence. Past attempts at simulating the sub-critical regime with a $k - \epsilon$ model reveal the inability of the Reynolds-averaged approach to accurately predict the near-wake statistics. The previous results of large-eddy simulations using the Smagorinsky model and coarse direct simulations were restricted in scope to evaluating the forces acting on the cylinder. The sub-critical cylinder wake flow is then appropriately suited for a validation study of a dynamic subgrid-scale eddy viscosity model, which adapts to local flow conditions without using adjustable constants.

Assessing the importance of three-dimensional effects is another objective of this work. To this end, the near-wake and cylinder-surface statistics obtained from two-dimensional and large-eddy simulations are compared.

The contribution of the subgrid-scale eddy viscosity model *per se* is evaluated by comparing mean velocities and Reynolds stresses computed from simulations without a turbulence model, with the dynamic subgrid-scale model, and with a fixed-coefficient Smagorinsky model.

Finally, one of our objectives is to evaluate the suitability of high-order accurate, upwind-biased finite-difference methods for the large-eddy simulation of flows in complex geometry. Results of two simulations which use the dynamic subgrid-scale turbulence model are compared to evaluate the impact of upwinding on the computed solution. One uses a fifth-order accurate, one point upwind-biased method (Rai & Moin 1991), the other a seventh-order accurate, one point upwind-biased scheme to discretize the convective derivatives. In both cases, viscous fluxes are evaluated using sixth-order accurate, central differencing schemes.

This study describes one of several concurrent efforts at Stanford to evaluate various formulations of dynamic models in complex flows. These include a curved boundary layer at Reynolds number $1,200$ based on momentum thickness, the flow around an airfoil at Reynolds number 10^6, and the flow through a plane diffuser at Reynolds number $9,000$. For further information on these calculations, the reader is referred to forthcoming reports published by the Center for Turbulence Research.

The findings and contributions of this report are as follows:

• A high-order accurate, upwind-biased numerical method was developed for solving compressible flow problems in generalized coordinates.

• At Reynolds number $3,900$, the near-wake behind the circular cylinder contains pairs of counter-rotating streamwise vortices between the spanwise rollers. It is strongly three-dimensional, and cannot be accurately simulated with a two-dimensional calculation.

• At the same Reynolds number, a large-eddy simulation using the least-squares version of the dynamic subgrid-scale eddy-viscosity model was overall more accurate in the first four diameters of the wake than its counterparts using the fixed-coefficient Smagorinsky model or no subgrid-scale model.

• The magnitude of the eddy viscosity in the separated free shear layers and the near-wake region is in better agreement with expectations based on the flow physics when using the dynamic model rather than the fixed-coefficient model.

• The numerical dissipation generated by the fifth-order accurate, upwind-biased scheme applied to the convective fluxes, was found to have a significant impact on the turbulence in the near-wake.

• The simulation using the seventh-order accurate, upwind-biased scheme applied to the convective terms demonstrated the effects of decreased numerical dissipation on the computed solution. Smaller-scale structures appeared in the near-wake that were not present when using the fifth-order accurate upwind-biased scheme, and the energy of the computed solution was substantially increased at higher frequencies.

1.6   Summary

The next chapter describes the numerical method used in all the simulations in this report. Chapter 3 presents the test-problems validating the method and its implementation: the laminar, two-dimensional flow over a circular cylinder at steady and unsteady Reynolds numbers, as well as the linear-stability analysis of a forced channel flow in three dimensions. Large-eddy simulations of the flow over a circular cylinder at Reynolds number $3,900$ are documented in chapter 4, where the dynamic eddy viscosity model is evaluated and compared to the Smagorinsky model. Comparisons of the results obtained with the fifth and seventh-order accurate, upwind biased differencing schemes are presented in chapter 5. Conclusions regarding the performance of the dynamic model and the suitability of the numerical method are presented in chapter 6, where recommendations for extensions of this work are provided.

Regime	Reynolds number	Flow characteristics	Experiments
Steady	$0 \to \sim 5$	Attached boundary layer	Kovasznay 1949 Coutanceau & Bouard 1977
	~ 5	Flow convectively unstable	
	$5 \to \sim 40$	Symmetric, attached twin vortices	
	~ 25	Flow absolutely unstable (parallel stability theory)	
Unsteady Laminar	$40 \to 150$	Stable vortex street, decaying downstream	Tritton 1959,1971
	~ 90	Oblique vortex shedding	
Transitional	$150 \to 300$	Transition to turbulence in the wake. Fully turbulent wake in $40 \sim 50D$ downstream	Williamson 1989
Sub-critical	$300 \to 2 \times 10^5$	Transition in the free shear layers	Cantwell & Coles 1983 Roshko 1954a
	$\geq 10^4$	Most of the shear layers is turbulent Base pressure insensitive to Re	
Critical	$2 \times 10^5 \to 5 \times 10^5$	Lower transition in C_D from ~ 1.2 to ~ 0.3 Near wake width decreases to less than $1D$ Separation moves to rear of cylinder Laminar separation, transition, reattachment and turbulent separation of boundary layer	Achenbach 1968 Norberg 1987 Delaney & Sorensen 1953
	$5 \times 10^5 \to 3.5 \times 10^6$	Upper transition in C_D from ~ 0.3 to ~ 0.7 Near wake width increases (stays less than $1D$) Separation point moves forward	
Post-critical	$\geq 3.5 \times 10^6$	Turbulent cylinder boundary layer Regular vortex shedding ($St \simeq 0.27$), $C_D \sim 0.7$ Transition precedes separation, no reattachment	Roshko 1961 Shih et al. 1992

Table 1: Summary of cylinder flow regimes

Re Range → ↓ Simulation ↓	Transitional regime	Sub-critical regime	Critical regime	Post-critical regime
Two-dimensional Unsteady Navier-Stokes	$\overline{C}_D, \; St$	Unreliable		
RANS with $k - \epsilon$ model		Wall shear ahead of separation		Wall $\overline{C}_P$ up to recovery
		Inaccurate near-wake velocity and Reynolds stress distributions		
LES		$\overline{C}_D, \; St$, Wall $\overline{C}_P$ (Wake not resolved, $Re = 10^4$)		
DNS	Onset of 3-D	Transition ($Re = 500$)	$\overline{C}_D$ (Wake not resolved)	

Table 2: Status of prediction capabilities for flow over a cylinder

Chapter 2

Mathematical Formulation

2.1   Large-Scale Equations of Motion

The equations governing large-scale motions of the flow are derived by first considering the continuity, momentum and total energy equations:

$$\frac{\partial}{\partial t}\rho + \frac{\partial}{\partial x_k}(\rho u_k) = 0 \tag{2}$$

$$\frac{\partial}{\partial t}(\rho u_i) + \frac{\partial}{\partial x_k}(\rho u_k u_i + p\delta_{ik} - \sigma_{ik}) = 0 \tag{3}$$

$$\frac{\partial}{\partial t}e + \frac{\partial}{\partial x_k}(u_k(e+p) - \sigma_{ik}u_i + Q_k) = 0 \tag{4}$$

where the molecular heat flux and stress tensor are given by

$$Q_i = -\frac{\gamma}{(\gamma-1)RePr}\frac{\partial T}{\partial x_i} \tag{5}$$

$$\sigma_{ik} = \frac{1}{Re}\left(\frac{\partial u_i}{\partial x_k} + \frac{\partial u_k}{\partial x_i}\right) - \frac{2}{3}\frac{1}{Re}\delta_{ik}\frac{\partial u_j}{\partial x_j}. \tag{6}$$

The fluid is assumed to obey the perfect-gas law. The total energy and pressure are thus related through

$$e = \frac{p}{\gamma-1} + \frac{1}{2}\rho u_k u_k \tag{7}$$

These equations are normalized with free-stream sound-speed c_∞ and cylinder radius R_c. The quantity Re refers to the Reynolds number, $Re = \rho_\infty c_\infty R_c/\mu$; the molecular

19

viscosity μ is assumed to be independent of temperature; the Prandtl number Pr and Mach number M_∞ are fixed at 0.72 and 0.2 respectively in all cylinder simulations.

The compressible formulation is chosen to facilitate the potential inclusion of zonal methods into the numerical scheme. The principal issue in these methods is the prescription of boundary conditions at zonal interfaces. Boundary conditions based on momentum and energy fluxes across sub-volumes can be easily implemented for compressible methods, and have been successfully applied to a variety of flow situations (Rai 1985, 1986a,b).

The large-scale equations are obtained by applying a filtering operation, denoted by an overbar, to the governing equations. A filtered quantity $\overline{\phi}$ is defined as:

$$\overline{\phi}(\vec{x}) = \int_D G(\vec{x}, \vec{y})\phi(\vec{y})d\vec{y} \tag{8}$$

where D is the entire flow domain. G is a spatial filter which removes high spatial-frequency information, with characteristic length in direction x_i given by Δ_i. Filtering the equations leads to:

$$\frac{\partial}{\partial t}\overline{\rho} + \frac{\partial}{\partial x_k}\overline{\rho u_k} = 0 \tag{9}$$

$$\frac{\partial}{\partial t}\overline{\rho u_i} + \frac{\partial}{\partial x_k}(\overline{\rho u_k u_i} + \overline{p}\delta_{ik} - \overline{\sigma}_{ik}) = 0. \tag{10}$$

$$\frac{\partial}{\partial t}\overline{e} + \frac{\partial}{\partial x_k}\left(\overline{u_k(e+p)} - \overline{\sigma_{ik}\,u_i} - \frac{\gamma}{(\gamma-1)PrRe}\frac{\partial}{\partial x_k}\overline{T}\right) = 0. \tag{11}$$

Momentum fluxes are decomposed into resolvable and modeled components as

$$\overline{\rho u_k u_i} = \frac{\overline{\rho u_i}\,\overline{\rho u_k}}{\overline{\rho}} + \underbrace{\left[\overline{\rho u_k u_i} - \frac{\overline{\rho u_i}\,\overline{\rho u_k}}{\overline{\rho}}\right]}_{\tau_{ik}} \tag{12}$$

where τ_{ik} is the subgrid-scale stress tensor. Following Moin *et al.* (1991), the subgrid-scale viscous work is assumed to be negligible in the energy balance, leading to:

$$\overline{\sigma_{ik}u_i} = \overline{\sigma_{ik}}\,\overline{u_i} \tag{13}$$

The subgrid-scale transport term to be modeled in the filtered energy equation:

$$\overline{u_k(e+p)} - \overline{u}_k(\overline{e}+\overline{p}), \tag{14}$$

upon using (7) for the total energy, can be written as:

$$\overline{u_k(e+p)} - \overline{u}_k(\overline{e}+\overline{p}) = \frac{\gamma}{\gamma-1}q_k + \frac{1}{2}(\overline{\rho u_k u_j u_j} - \overline{u_k \rho u_j u_j}) \tag{15}$$

where q_k is the subgrid-scale heat flux:

$$q_k = \overline{\rho T u_k} - \overline{T}\,\overline{\rho u_k} = \overline{p u_k} - \frac{\overline{p}\,\overline{\rho u_k}}{\overline{\rho}} \tag{16}$$

The second term on the right-hand side of (15) represents the subgrid-scale transport of total kinetic energy, which is smaller than the subgrid-scale heat flux by a factor proportional to M_∞^2. It is neglected for the present low Mach number applications. The large-scale equations of motion are then:

$$\frac{\partial}{\partial t}\overline{\rho} + \frac{\partial}{\partial x_k}\overline{\rho u_k} = 0 \tag{17}$$

$$\frac{\partial}{\partial t}\overline{\rho u_i} + \frac{\partial}{\partial x_k}\left(\frac{\overline{\rho u_i}\,\overline{\rho u_k}}{\overline{\rho}} + \overline{p}\delta_{ik} - \overline{\sigma}_{ik} + \tau_{ik}\right) = 0 \tag{18}$$

$$\frac{\partial}{\partial t}\overline{e} + \frac{\partial}{\partial x_k}\left(\overline{u}_k(\overline{e}+\overline{p}) - \overline{\sigma}_{ik}\overline{u}_i - \frac{\gamma}{(\gamma-1)PrRe}\frac{\partial}{\partial x_k}\overline{T} + \frac{\gamma}{\gamma-1}q_k\right) = 0 \tag{19}$$

2.2   Turbulence Models

The large-scale momentum and energy equations are closed by modeling the subgrid-scale Reynolds stress tensor τ_{ij} and heat flux vector q_k. Comparisons will be presented in Chapter 4 between closures obtained from dynamic modeling and the Smagorinsky model with a damping function and a fixed coefficient. Each approach is described in the remainder of this Section.

In the first approach, subgrid-scale terms are evaluated with the local least-squares version of dynamic turbulence models (Moin *et al.* 1991, Lilly 1992), in which model coefficients are only functions of time and azimuthal and radial directions. These models use large-scale information extracted from the computed fields via a test-filtering operation. In the following derivations, a test-filtered function f is denoted by the symbol $\hat{f}$. In this work, the test-filter is chosen as a tophat filter in physical

21

space, and is applied in all spatial directions. The trapezoidal rule is used to evaluate the resulting volume integrals numerically. The characteristic scales of the grid and test-filtering operations are denoted by Δ and $\hat{\Delta}$ respectively.

2.2.1 Subgrid-Scale Reynolds Stresses

A subgrid-scale stress tensor T_{ij} at the test-filter scale $\hat{\Delta}$ is defined by analogy with the subgrid-scale Reynolds stress τ_{ij} as

$$T_{ij} = \widehat{\overline{\rho u_i u_j}} - \frac{\widehat{\overline{\rho u_i}}\,\widehat{\overline{\rho u_j}}}{\widehat{\overline{\rho}}}. \tag{20}$$

The subgrid-scale stress tensors at both grid and test-filter levels are modeled using a trace-free Smagorinsky formulation:

$$\tau_{ij} - \frac{\delta_{ij}}{3}\tau_{kk} = -2C(x,y,t)\overline{\rho}\,\Delta^2\,|\,\overline{S}\,|\,\overline{S_{ij}^*} \tag{21}$$

$$T_{ij} - \frac{\delta_{ij}}{3}T_{kk} = -2C(x,y,t)\widehat{\overline{\rho}}\,\hat{\Delta}^2\widehat{|\overline{S}|\overline{S_{ij}^*}} \tag{22}$$

where $\overline{S_{ij}^*}$ is the trace-free rate of strain tensor,

$$\overline{S_{ij}^*} = \overline{S}_{ij} - \frac{\delta_{ij}}{3}\overline{S}_{kk}, \tag{23}$$

and $|\overline{S}|$ is the norm of $\overline{S}_{ij}$:

$$|\overline{S}| = \sqrt{2\overline{S}_{ij}\overline{S}_{ij}}. \tag{24}$$

$C(\vec{x},t)$ is a model coefficient to be determined. T_{ij} and $\hat{\tau}_{ij}$ can be related through the Germano identity to the Leonard stress tensor L_{ij}:

$$\widehat{\left(\frac{\overline{\rho u_i}\,\overline{\rho u_j}}{\overline{\rho}}\right)} - \frac{\widehat{\overline{\rho u_i}}\,\widehat{\overline{\rho u_j}}}{\widehat{\overline{\rho}}} \equiv L_{ij} = T_{ij} - \hat{\tau}_{ij}, \tag{25}$$

where L_{ij} is computable from the resolved large-scale field. The model coefficient $C(x,y,t)$ is determined by substituting (21) and (22) into (25). The resulting relation

$$L_{ij} = 2C(x,y,t)\Delta^2\,M_{ij} \tag{26}$$

22

where

$$M_{ij} = \widehat{\overline{\rho}|\overline{S}|\overline{S}_{ij}^*} - \widehat{\overline{\rho}}\left(\frac{\widehat{\Delta}}{\Delta}\right)^2 \widehat{|\overline{S}|}\widehat{\overline{S}_{ij}^*} \tag{27}$$

is solved for C by contracting both sides with the tensor M_{ij}, which is equivalent to a least-squares minimization procedure (Lilly 1992). Denoting the spatial average in the spanwise direction by $< \; >$, $C\Delta^2$ is given by:

$$C(x,y,t)\Delta^2 = \frac{1}{2}\frac{< L_{ij}M_{ji} >}{< M_{ij}M_{ji} >}. \tag{28}$$

For reasons of numerical stability, negative values of the model coefficient C are discarded by an *ad hoc* clipping operation, which results in a modified coefficient C^*:

$$C^*(x,y,t)\Delta^2 = \frac{1}{2}(|C\Delta^2| + C\Delta^2) \tag{29}$$

The only adjustable constant in the model is the ratio of the test to grid-filter widths $\widehat{\Delta}/\Delta$. In all calculations, this ratio is chosen to be 2 (Germano *et al.*, 1991). The turbulent eddy viscosity is found from (21) as:

$$\mu_t = C^*\Delta^2\overline{\rho}\,|\overline{S}|. \tag{30}$$

2.2.2   Subgrid-Scale Energy

In compressible flow, the isotropic part of the subgrid-scale Reynolds stress tensor $\tau_{kk} = q^2$ cannot be combined with the thermodynamic pressure. Following Moin *et al.* (1991), q^2 is modeled using the relation:

$$q^2 = 2C_I(x,y,t)\overline{\rho}\,\Delta^2|\overline{S}|^2. \tag{31}$$

Contracting (25) and substituting (31) and a similar expression for T_{kk} leads to an expression for

$$\widehat{\left(\frac{\overline{\rho u_i}\,\overline{\rho u_i}}{\overline{\rho}}\right)} - \frac{\widehat{\overline{\rho u_i}}\,\widehat{\overline{\rho u_i}}}{\widehat{\overline{\rho}}} = 2C_I\left(\widehat{\overline{\rho}}\widehat{\Delta}^2\widehat{|\overline{S}|}^2 - \Delta^2\widehat{\rho|\overline{S}|^2}\right). \tag{32}$$

Averaging this expression in the spanwise direction and substituting in (31) gives the subgrid-scale energy q^2:

$$q^2 = \overline{\rho}\frac{< (\widehat{\frac{\overline{\rho u_i}\ \overline{\rho u_i}}{\overline{\rho}}}) - \frac{\widehat{\overline{\rho u_i}}\ \widehat{\overline{\rho u_i}}}{\widehat{\overline{\rho}}} >}{< \widehat{\overline{\rho}}(\frac{\widehat{\Delta}}{\Delta})^2\widehat{|\overline{S}|}^2 - \widehat{\overline{\rho}|\overline{S}|^2} >}|\overline{S}|^2.$$ (33)

The expressions (29) and (33) define the subgrid-scale Reynolds stress tensor τ_{ij}, closing the filtered momentum equations.

2.2.3   Subgrid-Scale Heat Flux

A model for subgrid-scale heat flux q_k is needed to close the energy equation. An eddy-diffusivity model is used, which introduces a turbulent Prandtl number Pr_t to be determined dynamically:

$$q_k = -\overline{\rho}\frac{\nu_t}{Pr_t}\frac{\partial\overline{T}}{\partial x_k} = -\overline{\rho}\frac{C^*(x,y,t)\Delta^2|\overline{S}|}{Pr_t}\frac{\partial\overline{T}}{\partial x_k}.$$ (34)

Writing the heat flux at the test-filter level as H_k using the same eddy-diffusivity model:

$$H_k = \widehat{\overline{\rho u_k}} - \frac{\widehat{\overline{\rho}}\ \widehat{\overline{\rho u_k}}}{\widehat{\overline{\rho}}} = -\widehat{\overline{\rho}}\frac{C^*\widehat{\Delta}^2\widehat{|\overline{S}|}}{Pr_t}\frac{\partial\widehat{\overline{T}}}{\partial x_k},$$ (35)

the difference $H_k - \widehat{q_k}$ is computable from the large-scale field:

$$H_k - \widehat{q_k} = \frac{\widehat{\overline{\rho}\overline{\rho u_k}}}{\overline{\rho}} - \frac{\widehat{\overline{\rho}}\ \widehat{\overline{\rho u_k}}}{\widehat{\overline{\rho}}} = -\frac{C^*\Delta^2}{Pr_t}\left(\left(\frac{\widehat{\Delta}}{\Delta}\right)^2\widehat{\overline{\rho}|\overline{S}|\frac{\partial\overline{T}}{\partial x_k}} - \widehat{\overline{\rho}}\widehat{|\overline{S}|}\frac{\partial\widehat{\overline{T}}}{\partial x_k}\right)$$ (36)

Following Moin *et al.* (1991), the expression for the turbulent Prandtl number is found by contracting the equation above with $\partial\overline{T}/\partial x_k$ and averaging in the homogeneous spanwise direction:

$$Pr_t = C^*(x,y,t)\Delta^2\frac{< (\frac{\widehat{\Delta}}{\Delta})^2\widehat{\overline{\rho}}\widehat{|\overline{S}|}\frac{\partial\widehat{\overline{T}}}{\partial x_k}\frac{\partial\overline{T}}{\partial x_k} - \widehat{\overline{\rho}|\overline{S}|\frac{\partial\overline{T}}{\partial x_k}}\frac{\partial\overline{T}}{\partial x_k} >}{< [\frac{\widehat{\overline{\rho}\overline{\rho u_k}}}{\overline{\rho}} - \frac{\widehat{\overline{\rho}}\ \widehat{\overline{\rho u_k}}}{\widehat{\overline{\rho}}}]\frac{\partial\overline{T}}{\partial x_k} >}.$$ (37)

This expression closes the large-scale energy equation. The filtered equations and associated subgrid-scale models have been presented in physical space. The corresponding discrete equations to be solved numerically are formulated in computational space. The transformation between the physical and computational spaces is presented in Section 2.3.

2.2.4   Fixed-Coefficient Smagorinsky Model

In simulations which use a fixed-coefficient Smagorinsky model, the subgrid-scale energy q^2 (equation 31) is neglected (*i.e.* $\tau_{kk} = 0$) and the turbulent Prandtl number is set to 1. The residual stress is:

$$\tau_{ij} = -2 C_s \overline{\rho} \, \Delta^2 \mid \overline{S^*} \mid \overline{S^*_{ij}}. \tag{38}$$

The eddy viscosity μ_t is related to the length scale l of the model by:

$$\mu_t = C_s \overline{\Delta}^2 \overline{\rho} \mid \overline{S^*} \mid = l^2 \overline{\rho} \mid \overline{S^*} \mid . \tag{39}$$

The length scale, chosen to match that used by Piomelli, Ferziger & Moin (1987), is given in generalized coordinates by:

$$l = C_s \sqrt{1 - e^{-(r-1)^{+3}/A^{+3}}} (J \Delta \xi \Delta \eta \Delta z)^{1/3} \tag{40}$$

with $C_s = 0.065$ and $A^+ = 25$. The Jacobian J of the two-dimensional coordinate transformation from (x, y) to (ξ, η)-space is defined in (42), $r = r(\xi, \eta)$ denotes the radial distance from the wall, ξ is the wall normal direction. Wall coordinates are defined using the mean skin-friction coefficient $\overline{C}_f$ to provide a velocity scale:

$$(\xi - 1)^+ = (\xi - 1) M_\infty Re \sqrt{\frac{\overline{C}_f}{2}}. \tag{41}$$

The Mach number appears in this relation since the Reynolds number is defined with the freestream sound speed as a velocity scale.

2.3 Transformation to Generalized Coordinates

The governing equations in physical space (x, y, z, t) are transformed to their homologues in computational space (ξ, η, z, t) via a two-dimensional time-independent mapping. In the cylinder simulations, ξ, η and z correspond to generalized radial, azimuthal and spanwise directions respectively. Letting J represent the Jacobian of this coordinate transformation

$$J = x_\xi y_\eta - x_\eta y_\xi, \tag{42}$$

derivatives in physical and computational spaces are related by the expression

$$\begin{pmatrix} \partial/\partial x \\ \partial/\partial y \end{pmatrix} = 1/J \begin{pmatrix} y_\eta & -y_\xi \\ -x_\eta & x_\xi \end{pmatrix} \begin{pmatrix} \partial/\partial \xi \\ \partial/\partial \eta \end{pmatrix}. \tag{43}$$

The computational space is a cube with equispaced point distributions in all directions. The mesh spacing in the transformed ξ and η directions are set to $\Delta\xi = \Delta\eta = 1$ for convenience, while the spacing in the spanwise direction is determined by the spanwise box and mesh sizes. Denoting as $\vec{Q}$ the conservative-variable vector

$$\vec{Q} = \begin{pmatrix} q_1 \\ q_2 \\ q_3 \\ q_4 \\ q_5 \end{pmatrix} = J \begin{pmatrix} \overline{\rho} \\ \overline{\rho u} \\ \overline{\rho v} \\ \overline{\rho w} \\ \overline{e} \end{pmatrix} \tag{44}$$

the large-scale equations can be formally written as

$$\frac{\partial}{\partial t}\vec{Q} + \frac{\partial}{\partial \xi}\vec{F}_\xi + \frac{\partial}{\partial \eta}\vec{F}_\eta + \frac{\partial}{\partial z}\vec{F}_z = \vec{0} \tag{45}$$

where $\vec{F}_\xi$ represents the total flux along the ξ direction. Detailed expressions for the fluxes appearing in (45) are given in Appendix A.

2.4   Spatial Discretization

2.4.1   Flux-Splitting and Non-Conservative Viscous-Flux Formulation

The governing equations in generalized coordinates (45) were presented in terms of the total fluxes $\vec{F}_\xi, \vec{F}_\eta$ and $\vec{F}_z$ along each direction. Each of these fluxes can be written as the sum of convective, viscous and heat flux components. In a generic direction x, these are given by $\vec{F}_x^e, \vec{F}_x^v$ and $\vec{F}_x^h$ respectively:

$$\vec{F}_x = \vec{F}_x^e + \vec{F}_x^v + \vec{F}_x^h \tag{46}$$

Before differencing these three fluxes numerically, it is necessary to rewrite each into different forms as follows.

The inviscid 'Euler' flux $\vec{F}_x^e$ is decomposed into signals propagating in opposite directions along all axes of the computational grid using flux-vector splitting (Steger & Warming 1981). The flux is diagonalized as

$$\vec{F}_x^e = P_x \Lambda_x P_x^{-1} \vec{Q}. \tag{47}$$

where Λ_x represents the diagonal eigenvalue matrix. The total convective flux is then written as

$$\vec{F}_x^e = \vec{F}_x^{e+} + \vec{F}_x^{e-} = P_x \Lambda_x^+ P_x^{-1} \vec{Q} + P_x \Lambda_x^- P_x^{-1} \vec{Q} \tag{48}$$

where

$$\Lambda_x^\pm = \frac{1}{2}(\Lambda_x \pm |\Lambda_x|). \tag{49}$$

Viscous and heat fluxes are decomposed into three components each, $\vec{F}_{\xi x}, \vec{F}_{\eta x}$ and $\vec{F}_{zx}$, which contain terms involving only primitive variable derivatives along the ξ, η and z directions respectively. Thus in each flux vector $\vec{F}_{x_1 x_2}$, the first index (x_1) indicates that the vector contains derivatives of primitive variables along the x_1 direction only, while the second index (x_2) indicates the direction of the flux. For the

two-dimensional coordinate mapping described in the previous section, the viscous and heat fluxes are:

$$\vec{F}_\xi^v = \vec{F}_{\xi\xi}^v + \vec{F}_{\eta\xi}^v + \vec{F}_{z\xi}^v; \quad \vec{F}_\xi^h = \vec{F}_{\xi\xi}^h + \vec{F}_{\eta\xi}^h \tag{50}$$

$$\vec{F}_\eta^v = \vec{F}_{\xi\eta}^v + \vec{F}_{\eta\eta}^v + \vec{F}_{z\eta}^v; \quad \vec{F}_\eta^h = \vec{F}_{\xi\eta}^h + \vec{F}_{\eta\eta}^h \tag{51}$$

$$\vec{F}_z^v = \vec{F}_{\xi z}^v + \vec{F}_{\eta z}^v + \vec{F}_{zz}^v; \quad \vec{F}_z^h = \vec{F}_{zz}^h \tag{52}$$

For numerical stability reasons, the second derivative operators acting on the primitive variables must be expressed separately from first derivative operators. Second derivatives appear in the governing equations through the viscous and heat fluxes, which are functions of $\vec{Q}$ and its spatial derivatives: $\vec{F}_{\xi\xi} = \vec{F}_{\xi\xi}(\vec{Q}, \vec{Q}_\xi)$, $\vec{F}_{\eta\eta} = \vec{F}_{\eta\eta}(\vec{Q}, \vec{Q}_\eta)$ and $\vec{F}_{zz} = \vec{F}_{zz}(\vec{Q}, \vec{Q}_z)$. Each of these fluxes can be written as

$$\vec{F}_{xx}(\vec{Q}, \vec{Q}_x) = A_{xx} \frac{\partial \vec{Q}}{\partial x} \tag{53}$$

where $A_{xx} = \partial \vec{F}_{xx}/\partial \vec{Q}_x$. The flux $\vec{F}_{xx}$ and is operated on in (45) by the operator $\partial/\partial x$, leading to

$$\frac{\partial \vec{F}_{xx}}{\partial x} = A_{xx} \frac{\partial^2 \vec{Q}}{\partial x^2} + \frac{\partial A_{xx}}{\partial x} \frac{\partial \vec{Q}}{\partial x}. \tag{54}$$

This chain-rule expansion yields non-conservative viscous flux terms.

Combining these transformations in the expressions for the convective, viscous and heat fluxes, the governing equations (45) become:

$$\frac{\partial}{\partial t}\vec{Q} + \overbrace{\frac{\partial}{\partial \xi}\vec{F}_\xi^{e+} + \frac{\partial}{\partial \eta}\vec{F}_\eta^{e+} + \frac{\partial}{\partial z}\vec{F}_z^{e+}}^{\text{upwind inviscid fluxes}} + \overbrace{\frac{\partial}{\partial \xi}\vec{F}_\xi^{e-} + \frac{\partial}{\partial \eta}\vec{F}_\eta^{e-} + \frac{\partial}{\partial z}\vec{F}_z^{e-}}^{\text{downwind inviscid fluxes}}$$

$$+ \frac{\partial}{\partial \xi}\left(\vec{F}_{\eta\xi}^v + \vec{F}_{z\xi}^v + \vec{F}_{\eta\xi}^h\right) + (A_{\xi\xi}^v + A_{\xi\xi}^h)\frac{\partial^2 \vec{Q}}{\partial \xi^2} + \frac{\partial}{\partial \xi}(A_{\xi\xi}^v + A_{\xi\xi}^h)\frac{\partial \vec{Q}}{\partial \xi}$$

$$+ \frac{\partial}{\partial \eta}\left(\vec{F}_{\xi\eta}^v + \vec{F}_{z\eta}^v + \vec{F}_{\xi\eta}^h\right) + (A_{\eta\eta}^v + A_{\eta\eta}^h)\frac{\partial^2 \vec{Q}}{\partial \eta^2} + \frac{\partial}{\partial \eta}(A_{\eta\eta}^v + A_{\eta\eta}^h)\frac{\partial \vec{Q}}{\partial \eta}$$

$$+ \frac{\partial}{\partial z}\left(\vec{F}_{\xi z}^v + \vec{F}_{\eta z}^v\right) + (A_{zz}^v + A_{zz}^h)\frac{\partial^2 \vec{Q}}{\partial z^2} + \frac{\partial}{\partial z}(A_{zz}^v + A_{zz}^h)\frac{\partial \vec{Q}}{\partial z} = \vec{0}. \tag{55}$$

Each flux and matrix appearing in (55) is described in Appendix A. Numerical discretization of this equation requires the use of two distinct spatial differencing schemes to be applied to the upwind and downwind convective fluxes, as well as first and second derivative schemes for the various components of the viscous terms.

2.4.2 Convective and Viscous Differencing Schemes

In the present work, convective derivatives are evaluated with two high-order accurate, one-point upwind-biased schemes in two different simulations. The fifth-order accurate scheme (Rai & Moin 1991) is given on a uniform mesh at grid location x_i by

$$\Delta \frac{\partial^+ f}{\partial x^+}\bigg|_i = -\frac{1}{30}f_{i-3} + \frac{1}{4}f_{i-2} - f_{i-1} + \frac{1}{3}f_i + \frac{1}{2}f_{i+1} - \frac{1}{20}f_{i+2} + \frac{\Delta^6}{60}\frac{\partial^6 f}{\partial x^6}\bigg|_i \qquad (56)$$

$$\Delta \frac{\partial^- f}{\partial x^-}\bigg|_i = \frac{1}{20}f_{i-2} - \frac{1}{2}f_{i-1} - \frac{1}{3}f_i + f_{i+1} - \frac{1}{4}f_{i+2} + \frac{1}{30}f_{i+3} - \frac{\Delta^6}{60}\frac{\partial^6 f}{\partial x^6}\bigg|_i \qquad (57)$$

where Δ represents the mesh spacing. The seventh-order accurate scheme is

$$\Delta \frac{\partial^+ f}{\partial x^+}\bigg|_i = \frac{1}{140}f_{i-4} - \frac{1}{15}f_{i-3} + \frac{3}{10}f_{i-2} - f_{i-1} + \frac{1}{4}f_i$$
$$+ \frac{3}{5}f_{i+1} - \frac{1}{10}f_{i+2} + \frac{1}{105}f_{i+3} - \frac{\Delta^8}{280}\frac{\partial^8 f}{\partial x^8}\bigg|_i \qquad (58)$$

$$\Delta \frac{\partial^- f}{\partial x^-}\bigg|_i = -\frac{1}{105}f_{i-3} + \frac{1}{10}f_{i-2} - \frac{3}{5}f_{i-1} - \frac{1}{4}f_i$$
$$+ f_{i+1} - \frac{3}{10}f_{i+2} + \frac{1}{15}f_{i+3} - \frac{1}{140}f_{i+4} + \frac{\Delta^8}{280}\frac{\partial^8 f}{\partial x^8}\bigg|_i \qquad (59)$$

The first and second derivatives appearing in the viscous terms are evaluated using central, sixth-order accurate schemes:

$$\Delta \frac{\partial f}{\partial x}\bigg|_i = \frac{1}{60}(f_{i+3} - f_{i-3}) + \frac{3}{20}(f_{i-2} - f_{i+2}) + \frac{3}{4}(f_{i+1} - f_{i-1}) - \frac{\Delta^7}{140}\frac{\partial^7 f}{\partial x^7}\bigg|_i \qquad (60)$$

$$\Delta^2 \frac{\partial^2 f}{\partial x^2}\bigg|_i = \frac{1}{90}(f_{i-3} + f_{i+3}) - \frac{3}{20}(f_{i-2} + f_{i+2}) + \frac{3}{2}(f_{i-1} + f_{i+1}) - \frac{49}{18}f_i - \frac{\Delta^8}{560}\frac{\partial^8 f}{\partial x^8}\bigg|_i \qquad (61)$$

Since the schemes applied to the convective terms are biased one point upwind, introducing sixth-order accurate first derivatives does not increase the global stencil size.

2.4.3 Modified Wave-Numbers

Applying the convective upwind schemes to a function $f(k)e^{ikx}$, letting $\theta = k\Delta$, and denoting the modified wave-number of the scheme by $\widehat{\theta} = \widehat{k}\Delta$, the fifth and seventh-order accurate schemes yield $\widehat{\theta}$ respectively given by:

$$\widehat{\theta} = \frac{1}{30}\sin 3\theta - \frac{3}{10}\sin 2\theta + \frac{3}{2}\sin\theta - i\left(-\frac{1}{30}\cos 3\theta + \frac{1}{5}\cos 2\theta - \frac{1}{2}\cos\theta + \frac{1}{3}\right) \quad (62)$$

$$\begin{aligned}
\widehat{\theta} = \ & -\frac{1}{140}\sin 4\theta + \frac{8}{105}\sin 3\theta - \frac{2}{5}\sin 2\theta + \frac{8}{5}\sin\theta \\
& + i\left(-\frac{1}{140}\cos 4\theta + \frac{2}{35}\cos 3\theta - \frac{1}{5}\cos 2\theta + \frac{2}{5}\cos\theta - \frac{1}{4}\right)
\end{aligned} \quad (63)$$

Real and imaginary parts of these modified wave-numbers are displayed in figures (1) and (2) respectively. The imaginary parts of the wave-numbers arises because of the upwind biasing. Their presence introduces a damping in an otherwise purely oscillatory system. This is clearly illustrated by considering the one-dimensional wave equation $\partial u/\partial t + \partial u/\partial x = 0$. A Fourier mode of u can be written as $f(t)e^{ikx}$, where $f(t) = f(0)e^{-ikt}$. Substituting for k the modified wave-number of the scheme $\widehat{k} = \widehat{k}_r + i\widehat{k}_i$ introduces in the response of $f(t)$ the term $e^{\widehat{k}_i t}$. For the fifth-order scheme, since $\widehat{k}_i$ is negative at wave numbers larger than $0.35\pi/\Delta$ (figure 2), where the differencing scheme starts being inaccurate, this exponential term damps the response at frequencies which are too high to be accurately differentiated by the scheme on a given mesh. The real part of $\widehat{\theta}$ is compared in figure (1) with the modified wave-numbers of the fourth-order central scheme:

$$f'_j = \frac{1}{12\Delta}(f_{j-2} - 8f_{j-1} + 8f_{j+1} - f_{j-2}) \quad (64)$$

which is

$$\widehat{\theta} = \frac{1}{6}(8\sin\theta - \sin 2\theta), \quad (65)$$

as well as with the modified wave-number of the fourth-order accurate Padé scheme

$$f'_{j+1} + f'_{j-1} + 4f'_j = \frac{3}{\Delta}(f_{j+1} - f_{j-1}) + \frac{\Delta^4}{30}\frac{\partial^4 f}{\partial x^4}\bigg|_j \quad (66)$$

30

given by

$$\widehat{\theta} = \frac{3\sin\theta}{2 + \cos\theta}. \tag{67}$$

The fourth-order Padé and fifth-order upwind schemes have nearly identical modified wave-numbers up to $k \simeq 0.45\pi/\Delta$. At higher wave-numbers the error in the Padé scheme is consistently smaller than that in the upwind scheme. The Padé scheme has a purely real modified wave number, indicating that the scheme does not generate numerical dissipation on a uniform grid.

The modified wave-number for the second derivative scheme (61) applied to viscous fluxes

$$\widehat{\theta}^2 = -\frac{1}{45}\cos 3\theta + \frac{3}{10}\cos 2\theta - 3\cos\theta + \frac{49}{18} \tag{68}$$

is shown in figure (3) compared with the modified wave-number of a second-order accurate central difference scheme, for which $\widehat{\theta}^2 = 2(1 - \cos\theta)$. The second-order scheme is accurate for wave-numbers below approximately $0.3\pi/\Delta$, whereas the sixth-order scheme is close to the exact solution for wave-numbers up to $0.6\pi/\Delta$. Wave-numbers higher than these limiting values are under-damped in the respective schemes, but the sixth-order method provides 50% more dissipation than the second-order one at the highest wave-number of $k = \pi/\Delta$.

Near the wall and outer boundaries, spatial differencing schemes must be modified with a corresponding reduction in order of accuracy. At these boundaries, convective and viscous derivatives are second-order accurate. Details of the schemes used in these regions are provided in Appendix (A).

2.5   Time Integration

The governing equations are marched forward in time using a variable time-step, fully implicit scheme defined at time-level $n + 1$ by:

$$\frac{\partial \vec{Q}^{n+1}}{\partial t} \simeq \frac{\alpha + \beta}{\alpha\beta}\vec{Q}^{n+1} + \frac{\beta}{\alpha(\alpha - \beta)}\vec{Q}^n + \frac{\alpha}{\beta(\beta - \alpha)}\vec{Q}^{n-1} \tag{69}$$

where $\alpha = \Delta t^{n+1}$ is the time step at time level $n + 1$, and $\beta = \Delta t^{n+1} + \Delta t^n$. For constant time-steps this scheme is second-order accurate. In the turbulent cylinder

31

calculations presented in Chapter 4 and Appendix F, time steps were defined by constant Courant numbers. The mean variation in Δt from step to step was approximately 0.01% for a typical simulation. The time derivative $\partial \vec{Q}^{n+1}/\partial t$ appearing in (69) is given by the governing equations (55). Equation (69) represents a system of coupled non-linear equations. It is solved at each time step with a modified Newton-Raphson iteration technique (Rai & Moin 1993). An iterative approach was chosen because the direct construction and inversion of the implicit systems defined by (69) present several difficulties. The fifth-order upwind spatial differencing scheme leads to block hepta-diagonal implicit matrices, which are expensive to generate and invert. In three dimensions, the size of the implicit systems requires the use of a factored approach. However a direct factored scheme involves two additional difficulties which can restrict the time-step size. The viscous fluxes which involve spatial cross-derivatives (e.g. $\partial^2 \vec{Q}/\partial \xi \partial \eta$) must be evaluated explicitly (Beam & Warming 1978), generating a time error of order dependent on the type of explicit scheme, and the factoring error, of order Δt^2, cannot be eliminated.

An iterative technique can circumvent these difficulties. The iterative scheme is based on expressing the solution vector field $\vec{Q}^{n+1}$ at time-level t^{n+1} as the zero of the function

$$f[\vec{Q}^{n+1}] = -\vec{Q}^{n+1} + c_1 \vec{Q}^n + c_2 \vec{Q}^{n-1} + c_3 \frac{\partial}{\partial t} \vec{Q}^{n+1} \tag{70}$$

which is a statement equivalent to (69). The coefficients c_1 through c_3 represent the corresponding combinations of α and β in (69). The root of f is sought using a classical Newton approach:

$$-\left(\frac{\partial}{\partial \vec{Q}} f[\vec{Q}]\right)^p (Q^{p+1} - Q^p) = f[\vec{Q}^p], \tag{71}$$

where p is the iteration index. The Jacobian on the left-hand side is obtained from (70) as

$$-\frac{\partial}{\partial \vec{Q}} f[\vec{Q}] = \frac{\partial}{\partial \vec{Q}} [\vec{Q} - c_3 \frac{\partial}{\partial t} \vec{Q}] = I - c_3 \frac{\partial}{\partial \vec{Q}} \left(\frac{\partial}{\partial t} \vec{Q}\right). \tag{72}$$

The full iterative scheme is written by substituting (72) and (70) into (71), leading to:

$$\left[I - c_3 \frac{\partial}{\partial \vec{Q}} \left(\frac{\partial}{\partial t} \vec{Q}\right)\right]^p (\vec{Q}^{p+1} - \vec{Q}^p) = \vec{R}^{n,p} \tag{73}$$

32

where the right-hand side vector is

$$\vec{R}^{n,p} = -\vec{Q}^p + c_1\vec{Q}^n + c_2\vec{Q}^{n-1} + c_3\frac{\partial}{\partial t}\vec{Q}^p. \tag{74}$$

The time derivative of $\vec{Q}$ in this relation is given by (55). Upon convergence of the iterations, $\vec{Q}^{p+1} = \vec{Q}^p = \vec{Q}^{n+1}$, and the left-hand side of (73) is zero regardless of any approximation made in evaluating the Jacobian terms $\partial(\partial\vec{Q}/\partial t)/\partial\vec{Q}$. The implicit system (73) is inverted by factoring the equations. The factoring error is also driven to zero upon convergence of the iterations. Schematically, the three resulting factored systems are written as:

$$(I + c_3 M_\eta)^p \vec{Q}^* = \vec{R}^{n,p} \tag{75}$$

$$(I + c_3 M_z)^p \vec{Q}^{**} = \vec{Q}^* \tag{76}$$

$$(I + c_3 M_\xi)^p \Delta\vec{Q}^{p+1} = \vec{Q}^{**} \tag{77}$$

where M_η, M_z and M_ξ represent linearized Jacobians in the η, z and ξ directions respectively. The crux of the method lies in approximating these Jacobians so that they are inexpensive to compute, define easily invertible matrices, and lead to stable iterations. The construction of the Jacobians in this work follows the discussions of Rai & Moin (1991) and Pulliam & Chaussee (1981). At each iteration, viscous stresses are treated implicitly in the wall-normal direction ξ, but are neglected in the periodic azimuthal (η) and spanwise (z) directions. The iterative scheme finally becomes:

$$\left(I + c_3\Lambda_\eta^+\frac{\partial^+}{\partial\eta} + c_3\Lambda_\eta^-\frac{\partial^-}{\partial\eta}\right)^p \vec{Q}^* = P_\eta^{-1}\vec{R}^{n,p} \tag{78}$$

$$\left(I + c_3\Lambda_z^+\frac{\partial^+}{\partial z} + c_3\Lambda_z^-\frac{\partial^-}{\partial z}\right)^p Q^{**} = P_z^{-1}P_\eta\vec{Q}^* \tag{79}$$

$$\left(I + c_3\frac{\partial\vec{F}_\xi^{e+}}{\partial\vec{Q}}\frac{\partial^+}{\partial\xi} + c_3\frac{\partial\vec{F}_\xi^{e-}}{\partial\vec{Q}}\frac{\partial^-}{\partial\xi} + c_3\frac{\partial^v}{\partial\xi}\left(\frac{\partial\vec{F}_{\xi\xi}^v}{\partial\vec{Q}} + \frac{\partial\vec{F}_{\xi\xi}^h}{\partial\vec{Q}}\right)\right.$$
$$\left. + c_3\frac{\partial^v}{\partial\xi}\left(\frac{\partial\vec{F}_{\xi\xi}^v}{\partial\vec{Q}_\xi} + \frac{\partial\vec{F}_{\xi\xi}^h}{\partial\vec{Q}_\xi}\right)\frac{\partial^v}{\partial\xi} + c_3\left(\frac{\partial\vec{F}_{\xi\xi}^v}{\partial\vec{Q}_\xi} + \frac{\partial\vec{F}_{\xi\xi}^h}{\partial\vec{Q}_\xi}\right)\frac{\partial^2}{\partial\xi^2}\right)^p \Delta\vec{Q}^{p+1} = P_z\vec{Q}^{**} \tag{80}$$

The eigenvector matrices P_η and P_z, obtained from the diagonalization of the azimuthal and spanwise Euler fluxes, are described in Appendix A. On the left-hand

33

side of these systems, convective derivatives are approximated with upwind first-order accurate schemes, while central second-order accurate schemes are applied for viscous derivatives. This results in tridiagonal scalar systems in the periodic directions and a block-tridiagonal system in the wall-normal direction, which are inverted directly.

In all laminar and turbulent computations in this report, the number of iterations per time-step is set to three, which is shown to be sufficient to reduce the residual norm ($|\vec{R}^{n,p}|$) by a factor of 10^2 to 10^4 at each time step (Appendix D, Section D.3.3 and Appendix F, Section F.3.2). Validation tests in the laminar vortex-shedding regime of the flow over a circular cylinder (Chapter 3) provide some indication that this level of convergence is sufficient to ensure that the residual error does not noticeably affect the accuracy of the computed solution.

Applied to the model equation

$$\frac{\partial u}{\partial t} = \lambda u \tag{81}$$

the time advancement scheme (69) is stable for a given time-step Δt provided the inequality

$$|\sigma|^2 = \frac{|2 \pm \sqrt{1 + 2\lambda\Delta t}|^2}{|3 - 2\lambda\Delta t|^2} \leq 1 \tag{82}$$

holds. The relation above also defines the stability criterion for the model equation

$$\frac{\partial u}{\partial t} + c\frac{\partial u}{\partial x} = 0 \tag{83}$$

applied to one Fourier component $\hat{f}(k)e^{ikx}$ of u, provided the coefficient λ is set to the complex expression

$$\lambda = -\frac{c}{\Delta x}\left(\frac{1}{30}\sin 3\theta - \frac{3}{10}\sin 2\theta + \frac{3}{2}\sin\theta - i(-\frac{1}{30}\cos 3\theta + \frac{1}{5}\cos 2\theta - \frac{1}{2}\cos\theta + \frac{1}{3})\right) \tag{84}$$

where the term between parentheses represents the modified wave number of the fifth-order accurate upwind convective scheme (62). The envelope $(\lambda_r\Delta x\Delta t/c, \lambda_i\Delta x\Delta t/c)$ corresponding to $|\sigma|^2 = 1$ is displayed in figure (4). The scheme is unconditionally stable for $\lambda_r < 0$.

34

2.6   Boundary Conditions

The boundary conditions needed for the simulation of the flow over a circular cylinder are wall and far-field boundary conditions applicable to the conservative variable increment $\Delta \vec{Q}$ (see equation 80). Spanwise and azimuthal directions being periodic, the appropriate boundary conditions on the intermediate fields $\vec{Q}^*$ (equation 78) and $\vec{Q}^{**}$ (equation 79) are periodic conditions. Wall and far-field conditions are imposed implicitly for improved numerical stability, and are updated after each time-step to prevent drifting. Their precise formulation is presented in Appendix B.

At the cylinder surface, no-slip boundary conditions are applied. The pressure derivative is evaluated from the normal-momentum equation, and the surface heat-flux is set to zero.

Free surfaces are divided into potential and wake-region boundaries, each one of which admits a different set of boundary conditions. The conditions imposed in the potential region are based on locally one-dimensional Riemann invariants (Pulliam 1986b) and neglect all viscous contributions. At the subsonic outflow, the value of the first Riemann invariant is imposed as that given by the potential flow around a circular cylinder. At the subsonic inflow, the required four boundary conditions on entropy, spanwise and tangential velocities, and a Riemann invariant, are similarly based on the potential flow solution.

The edges of the wake layer at the domain boundary are determined using a δ_{99} boundary-layer criterion. Within the wake outflow region, primitive variables are extrapolated with a first-order accurate scheme. These boundary conditions are found to be stable, but are inaccurate and generate perturbation waves which propagate from the outer boundary toward the center of the computational domain. In all simulations, a long region of highly stretched mesh minimizes the influence of the boundary conditions on the region of interest.

2.7   Numerical Dissipation and Aliasing Control

The upwind-biased scheme chosen to evaluate the derivative of the convective fluxes in the equations of motions introduces numerical dissipation in the computation. This dissipation can affect the accuracy of the computed solution in regions where it is of the same order as the sum of its molecular and subgrid-scale counterparts. On the other hand numerical dissipation is instrumental in stabilizing the numerical method, by dissipating the energy content of the high frequencies in the flow, and thereby acting as a built-in aliasing control (not removal) mechanism.

In direct simulations of incompressible turbulent channel flow at Reynolds number 180 based on wall shear-velocity and channel half-width, Rai & Moin (1991) observed that the numerical dissipation introduced by the upwind-biased scheme presented above (equation 56), was apparently large enough to control aliasing by dissipating the high frequency content of the solution fields. However a precise analysis of numerical dissipation was not provided. Further the ability of a scheme to control aliasing errors in an incompressible calculations may not extend to compressible calculations, the latter involving many more divisions and multiplications of the primitive variables than the former. It was observed from the vorticity fluctuations that small-scale motions were damped in a coarse simulation which resolved the mean flow accurately. Energy spectra for this coarse simulation were not presented. Root mean square vorticity fluctuations agreed well with spectral calculation results in a fine-mesh simulation. The one-dimensional streamwise energy spectra in that simulation showed that the energy at high frequencies was about two and a half decades below the values obtained from spectral calculations. The spectral simulation used for comparison required $(192 \times 129 \times 160)$ grid-points, while the upwind-biased finite-difference calculations used a $(192 \times 101 \times 192)$-point mesh. Thus although the study by Rai & Moin concluded that high-order upwind-biased finite-difference methods were good candidates for direct simulations of complex-geometry flows, the applicability of such methods to large-eddy simulations was not investigated.

In a large-eddy simulation the prime objective is to accurately resolve low-order statistics on a coarse mesh. The use of an upwind-biased scheme constrains the grid to

be fine enough that the large scales are not affected by numerical dissipation. Further in such a simulation, a turbulence model will impact the computed large scales only if the magnitude of the numerical dissipation is sufficiently small compared to that of the molecular dissipation.

In the simulations at Reynolds number $3,900$ the numerical dissipation generated by the fifth-order upwind-biased scheme was found to significantly damp the one-dimensional frequency spectra between five and ten diameters downstream of the cylinder. The level of numerical dissipation present in the computed solution overwhelmed the turbulence model, which did not have an impact on the mean velocities and Reynolds shear stresses in that region. The simulation with the seventh-order accurate upwind-biased scheme demonstrated that reducing numerical dissipation led to more energetic small scales in the near-wake. These results are further discussed in chapters 4 and 5.

2.8   Triple Flow Decomposition

The flow in the cylinder near-wake is characterized by a periodic vortex shedding motion, which at sub-critical Reynolds numbers contributes between a half and a third of the total Reynolds stresses (Cantwell & Coles 1983, Matsumura & Antonia 1993). To differentiate between the random and periodic components of the Reynolds stresses, a flow variable can be decomposed into a global mean component $\bar{s}$, a periodic component $\tilde{s}$, and a random motion s' (Reynolds & Hussain 1972, Hussain 1983, 1986). The total variable is given by

$$s(x, y, z, t) = \bar{s}(x, y) + \tilde{s}(x, y, t) + s'(x, y, z, t) \tag{85}$$

A precise definition of the periodic and random components is as follows. The spanwise-averaged lift coefficient as a function of time $C_L(t)$ oscillates quasi-periodically around zero due to vortex shedding. Each period of oscillation is divided into $N_p = 16$ segments. The first segment is chosen to coincide with a zero lift coefficient. Over a time interval $0 \le t \le T$ which includes N_T vortex shedding periods, the instants corresponding to a particular segment k are denoted by t_n^k, for $n = 1, 2, \cdots, N_T$. Given

the spanwise average $< s(x, y, t) >$ of $s(x, y, z, t)$, the spanwise-average at constant phase k, also called a phase-average, is computed by averaging values of $< s(x, y, t) >$ corresponding to identical phases in the time series:

$$< s(x, y) >_k = \frac{1}{N_T} \sum_{n=1}^{N_T} < s(x, y, t_n^k) > \quad k = 1, \cdots, N_p. \tag{86}$$

The periodic response at constant phase $\tilde{s}_k$ is obtained from the N_p averages at constant phase by subtracting the spanwise- and time-averaged component $\bar{s}(x, y)$:

$$\tilde{s}(x, y)_k = < s(x, y) >_k - \bar{s}(x, y) \tag{87}$$

Once the periodic component is known at each phase, the random fluctuation s' can be found from (85). By construction, the time-averaged periodic component $\bar{\tilde{s}}(x, y)$, as well as the time- and spanwise-averaged random fluctuations $\overline{s'}(x, y)$ are zero. The triple decomposition leads to the definition of Reynolds stresses which represent the distinct contributions of the random and periodic motions, denoted as $\overline{u_i' u_j'}$ and $\overline{\tilde{u}_i \tilde{u}_j}$ respectively, and related by the equation:

$$\overline{u_i' u_j'} = \overline{u_i u_j} - \overline{u_i}\,\overline{u_j} - \overline{\tilde{u}_i \tilde{u}_j}. \tag{88}$$

38
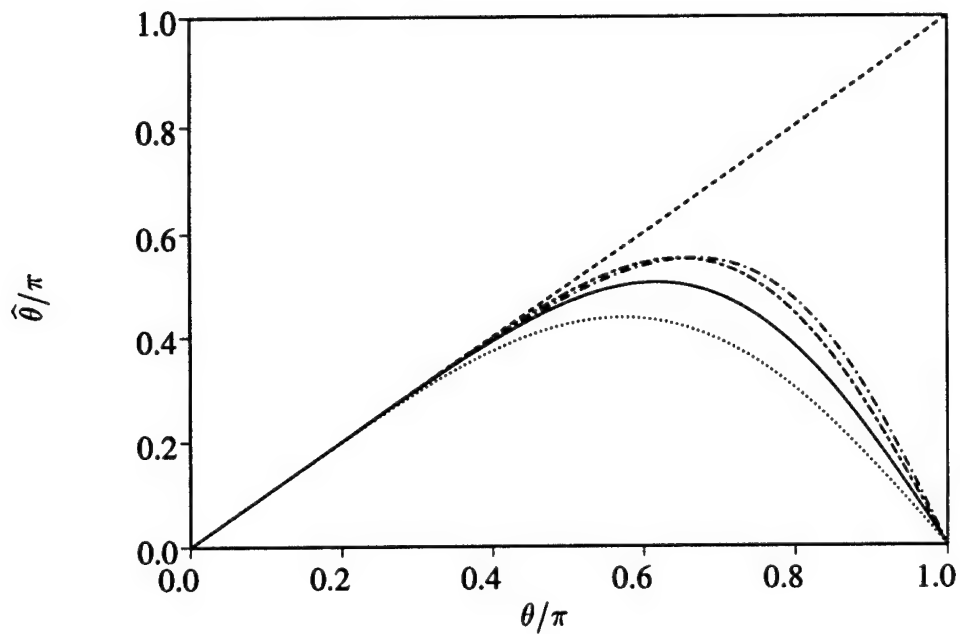
Figure 1: Real part of the inviscid modified wave number
---- : Exact; —— : Fifth order upwind; —·— : Seventh order upwind
—·— : 4$^{\text{th}}$ order Padé; · · · : 4$^{\text{th}}$ order central
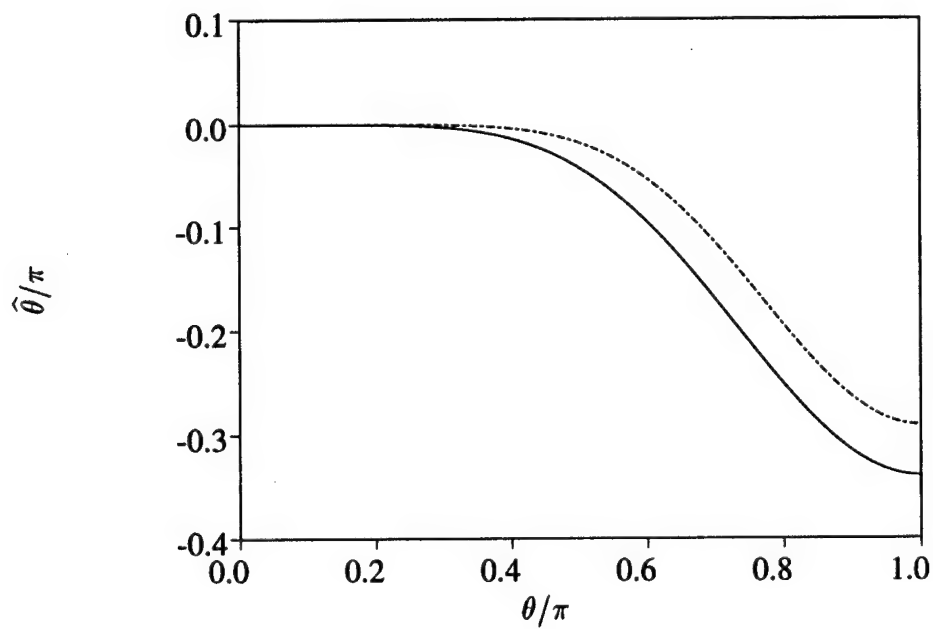
Figure 2: Imaginary part of the inviscid modified wave number
—— : Fifth order upwind biased; ——— : Seventh order upwind biased
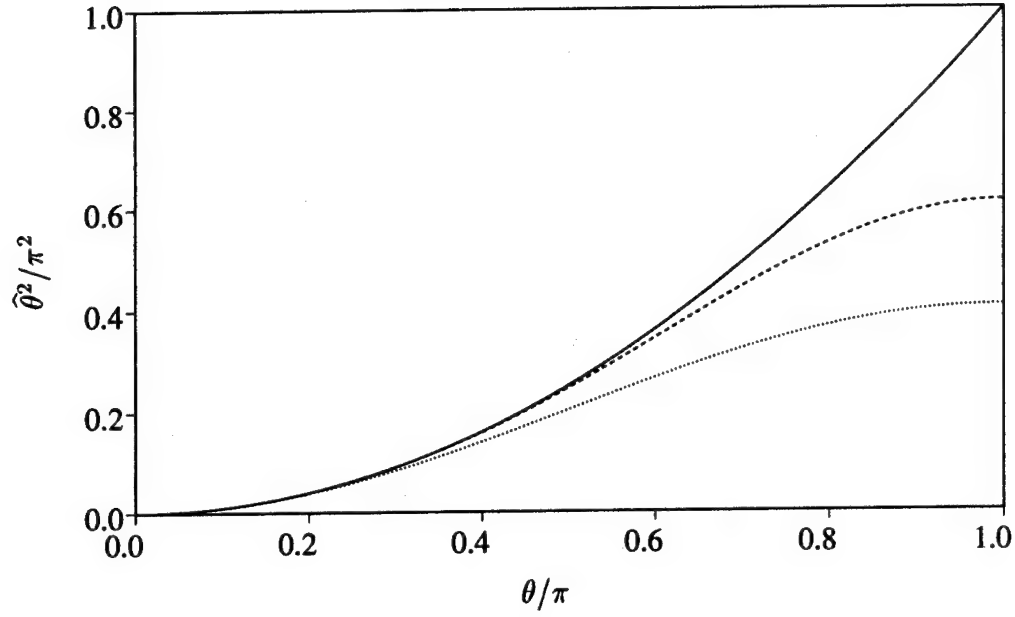
Figure 3: Modified wave number of the viscous second derivative scheme
——— : Exact; - - - - : Sixth order central; $\cdots$: Second order central
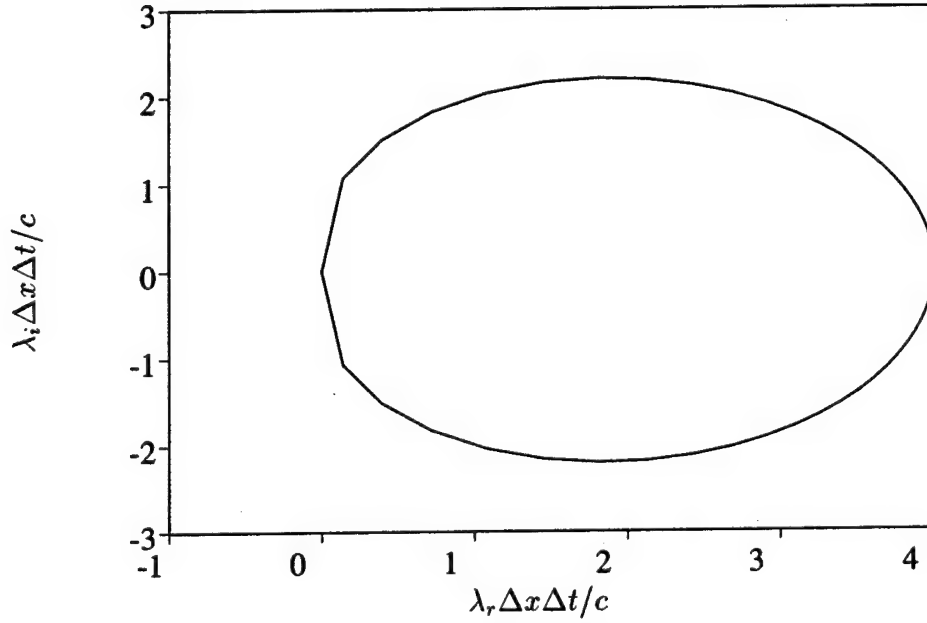
Figure 4: Time scheme stability diagram: the region within the ellipsoid is unstable.

Chapter 3

Validation of the Numerical Method

3.1 Introduction

At Reynolds numbers below 90, the flow over a circular cylinder is two-dimensional (Bloor 1964, Williamson 1989, 1991a). Its mean properties in the near-wake and on the cylinder surface have been extensively documented numerically and experimentally. In Section 3.2, the accuracy of the numerical method is examined in the computation of the steady near-wake region at Reynolds number 20. The computational domain radius required to minimize the effect of boundary conditions on near-wake quantities is found by observation of the pressure distribution in the wake to be $300R_c$, where R_c is the cylinder radius. Pressure and drag coefficients at the cylinder surface, as well as the near-wake velocity distribution are found to compare well with experimental and other computational results.

At Reynolds numbers between 40 and 150, two-dimensional vortex shedding occurs according to a well defined Strouhal-Reynolds number relation (equation 1). Section 3.3 presents the results of two-dimensional simulations at Reynolds numbers of 80 and 100. The computed Strouhal frequencies are in good agreement with the measurements of Williamson.

The computation of the linear stability of a periodic channel flow at Reynolds

41

number 7,500, based on channel half-width and centerline velocity, provides a three-dimensional test of the numerical method. Because the corresponding perturbation equations do not admit three-dimensional growing modes, the perturbation is chosen as the slowest decaying Orr-Sommerfeld mode. The error in the perturbation-energy growth-rate, computed with a time step of $0.02h/U_\infty$, is less than 1% of its exact value on a mesh containing $(129 \times 32 \times 32)$ points in the cross-channel, streamwise and spanwise directions respectively. The parameters h and U_∞ above refer to the channel half-width and the steady-state streamwise velocity at the channel centerline. The validations described in this chapter were performed with the fifth-order accurate, upwind-biased scheme.

3.2   Steady Cylinder Flow

At a Reynolds number of 20, a steady recirculation bubble is attached to the cylinder surface. The salient features of this flow are the bubble length, its velocity distribution, the drag coefficient, the pressure and vorticity distributions on the cylinder surface and the angle of separation of the boundary layer. This Reynolds number is chosen because its properties are well documented. It has been investigated experimentally by Tritton (1959), Coutanceau & Bouard (1977), Thom (1933) and Taneda (1956), semi-analytically by Imai (1951) and Nieuwstadt & Keller (1973), and numerically by Dennis & Chang (1970), Nieuwstadt & Keller (1973), Takami & Keller (1969) and Fornberg (1980) amongst others.

The grid-converged results presented below were obtained on a computational domain of radius $300R_c$, with a mesh containing (256×300) points in the radial and azimuthal directions respectively (Appendix D). Azimuthal points are equispaced, while the radial grid-spacing increases geometrically with a stretching factor of 1.03.

Table (3) summarizes the values of the principal flow features of the near wake. At Reynolds number 20, the computed drag coefficient (1.99) is within 3% of Tritton's experimental value of 2.05. The velocity in the recirculating region is very small and difficult to measure experimentally. Coutanceau & Bouard (1977) measured

	Simulation	Experiment	Asymptotic
Drag Coefficient	1.99	2.05	2.05
Bubble Length	0.93 D	0.93 D	0.93 D
Separation Angle	43.8 Deg.	41.6 Deg.	45.8 Deg.
Minimum Velocity in Bubble	$-0.031U_\infty$	$-0.040U_\infty$	$-0.030U_\infty$
Position of Velocity Minimum	0.42 D	0.36 D	0.43 D

Table 3: Steady-flow topology at Reynolds number 20

a minimum velocity in the bubble of $-0.040U_\infty$, located $0.36D$ downstream of the cylinder surface. The computed values for these parameters are $-0.031U_\infty$ and $0.42D$ respectively. They are within 3% of the asymptotic solution of Nieuwstadt & Keller (1973), which predicts a minimum velocity of $-0.030U_\infty$ at $0.43\ D$.

The separation angle of the boundary-layer and the wall vorticity (figure 6) compare well with other computational and experimental results. In the separated flow region, the wall vorticity magnitude is smaller than Fornberg's prediction (1980), but in good agreement with the results of Dennis & Chang and Nieuwstadt & Keller. The wall pressure coefficient (figure 5), agrees well with the results of these three computational groups.

Outside the recirculation zone, within 2.5 diameters downstream of the cylinder, experimental and asymptotic streamwise velocities coincide (figure 7), and differ from the computation by less than one percent. From 5 to 20 diameters downstream (figure 8), the computed streamwise velocity agrees well with Imai's analytical results (1951), as well as with Nishioka & Sato's simulations (1974), but not with the results

of Takami & Keller (1969).

3.3   Laminar Vortex Shedding

Two-dimensional simulations in the regular vortex-shedding Reynolds number range establish the temporal accuracy of the numerical method. These simulations, at Reynolds numbers 80 and 100, further test the robustness of the far-field boundary conditions in unsteady flow. Details of the grid construction and mesh refinement studies at each Reynolds number are provided in Appendix D.

The computed Strouhal numbers are 0.152 and 0.164 at Reynolds numbers 80 and 100 respectively (figure 9). These agree well with the experimental data of Williamson (1989), given by equation (1) as 0.153 and 0.164 at the same Reynolds numbers. The lift coefficient time histories at both Reynolds numbers (figures 93 and 97, Appendix D) demonstrate that the flow is energetic only at the Strouhal frequency in the near wake. Don (1989) suggested that numerical boundary conditions could generate spurious modulating frequencies in the lift response. The absence of such modes in the present simulations indicates that inaccuracies at the outer domain boundaries do not unduly affect the solution in the near wake.

3.4   Linear Stability of a Forced Channel Flow

The mathematical formulation of the linear stability of a periodic channel is presented in Appendix E. The salient feature of this problem is the forcing introduced to drive the flow along the channel. This external forcing is necessary because a constant pressure gradient, corresponding to a linear pressure distribution along the channel, is not a solution to the compressible boundary-value problem, and cannot be used as a momentum source. In the forced compressible channel formulation, the pressure is constant while the external forcing acts as a source of momentum in the streamwise direction.

Appendix E presents the analytical steady-state channel solution, as well as the

44

Mesh size	Time step	Decay rate	Error in decay rate
$65 \times 16 \times 16$	1.00×10^{-2}	-3.19×10^{-3}	-27.5%
$129 \times 16 \times 16$	0.97×10^{-2}	-4.92×10^{-3}	-11.8%
$129 \times 32 \times 32$	1.94×10^{-2}	-4.45×10^{-3}	1.0%

Table 4: Linear stability: computed energy-decay rates

derivation of the appropriate small-disturbance equations. The Mach number in this stability analysis is set to $M_\infty = 0.1$. The Reynolds number is $Re = 7,500$, chosen to match that in the work of Malik, Zang & Hussaini (1985).

In three dimensions, the slowest decaying Orr-Sommerfeld mode is chosen as the perturbation of the steady-state solution. The eigenvalue of this mode (equation 207) is $c = c_r + i c_i = 0.02962395 - i0.00220154$, corresponding to a perturbation-energy decay-rate of $2c_i = 4.40 \times 10^{-3}$.

Three simulations are performed on a computational box of size ($2h \times 2\pi h \times 2\pi h$) where h is the channel half-width. The three meshes contain ($65 \times 16 \times 16$), ($129 \times 16 \times 16$) and ($129 \times 32 \times 32$) points in the vertical, streamwise and spanwise directions respectively. Both periodic directions have equispaced point distributions, while a hyperbolic tangent with a stretching factor $\alpha = 4.5$ (equation 215) is used across the channel. The initial perturbation field is scaled so that the amplitude of the maximum vertical velocity across the channel is $10^{-4}U_\infty$, where U_∞ is the steady-state channel-centerline streamwise velocity.

The equations are marched forward in time with the second-order accurate implicit scheme described in Chapter 2, using a velocity-based Courant number of 0.025 for the ($65 \times 16 \times 16$) and ($129 \times 16 \times 16$) cases, and of 0.1 for the calculation with the finest mesh. All simulations are run for $2T_0$, where $T_0 = 21.21h/U_\infty$ is the time

necessary for the perturbation wave to propagate through the streamwise length of the computational box. The computed perturbation energy decay-rates and associated time-steps on each grid are displayed in table (4). On the finest mesh, the decay rate is predicted within 1% of its exact value. In their incompressible two-dimensional computation of a growing perturbation, Malik *et al.* used a Fourier method with 4 collocation points in the streamwise direction, and a second-order finite difference scheme on a Chebyshev mesh in the vertical direction. With 64 and 128 points across the channel, the errors in perturbation energy magnitude after two periods $(t = 2T_0)$ were 20% and 4.7% respectively.
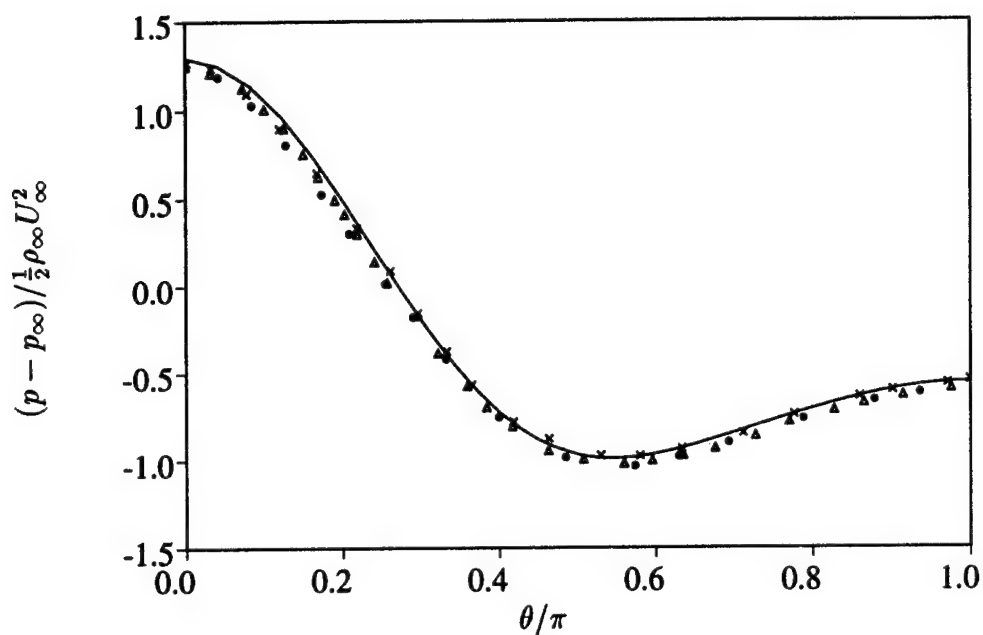
Figure 5: Re=20; Wall pressure coefficient
——— : Present results; ● : Dennis & Chang (1970)
× : Fornberg (1980); △ : Nieuwstadt & Keller (1973)
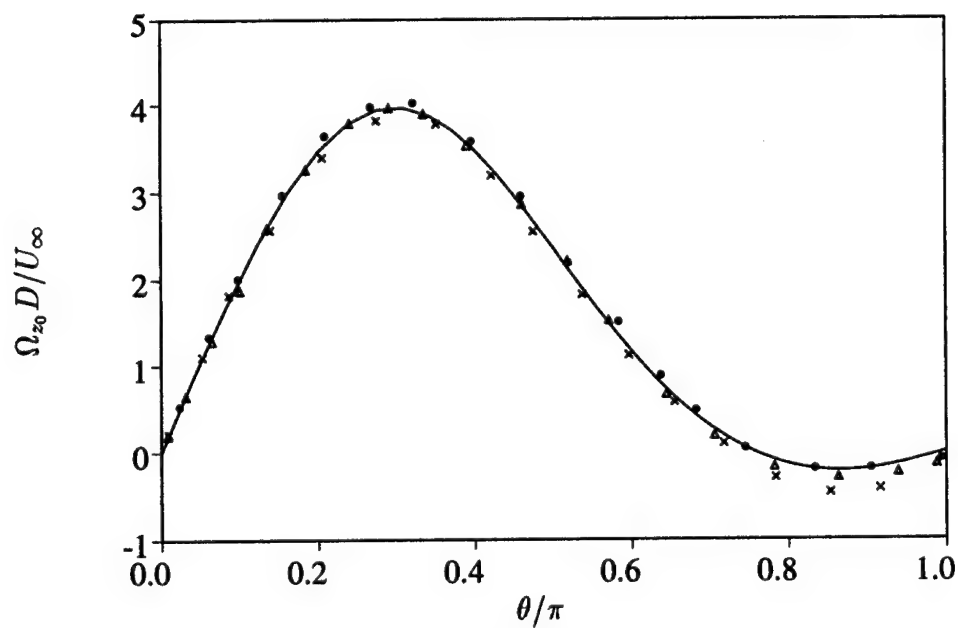
Figure 6: Re=20; Wall vorticity
——— : Present results; ● : Dennis & Chang (1970)
× : Fornberg (1980); △ : Nieuwstadt & Keller (1973)
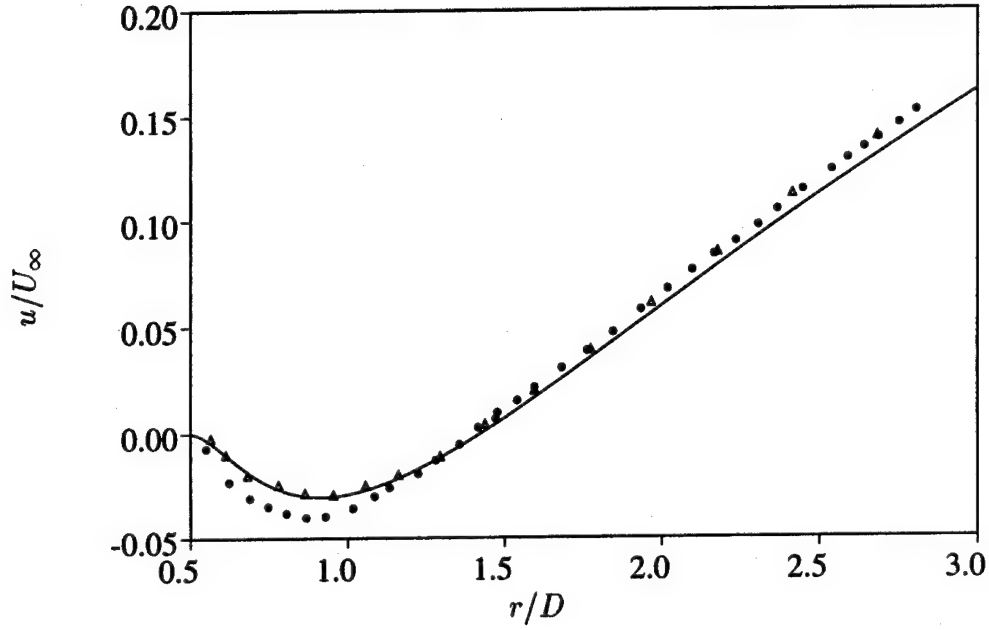
Figure 7: Re=20; Rear axis streamwise velocity
—— : Present results; ● : Coutanceau & Bouard (1977); △ : Nieuwstadt & Keller (1973)
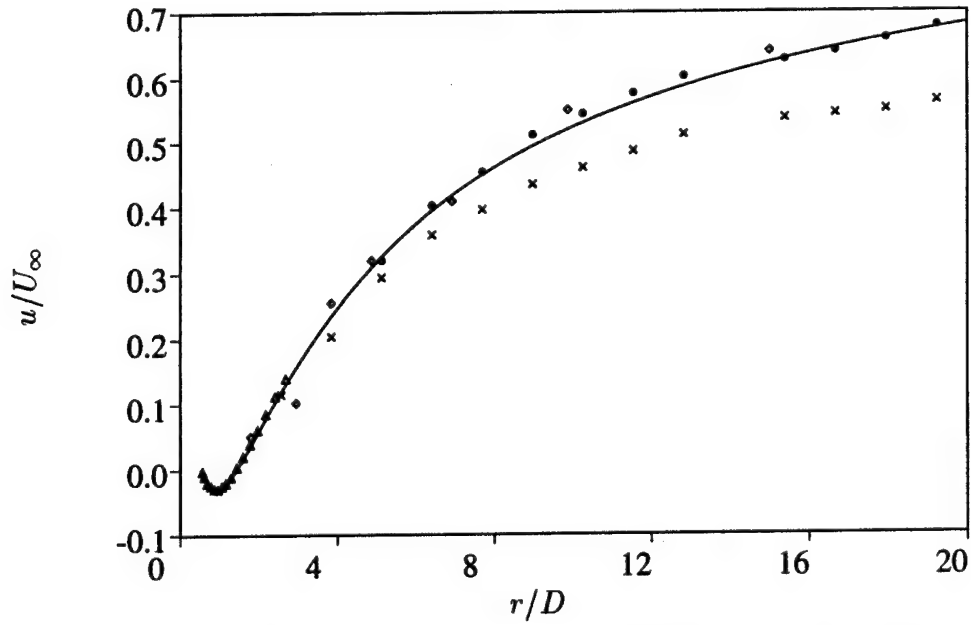
Figure 8: Re=20; Rear axis streamwise velocity in the near wake
—— : Present results; ● : Imai (1951); × : Takami & Keller (1969)
◇ : Nishioka & Sato (1974); △ : Nieuwstadt & Keller (1973)
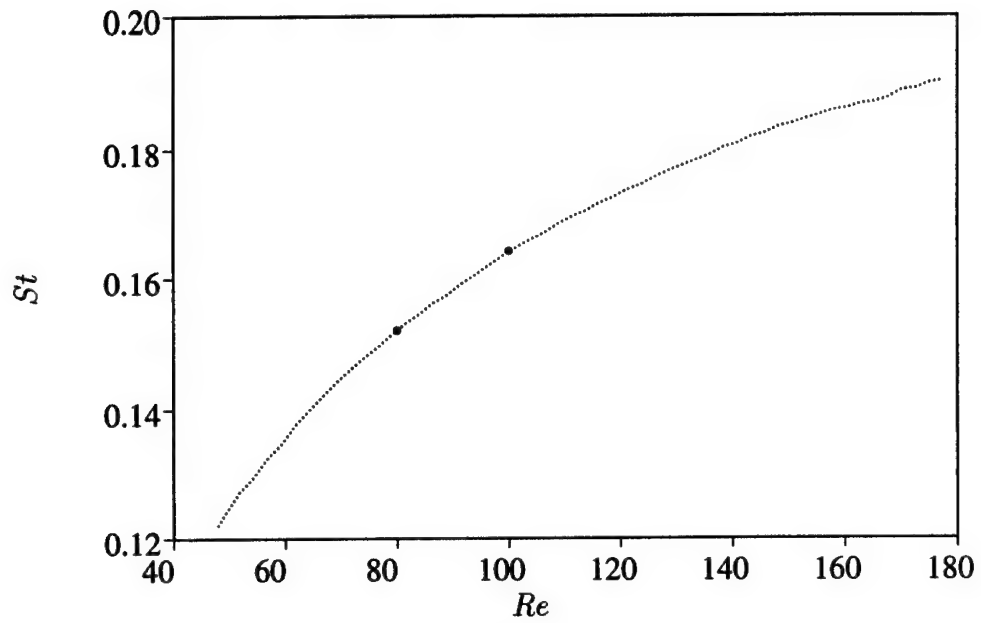
Figure 9: Shedding frequency versus Reynolds number
● : Present results; ⋯ : Williamson (1989)

Chapter 4

Subgrid-Scale Model Performance

4.1   Physical and Numerical Parameters

In this chapter, results from three large-eddy simulations of the wake behind a circular cylinder at a Reynolds number of $3,900$, based on cylinder diameter and free-stream velocity, are examined. The three simulations are based on the fifth-order accurate, upwind-biased scheme for the convective fluxes. They use respectively no subgrid-scale model, the fixed-coefficient Smagorinsky model and the dynamic model. In the reversed flow region, mean velocities, as well as mean turbulent and periodic Reynolds stresses are compared to experimental data obtained using a Particle Image Velocimetry technique (Lourenco & Shih 1993). Downstream from the recirculation zone, within the first 10 diameters of the wake, mean velocities and total Reynolds stresses available from a hot-wire experiment (Ong & Wallace 1994) are used for comparison. Both experiments were conducted at $Re \simeq 3,900$.

The grid selected for the simulations is described in section C.3.4 of Appendix C. The mean velocities and total Reynolds shear stress obtained on this mesh using the dynamic subgrid-scale model are grid independent in the first ten diameters of the wake (Appendix F). The time-step used in all simulations, $\Delta t = 0.004 R_c / U_\infty$, corresponds to a free-stream velocity based Courant number of about 0.3. Statistics were compiled over approximately 6 vortex shedding cycles, or about $60 R_c / U_\infty$ time units.

The remainder of this chapter consists of five main sections. Section 4.2 examines the issue of experimental uncertainty in the P.I.V. and hot-wire measurements. The impact of three-dimensionality on the computed flow field is examined in section 4.3, where in addition results of two- and three-dimensional simulations without subgrid-scale eddy viscosity models are compared. Differences between the three-dimensional simulations are discussed in section 4.4.

4.2   Experimental Parameters

4.2.1   P.I.V. Experimental Uncertainty

The Particle Image Velocimetry experimental set-up is described in detail by Lourenco & Krothapalli (1988). In this experiment, the cylinder has a diameter of 1.905 centimeters and is 39 centimeters long. The free-stream velocity is 20.67 cm/s, and the Reynolds number based on diameter and free-stream velocity is $3,900$.

The cylinder is impulsively accelerated to a constant velocity in a towing tank facility. The flow in the wake is seeded with tracer particles, and a plane in the wake is illuminated with a pulsed laser beam. Photographs of the pattern projected by the tracers are taken at a frequency of $6Hz$, from which velocity information is extracted. The data in the recirculation bubble downstream of the cylinder is obtained from 93 instantaneous velocity-field images spanning 29 vortex shedding cycles. These data form the basis for the comparisons between simulations and experiments within the first 3 diameters of the wake.

The experimental mean velocity and Reynolds stress fields provided to us did not display the expected symmetries and anti-symmetries about the wake center-line. Experimental profiles displayed in this chapter have been symmetrized in a post-processing operation. Denoting mean streamwise and vertical velocities by $\overline{u}$ and $\overline{v}$ respectively, and symmetrized fields by the subscript $'s'$, the post-processing operations were:

$$\overline{u}_s(\xi, \eta) = \frac{\overline{u}(\xi, \eta) + \overline{u}(\xi, -\eta)}{2} \quad \overline{v}_s(\xi, \eta) = \frac{\overline{v}(\xi, \eta) - \overline{v}(\xi, -\eta)}{2} \tag{89}$$

51

$$\overline{u'u'}_s(\xi,\eta) = \frac{\overline{u'u'}(\xi,\eta) + \overline{u'u'}(\xi,-\eta)}{2} \tag{90}$$

$$\overline{v'v'}_s(\xi,\eta) = \frac{\overline{v'v'}(\xi,\eta) + \overline{v'v'}(\xi,-\eta)}{2} \tag{91}$$

$$\overline{u'v'}_s(\xi,\eta) = \frac{\overline{u'v'}(\xi,\eta) - \overline{u'v'}(\xi,-\eta)}{2} \tag{92}$$

The representative symmetry error Δf in a symmetrized quantity $f_s(\xi,\eta)$ is chosen as the maximum error at each location ξ normalized by the maximum of f at ξ:

$$\Delta f(\xi) = \frac{\max_\eta |f_s(\xi,\eta) - f(\xi,\eta)|}{\max_\eta |f(\xi,\eta)|}. \tag{93}$$

Symmetry errors in Reynolds stresses, streamwise and vertical velocities are displayed in figures (10) and (11). Errors in the vertical mean velocity $\overline{v}$ are comparable to $\overline{v}$ itself over the entire domain of measurement. Past 1 cylinder diameter downstream, symmetry errors in the streamwise velocity stand at approximately 5% of the maximum local velocity. Global Reynolds shear stresses have a 20% error for $x/D \leq 2$. At radial locations between $2.5D$ and $4D$, the error is around 30%.

4.2.2   Hot-Wire Experimental Parameters

The experiments were conducted in the windtunnel of the Turbulence Laboratory, at the University of Maryland. The test-section of the windtunnel has a rectangular exit cross-section of 1.2×0.7 meters. The freestream velocity was 4.2 meters per second, with a turbulent intensity of 0.7%. The Reynolds number was $3,900$. A circular cylinder of 1.43 centimeters in diameter was mounted across the test-section at the tunnel half-height location, approximately 7.3 meters from the end of the contraction.

The hot-wire probes were operated in constant-temperature mode with an overheat ratio of 1.35, with a 12-Channel A.A. Lab Systems Hot-wire Anemometer System. The tunnel velocity was monitored using a pitot-static probe connected to a Barocel Electronic Manometer.

Experimental uncertainties, provided by Ong & Wallace, were $0.02\,U_\infty$ on mean velocities, $0.03\,U_\infty^2$ on Reynolds stresses. Symmetry errors, derived by post-processing

the experimental data according to equations 89 through 92, were negligible compared to these experimental uncertainties.

4.3   Impact of Three-Dimensionality on Mean Flow Characteristics

The impact on mean flow quantities of three-dimensionality is examined by comparing the results of two- and three-dimensional simulations which use no subgrid-scale eddy viscosity model. Both calculations were performed on the same grid in the plane of mean motion.

At the cylinder surface, the two-dimensional simulation yields drag and rms lift coefficients of 1.42 and 1.74 respectively. These are substantially higher than the experimental values of 0.98 and 0.1 ± 0.05 (Norberg 1987). The computed three-dimensional mean drag and rms lift coefficients are 0.96 and 0.07, which are within experimental uncertainty. The skin-friction obtained from the two-dimensional simulation (1.33×10^{-2}), is about 50% higher than in the three-dimensional calculation (0.87×10^{-2}). These differences in magnitude can be directly observed from the time history of the lift and drag coefficients, displayed in figures 12 and 13. The time-averaged lift coefficient in the two- and three-dimensional calculations is of the order of 10^{-3}. These results are in accordance with the conclusions of other researchers (Braza *et al.* 1986, 1990; Tamura *et al.* 1990). The irregularity of the vortex shedding at subcritical Reynolds number, illustrated by the modulation of the lift coefficient in the three-dimensional calculation (figure 12), is not as pronounced in the two-dimensional simulation. The qualitative behavior of the lift response at Reynolds number $3,900$ is similar to that observed by Schewe (1986, figure 4.a, page 38) at Reynolds number 2.64×10^5, shortly before the Reynolds number at which the drag crisis occurs. Although the vortex shedding irregularity in the three-dimensional flow was not investigated in the present study, some factors which cannot be at its origin in the numerical simulations include: free-stream turbulence in the oncoming flow, the effect of spanwise end plates and their orientations, the influence of size or

geometry in a wind-tunnel, and an interaction between the vortex shedding process and the flow in the wake past ten diameters downstream.

The most outstanding feature of the two-dimensional simulation however is the absence of an attached recirculation region behind the cylinder (figure 14). The mean centerline streamwise velocity is positive at all stations downstream in the two-dimensional calculation (figure 15). The wall vorticity distribution (figure 16), indicates that separation bubbles at the cylinder surface, located symmetrically above and below the wake centerline at $(108.1° \leq |\theta| \leq 124.6°)$, are present in both two and three dimensions. Additionally a separation bubble is attached to the downstream face of the cylinder in three-dimensional flow. Originating at $\theta = 85.3°$ on the cylinder surface, its closure point lies at the wake centerline at $L/D = 1.56$. In the two-dimensional simulation the pressure drop behind the cylinder is about twice as large as in the three-dimensional case (figure 17). The tangential velocities in the cylinder-surface boundary layer are correspondingly greater in two dimensions (figure 18).

These differences between two- and three-dimensional simulation results indicate that three-dimensional structures strongly influence the near-wake at Reynolds number 3,900. These structures consist of pairs of counter-rotating streamwise vortices (Hayakawa & Hussain 1989, Bays-Muchmore & Ahmed 1993, Mansy & al. 1994). Instantaneous surfaces of constant vorticity norm in the near-wake (figure 19) show that these structures observed experimentally are present in the three-dimensional simulation. The cylinder stands at the bottom of the figure, the flow evolving vertically along the page. The detached shear layers are visible at the top and bottom edges of the cylinder. The πD spanwise extent of the computational domain contains three pairs of counter-rotating streamwise vortices. This is consistent with the observation of Bays-Muchmore & Ahmed that there is about one pair of counter-rotating streamwise vortices per cylinder diameter in this range of the Reynolds number. In the present simulation, these vortices are present between the two primary spanwise rollers in the first five diameters of the wake. In the second half of the domain $(5 \leq x/D \leq 10)$, streamwise structures appear to be shorter and more diffused than in the first half. This point is further examined in chapter 5.

4.4 Simulations With and Without Subgrid-Scale Models

This section discusses the mean flow and Reynolds stresses predicted by three simulations. One simulation uses no subgrid-scale eddy viscosity model, a second one is performed with the standard fixed-coefficient Smagorinsky model (chapter 2), the third one with the least-squares version of the dynamic model. Two distinct regions of the flow-field are examined successively: the vortex formation region $(x/D \leq 4)$, which includes the cylinder surface, recirculation bubble and recovery zone, and the near wake from 4 to 10 diameters downstream.

In the following, the expression 'total Reynolds stress' refers to the sum of the periodic $(\overline{\tilde{u}_i \, \tilde{u}_j})$, turbulent $(\overline{u'_i \, u'_j})$, and subgrid-scale $(\overline{\tau}_{ij})$ components of the Reynolds stresses.

4.4.1 Cylinder Surface

The main features of the mean flow at the cylinder surface, which include the skin-friction, back-pressure and drag coefficients, the Strouhal number and the flow separation angles, are summarized in table 5.

The drag coefficient $\overline{C}_D$ and the back-pressure coefficient $\overline{C}_{P_b}$ are functions of the Reynolds number (Roshko & Fiszdon 1969, Cardell 1993): In the neighborhood of $Re = 3,900$, the drag coefficient increases, while the back-pressure coefficient decreases with increasing Reynolds number. At Reynolds number 3,900, their values are respectively 0.98 ± 0.05, and -0.90 ± 0.05.

The mean drag and back-pressure coefficients are determined by the mean velocities, viscous and Reynolds stresses in the wake: letting overbars indicate time and spanwise averaging, the mean large-scale streamwise momentum equation

$$\frac{\partial}{\partial x}\left(\overline{\rho}\, \overline{u}^2 + \overline{\rho}\, \overline{u'^2} + \overline{p} - \overline{\sigma}_{11} + \overline{\tau}_{11} \right) + \frac{\partial}{\partial y}\left(\overline{\rho}\, \overline{u}\, \overline{v} + \overline{\rho}\, \overline{u'v'} - \overline{\sigma}_{12} + \overline{\tau}_{12} \right) = 0 \qquad (94)$$

integrated on the rear flow axis $(y = 0)$ from the cylinder surface $(x/D = 0.5)$ to

infinity leads to

$$\overline{\rho}_\infty \overline{u}_\infty^2 + \overline{p}_\infty - \overline{p}_{x/D=0.5} + \frac{\partial}{\partial y} \int_{0.5}^\infty (\overline{\rho}\,\overline{u}\,\overline{v} + \overline{\rho}\,\overline{u'v'} - \overline{\sigma}_{12} + \overline{\tau}_{12})\partial x = 0 \qquad (95)$$

Dividing this expression by $\overline{\rho}_\infty \overline{u}_\infty^2/2$ yields the back pressure coefficient as

$$\overline{C}_{P_b} = 2 + 2\frac{\partial}{\partial y} \int_{0.5}^\infty (\overline{\rho}\,\overline{u}\,\overline{v} + \overline{\rho}\,\overline{u'v'} - \overline{\sigma}_{12} + \overline{\tau}_{12})\partial x \qquad (96)$$

where all quantities are referenced to the freestream values ρ_∞, u_∞ and the cylinder diameter. A momentum balance analysis around the cylinder relates at each streamwise position (x) the drag coefficient and momentum thickness $(\overline{\theta}_m)$ to turbulent intensities, pressure coefficient, viscous and subgrid-scale stresses:

$$\overline{C}_D - 2\overline{\theta}_m(x) = \int_{-\infty}^{+\infty} \overline{C}_P \partial y - 2\int_{-\infty}^{+\infty} \overline{\rho}\,\overline{u'^2}\partial y + 2\int_{-\infty}^{+\infty} (\overline{\sigma}_{11} - \overline{\tau}_{11})\partial y \qquad (97)$$

Note that at Reynolds number $3,900$, the far-wake momentum-thickness Reynolds number $U_\infty \overline{\theta}_m/\nu$ is approximately $1,911$, since

$$\lim_{x \to \infty} \overline{\theta}_m(x) \simeq \frac{1}{2}\overline{C}_D \simeq 0.49 \qquad (98)$$

Since they are directly related to spatially integrated mean quantities in the wake region, $\overline{C}_D$ and $\overline{C}_{P_b}$ are some of the most aggregate quantities of the flow. As such, they are relatively insensitive the subgrid-scale turbulence model used in the large-eddy simulations. The three simulations predict these coefficients within experimental uncertainty. Similarly, the computed surface separation angles and the skin-friction coefficient are not significantly different in the three separate calculations. A small difference is however observed in the predictions of the Strouhal number, which are 5% and 3% below the experimental value of 0.215 in the dynamic and fixed-coefficient model simulations respectively.

Overall, the observation of wall statistics reveals insufficient distinctions between the three calculations to establish a performance hierarchy. We turn in the following section to a more detailed examination of the computed mean wake statistics for this purpose.

4.4.2   Vortex Formation Region

Recirculation Zone

The analysis of differences between the three simulations indicates that overall, the dynamic model gives the most accurate prediction of the mean flow in the recirculation region. The length and streamwise velocity distribution in the mean separation bubble are close to experimental observations when computed with the dynamic model (table 5). In the calculations without model or with the fixed-coefficient model, the bubble length is over-predicted by 17% and 29% respectively. The prediction with the dynamic model ($L/D = 1.36$) is within two percent of the experimental value.

The mean streamwise and vertical velocities within the recirculation bubble are displayed in figures 20 and 21. The experimental uncertainty of around 50% (figure 10) on the bubble mean vertical velocities makes comparisons between the vertical velocities predicted by different simulations difficult. The streamwise velocity profiles across the wake however indicate that the dynamic model simulation offers more accurate predictions than simulations with no model or with the fixed-coefficient Smagorinsky model. The longer recirculation zone in the latter two induces a downstream shift of the entire streamwise velocity distribution on the rear centerline (figure 15) compared to the distribution obtained with the dynamic model. This shift is apparent in the profiles shown in figure 20 at stations $x/D = 1.54$ and 2, where the wake is wider and the velocity deficit is larger in the fixed-coefficient Smagorinsky model simulation than in the computation without model.

The Reynolds stresses at $x/D = 1.54$ (figure 22) illustrate the differences between the three simulations in the recirculation zone. The dynamic model simulation reproduces the streamwise stress accurately over the entire width of the wake layer. Without subgrid-scale model, the peaks of the streamwise intensities are underpredicted by 18%. In the fixed coefficient Smagorinsky calculation, the streamwise intensity is damped in the wake-layer center ($-0.5 \leq y/D \leq 0.5$): its peaks lay 43% below their expected value. A similar pattern appears in the vertical intensity and Reynolds shear stress. At the wake center, the experimental vertical intensity is $0.35 \pm 0.04\ U_\infty^2$. The dynamic model prediction ($0.29\ U_\infty^2$) is close to the lower experimental bound, while

the simulations without model ($0.19\ U^2_\infty$) and with the fixed-coefficient Smagorinsky model ($0.10\ U^2_\infty$) underestimate the vertical intensity. Near the center of the wake, for $-0.3 \leq y/D \leq 0.3$, the calculation with the fixed-coefficient Smagorinsky model gives a Reynolds shear stress of the wrong sign. All simulations predict that at $x/D = 1.54$, the periodic Reynolds shear stress has the sign opposite of the turbulent shear stress near the wake center. The fixed coefficient Smagorinsky model result displays a large region with periodic Reynolds shear stress of reversed sign (figure 23), where the maximum amplitude of the stress ($0.029\ U^2_\infty$) is more than twice that obtained with the dynamic model ($0.013\ U^2_\infty$).

Recovery Region

In the recovery region, between the bubble closure point and $x/D = 4$, where the flow accelerates despite the adverse pressure gradient it faces (figure 15), the Reynolds stress prediction ability of the three simulations is qualitatively identical to that in the recirculation bubble. The periodic Reynolds stresses at $x/D = 2.5$, displayed in figure 24, are underpredicted by simulations without model and with the fixed-coefficient Smagorinsky model. The dynamic model calculation predicts all Reynolds stresses within the experimental uncertainty.

Spanwise intensities are not available experimentally, but the predictions of the three simulations are not significantly different in the recirculation region except near the wake center (figure 22). The observable differences in the total fluctuating kinetic energy (figure 25) in that region are thus largely due to the streamwise and vertical Reynolds stresses. The dynamic model calculation predicts total fluctuating kinetic energy levels up to about 30% and 90% higher than those obtained without model and with the fixed-coefficient Smagorinsky model respectively.

4.4.3   Near-Wake Region

Mean Velocities and Total Reynolds Stresses

In the near-wake, between 4 and 10 D downstream, the significant differences between the three simulations in the predicted mean velocities disappear almost entirely (figures 26 and 27). Vertical velocity profiles in figure 27 are displayed at $x/D = 3$ and $x/D = 4$, the only two locations provided by Ong & Wallace where the magnitude of v/U_∞ is substantially larger than the experimental uncertainty of $0.02U_\infty$. The streamwise velocity at $x/D = 4$, which is the end of the recovery region, is more accurately predicted by the dynamic model. Aside from this residual effect from the recirculation zone, streamwise and vertical velocities are within experimental uncertainty at all downstream stations.

At the streamwise locations $x/D \geq 4$, the experimental uncertainty on the total Reynolds stresses is approximately $0.03U_\infty^2$. The three simulations yield streamwise intensities and Reynolds shear stresses within the experimental uncertainty. The vertical intensity is significantly underpredicted by the fixed-coefficient Smagorinsky model calculation at $x/D = 4$, 7 and 10 (figures 28 through 31). These figures further indicate that the differences between the Reynolds stresses in the three simulations diminish with downstream distance.

Time and spanwise averaged total Reynolds stress contours in the near-wake are displayed in figure 32. The Reynolds stress distributions at $Re = 3,900$ are qualitatively similar to those at Reynolds number 1.4×10^5 (Cantwell & Coles 1983). In both cases in particular, the maximum mean streamwise and vertical intensities occur near the mean bubble closure point, away from and on the wake centerline respectively. At $Re = 3,900$, the maximum mean streamwise intensity ($0.18U_\infty^2$) is 19% lower than at $Re = 1.4 \times 10^5$. This difference is 10% in the case of the maximum mean vertical intensity, which stands at $0.39U_\infty^2$ at $Re = 3,900$. The distribution of the Reynolds shear stress inside the recirculation bubble cannot be compared at both Reynolds numbers because it was not provided by Cantwell & Coles. However the maximum value of the shear stress ($0.13U_\infty^2$) at $Re = 1.4 \times 10^5$ appears to be only 4% higher than that computed at $Re = 3,900$.

59

Model Coefficients and Eddy Viscosities

The time-averaged dynamic model coefficient $\overline{C}(x,y)$ (equation 28) scaled on the squared Smagorinsky constant ($C_s^2 = 0.065^2$), is displayed in figures 33 and 34. The ratio of the fixed Smagorinsky coefficient C_s to its dynamic counterpart $\sqrt{\overline{C}(x,y)}$ is about 2 at $x/D = 1$, 2.5 at $x/D = 5$ and 3 at $x/D = 10$. The dynamic model coefficient within the turbulent core of the wake-layer thus generates a value of $\sqrt{\overline{C}(x,y)}$ varying between 0.13 and 0.2 in the first 10 diameters of the wake.

Mean eddy viscosities obtained from the fixed-coefficient and dynamic model calculations are displayed in figure 35 scaled on their respective maximum values. At Reynolds number $3,900$, the free shear layers are laminar (Cardell 1993). It is thus expected that the eddy viscosity in the shear layers should be substantially less than further downstream in the wake, a behavior reproduced by the dynamic model, but not by the fixed-coefficient model (figures 35, 36). Another difference in the eddy viscosities is their vertical support: it is bounded by the wake edge at all downstream stations in the dynamic model simulation, but not in the fixed-coefficient Smagorinsky model case.

Ten diameters downstream of the cylinder, the dynamic eddy viscosity is about ten times larger than the eddy viscosity generated by the fixed-coefficient model. The resulting total viscosities ($\nu + \overline{\nu}_t$) are different by a factor of two in the dynamic and fixed-coefficient model simulations, and a factor of three in the calculations with the dynamic model and without model. Despite these differences, low-order statistics appear independent of the presence or absence of a subgrid-scale model at that location.

Periodic and Random Reynolds Stresses

The convergence of the results from all three simulations toward the experimental data in the near-wake occurs despite the decrease with downstream distance of the

60

contribution of the periodic motion to the total Reynolds stresses (figure 37), measured at each downstream location by the ratio (Matsumura & Antonia, 1993):

$$\int_{-\infty}^{+\infty} |\overline{\tilde{u}_i\,\tilde{u}_j}|\; \partial y \; \bigg/ \; \int_{-\infty}^{+\infty} |\overline{u'_i\,u'_j} + \overline{\tau}_{ij} + \overline{\tilde{u}_i\,\tilde{u}_j}|\; \partial y \tag{99}$$

The periodic component of the motion, a spanwise-averaged quantity, is two-dimensional: the periodic spanwise intensities are nearly zero at all locations inside the wake. At $x/D = 4$, the periodic contributions to the streamwise, vertical and shear stresses reach 28%, 60% and 26% respectively. Seven diameters downstream, they stand at 19%, 58% and 26%. Ten diameters downstream, the streamwise and vertical periodic components continue to diminish, with contributions at 13% and 46% respectively, while the periodic Reynolds shear stress maintains an approximately constant contribution level of 27%: within the first 10 diameters of the wake.

That the simulations with and without subgrid-scale model predict similarly accurate Reynolds stresses at $x/D = 10$ is thus not linked to the dominance of periodic stresses over random stresses. It is rather a consequence of the small magnitude of the subgrid-scale Reynolds shear stress $\overline{\tau}_{12}$ relative to the resolvable shear stress $\overline{u'v'}$ in the wake, an effect discussed below.

Subgrid-Scale Shear Stresses

Profiles of the subgrid-scale shear stress magnitude normalized on the resolved Reynolds shear stress, $|\overline{\tau}_{12}|/|\overline{u'\,v'}|$, at downstream stations $x/D = 3$, 5 and 10, are shown in figure 38 with the vertical direction y scaled on the wake half-width (H). They indicate that the relative magnitude of the subgrid-scale shear stress within the turbulent core of the wake increases with downstream distance. This behavior is expected because of the coarsening of the mesh (see Appendix C) and of the conversion of large-scale energy associated with the organized, periodic motion into turbulent kinetic energy as the flow evolves downstream.

The magnitude of the subgrid-scale shear stress relative to its resolvable counterpart is small however, even at $x/D = 10$. The overall magnitude of subgrid-scale

61

stresses scaled on resolvable stresses, measured as

$$\int_{-\infty}^{+\infty} |\bar{\tau}_{ij}| \, \partial y \left/ \int_{-\infty}^{+\infty} |\overline{u_i' \, u_j'}| \, \partial y \right. \tag{100}$$

is displayed in figure 39. The subgrid-scale shear stress norm achieves a maximum of 5% of the resolvable shear stress at $x/D \simeq 1.2$. From 4 to 10 diameters downstream, the same norm ranges between 1% and 2%.

These results confirm the earlier observation that the impact of the subgrid-scale model on the mean flow is small in the computed near-wake. It thus appears that the mean flow is principally governed by the largest scale motions of the flow, which are accurately resolved on the grid in the simulations. This conjecture is examined in the following two sections. The first section investigates the nature of the small-scales present in the near-wake at $Re = 3,900$. The second section compares experimental and computed one-dimensional energy spectra, and examines the impact of numerical dissipation on the computed fields.

Small-Scale Turbulence at $Re = 3,900$

Fifty diameters downstream of the cylinder in the center of the wake, Uberoi & Freymuth (1969) find an inertial range at Reynolds number $4,320$ spanning about half a wave-number decade. An inertial range over one wave-number decade develops at that location for Reynolds numbers greater than approximately $15,000$. In direct numerical simulations of a small-deficit, time-developing wake at a momentum-thickness Reynolds number of $2,000$, which is comparable to that of the present simulations, Moser & Rogers (1994) find a short inertial range, spanning about half a wave-number decade. Contours of instantaneous spanwise vorticity visually confirm the presence of small-scale turbulence in their simulations.

Experimental velocity spectra at Reynolds number $3,900$ provided by Ong & Wallace (1994) indicate that a $k^{-5/3}$ tangency at $x/D = 10$ occurs over a range of similar size to that of Moser & Rogers (figures 40, 41). In the $E_{22}(k_x)$ spectra however, the vortex shedding frequency, which represents a large-scale motion, lies at the edge of the $k^{-5/3}$ range at locations between five and ten diameters downstream.

Furthermore, the high wave-number end of the $k^{-5/3}$ range lays at approximately five times the Strouhal frequency (figure 41), a number lower than the transition frequency in the separated free shear layers at $Re = 3,900$, which stands at six times the vortex shedding frequency (see Bloor 1964, Norberg 1987, Wei & Smith 1986).

At Reynolds number $Re = 5,000$, visualizations of the free shear layers around the cylinder suggest that secondary vortices, formed in these layers and entrained into the wake at about two diameters downstream, are highly organized at that location (Ahmed *et al.* 1992). At $Re = 1,770$ the instantaneous flow pattern between 30 and 70 diameters downstream (Van Dyke 1982, p. 101), appears dominated by motions scaling on the cylinder diameter. This is in contrast with the flow at Reynolds number 1.1×10^5 (Van Dyke 1982, p.130), in which small-scales are clearly present in the near-wake region.

Based on the evidence above, it is unclear whether small-scale turbulence, such as that observable *de visu* in the simulation of Moser & Rogers, is present within the first ten diameters of the wake at $Re = 3,900$. The following section further examines this issue by presenting pictures of the computed instantaneous vorticity in the wake, which have no experimental equivalents, as well as one-dimensional energy spectra.

One-Dimensional Energy Spectra and Numerical Dissipation

Power spectra as a function of frequency presented in this chapter were calculated with the technique used by Choi & Moin (1990). The time series of a velocity component $g(x, y, z, t)$ is defined at $N_z = 48$ spanwise points on the interval $0 \leq t \leq T$. The series at each spanwise location is considered as a statistically independent realization. The power spectrum of the function g is then calculated as the average of the spectra of these 48 realizations. Each velocity record of N points in time at a given spanwise location is divided into m time intervals of length $T_m = 2T/(m + 1)$ with a 50% overlap, each containing $M = 2N/(m + 1)$ points. The frequency corresponding to the vortex shedding motion is $\omega_{St} = 2\pi f$ where f is the dimensional Strouhal number ($St = fD/U_\infty$). The maximum resolvable frequency is $\omega_{\max} = M\pi/T_m$, while the frequency resolution is given by $\Delta\omega = 2\pi/T_m$.

63

The power spectra presented in this section were obtained from the simulations using the dynamic subgrid-scale model and with no model. The data was collected at 88 points over a time interval $TU_\infty/D = 30$, which was divided into $m = 7$ overlapping segments of length $T_m U_\infty/D = 7.5$ containing 22 points each. The power spectra were thus ensemble-averaged over $7 \times 48 = 336$ velocity-trace sets. The maximum resolvable frequency was 7.3 ω_{St}, with a resolution of 0.67 ω_{St}.

In the present simulations, the grid is fine enough to resolve most of the energy in the near-wake (see vertical lines in figures 40, 41). Small-scale motions present in the flow are thus expected to be apparent in the simulation data.

Figures 42 and 43 respectively show the instantaneous vertical vorticity on the symmetry plane $y = 0$ for $5 \le x/D \le 10$, $0 \le z \le L_z$, and the streamwise vorticity at $r/D = 10$ in the simulation using the dynamic model. These contours reveal that only large-scale features, which scale on the cylinder diameter, are present in the simulation.

The absence of small scales in the large-eddy simulations is confirmed by the computed one-dimensional frequency spectra $E_{11}(\omega)$ shown in figure 44 compared to the experimental results of Ong & Wallace at stations $x/D = 5$, 7 and $x/D = 10$. The spectra obtained from the simulations with no subgrid-scale model and with the dynamic model are compared in figure 45 to confirm that the high-frequency damping observed in the large-eddy simulation is not attributable to the filtering operation. The computed spectra discussed below are those obtained from the dynamic model simulation.

The computed streamwise spectra agree well with the experiment for frequencies lower than approximately 2.5 ω_{St} at $x/D = 5$. At higher frequencies, the computed energy levels fall rapidly below their experimental values. At locations further downstream, the maximum well-resolved frequency decreases as the grid coarsens in the streamwise and azimuthal directions. Using Taylor's hypothesis, the maximum resolvable frequency on the grid is 10.5 ω_{St} at five diameters downstream. At that location, about three-quarters of the resolvable frequency range are thus affected by numerical dissipation.

The evolutions of the computed spanwise wave-number spectra with downstream distance are displayed in figure 46. These spectra are not available experimentally. The energy content at high wave-numbers increases between $x/D = 0.7$ and $x/D = 1$ in the three spectra. Past the bubble closure point however, the energy at a given wave-number decreases monotonically with downstream distance in all spanwise spectra.

That the influence of the subgrid-scale model on low-order statistics in the near-wake is small is thus attributable to the inability of the numerical simulation to accurately represent frequencies which should be resolvable on the grid. The observed resolved frequency range, which includes only a quarter of the frequencies sustainable on the mesh, makes the dynamic subgrid-scale model operate at scales which contain negligible amounts of energy.

These results indicate that the fifth-order accurate upwind scheme used to evaluate the convective derivatives generates enough numerical dissipation to affect the turbulence in regions where the mesh is fine enough to resolve the mean flow velocity and Reynolds stresses. Thus although this scheme appeared to be a good candidate for direct simulations (Rai & Moin 1991), its usefulness for large-eddy simulations is limited by the fact that the mesh size must be sufficiently fine everywhere in the flow for numerical dissipation to be negligible compared to its molecular counterpart. The consequent grid-size may be significantly dictated by that requirement, as the case of the cylinder near-wake presented above indicates. The adequacy of upwind-biased differentiation schemes to large-eddy simulations being in question, the following chapter examines whether the impact of numerical dissipation on the computed solution can be controlled by choosing higher-order accurate, one-point upwind schemes for such calculations

4.4.4 Simulation Comparison Summary

Significant differences in the mean velocity and total Reynolds stresses between the simulations without model, with a fixed-coefficient Smagorinsky model and with a dynamic model exist in the vortex formation zone. This zone consists of the first four

diameters of the wake, which includes the cylinder surface, the recirculation bubble and the recovery region. The dynamic model calculation predicts more accurate mean velocities and Reynolds stresses than the calculation without model. The fixed-coefficient Smagorinsky model simulation is the least accurate one.

The dynamic model gives rise to an eddy viscosity distribution which is in better agreement with our expectations based on the flow physics than the fixed-coefficient model. The maximum mean eddy viscosity computed with the dynamic model occurs in the wake region near the mean bubble closure location. On the contrary, the fixed-coefficient Smagorinsky model generates the highest level of eddy viscosity in the separated free shear layers, which are laminar at Reynolds number $3,900$.

Downstream of the formation region, between four and ten diameters downstream, there are no significant differences in the mean velocities, total streamwise, spanwise or shear Reynolds stresses obtained in the three simulations. Differences reside principally in the predictions of vertical intensities, which are more accurate with the dynamic model than without model or with the fixed-coefficient model. However these differences between the three simulations diminish with downstream distance. The fifth-order accurate, upwind-biased differencing scheme used for the convective terms appears to generate enough numerical dissipation to overwhelm the contribution of subgrid-scale eddy-viscosity models in coarse-mesh regions of the flow. The following chapter examines the impact of numerical dissipation on the computed flow-fields.
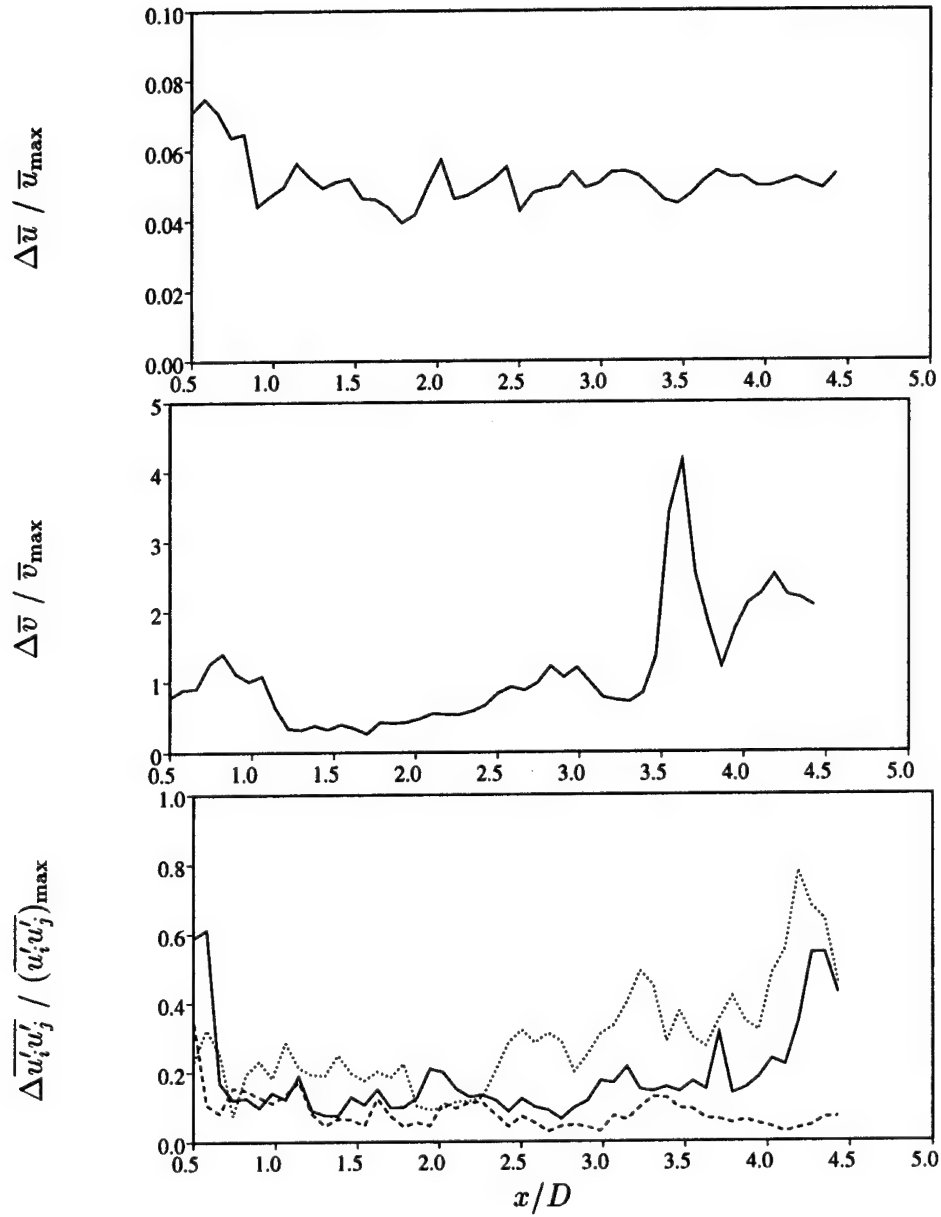
Figure 10: PIV Experiment. Symmetry errors in mean velocities and total Reynolds stresses

Reynolds stress: —— : $i = 1, j = 1$; ---- : $i = 2, j = 2$; $\cdots$: $i = 1, j = 2$

Figure 11: PIV experiment. Symmetry errors in periodic and turbulent Reynolds stresses

———— : $\Delta(\overline{\tilde{u}_i\tilde{u}_j})/(\overline{\tilde{u}_i\tilde{u}_j})_{\mathrm{max}}$ (Periodic); - - - - : $\Delta(\overline{u_i'u_j'})/(\overline{u_i'u_j'})_{\mathrm{max}}$ (Turbulent)

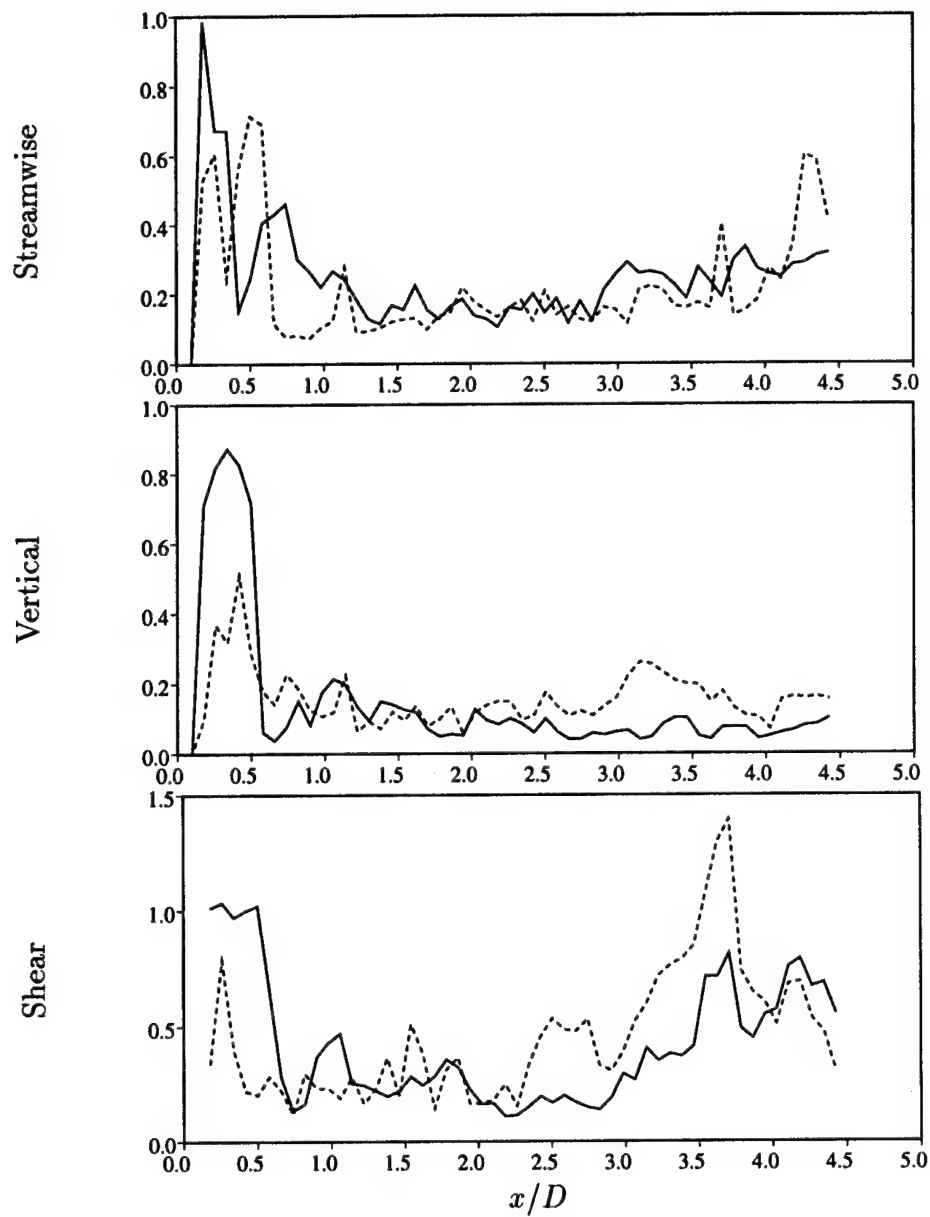|	Simulation $Re = 3,900$				Experiment
	2-D no model	3-D no model	Fixed coefficient	Dynamic model	
St Strouhal number	0.263	0.216	0.209	0.203	0.215 ± 0.005 (Cardell 1993)
$\overline{C}_{P_b}$ Back pressure	-2.16	-0.89	-0.81	-0.95	-0.90 ± 0.05 (Norberg 1987)
$\overline{C}_D$ Total drag	1.74	0.96	0.92	1.00	0.98 ± 0.05 (Norberg 1987)
$\overline{C}_f \times 100$ Skin-friction	1.33	0.87	0.86	0.91	$\cdots$
$\overline{\theta}_1$ Separation	± 108.1	± 85.3	± 84.8	± 85.8	$\pm 85 \pm 2$ (Son et al. 1969)
$\overline{\theta}_2$ Separation	± 124.6	± 109.7	± 110.5	± 110.6	$\cdots$
$\overline{\theta}_3$ Separation	——	± 154.1	± 146.2	± 158.3	$\cdots$
L/D Bubble length	No	1.56	1.74	1.36	1.33 ± 0.2 (Cardell 1993)
$\overline{u}_{\min}/U_\infty$ in bubble	separation	-0.33	-0.33	-0.32	-0.24 ± 0.1 (Lourenco 1993)
$r_{\min}/D$ $\overline{u}_{\min}$ location	bubble	1.00	1.10	0.88	0.72 ± 0.1 (Lourenco 1993)

Table 5: Cylinder surface and bubble region result summary
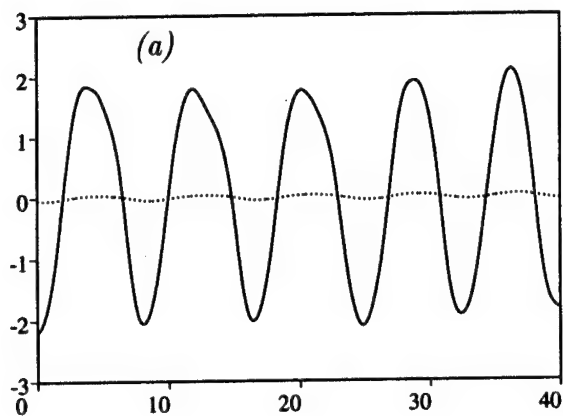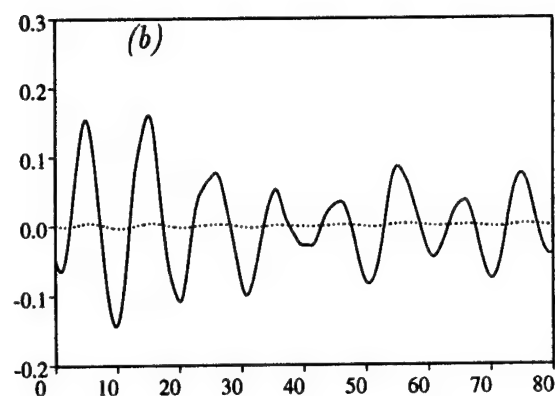
$U_\infty t/R_c$ $U_\infty t/R_c$

Figure 12: Lift coefficient at $Re = 3,900$; (a): 2D; (b): 3D
———— : Total lift; $\cdots$: Viscous lift
(Note the vertical scale difference)
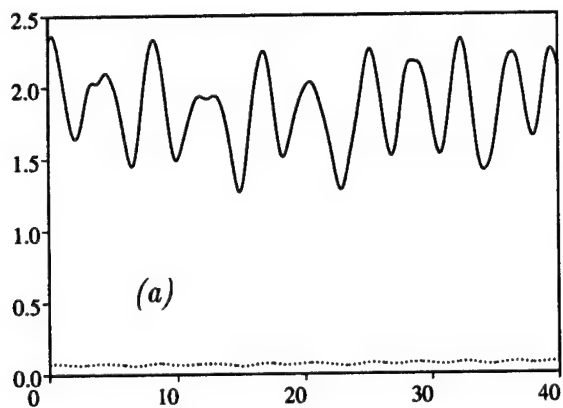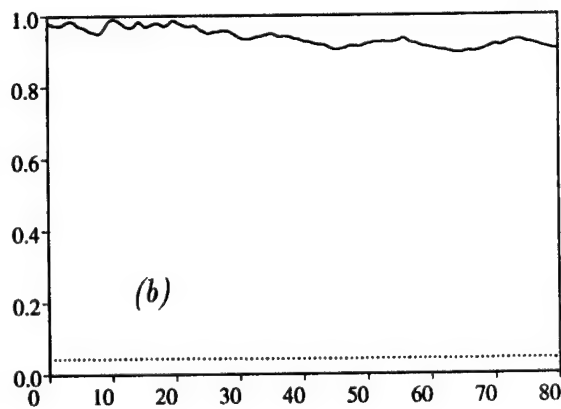
$U_\infty t/R_c$ $U_\infty t/R_c$

Figure 13: Drag coefficient at $Re = 3,900$; (a): 2D; (b): 3D
———— : Total drag; $\cdots$: Skin $-$ friction

70
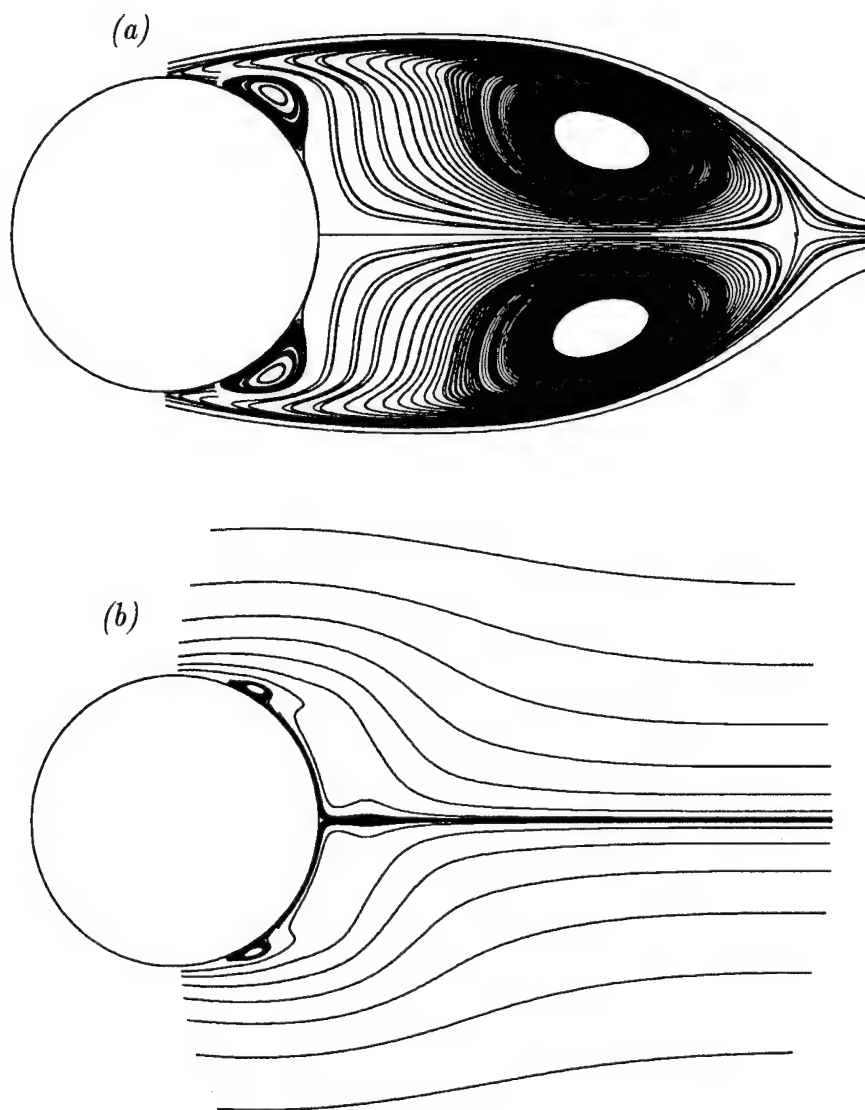
Figure 14: $Re = 3,900$; Mean streamlines in two- and three-dimensional calculations
(a): 3D no model; (b): 2D no model
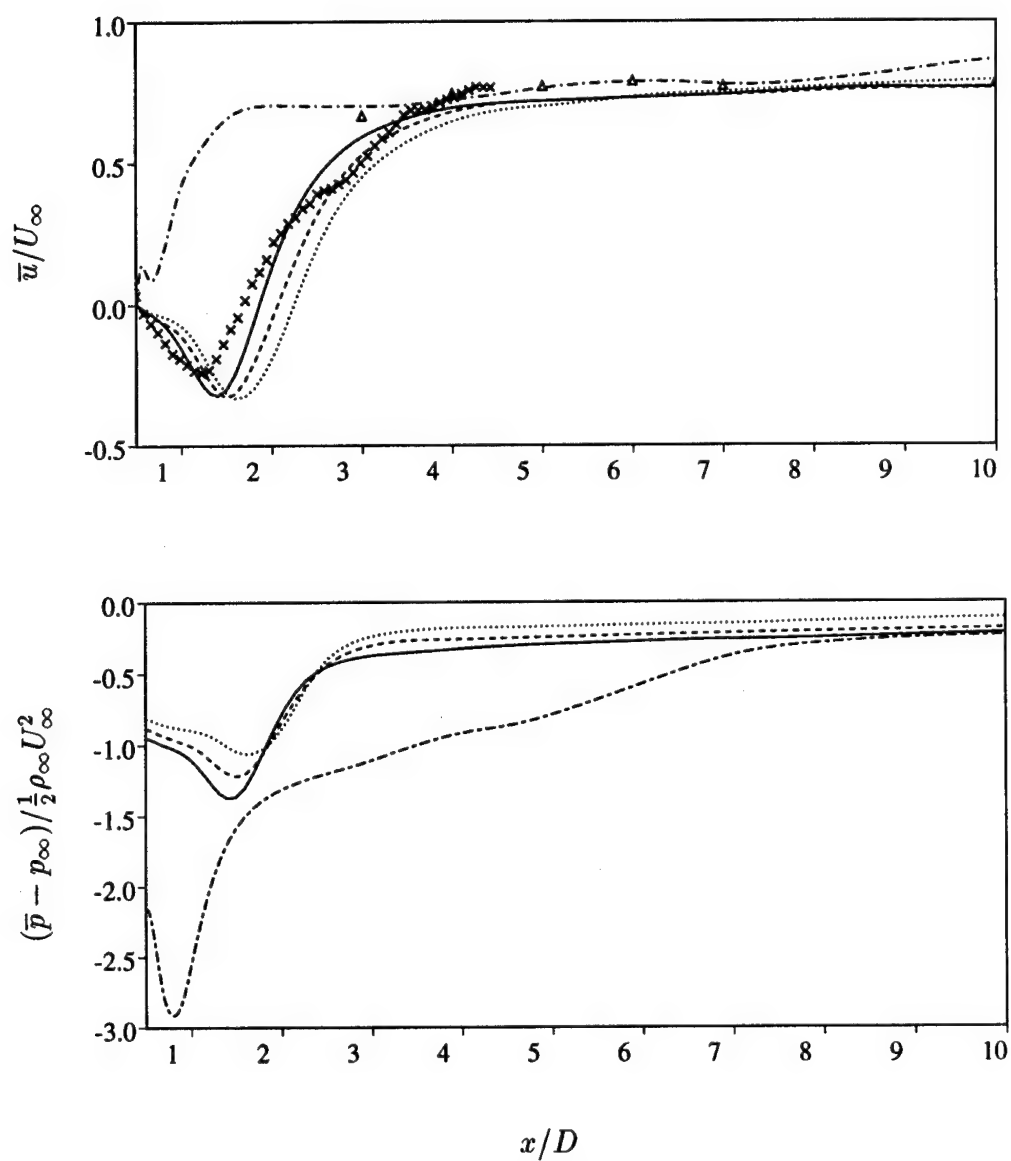
Figure 15: $Re = 3,900$; Centerline streamwise velocity and pressure coefficient
—— : Dynamic model; ---- : No model; $\cdots$: Fixed coefficient model
—·— : 2D no model; $\times$: Lourenco & Shih; $\triangle$: Ong & Wallace
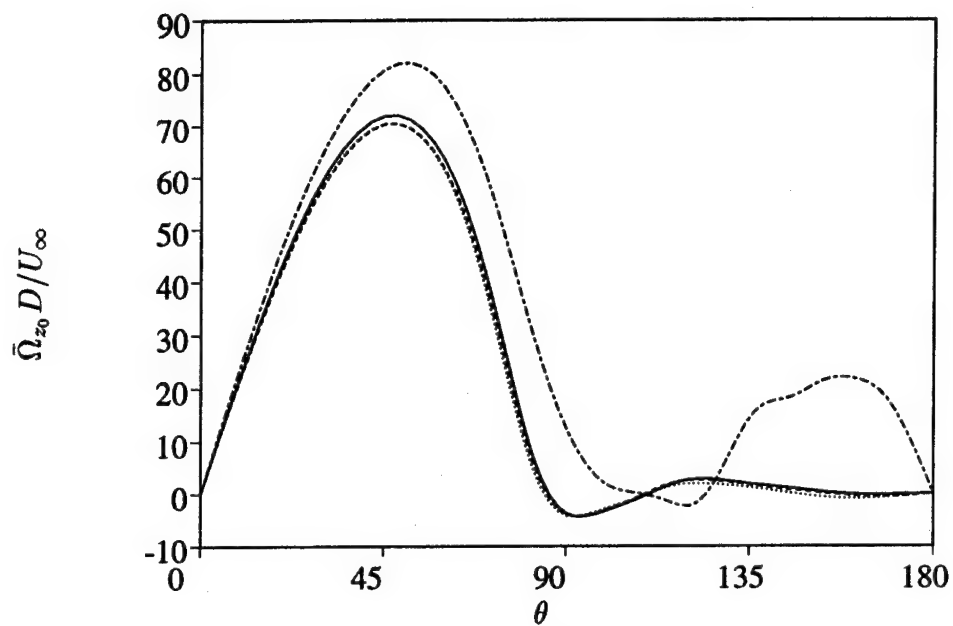
Figure 16: $Re = 3,900$; Wall vorticity
—— : Dynamic model; ---- : No model; $\cdots$: Fixed coefficient model
—·— : 2D no model
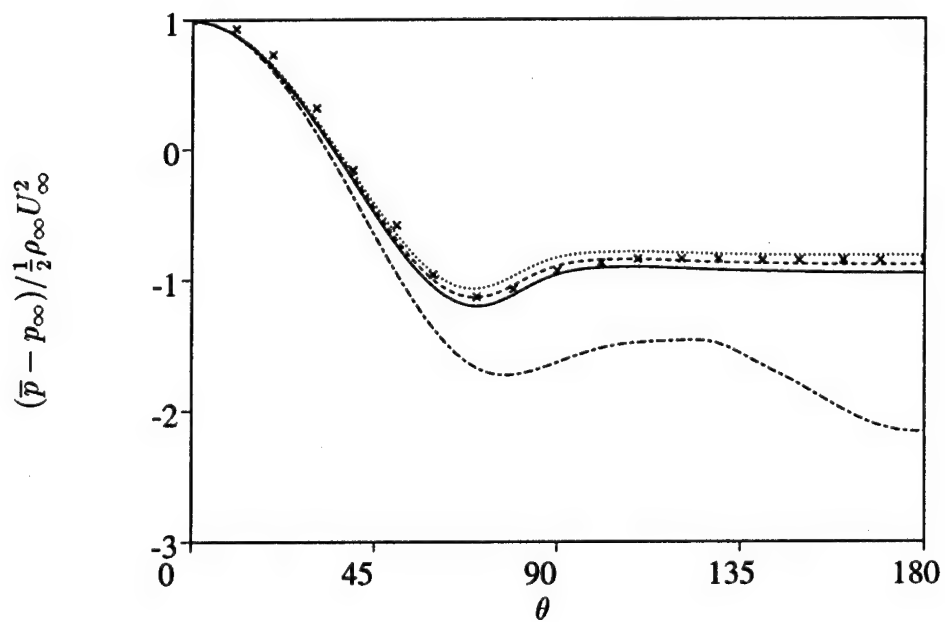
Figure 17: $Re = 3,900$; Wall pressure coefficient
—— : Dynamic model; ---- : No model; $\cdots$: Fixed coefficient model
—·— : 2D no model; $\times$: Experiment ($Re = 3,000$; Norberg1987)
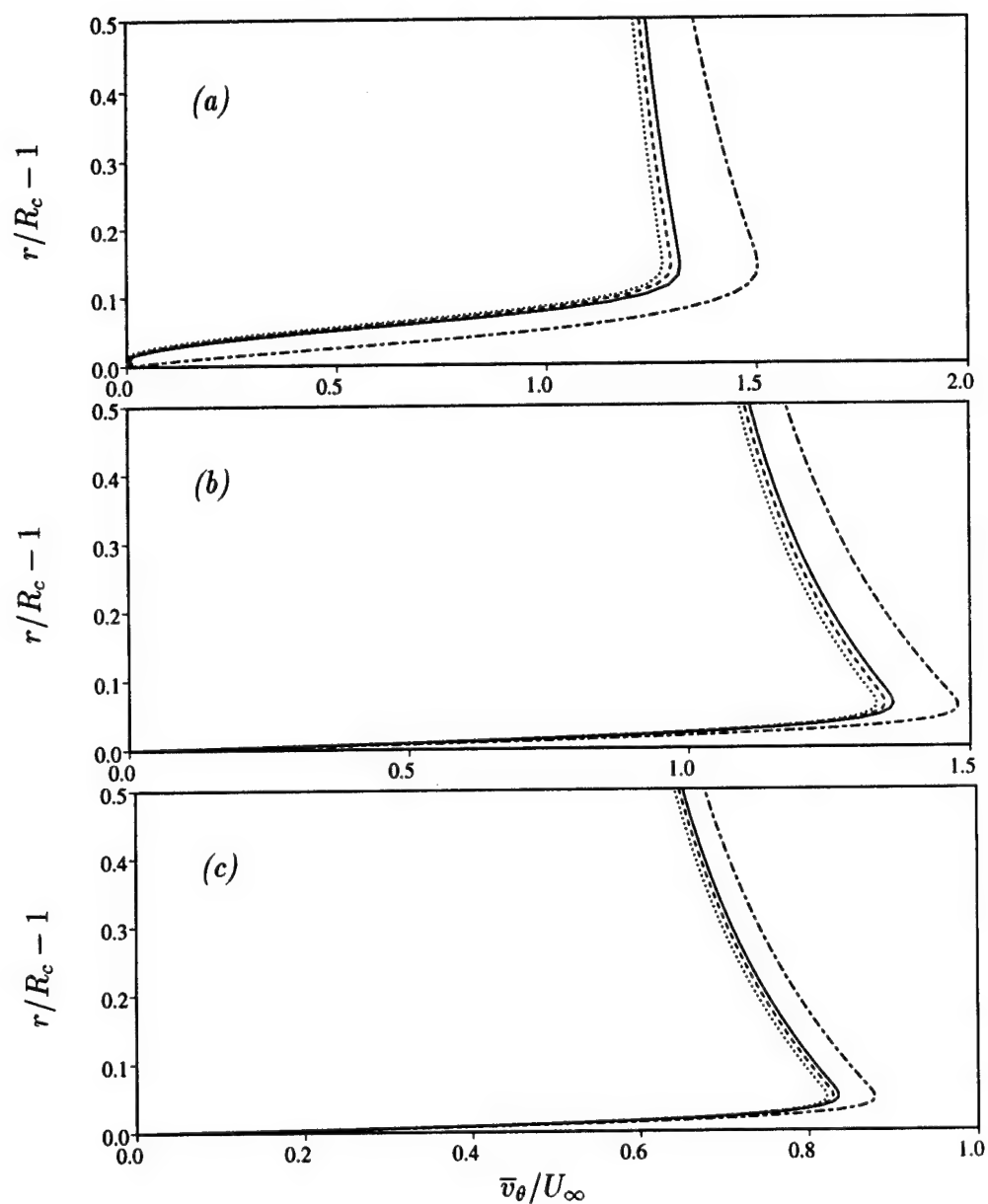
Figure 18: $Re = 3,900$; Tangential velocity in the cylinder surface boundary layer
(a): $\theta = 90^o$; (b): $\theta = 120^o$; (c): $\theta = 150^o$
—— : Dynamic model; ---- : No model; $\cdots$: Fixed coefficient model
—·— : 2D no model
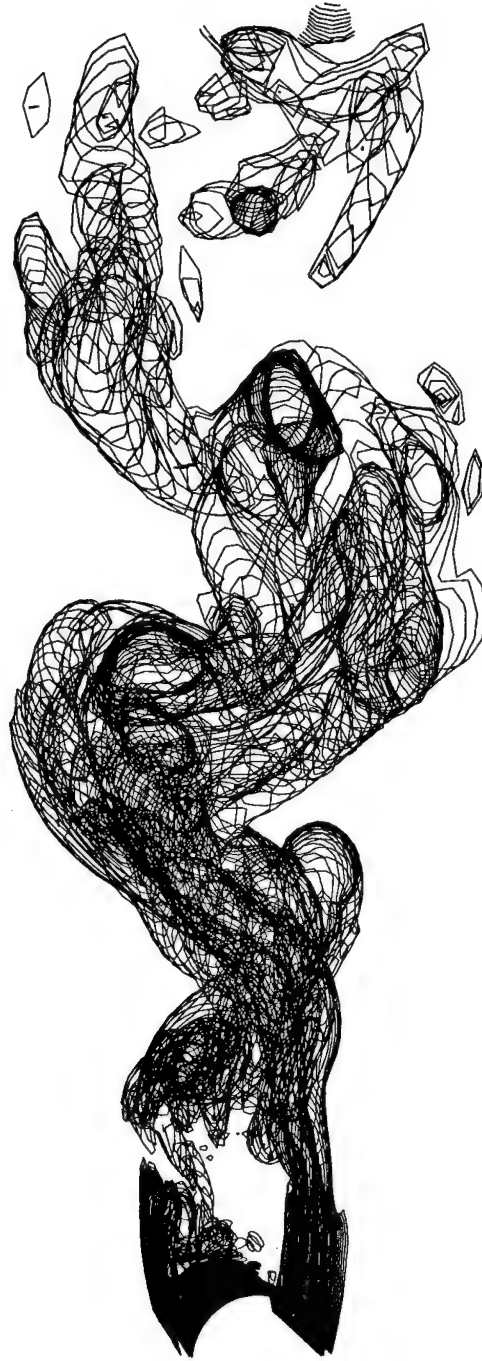
Figure 19: $Re = 3,900$; Instantaneous constant vorticity contours in the wake $|\vec{\omega}D/u_d| = 3$; Simulation without model
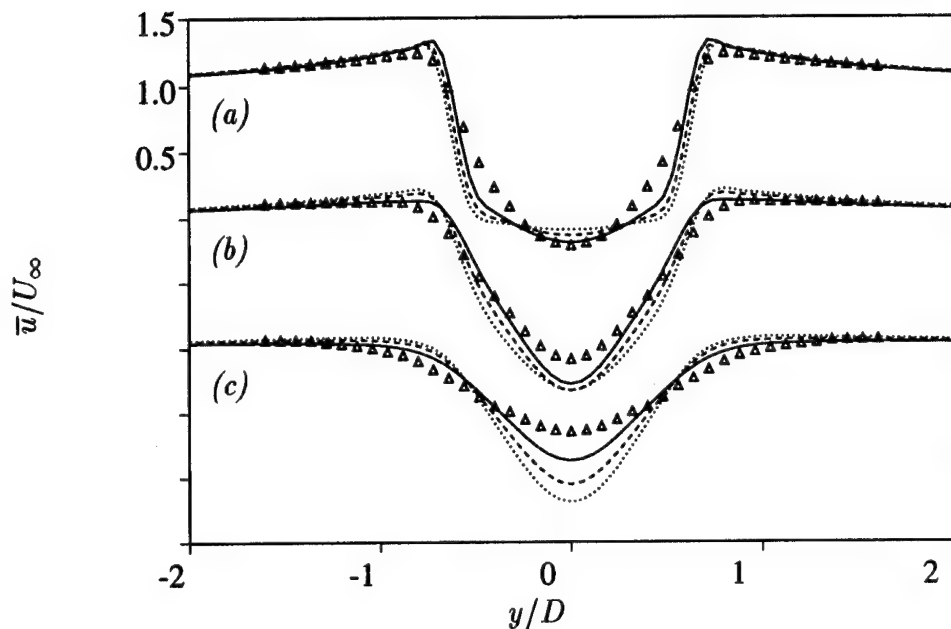
Figure 20: $Re = 3,900$; Streamwise velocity at $x/D = 1.06$ (a); 1.54 (b); 2.02 (c)
——— : Dynamic model; ---- : No model; ⋯ : Fixed coefficient model
$\triangle$: Lourenco & Shih
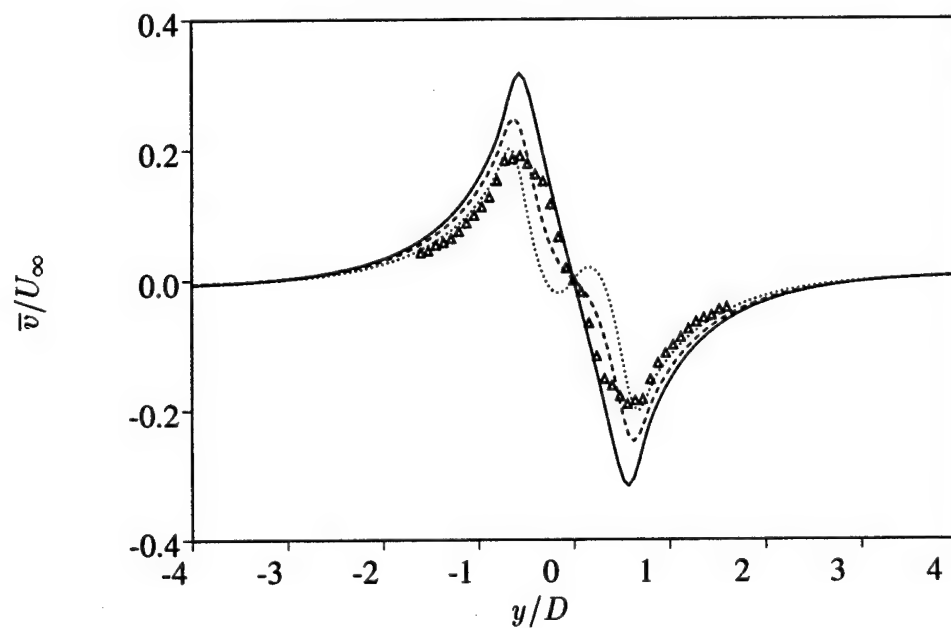
Figure 21: $Re = 3,900$; Vertical velocity at $x/D = 1.54$
——— : Dynamic model; ---- : No model; ⋯ : Fixed coefficient model
$\triangle$: Lourenco & Shih
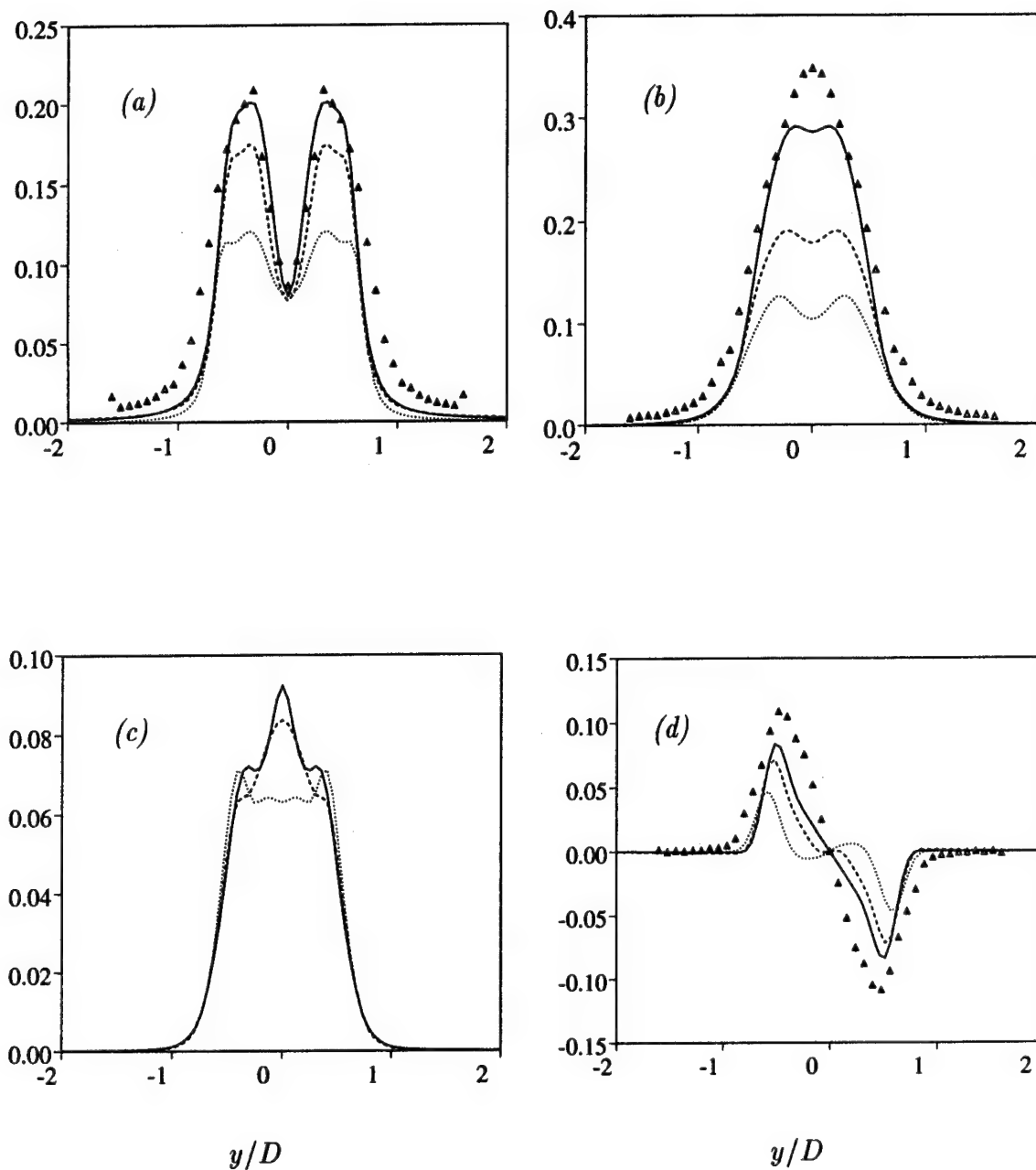
Figure 22: $Re = 3,900$; Total Reynolds stresses at $x/D = 1.54$
(a): Streamwise; (b): Vertical; (c): Spanwise; (d): Shear
—— : Dynamic model; ---- : No model; $\cdots$: Fixed coefficient model
$\triangle$: Lourenco & Shih
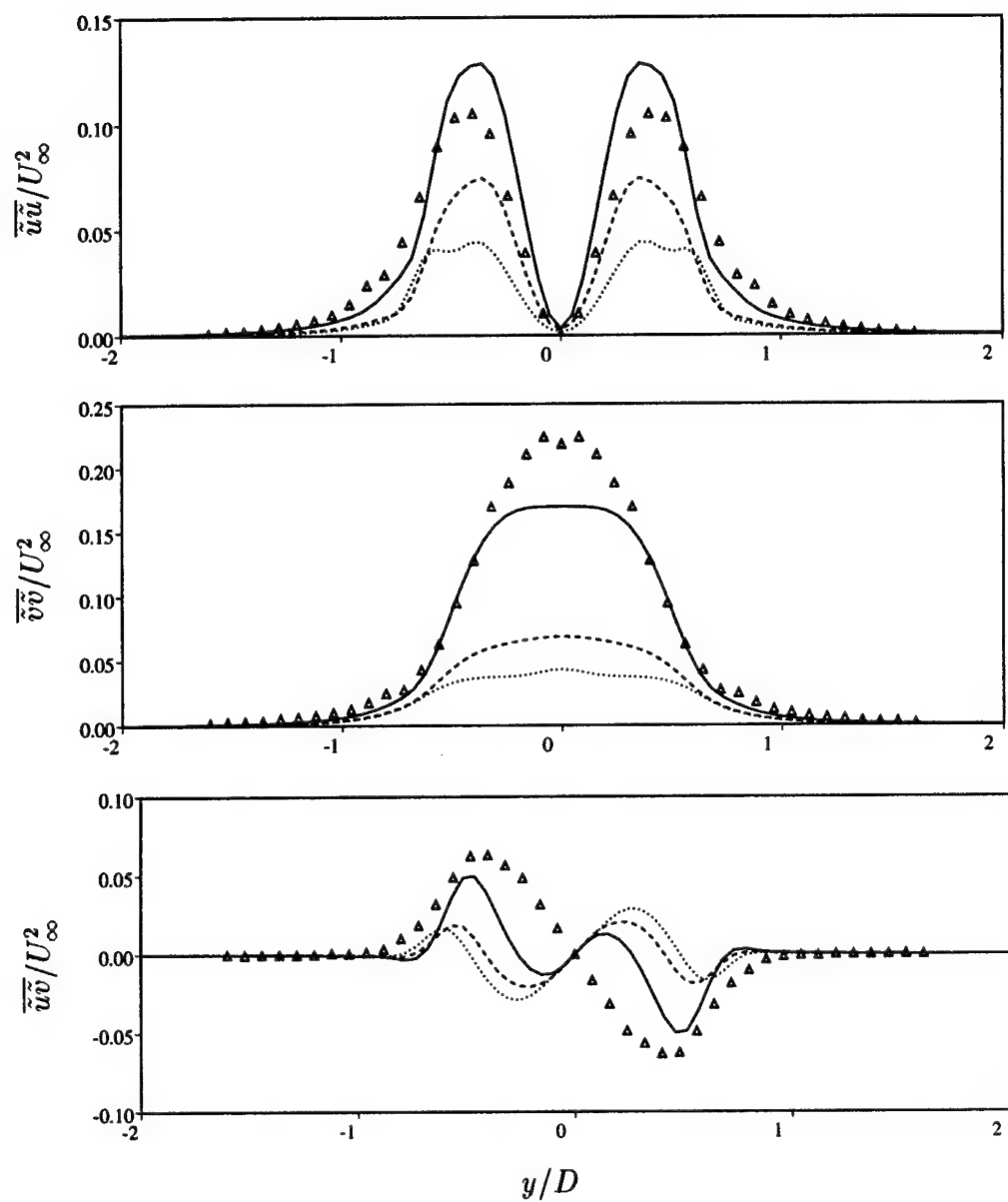
Figure 23: $Re = 3,900$; Periodic Reynolds stresses at $x/D = 1.54$
——— : Dynamic model; - - - - : No model; $\cdots$: Fixed coefficient model
$\triangle$: Lourenco & Shih

78
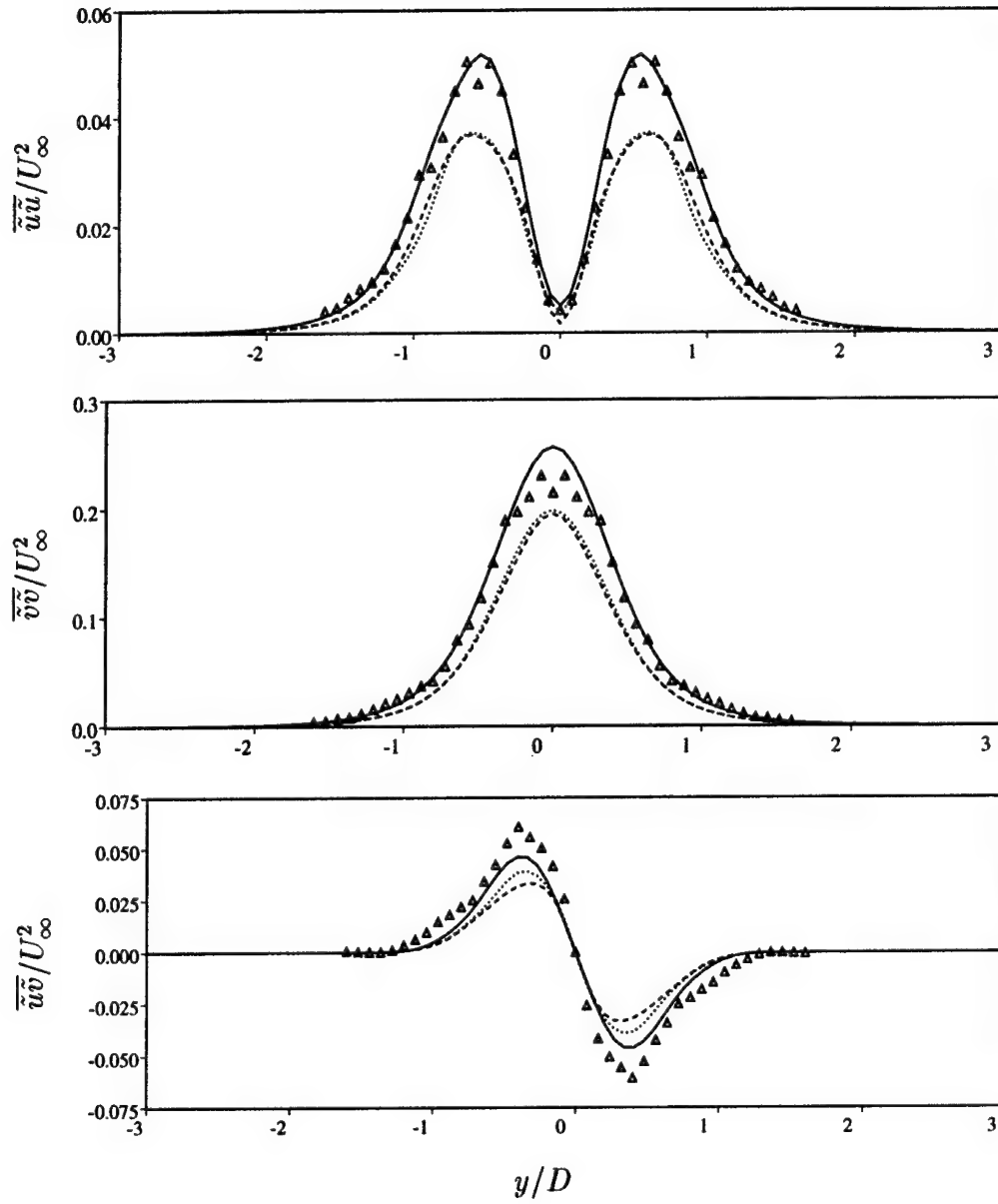
Figure 24: $Re = 3,900$; Periodic Reynolds stresses at $x/D = 2.5$
—— : Dynamic model; ---- : No model; $\cdots$: Fixed coefficient model
$\triangle$: Lourenco & Shih

79
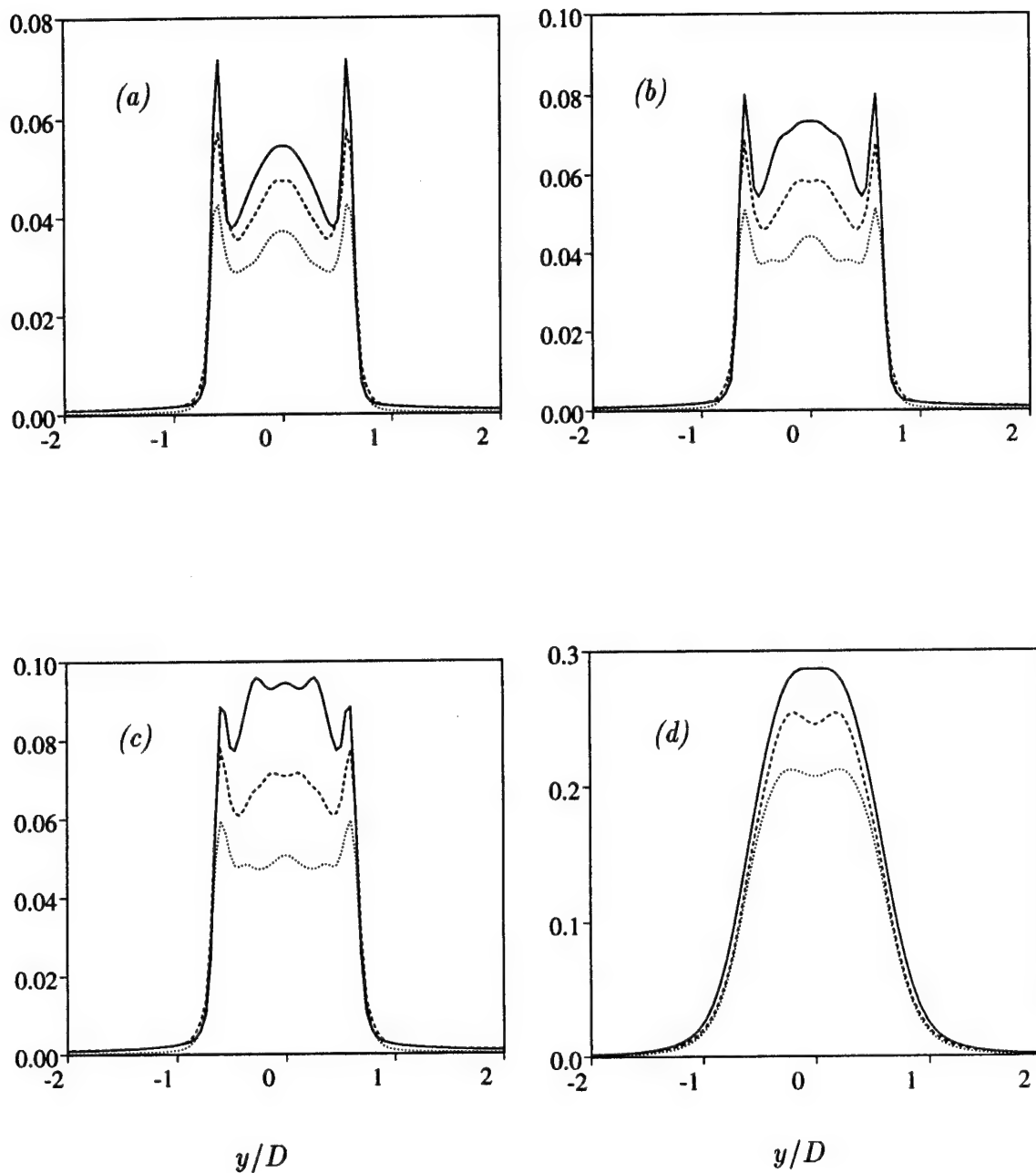
Figure 25: $Re = 3,900$; Total kinetic energy $(\overline{u'_k\,u'_k} + \overline{\tilde{u}_k\,\tilde{u}_k} + \overline{\tau}_{kk})/2U_\infty^2$
(a): $x/D = 0.8$; (b): $x/D = 0.9$; (c): $x/D = 1.0$; (d): $x/D = 2.0$
——— : Dynamic model; ---- : No model; ⋯ : Fixed coefficient model
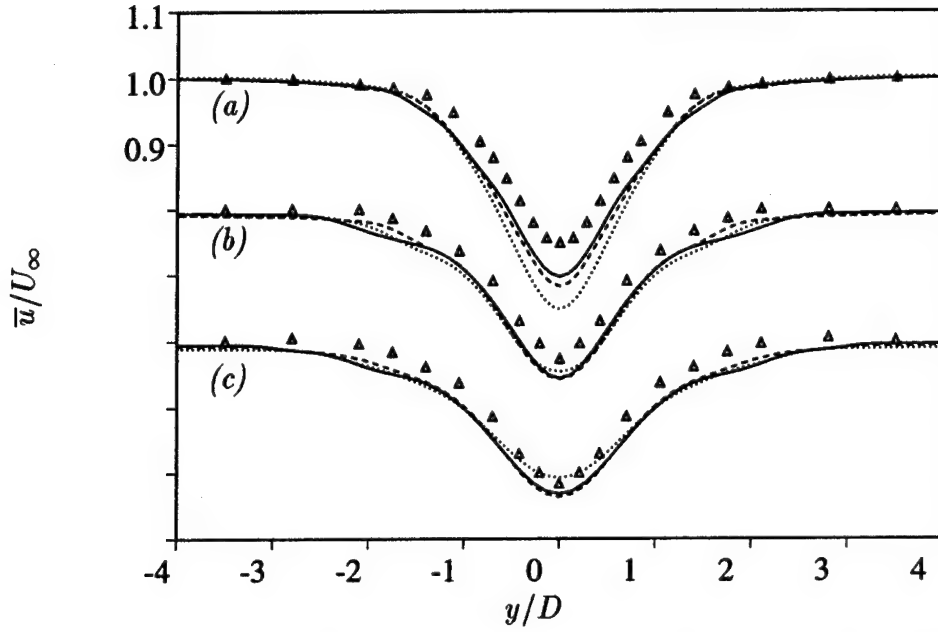
Figure 26: $Re = 3,900$; Streamwise velocity at $x/D = 4$ (a); 7 (b); 10 (c)
——— : Dynamic model; ---- : No model; $\cdots$: Fixed coefficient model
$\triangle$: Ong & Wallace
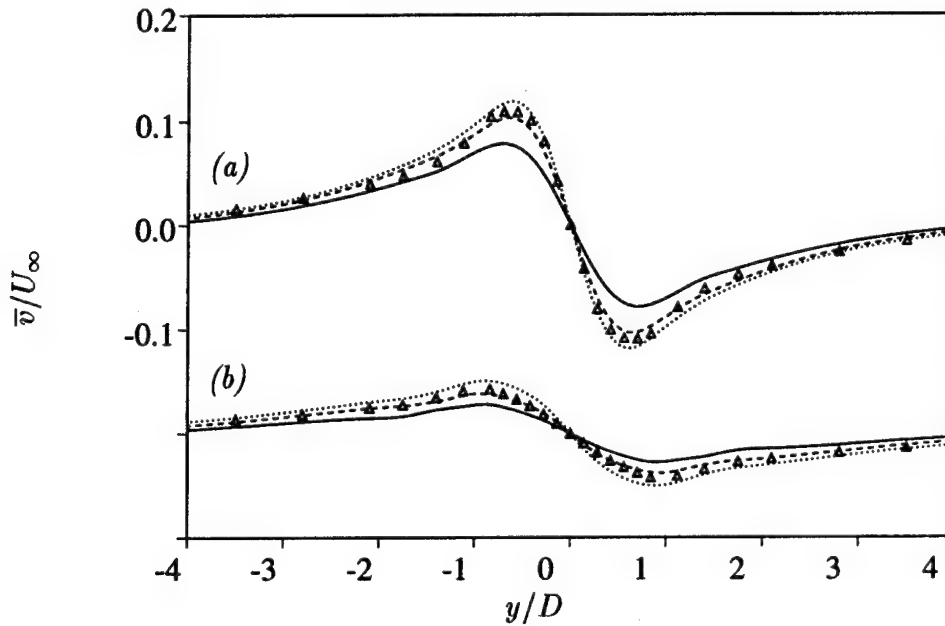
Figure 27: $Re = 3,900$; Vertical velocity at $x/D = 3$ (a); 4 (b)
——— : Dynamic model; ---- : No model; $\cdots$: Fixed coefficient model
$\triangle$: Ong & Wallace

81
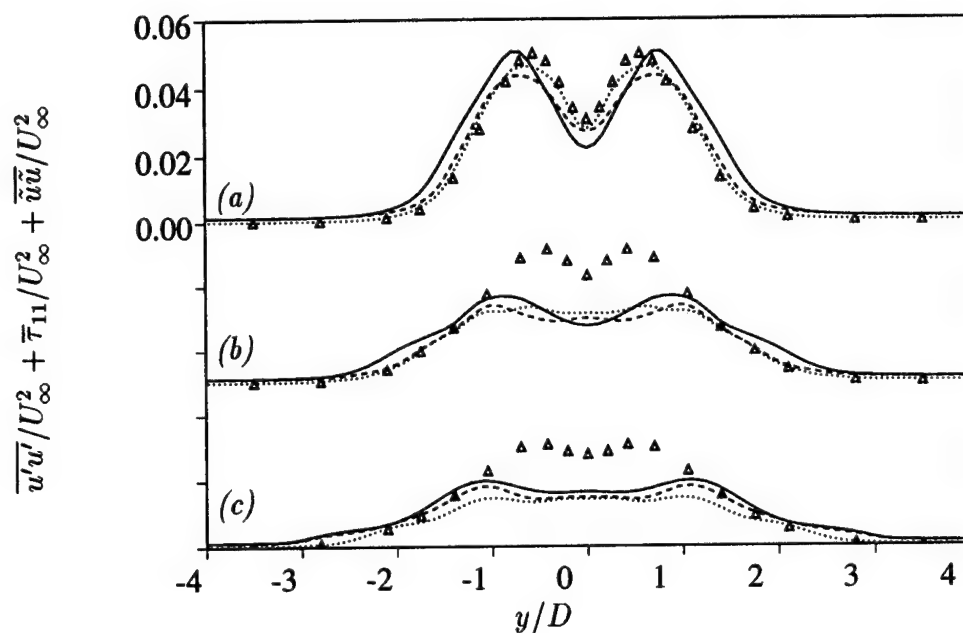
Figure 28: $Re = 3,900$; Total streamwise Reynolds stresses at $x/D = 4$ (a); 7 (b); 10 (c)

——— : Dynamic model; ---- : No model; $\cdots$: Fixed coefficient model
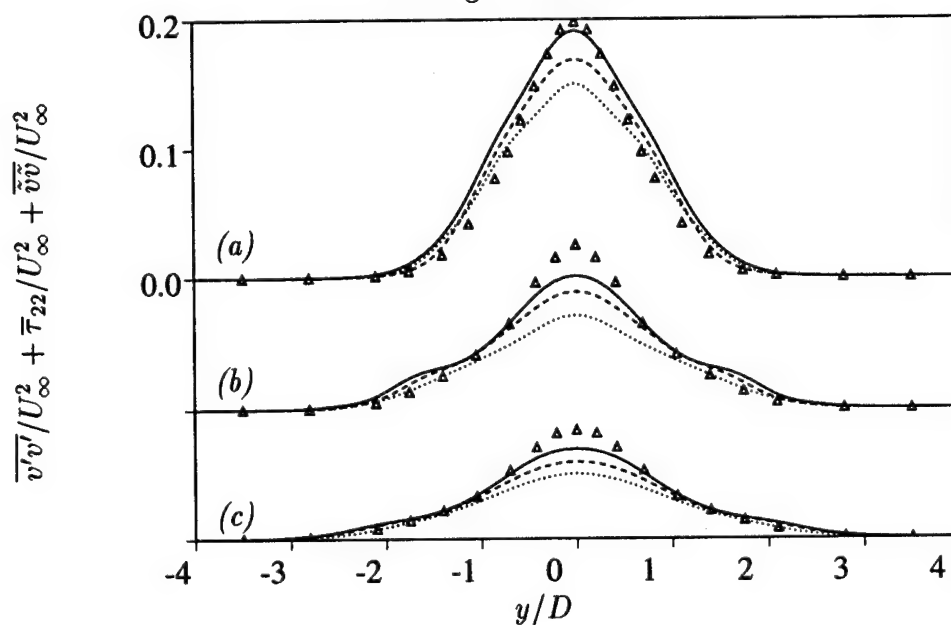
$\triangle$: Ong & Wallace

Figure 29: $Re = 3,900$; Total vertical Reynolds stresses at $x/D = 4$ (a); 7 (b); 10 (c)

——— : Dynamic model; ---- : No model; $\cdots$: Fixed coefficient model

$\triangle$: Ong & Wallace

82
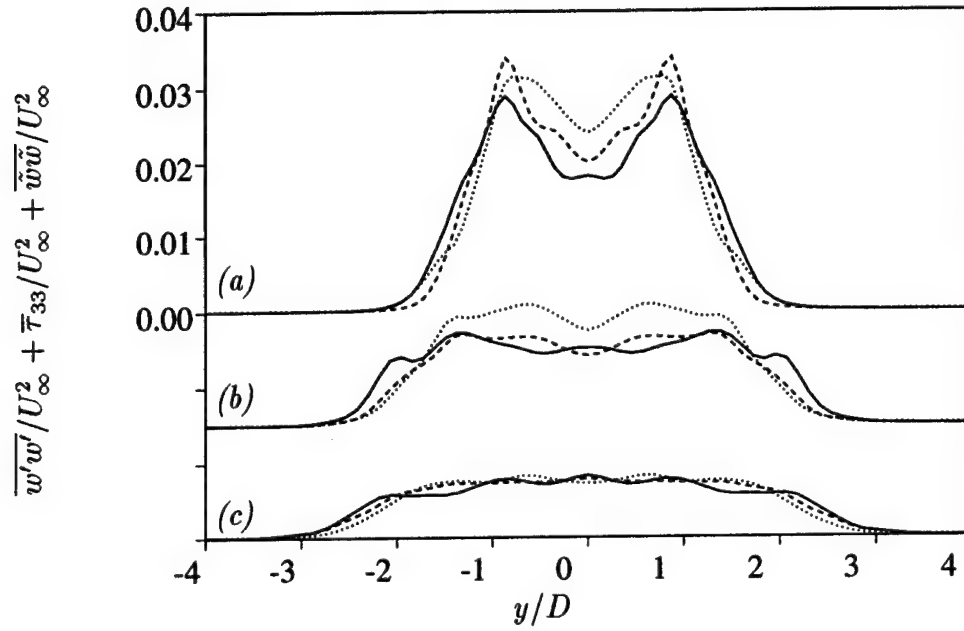
Figure 30: $Re = 3,900$; Total spanwise Reynolds stresses at $x/D = 4$ (a); 7 (b); 10 (c)

——— : Dynamic model; ---- : No model; $\cdots$: Fixed coefficient model
$\triangle$: Ong & Wallace
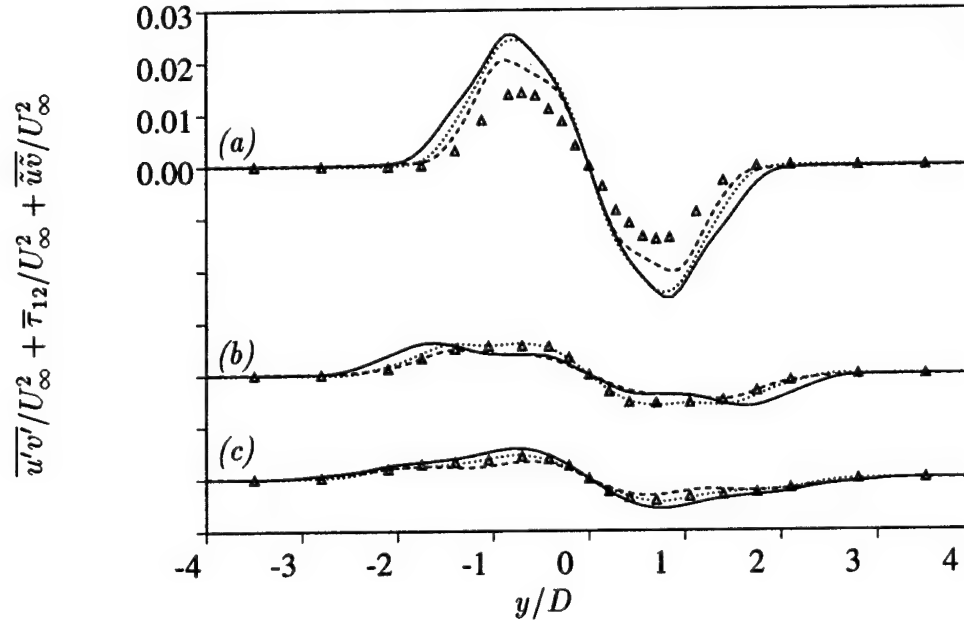
Figure 31: $Re = 3,900$; Total Reynolds shear stresses at $x/D = 4$ (a); 7 (b); 10 (c)
——— : Dynamic model; ---- : No model; $\cdots$: Fixed coefficient model
$\triangle$: Ong & Wallace
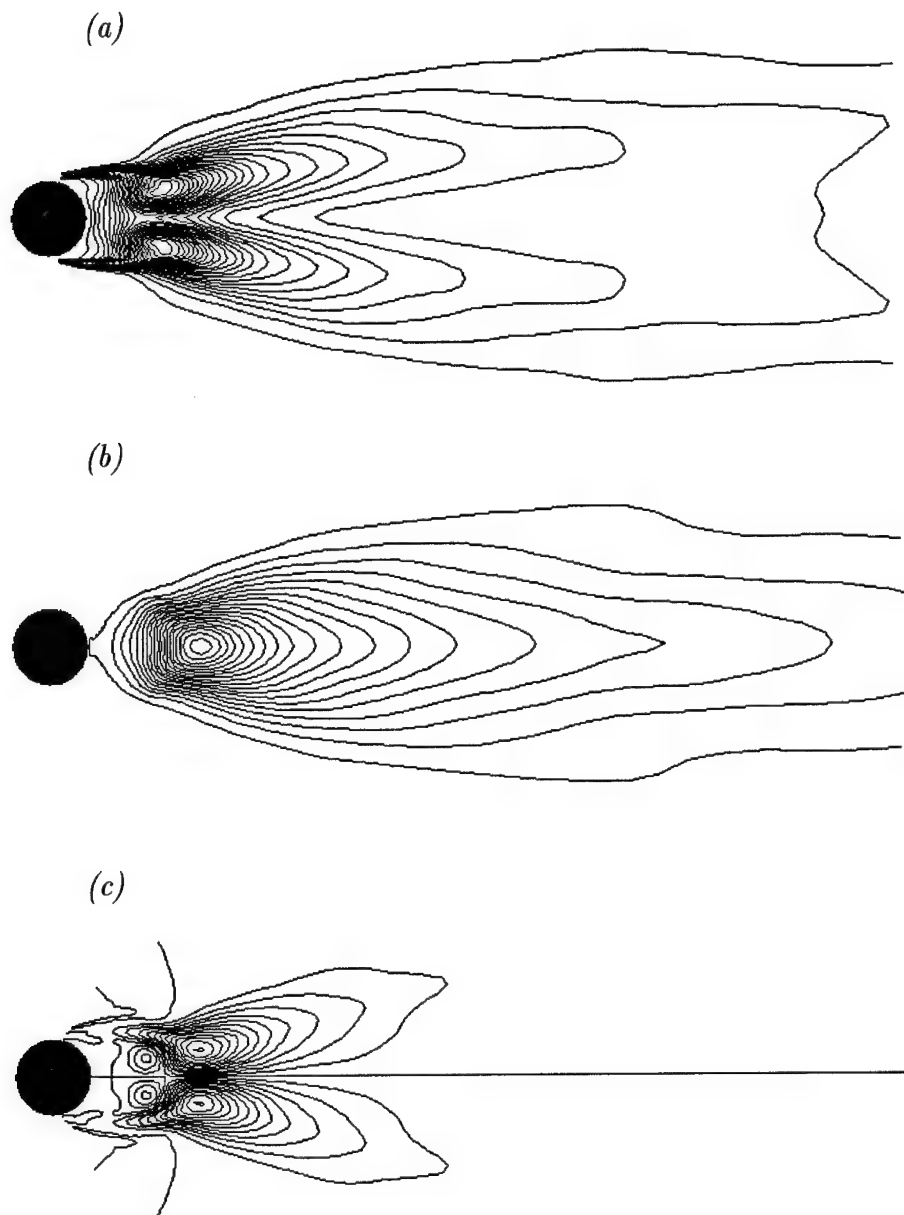
Figure 32: $Re = 3,900$; Time and spanwise averaged total Reynolds stresses in the first ten diameters of the wake
(a): Streamwise stress, contours from 0 to 0.18, increments 0.0075
(b): Vertical stress, contours from 0 to 0.4, increments 0.02
(c): Shear stress, contours from -0.12 to 0.12, increments 0.01
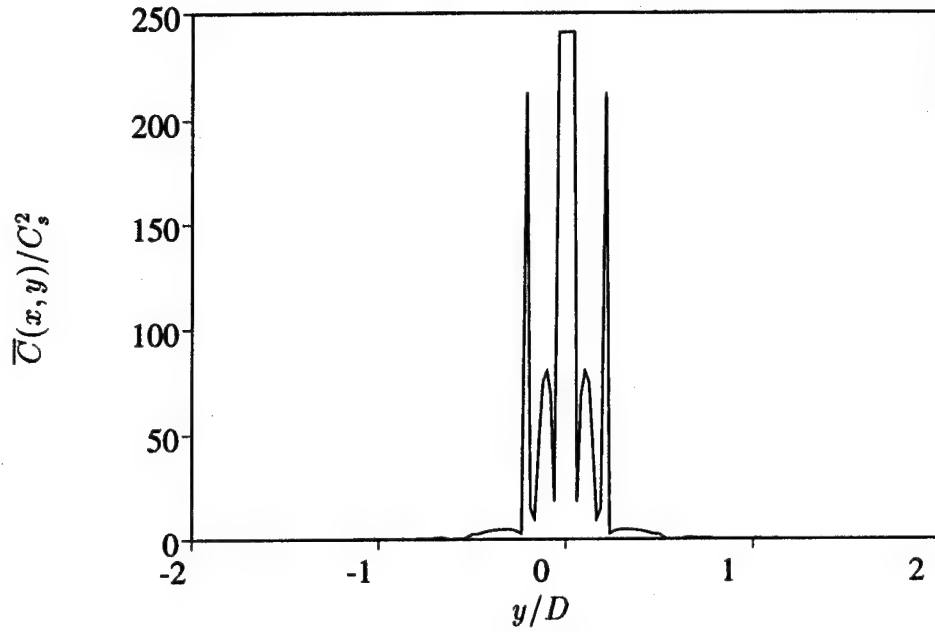
Figure 33: $Re = 3,900$; Dynamic model coefficient $\overline{C}(x,y)$ scaled on the squared Smagorinsky constant C_s^2 at $x/D = 0.5$
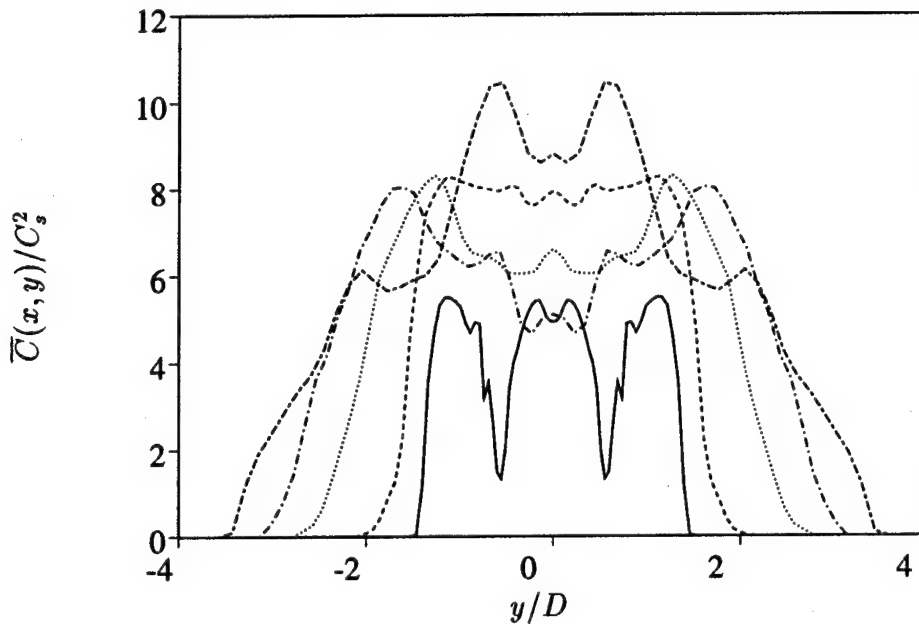
Figure 34: $Re = 3,900$; Dynamic model coefficient $\overline{C}(x,y)$ scaled on the squared Smagorinsky constant C_s^2

$$\text{———} : x/D = 1; \ \text{----} : x/D = 3; \ \cdots : x/D = 5$$
$$\text{—·—} : x/D = 7; \ \text{——} : x/D = 10$$
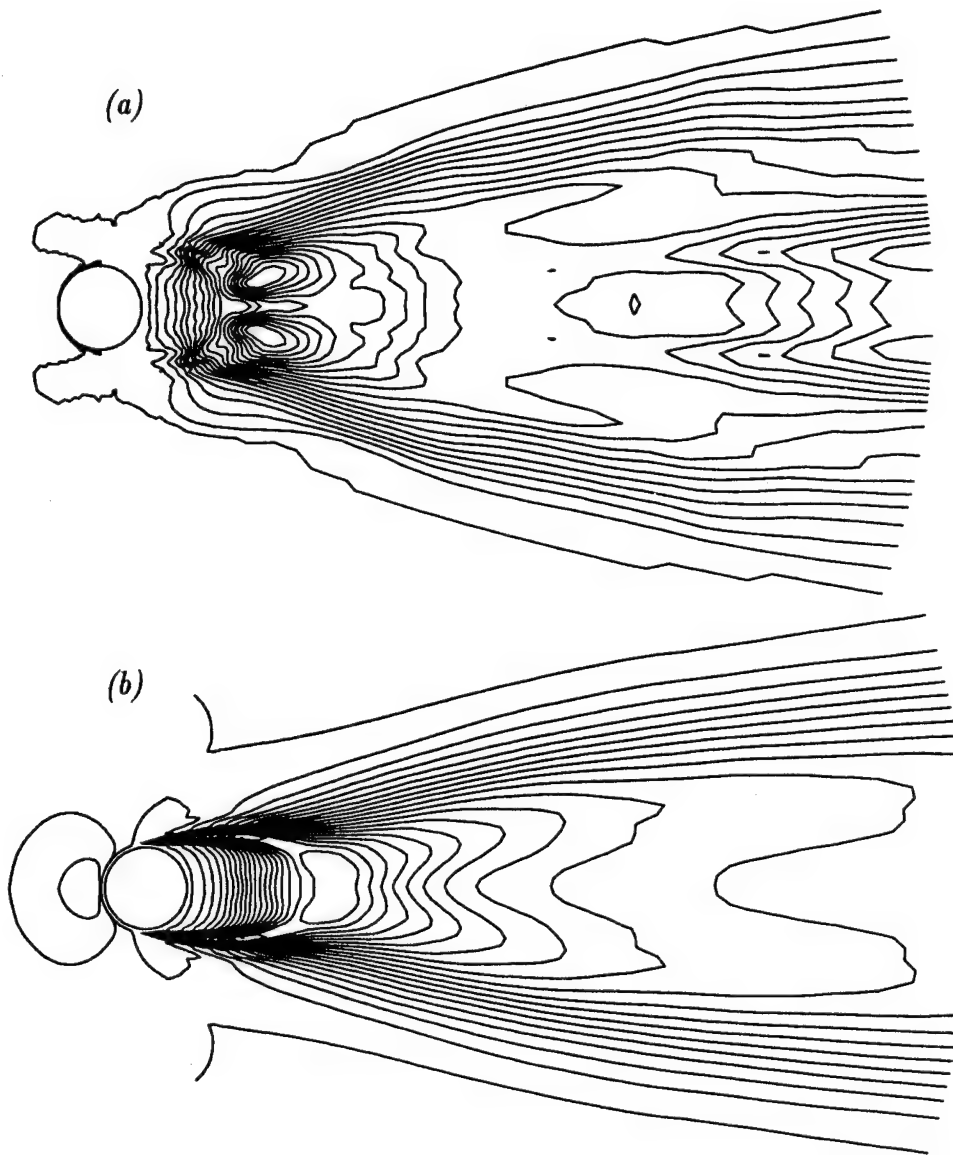
Figure 35: $Re = 3,900$; Normalized time and spanwise-averaged eddy viscosity $\overline{\nu}_t / \max(\overline{\nu}_t)$ in the first ten diameters of the wake

(a): Dynamic model; (b): Fixed coefficient model

Contours from 0 to 1; increments 0.05
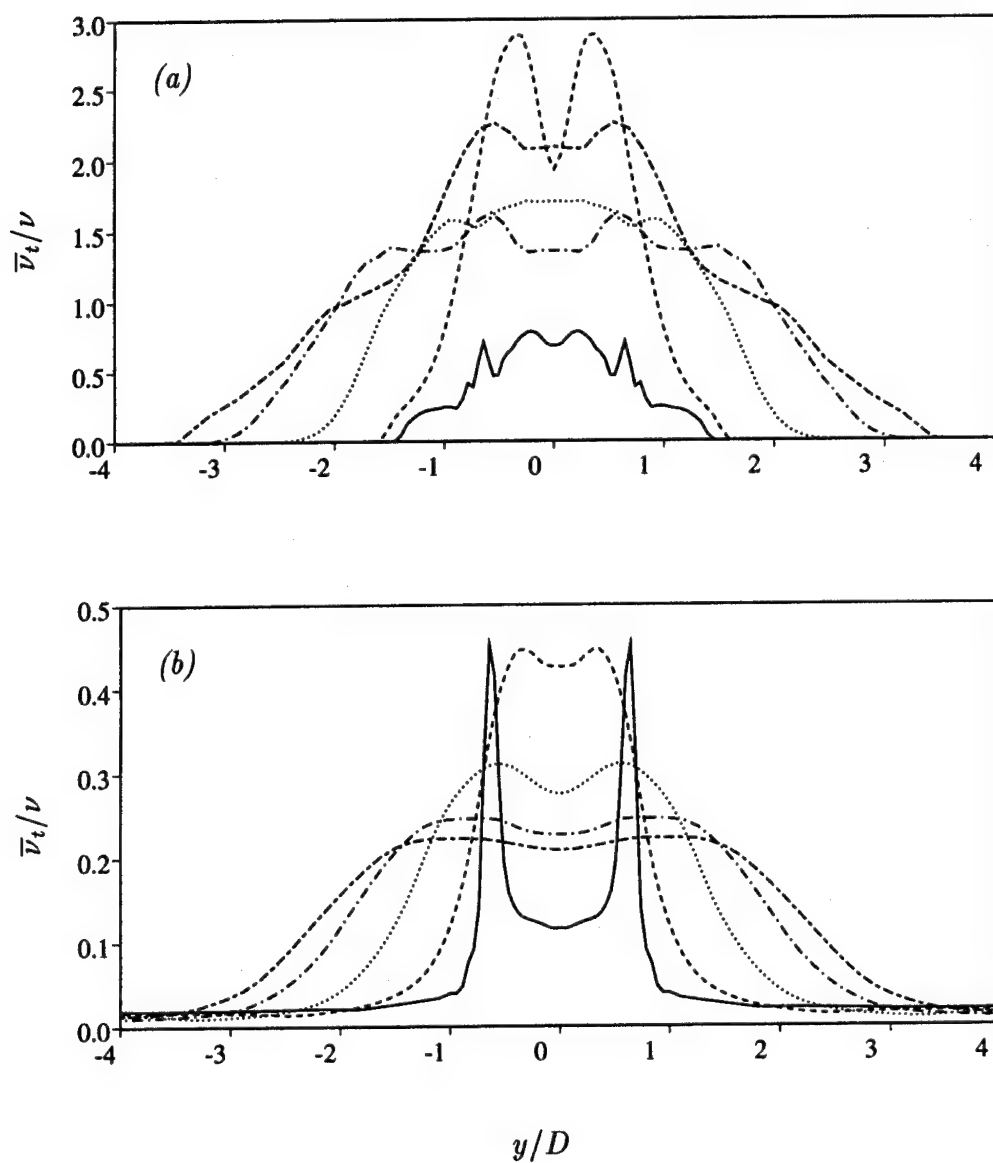
Figure 36: $Re = 3,900$; Time and spanwise-averaged eddy viscosity profiles
(a): Dynamic model; (b): Fixed coefficient model
——— : $x/D = 1$; –––– : $x/D = 2$; ⋯ : $x/D = 4$
—·— : $x/D = 7$; ––– : $x/D = 10$
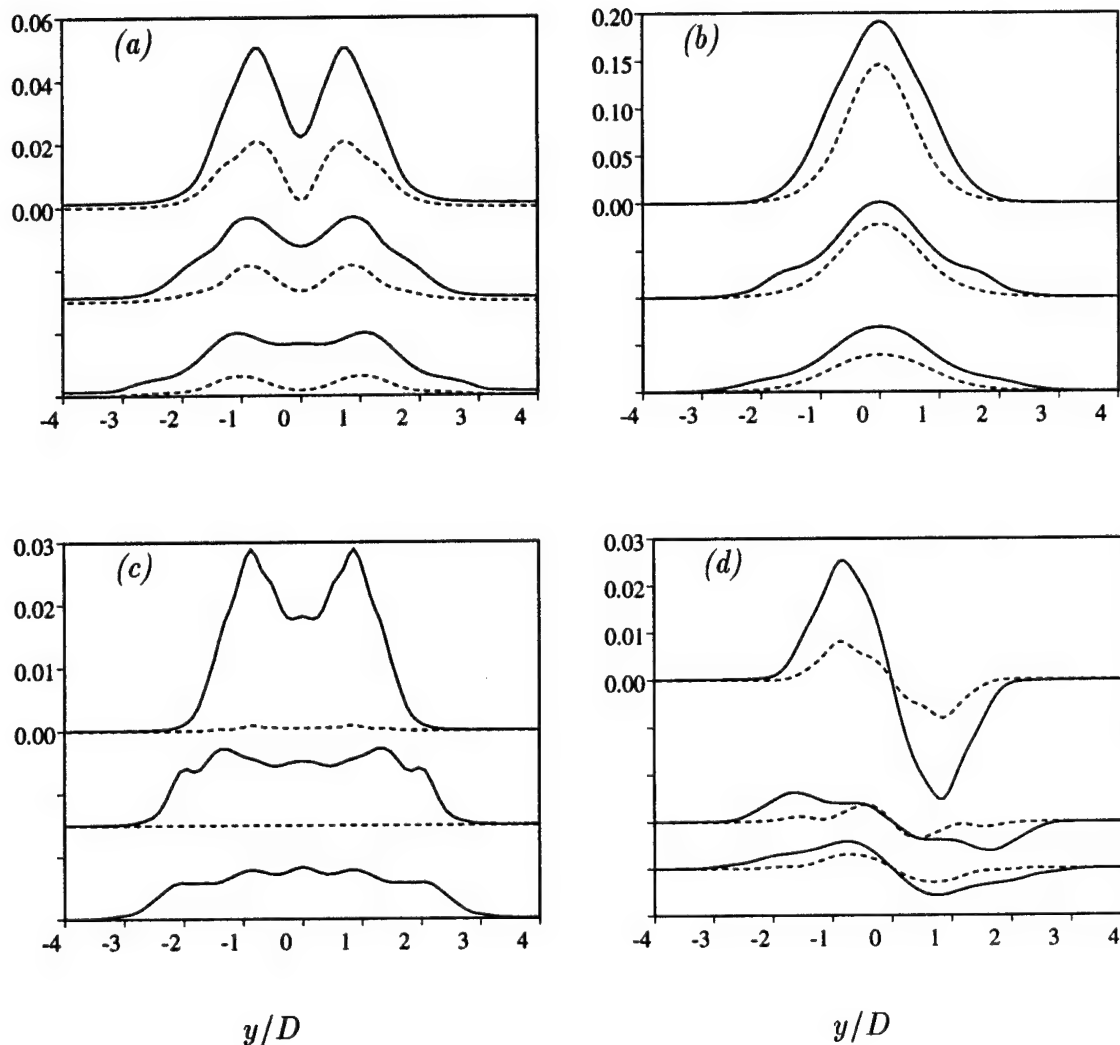
Figure 37: $Re = 3,900$; Total and periodic Reynolds stress components
(a): Streamwise; (b): Vertical; (c): Spanwise; (d): Shear
Dynamic model; —— : total; - - - - : periodic
In each figure: $x/D = 4$ (top); 7 (center); 10 (bottom)

88
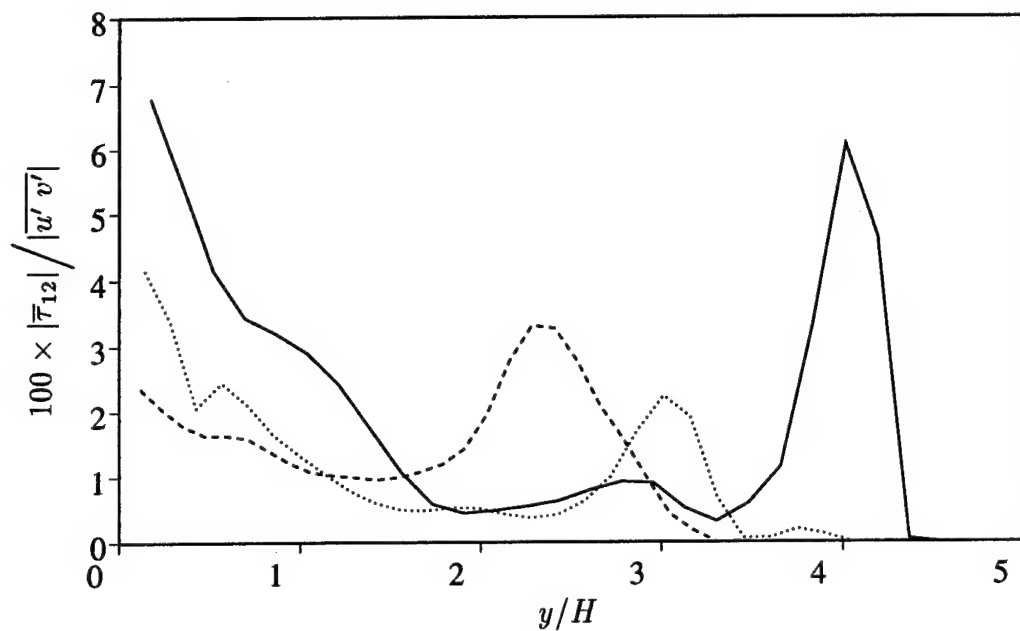
Figure 38: $Re = 3,900$; Percentage of subgrid-scale to resolvable Reynolds shear stress

$----$: $x/D = 3$; $\cdots$: $x/D = 5$; —— : $x/D = 10$
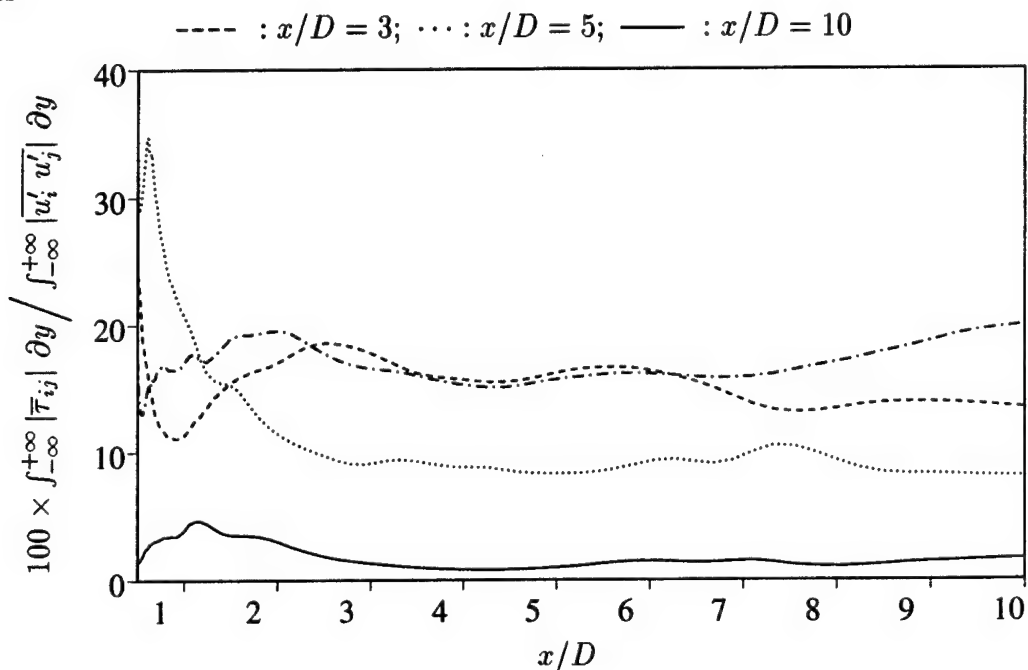
Figure 39: $Re = 3,900$; Percentage of vertically integrated subgrid-scale to resolvable Reynolds stresses

$----$: Streamwise; $\cdots$: Vertical; —·— : Spanwise; —— : Shear

Dynamic model simulation; $Re = 3,900$
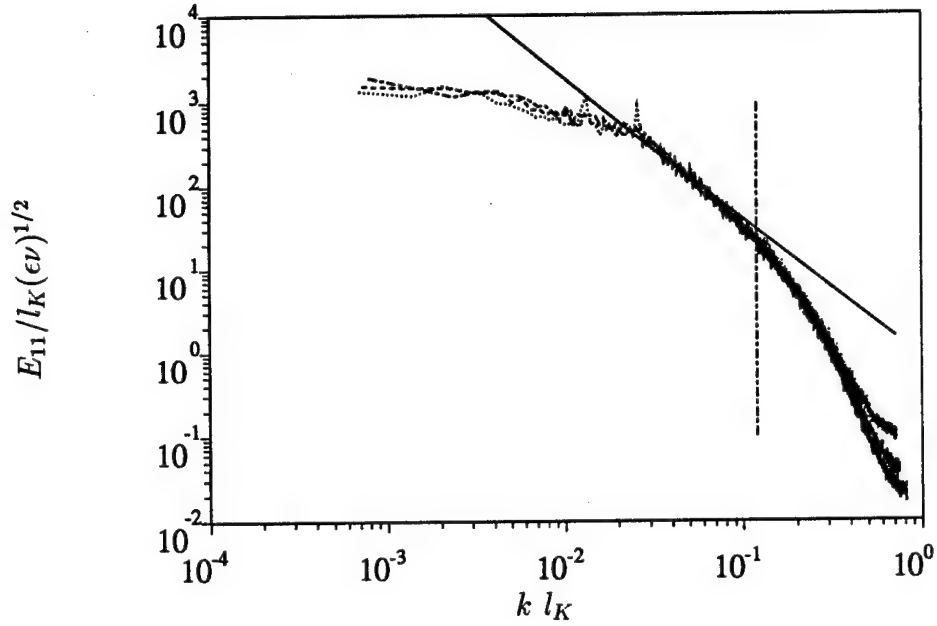
Figure 40: $Re = 3,900$; Experimental velocity power spectra E_{11} at $y = 0$ (Ong & Wallace, 1994); $\cdots$: $x/D = 5$; ---- : $x/D = 7$; —·— : $x/D = 10$; —— : $k^{-5/3}$; —·—·— grid cutoff at $x/D = 10$
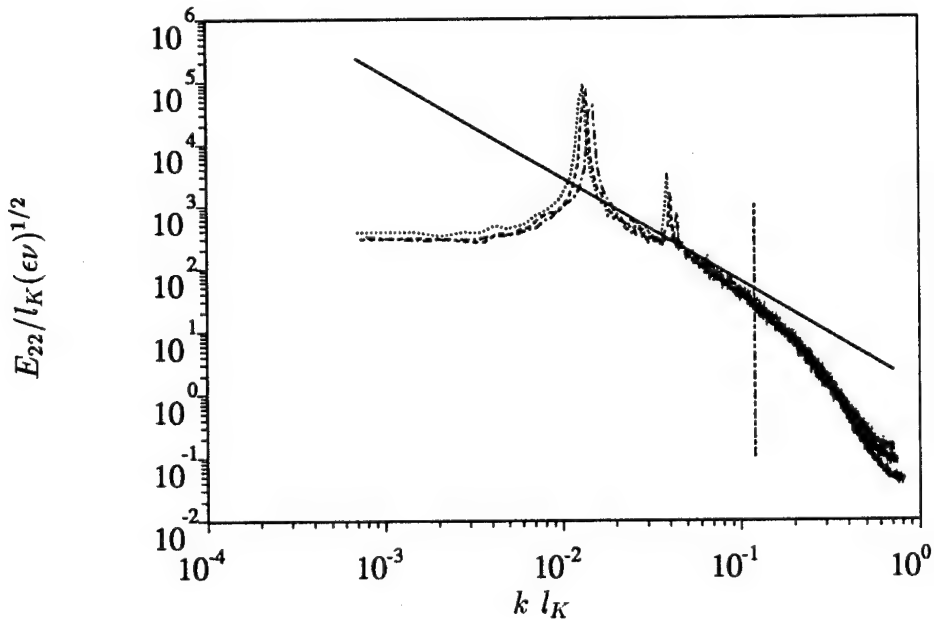
Figure 41: $Re = 3,900$; Experimental velocity power spectra E_{22} at $y = 0$ (Ong & Wallace, 1994); $\cdots$: $x/D = 5$; ---- : $x/D = 7$; —·— : $x/D = 10$; —— : $k^{-5/3}$; —·—·— grid cutoff at $x/D = 10$

x/D
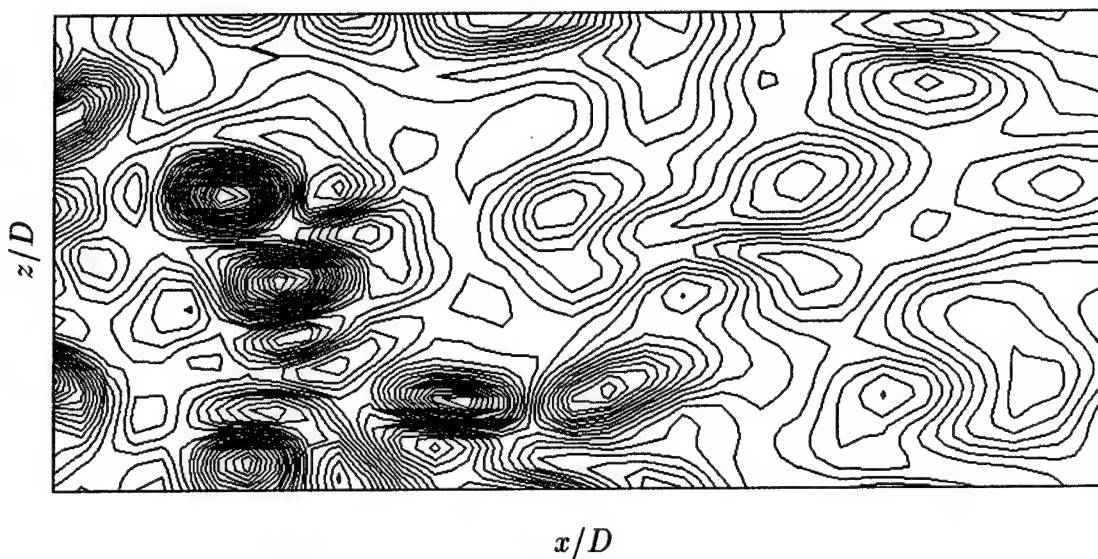
Figure 42: $Re = 3,900$; Instantaneous vertical vorticity at $y = 0$, $5 \leq x/D \leq 10$, $0 \leq z \leq L_z$. Dynamic model simulation.

Contours from -5 to 6 by 0.3

y/D
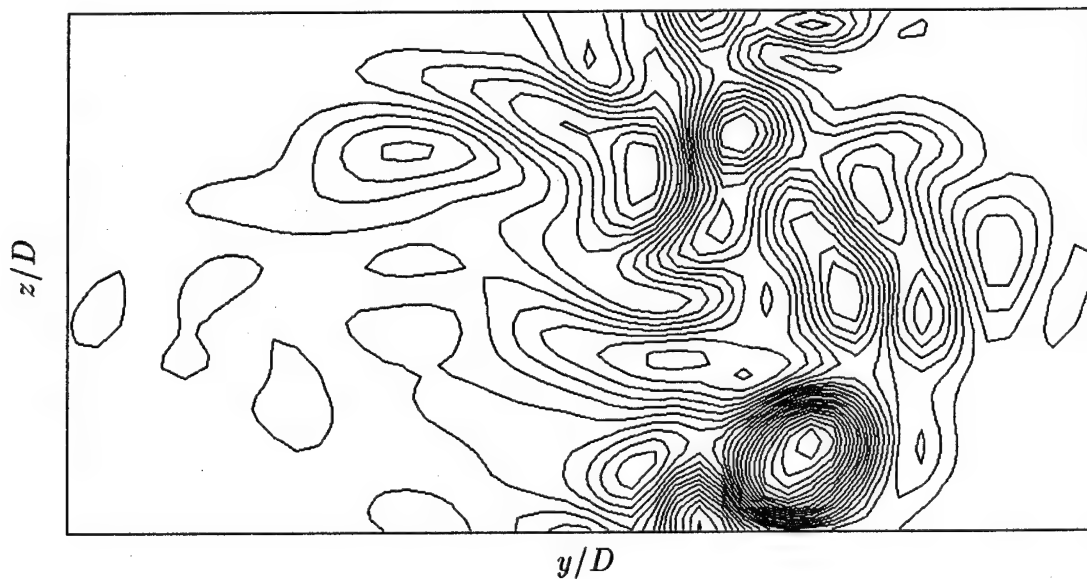
Figure 43: $Re = 3,900$; Instantaneous streamwise vorticity at $r/D = 10$, $-5 \leq y/D \leq 5$, $0 \leq z \leq L_z$. Dynamic model simulation.

Contours from -5 to 3 by 0.3

91
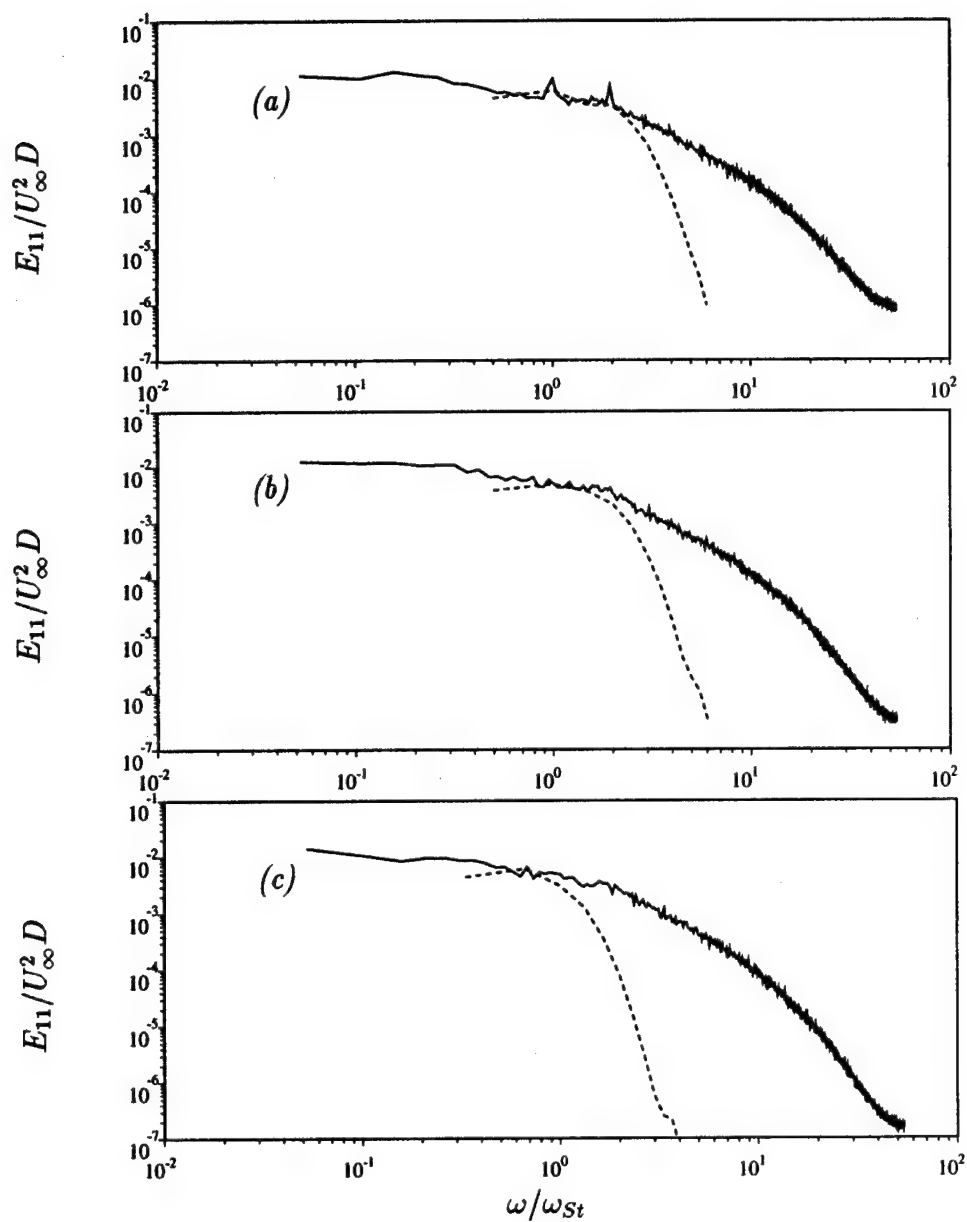
Figure 44: $Re = 3,900$; One-dimensional spectra E_{11} at (a): $x/D = 5$; (b) : $x/D = 7$; (c): $x/D = 10$

---- : Dynamic model; ——— : Ong & Wallace

92
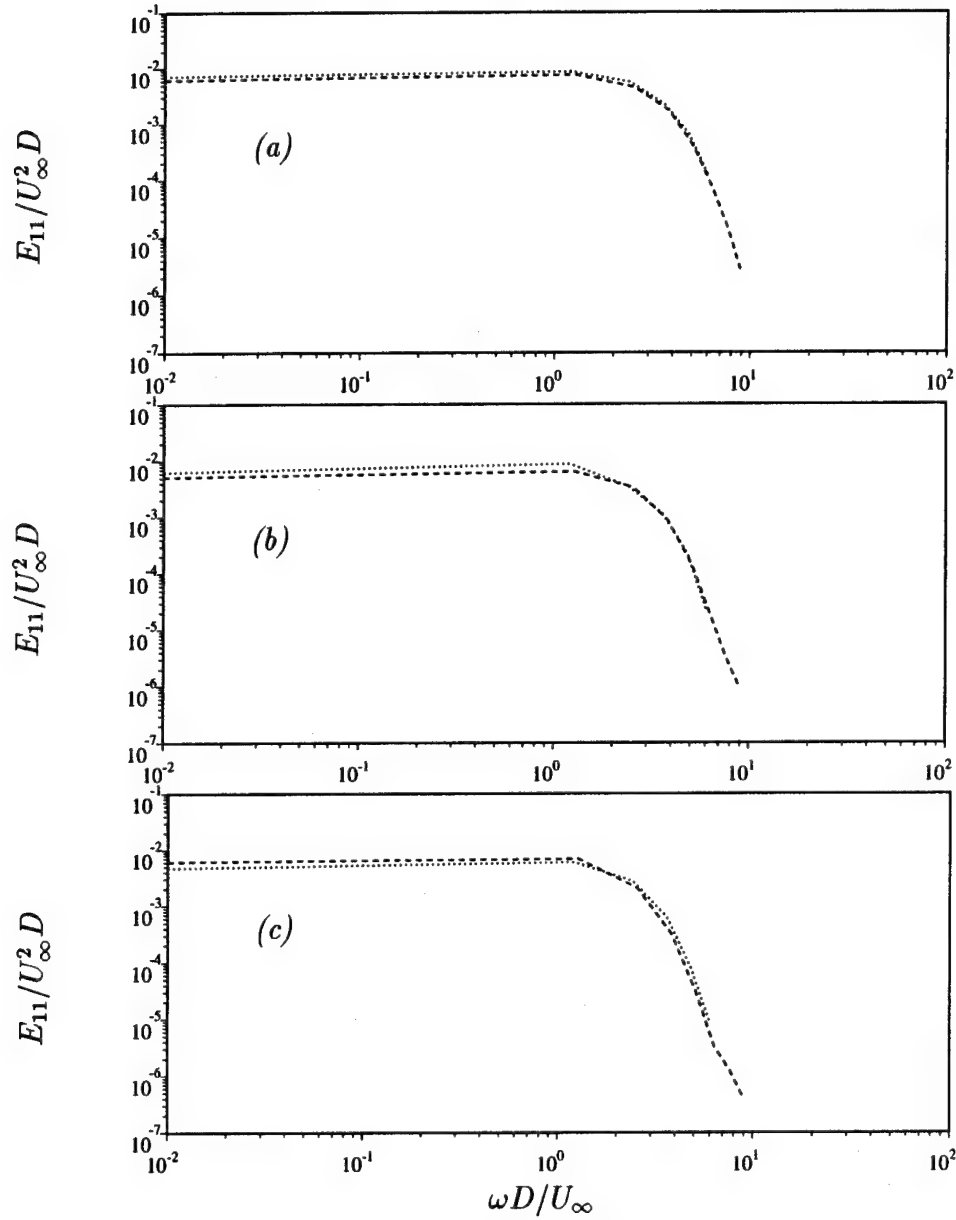
Figure 45: $Re = 3,900$; One-dimensional spectra E_{11} from LES and DNS at (a): $x/D = 5$; (b) : $x/D = 7$; (c): $x/D = 10$

---- : Dynamic model; $\cdots$: No model;

93
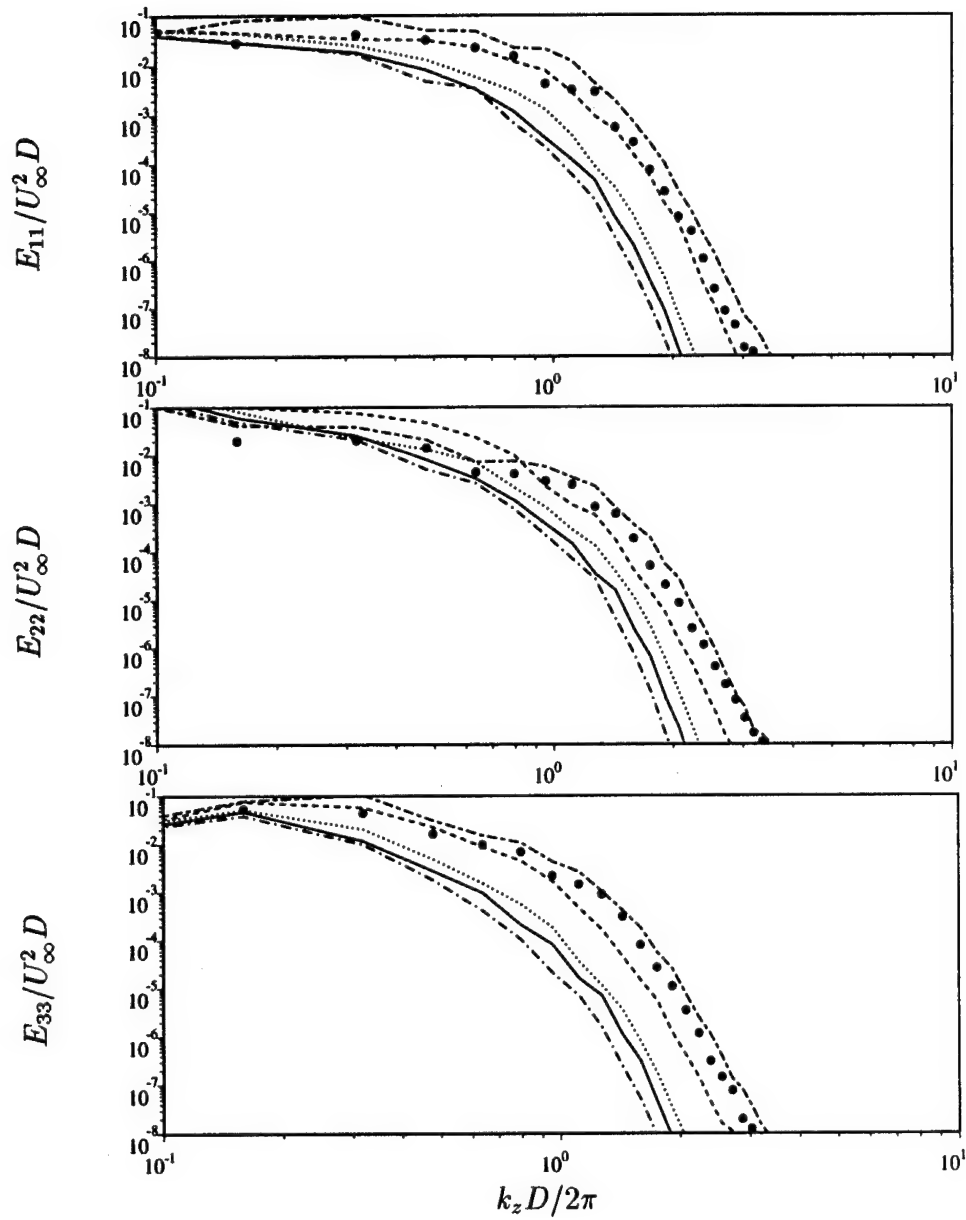
Figure 46: $Re = 3,900$; One-dimensional spectra E_{11}, E_{22} and E_{33} at $y = 0$ from the dynamic model simulation

$\bullet$: $x/D = 0.7$; $---$: $x/D = 1$; $----$: $x/D = 3$; $\cdots$: $x/D = 5$
$-\cdot-$: $x/D = 7$; $\rule{1cm}{0.4pt}$: $x/D = 10$

94

Chapter 5

Numerical Dissipation Impact on the Solution

5.1 Motivation and Objective

The results outlined in the previous chapter indicated that the numerical dissipation generated by the fifth-order accurate, one-point upwind biased scheme applied to the convective fluxes had a nefarious impact on the calculations. This scheme is referred to below as scheme A. In the near-wake region between four and ten diameters downstream of the cylinder, frequency spectra of the velocity indicated that a substantial range of frequencies resolvable on the grid were damped. This range widened with increasing downstream distance. As a direct consequence, the subgrid-scale eddy-viscosity models were probably overwhelmed by numerical dissipation in the near-wake.

To assess the impact of numerical dissipation on the computed solution, the results obtained with the fifth-order accurate, upwind-biased scheme must be compared with those generated using a scheme with less inherent numerical dissipation. The objective of this chapter is to establish such a comparison.

Rai & Moin (1991) used a sixth-order accurate central scheme for the convective

fluxes in an incompressible turbulent channel flow simulation. The solution was de-aliased in Fourier space, an approach not well suited for finite-difference methods in complex geometry. Further, incompressible Navier-Stokes solvers involve no divisions and fewer multiplications of primitive variables than compressible solvers. The severity of the aliasing problem may thus be different for incompressible and compressible numerical solutions.

A differencing scheme for convective fluxes which has been successfully applied in compressible simulations (Blaisdell *et al.* 1990, Lee *et al.* 1992) is a central scheme in which derivatives of the convective fluxes are computed as

$$
\begin{aligned}
\frac{\partial}{\partial x} \rho u_i(k_1 u \quad + \quad k_2 v + k_3 w) &= \frac{1}{2} \frac{\partial}{\partial x} \rho u_i(k_1 u + k_2 v + k_3 w) \\
&+ \quad \frac{1}{2} \rho u_i \frac{\partial}{\partial x}(k_1 u + k_2 v + k_3 w) + \frac{1}{2}(k_1 u + k_2 v + k_3 w) \frac{\partial}{\partial x} \rho u_i \quad (101)
\end{aligned}
$$

where k_1, k_2 and k_3 are geometric coefficients given in table 7 of appendix A. This formulation conserves total kinetic energy in the inviscid limit (Feiereisen *et al.* 1981), and has been demonstrated to control aliasing errors in the calculations of decaying homogenous turbulence (Blaisdell *et al.* 1990). Applied to the flow over a circular cylinder with a fourth-order accurate scheme, this method was found to be unstable with both the trapezoidal and the second-order backward time-integration schemes. It was discontinued in favor of a strategy to systematically reduce the level of numerical dissipation generated by upwind-biased schemes. This is achieved by comparing the velocity power spectra obtained from simulations with increasing order of accuracy which use one-point upwind-biased differencing schemes for the convective fluxes.

This chapter presents the results of such a computation, which uses a seventh-order accurate, upwind-biased scheme for the convective fluxes. This is referred to as scheme B below. The precise differencing stencil is given by equations 58 and 59 in chapter 2.

5.2　A Numerical Example

The solution to the one-dimensional wave equation provides some guidance on the improvements which may be expected with scheme B. The governing equation

$$\frac{\partial u}{\partial t} + \frac{\partial u}{\partial x} = 0 \quad 0 < x \leq L, \ t > 0 \tag{102}$$

with the associated boundary and initial conditions

$$u(x,0) = \exp(-\alpha(x - x_0)^2) \quad u(0,t) = \exp(-\alpha(x_0 + t)^2) \tag{103}$$

are advanced in time using the second-order accurate implicit scheme used in cylinder simulations. The domain length is chosen as $L = 126$, and the spatial discretization is uniform, with 221 points in a first case (1) and 442 points in a second case (2). The examples below are computed with the parameters $x_0 = 3$ and $\alpha = 4$, which translate into a Gaussian of half-width 1.07 spanned by four and eight computational points in cases (1) and (2) respectively. This numerical experiment can be thought of as describing the effect of upwinding on a coarsely resolved structure traveling on a large-eddy simulation mesh. The solutions using schemes A and B are compared at the time when the traveling Gaussian is centered at $x = 20$. The exact solution is a Gaussian of unit amplitude, unaltered in shape from its initial condition. Figures 47 and 48 display the profiles of the computed solutions at $t = 17$. Scheme B yields an 18% improvement over scheme A in the amplitude of the solution with four points per structure (Gaussian). With a doubling of the resolution, the improvement afforded by the seventh order scheme diminishes to 13%. Simulations with both schemes significantly damp the traveling Gaussian at both resolutions. Both solutions also exhibit the effect of numerical diffusion by widening the width of the traveling structure.

This one-dimensional example suggests that coarse to moderately resolved structures traveling in the cylinder wake are significantly damped by the numerical dissipation generated by upwinding, although the application of scheme B should result in a small but measurable improvement in the resolution of these structures. This conjecture is investigated below.

5.3   Cylinder Computations

The flow at Reynolds number $3,900$ was computed on the same $(144 \times 136 \times 48)$-point mesh which was used in the fifth-order accurate simulations presented in the previous chapter. The simulation was performed with the dynamic subgrid-scale eddy-viscosity model.

5.3.1   Instantaneous Wake Vorticity

This section provides a qualitative discussion of the differences observed in the vorticity fields obtained with schemes A and B. In all figures, the vorticity has been scaled on the local mean centerline streamwise velocity deficit.

The vertical vorticity contours at $r/D = 5$, displayed in figure 49, exhibits smaller vortices and sharper vorticity gradients obtained with the higher-order upwind scheme. Ten diameters downstream (figure 50), similar properties are discernable in the streamwise vorticity. In the calculation with scheme A, constant streamwise vorticity contours display larger structures than with the seventh-order scheme.

The breakup of spanwise vortical structures described above is visible in the spanwise vorticity contours on the rear plane of symmetry ($y = 0$), in the region $5 \leq x/D \leq 10$ (figure 51). The simulation with scheme A displays a quasi-regular pattern of primary rollers spanning the entire homogeneous direction. With scheme B, these regular rollers have been altered by smaller structures.

Finally, figures 52 and 53 display the instantaneous streamwise and vertical vorticities respectively, in a vertical plane at $z = 0$, between five and ten diameters downstream. Both figures exhibit the same features that were noted in the discussion above: the simulation with scheme B shows smaller and more numerous vortical structures in the wake, separated by regions of sharper vorticity gradients.

Differences in the three-dimensional structures of the respective wakes are further illustrated by the instantaneous constant vorticity contours ($|\vec{\omega}D/u_d| = 1,\ 3,\ 6$) shown in figures 54 through 56 respectively, where u_d is the mean centerline velocity

deficit. The first figure offers a qualitatively similar view of both simulations. Stream-wise structures of roughly equal size appear to connect the spanwise rollers. However at the higher levels of vorticity, the streamwise ribs are thinner in the higher-order accurate simulation. In the near-wake ($5 \leq x/D \leq 10$), streamwise structures appear as slender, coherent ribs extending from one spanwise vortex-core to the next with scheme B. On the contrary, in the same interval, structures computed with scheme A are shorter ribs which diffuse with downstream distance. This difference is most pronounced for $|\bar{\bar{\omega}}D/u_d| = 6$, the corresponding ribs having completely disappeared from the near-wake in the calculation with scheme A. This indicates that the ribs have gained in strength with the higher-order accurate scheme and lowered level of numerical dissipation. These structures are instrumental in ejecting low-speed fluid from the wake-layer and entraining irrotational fluid toward the turbulent core of the wake. Their increased strength thus corresponds to a more intense mixing process in the wake layer.

Instantaneous contours of the spanwise vorticity and vertical velocity computed with the seventh-order accurate scheme in the first ten diameters of the wake are displayed in figures 57 and 58 respectively. The first two Karmann vortices behind the cylinder form a pattern similar to that observed at laminar regimes. Past five diameters downstream, the breakup of the spanwise rollers into smaller structures is visible. In the free shear layer separating from the bottom side of the cylinder, the vertical velocity contours outline the presence of secondary vortices.

5.3.2 Velocity Power Spectra

The observations made in the previous section on the presence of sharper features and smaller-scale structures in the seventh-order accurate simulation are quantified in this section through a comparison the velocity power spectra obtained with schemes A and B.

At locations $x/D = 5$, 7 and $x/D = 10$, the spectra obtained from scheme B (figure 59), although substantially damped by numerical dissipation, display energy levels at resolvable frequencies increased by up to about eight tenths of a decade

99

relative to the results with scheme A. Five diameters downstream the spectra obtained from the seventh-order accurate calculation are damped at frequencies lower than that of the start of the $k^{-5/3}$ range displayed in the experiment. As the flow evolves downstream on a coarsening mesh, larger scales of motion are expectedly further damped. To accurately resolve these spectra at $x/D = 5$ past the start of the inertial range on the present grid would thus require at least a ninth-order accurate, one-point upwind scheme, which may encounter other numerical difficulties associated with Runge phenomenon.

Although spanwise wave-number spectra are not available experimentally, figure 60 shows that the gains in energy at high wave-numbers realized with scheme A are more substantial than in the streamwise frequency spectra. At $x/D = 7$ for instance, the energy level increased by up to two decades at wave-numbers between ten and fifteen.

5.3.3 Dynamic Subgrid-Scale Model Contribution

The magnitudes of the subgrid-scale intensities and shear stress relative to their resolvable counterparts are shown as a percentage ratio in figure 61 over the region $0.5 \leq x/D \leq 10$. In the near-wake region, the streamwise intensity ratios appear to be the same to within statistical fluctuations, whereas it is higher for scheme B beyond $x/D \simeq 7$. In the same zone, the vertical intensity ratio is relatively constant with both schemes. The shear stress ratio peaks at about 3.5% in the simulation with scheme B, which is 100% higher than the peak obtained with scheme A in the near-wake region. At locations $5 \leq x/D \leq 10$, the magnitude of the subgrid-scale shear stress relative to the resolvable shear stress is larger when computed with the scheme generating the least numerical dissipation.

At all stations downstream of the cylinder, the magnitude of the mean eddy-viscosity (figure 62) is larger with scheme B. A maximum gain of approximately 30% in $\overline{\nu}_t$ occurs at $x/D = 5$, at the downstream edge of the vortex formation zone. In the near wake, differences in $\overline{\nu}_t$ between the two differencing schemes decrease, so that at $x/D = 10$ both schemes yield comparable distributions of eddy viscosity.

5.3.4 Cylinder Surface and Near-Wake Mean Flow

The statistics of the flow at the cylinder surface are summarized in table 6. The Strouhal number is within experimental error with scheme B ($St = 0.217$), whereas it layed about 5% below Cardell's value of 0.215 in the calculation with scheme A. The back-pressure and drag coefficients are within experimental error with both schemes, although using scheme B improves their prediction. The wall vorticity and pressure distributions predicted by both methods (figures 63, 64) differ slightly on the wake-facing side of the cylinder, where scheme B yields a slightly more accurate prediction for the back-pressure coefficient ($C_{P_b} = -0.90$) than scheme A.

In the vortex-formation region, the centerline velocity is lower and the pressure coefficient larger with the higher-order scheme (table 6, figure 65). As a consequence, the recirculation bubble is longer than that obtained with scheme A. In this region, the turbulent kinetic energy is consistently higher with scheme B: the energy present in the separated free shear layers is several times larger than with scheme A, indicating that numerical dissipation has been significant (figure 66). At $x/D = 1$, the calculation with scheme A predicts a higher turbulent kinetic energy in the bubble core than in the shear layers. With scheme B, the shear layers at that location are clearly delineated and contain about 50% more energy than the bubble *per se*.

In the near-wake region, the streamwise velocity, scaled on the mean centerline velocity deficit and wake half-width, is better represented by method B across most of the wake layer (figure 67). Scheme A overpredicted the growth-rate of the wake layer. The improvement in the growth-rate prediction with scheme B is evident in the streamwise and vertical intensities (figures 68, 69) which peak at values closer to the experimental results. The Reynolds shear stresses similarly show a marked improvement with scheme B (figure 70). Ten diameters downstream, the shear stress profile predicted with scheme B is in good agreement with the experimental measurements.

101

5.4   Comparison Summary

The preceding results indicate that the reduction of numerical dissipation levels between the fifth- and seventh-order accurate schemes has a significant impact on the computed solution. The effect of switching from scheme A to B led to sharper resolution of the transitioning separated free shear layers, the increased energy levels at high frequencies and wave-numbers, as well as the thinning and strengthening of the rib vortices connecting spanwise rollers. Improvements in the solution computed with the higher-order scheme are equally apparent in the low-order wake statistics. Despite these ameliorations, the streamwise one-dimensional frequency spectra indicate that a substantial portion of the resolvable frequency range is damped even with scheme B. Resolving frequencies up to the inertial range past the vortex formation zone appears to require either a higher-order accurate scheme or finer resolution of the first five diameters of the wake.
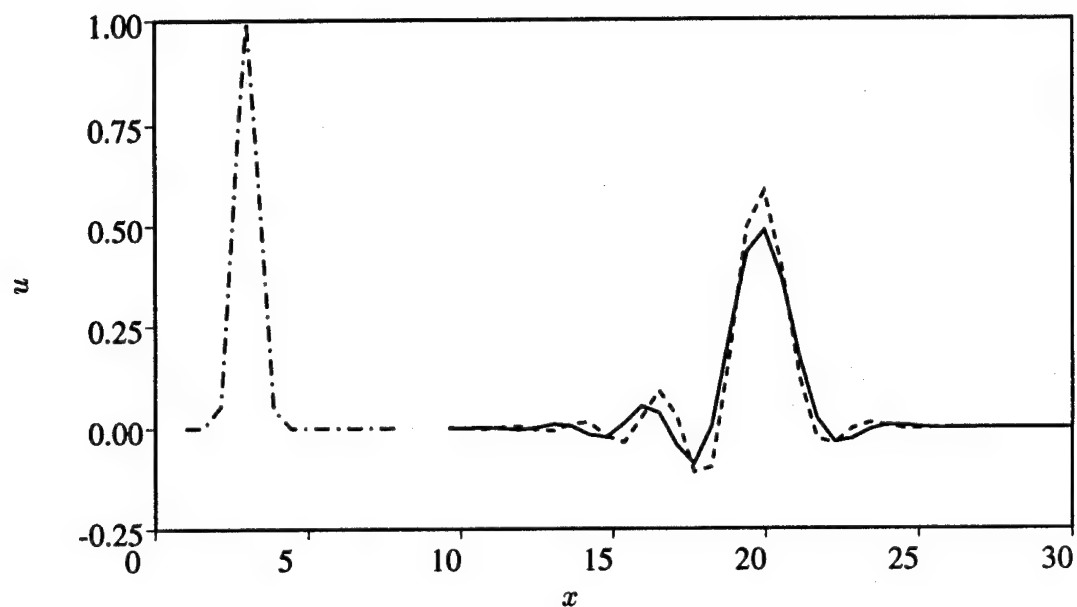
Figure 47: Traveling Gaussian, 4 points per structure
—·— : Initial condition $(t = 0)$
---- : 7th order scheme at $t = 17$; —— : 5th order scheme at $t = 17$
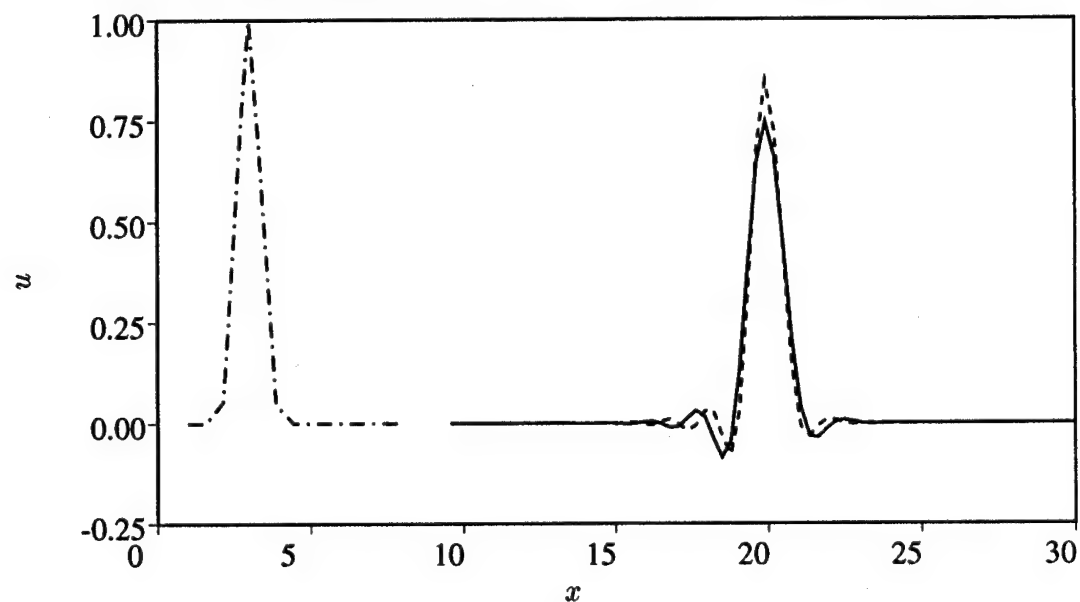
Figure 48: Traveling Gaussian, 8 points per structure
—·— : Initial condition $(t = 0)$
---- : 7th order scheme at $t = 17$; —— : 5th order scheme at $t = 17$
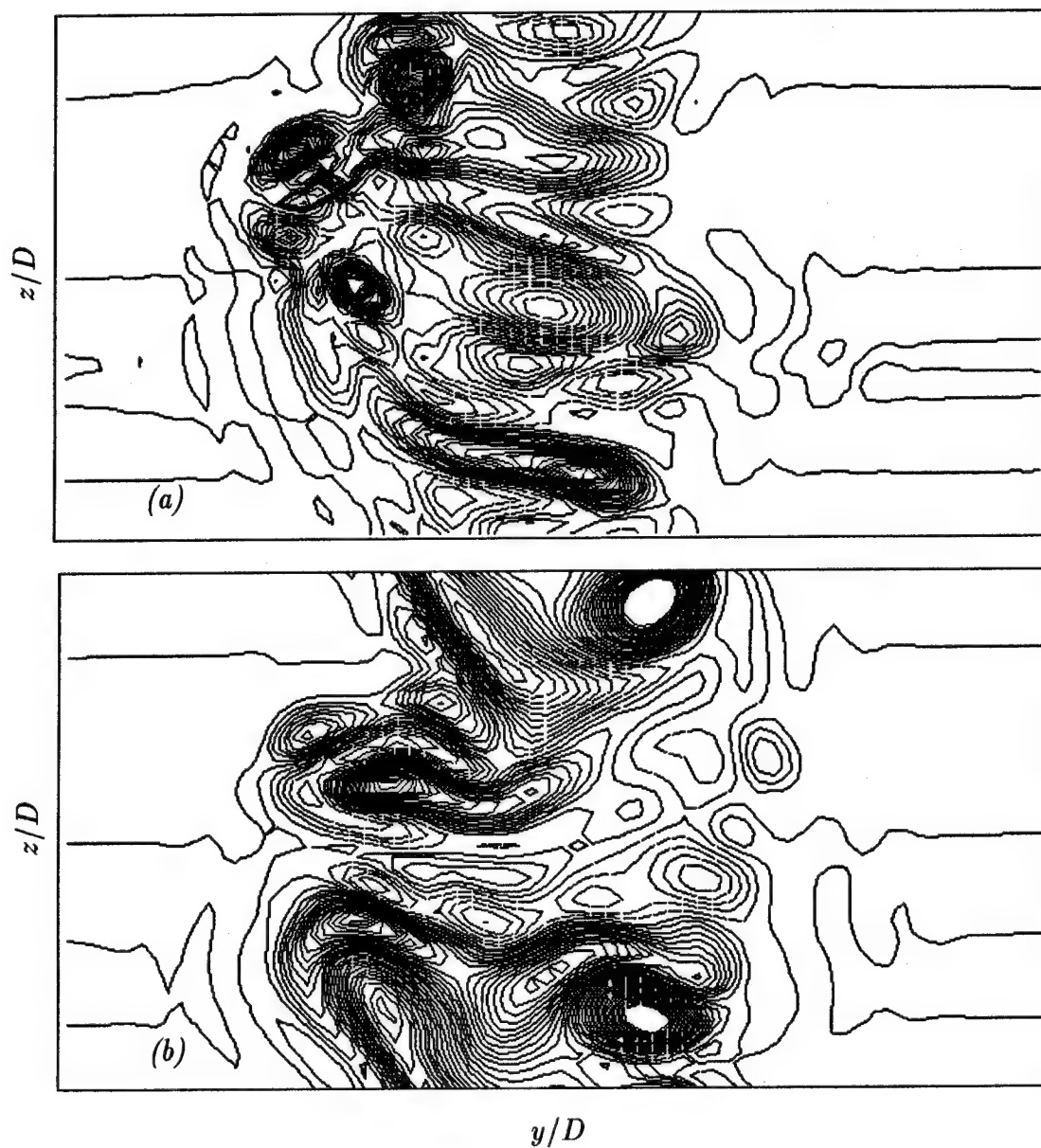
Figure 49: $Re = 3,900$; Instantaneous vertical vorticity at $r/D = 5$
Contours from -8 to 6 by 0.4
(a): 7th order accurate scheme; (b): 5th order accurate scheme
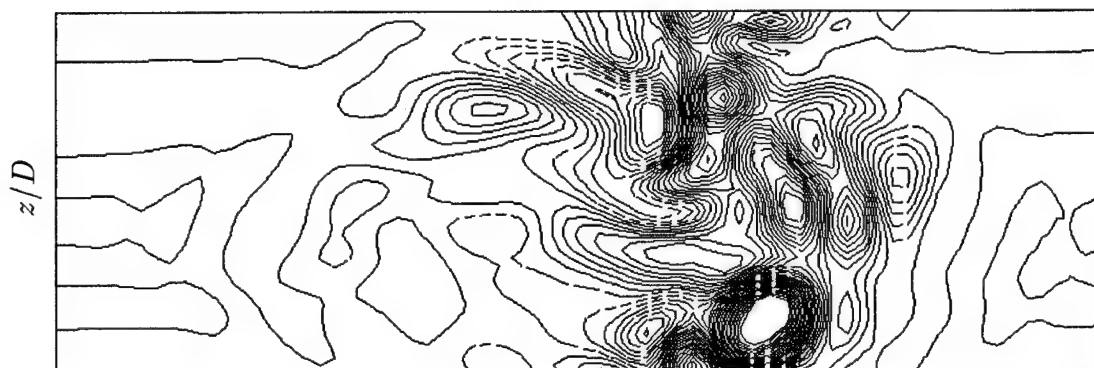
y/D

Figure 50: $Re = 3,900$; Instantaneous streamwise vorticity at $r/D = 10$
Contours from -4 to 4 by 0.2
(a): 7th order accurate scheme; (b): 5th order accurate scheme

x/D
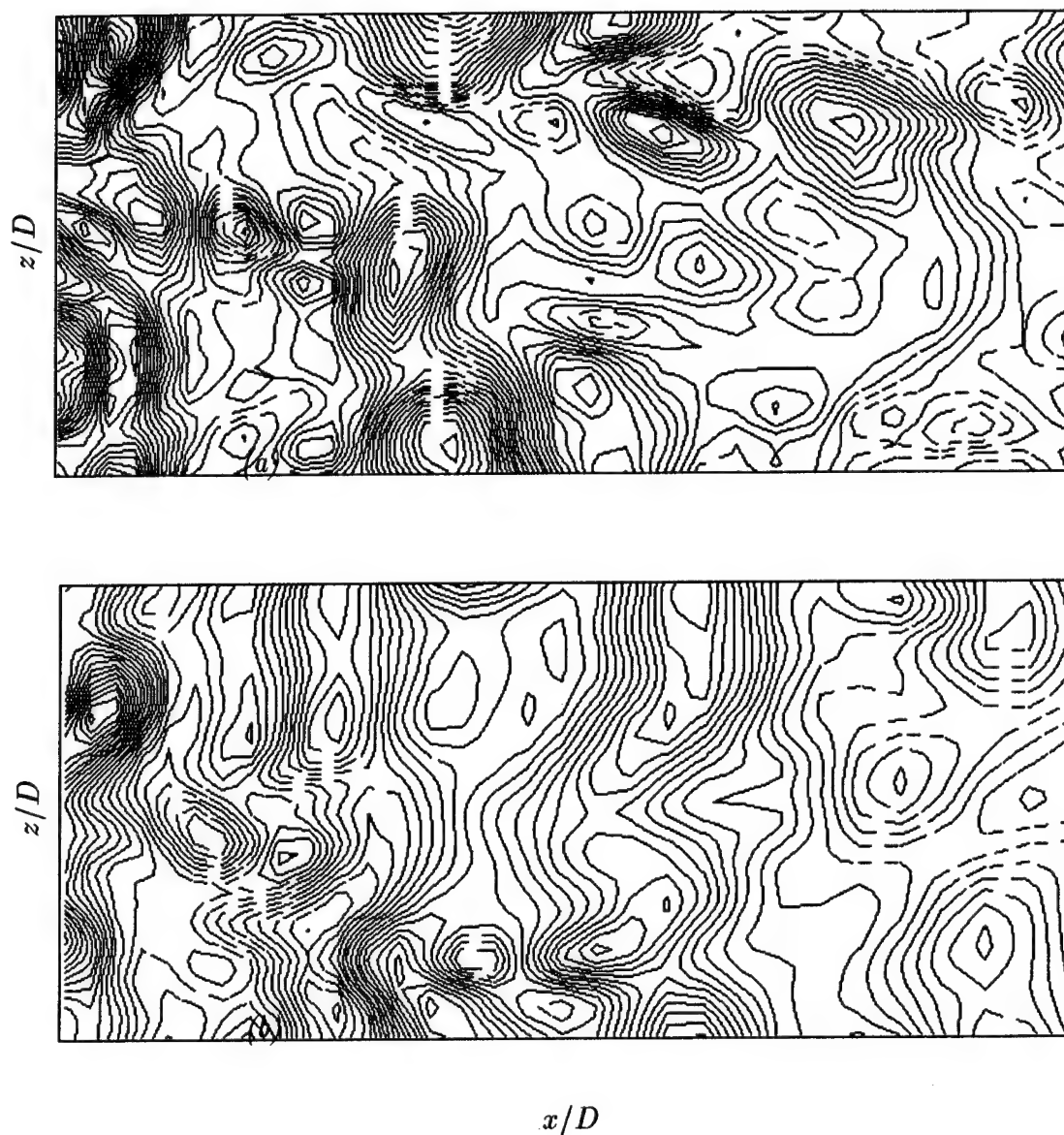
Figure 51: $Re = 3,900$; Instantaneous spanwise vorticity at $5 \leq x/D \leq 10$; $y = 0$
Contours from -6 to 6 by 0.3
(a): 7th order accurate scheme; (b): 5th order accurate scheme
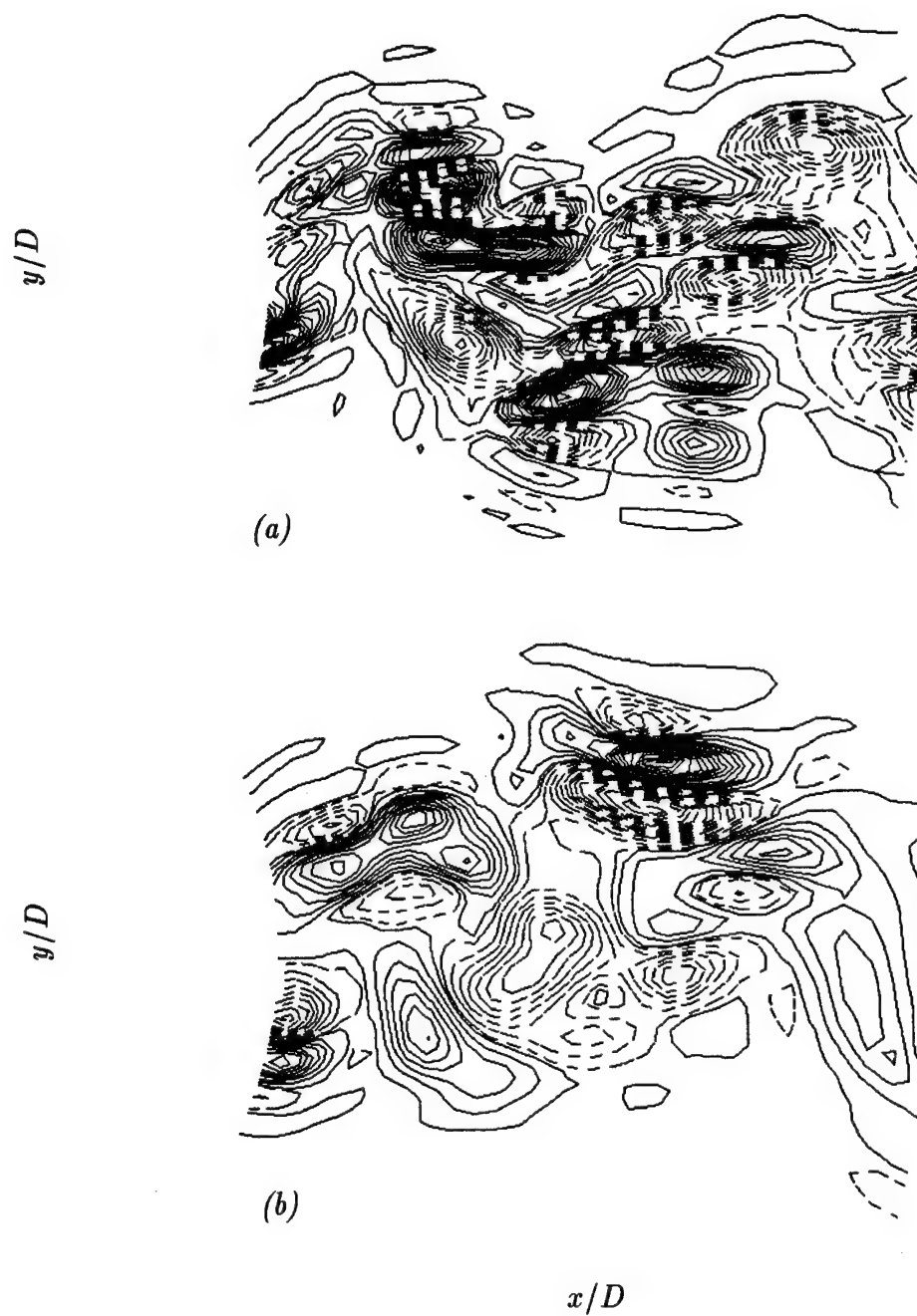
Figure 52: $Re = 3,900$; Instantaneous streamwise vorticity at $5 \leq r/D \leq 10$; $z = 0$
(a): 7th order accurate scheme; (b): 5th order accurate scheme
Contours from -6 to 9 by 0.4

107
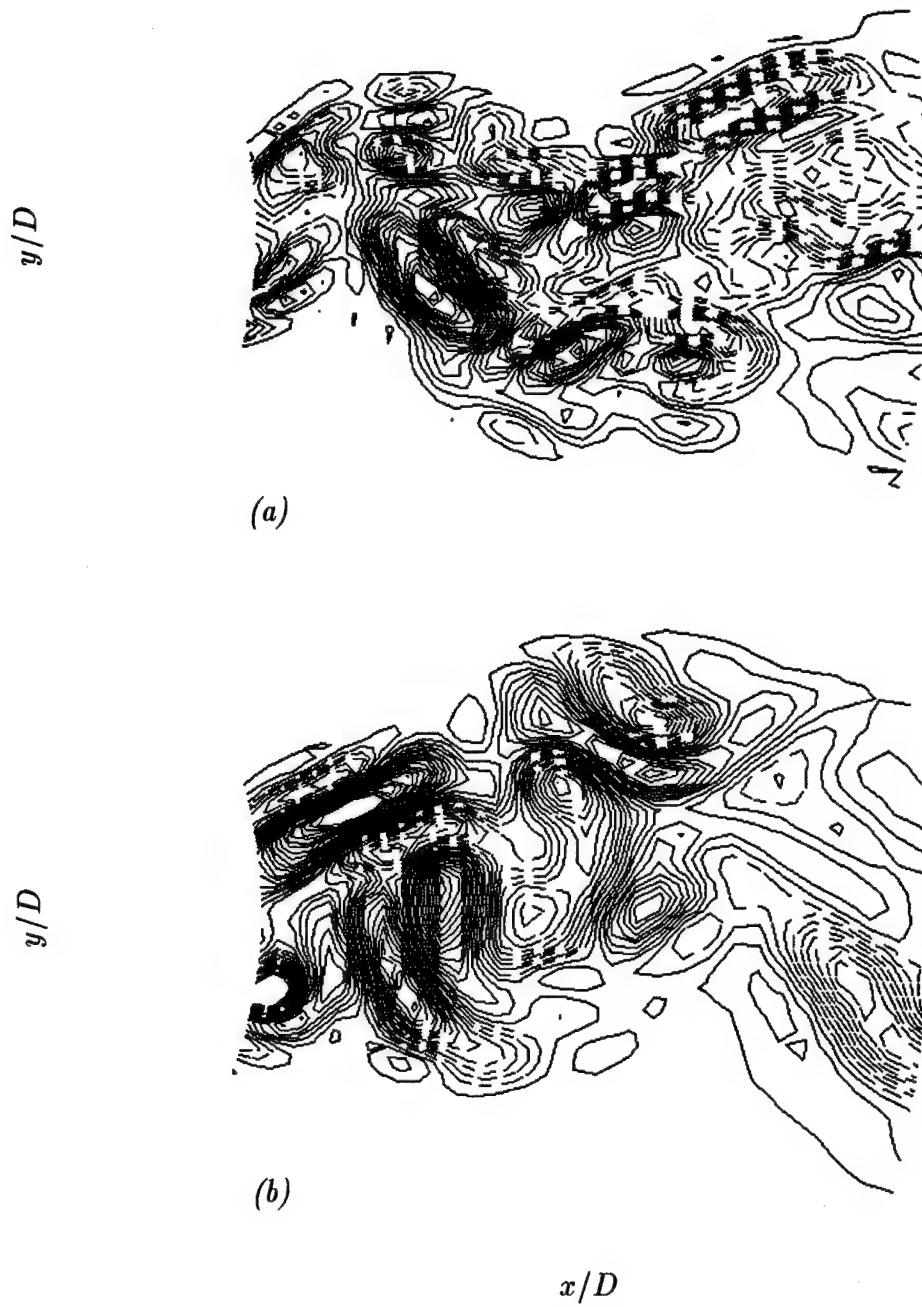
Figure 53: $Re = 3,900$; Instantaneous vertical vorticity at $5 \leq r/D \leq 10$; $z = 0$
(a): 7th order accurate scheme; (b): 5th order accurate scheme
Contours from -3 to 4 by 0.2

108
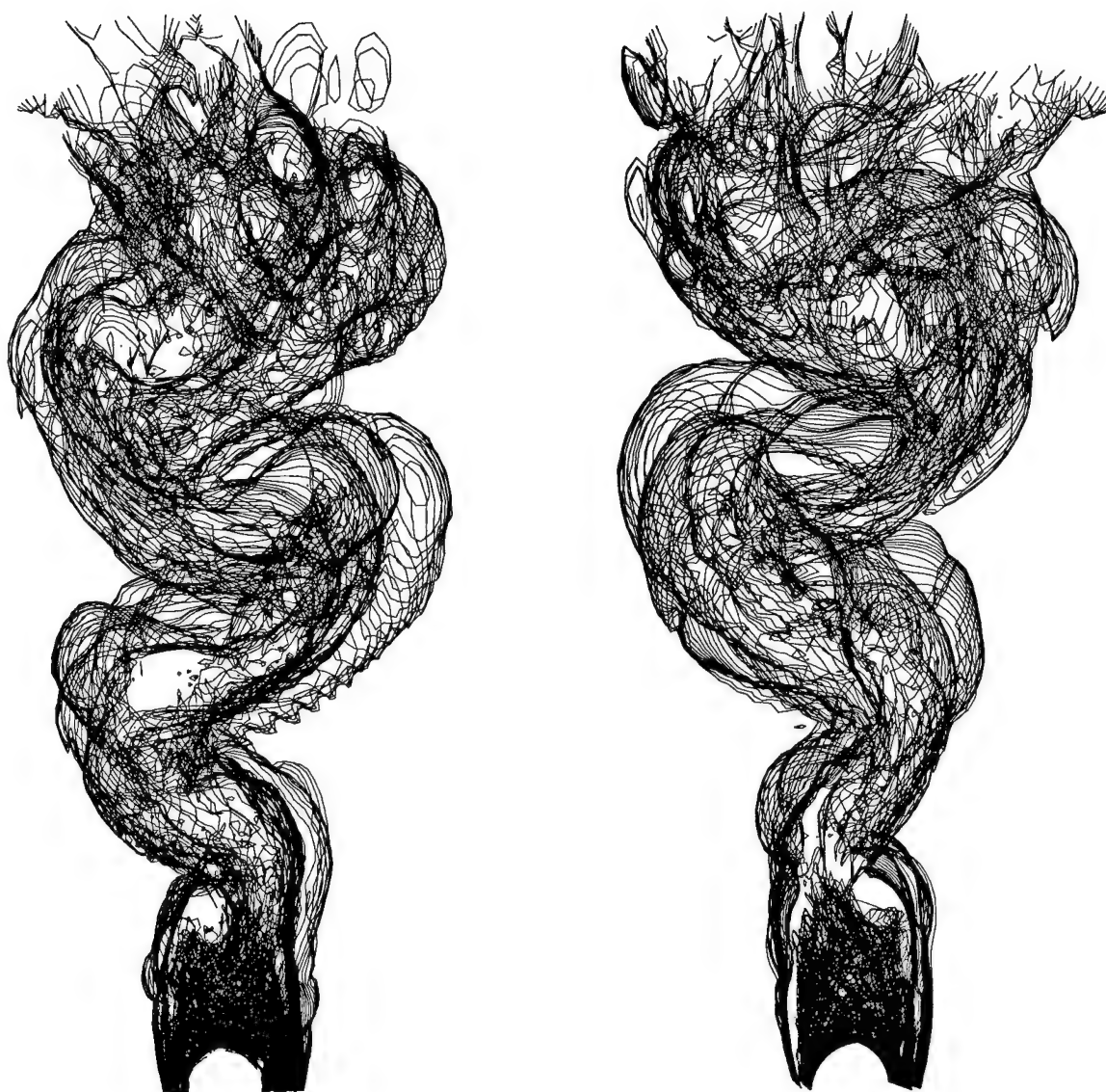
Figure 54: $Re = 3,900$; Instantaneous constant vorticity contours $|\vec{\omega} D / u_d| = 1$
left: 7th order-accurate simulation; right: 5th order-accurate simulation
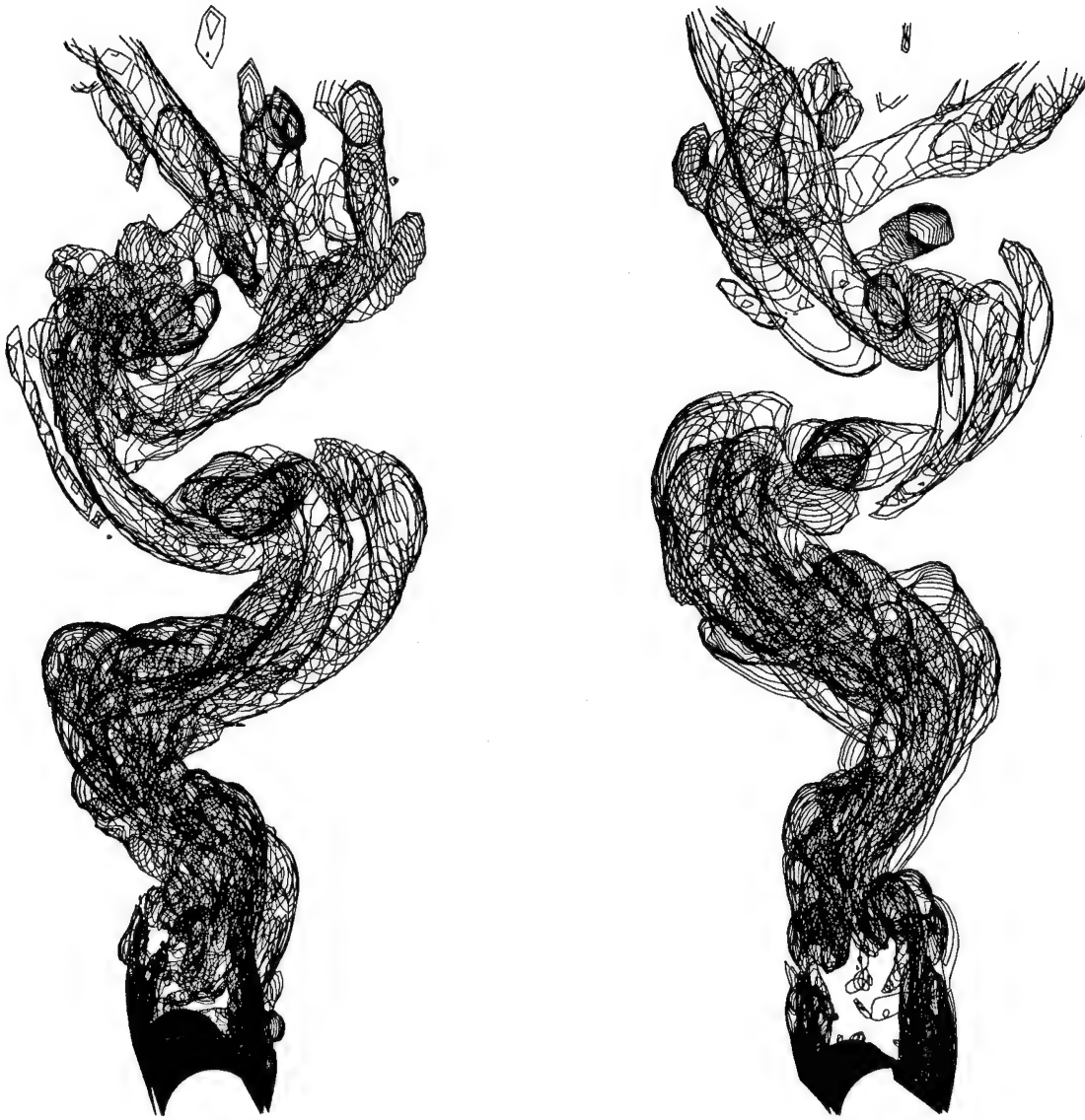
Figure 55: $Re = 3,900$; Instantaneous constant vorticity contours $|\vec{\omega}D/u_d| = 3$
left: 7th order-accurate simulation; right: 5th order-accurate simulation

Figure 56: $Re = 3,900$; Instantaneous constant vorticity contours $|\vec{\omega}D/u_d| = 6$
left: 7th order-accurate simulation; right: 5th order-accurate simulation

Figure 57: $Re = 3,900$; Instantaneous spanwise vorticity contours in the first 10 diameters of the vertical plane $z = 0$ (seventh-order scheme)
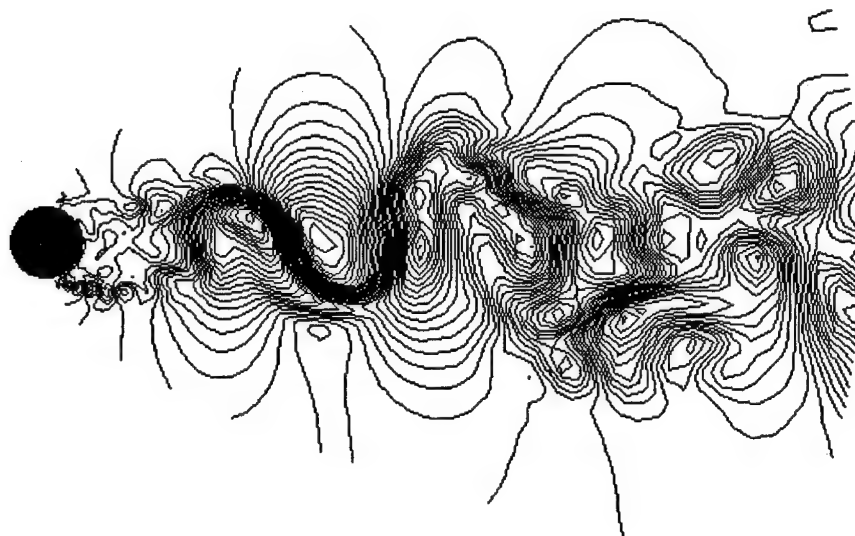
Figure 58: $Re = 3,900$; Instantaneous vertical velocity contours in the first 10 diameters of the vertical plane $z = 0$ (seventh-order scheme)

112
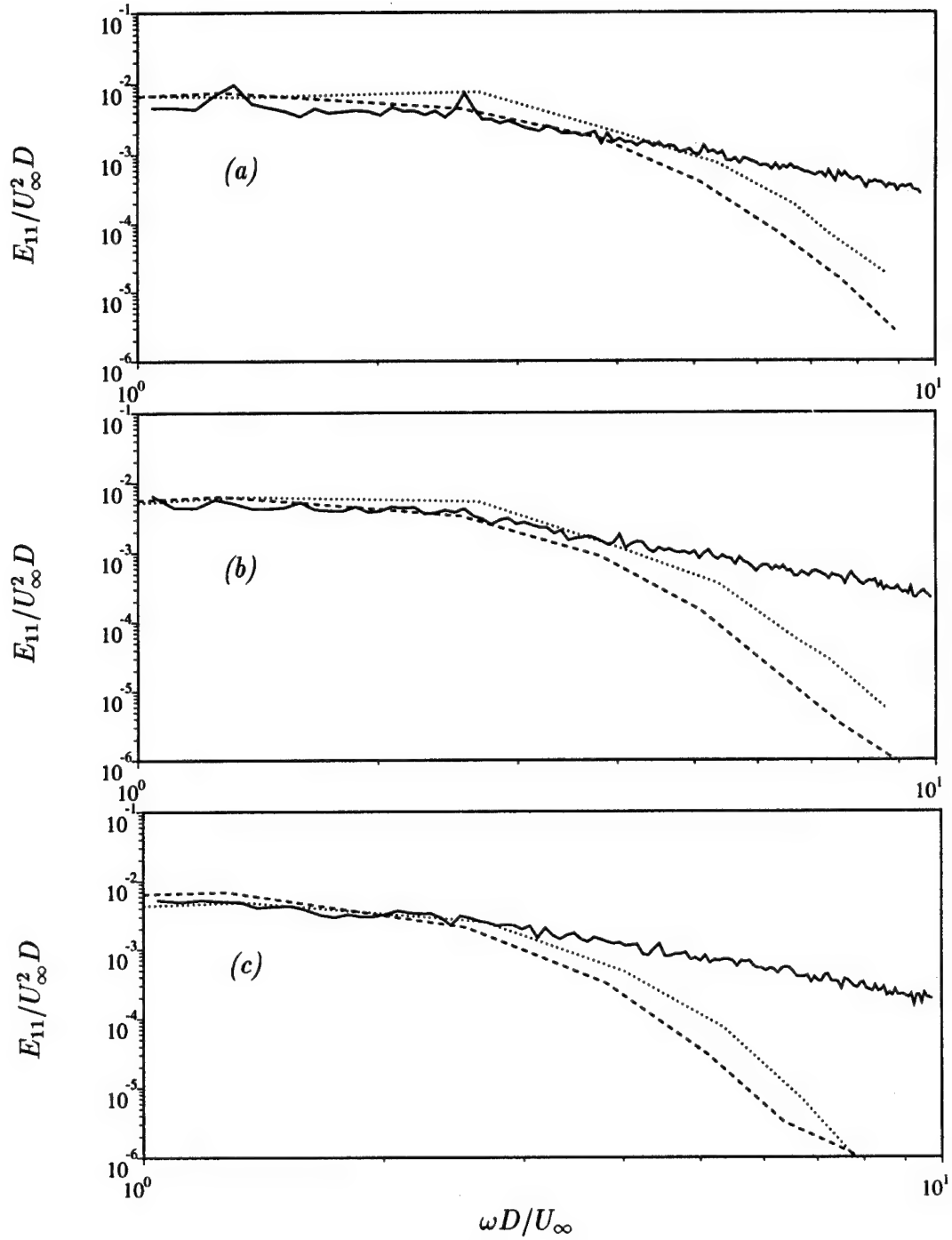
Figure 59: $Re = 3,900$; One-dimensional frequency spectra $E_{11}(\omega)$ at (a): $x/D = 5$; (b) : $x/D = 7$; (c): $x/D = 10$

$\cdots$: 7th order scheme; ---- : 5th order scheme; —— : Ong & Wallace

113
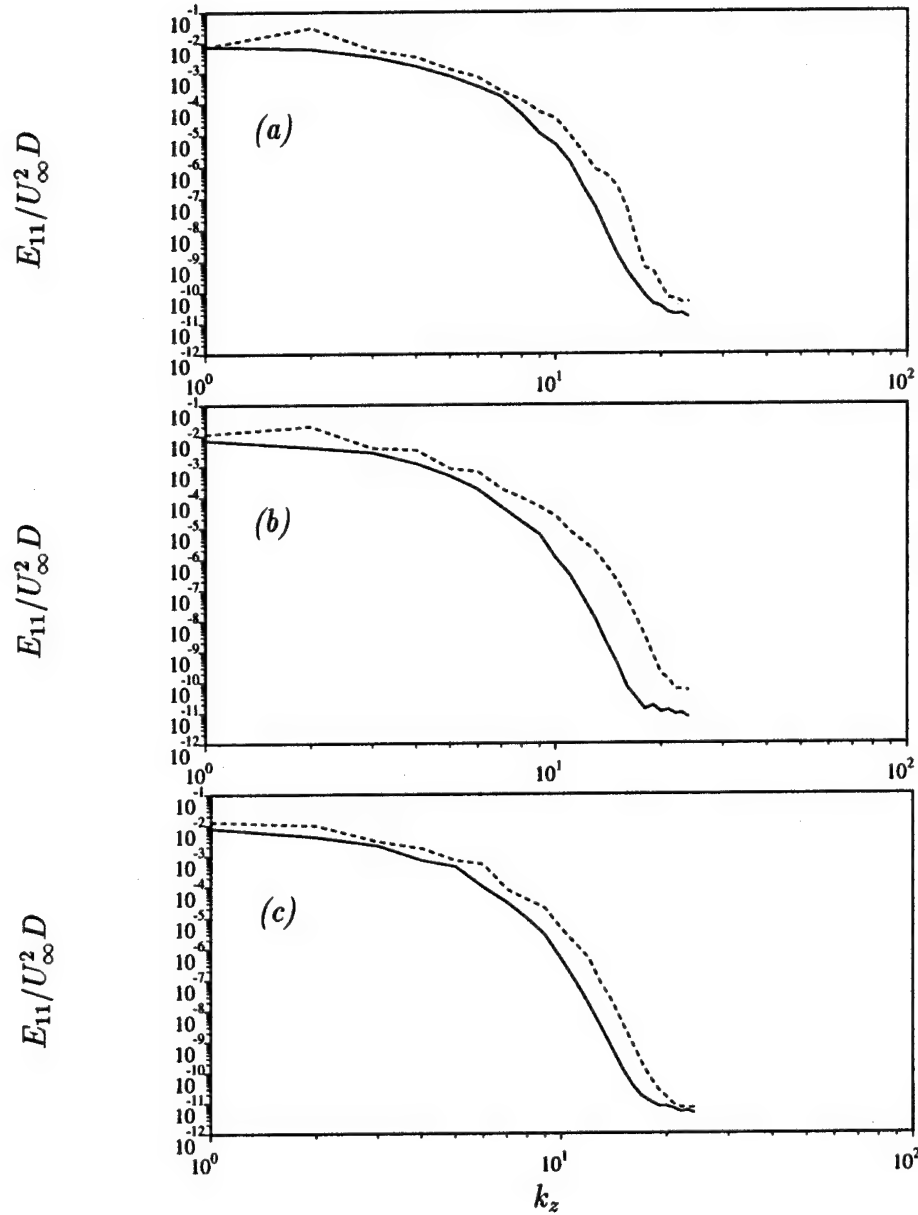
Figure 60: $Re = 3,900$; One-dimensional wave-number spectra $E_{11}(k_z)$ at (a): $x/D = 5$; (b) : $x/D = 7$; (c): $x/D = 10$

---- : 7^{th}order scheme; —— : 5^{th}order scheme
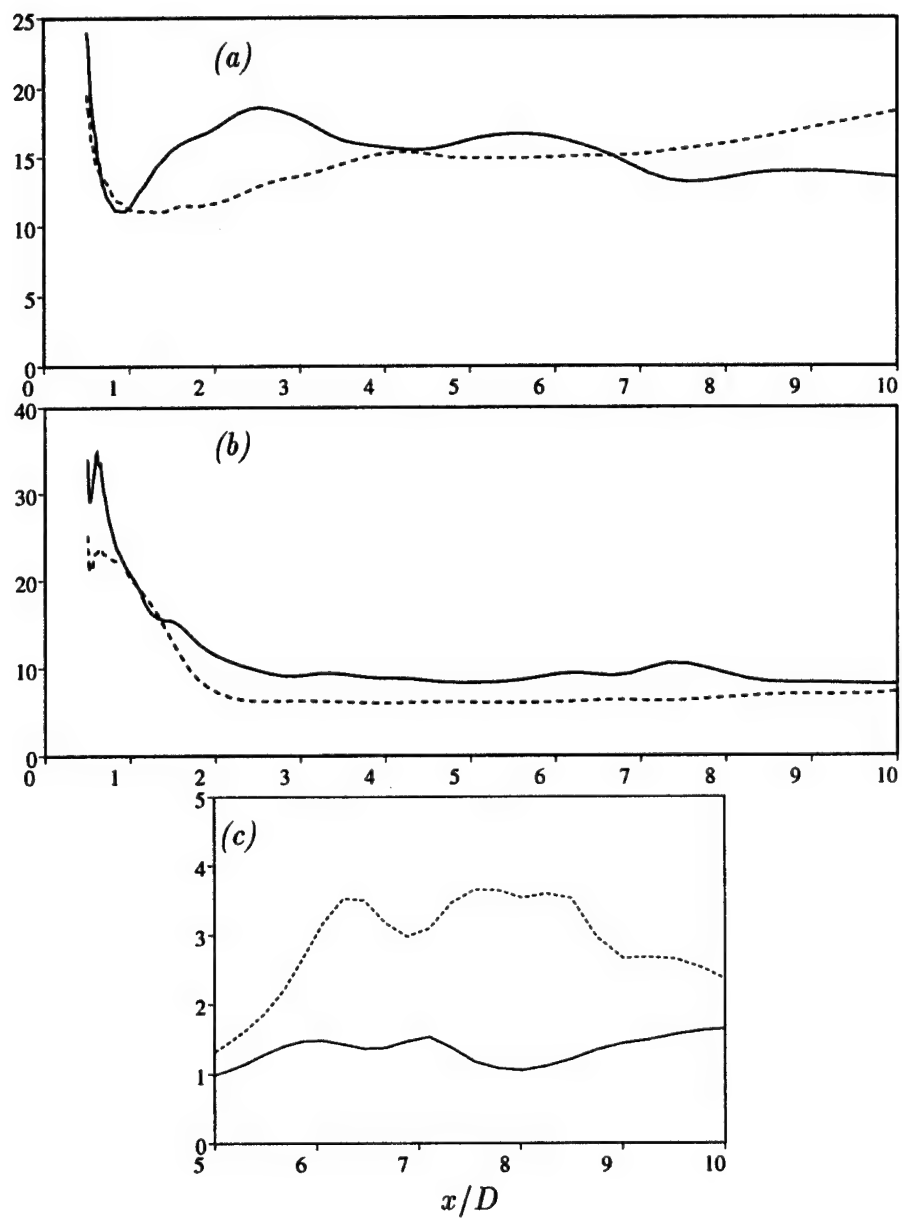
Figure 61: $Re = 3,900$; Subgrid-scale Reynolds stress as percentage of the resolvable stress

Streamwise intensity (a); Vertical intensity (b); Shear stress (c)
---- : 7^{th}order scheme; —— : 5^{th}order scheme
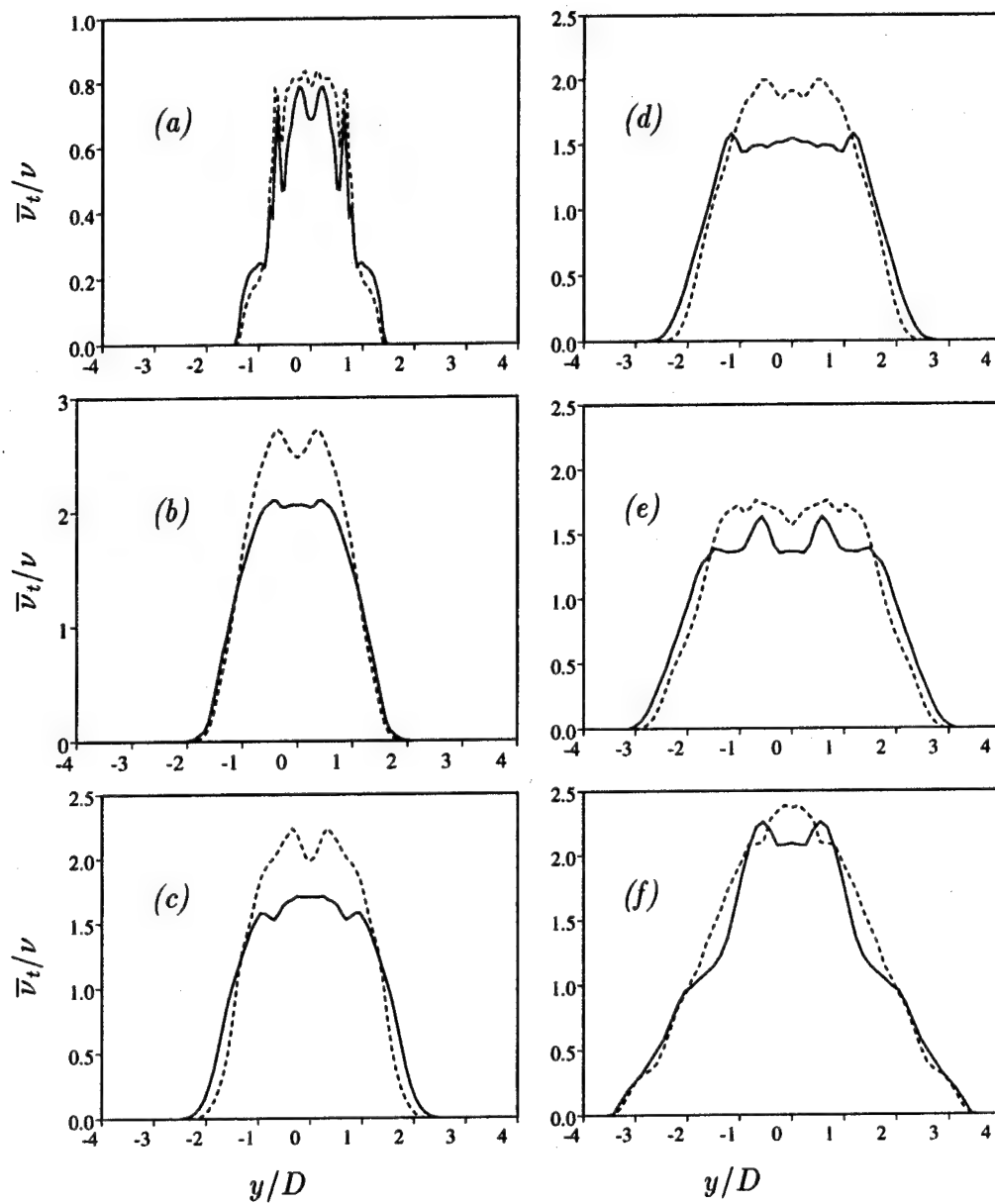
Figure 62: $Re = 3,900$; Mean eddy viscosity profiles
(a): $x/D = 1$; (b) : $x/D = 3$; (c): $x/D = 4$
(d): $x/D = 5$; (e) : $x/D = 7$; (f): $x/D = 10$
---- : 7^{th}order scheme; —— : 5^{th}order scheme

116

	Dynamic model simulation $Re = 3,900$		Experiment
	5th order scheme	7th order scheme	
St Strouhal number	0.203	0.217	0.215 ± 0.005 (Cardell 1993)
$\overline{C}_{P_b}$ Back pressure	-0.95	-0.90	-0.90 ± 0.05 (Norberg 1987)
$\overline{C}_D$ Total drag	1.00	0.96	0.98 ± 0.05 (Norberg 1987)
$\overline{C}_f \times 100$ Skin-friction	0.91	0.88	$\cdots$
$\overline{\theta}_1$ Separation	± 85.8	± 85.0	$\pm 85 \pm 2$ (Son *et al.* 1969)
$\overline{\theta}_2$ Separation	± 110.6	± 113.2	$\cdots$
$\overline{\theta}_3$ Separation	± 158.3	± 153.0	$\cdots$
L/D Bubble length	1.36	1.50	1.33 ± 0.2 (Cardell 1993)
$\overline{u}_{min}/U_\infty$ in bubble	-0.32	-0.30	-0.24 ± 0.1 (Lourenco 1993)
r_{min}/D $\overline{u}_{min}$ location	0.88	1.07	0.72 ± 0.1 (Lourenco 1993)

Table 6: Cylinder surface and bubble region comparisons
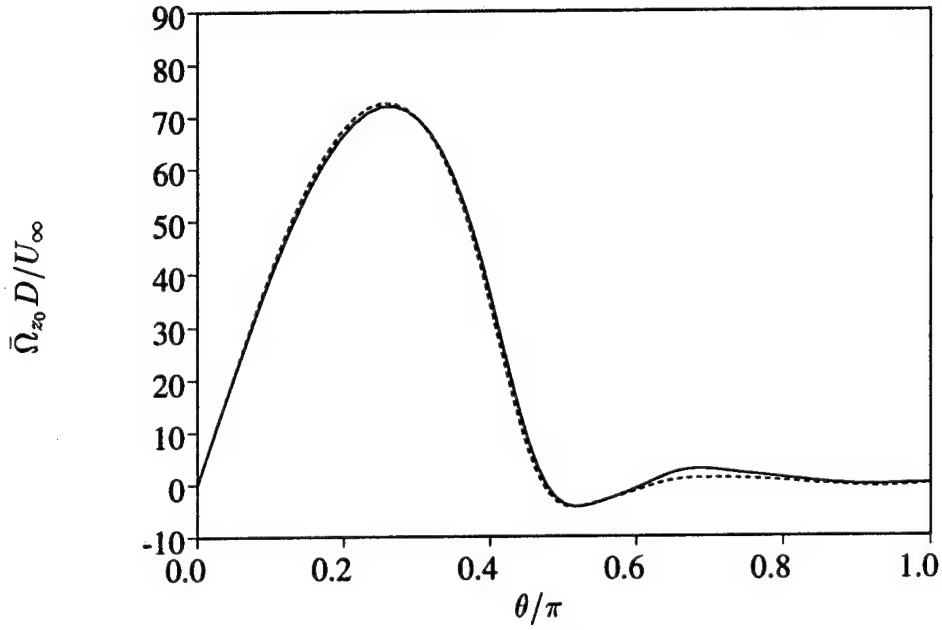
Figure 63: $Re = 3,900$; Wall vorticity

——— : 5^{th}order scheme; - - - - : 7^{th}order scheme
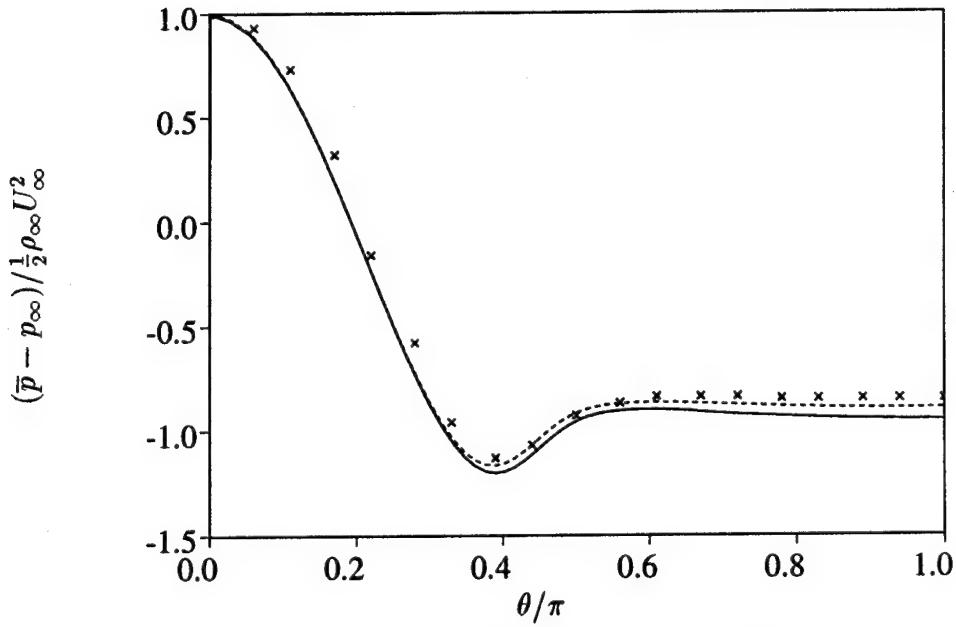
Figure 64: $Re = 3,900$; Wall pressure coefficient

——— : 5^{th}order scheme; - - - - : 7^{th}order scheme

$\times$: Experiment ($Re = 3,000$; Norberg1987)
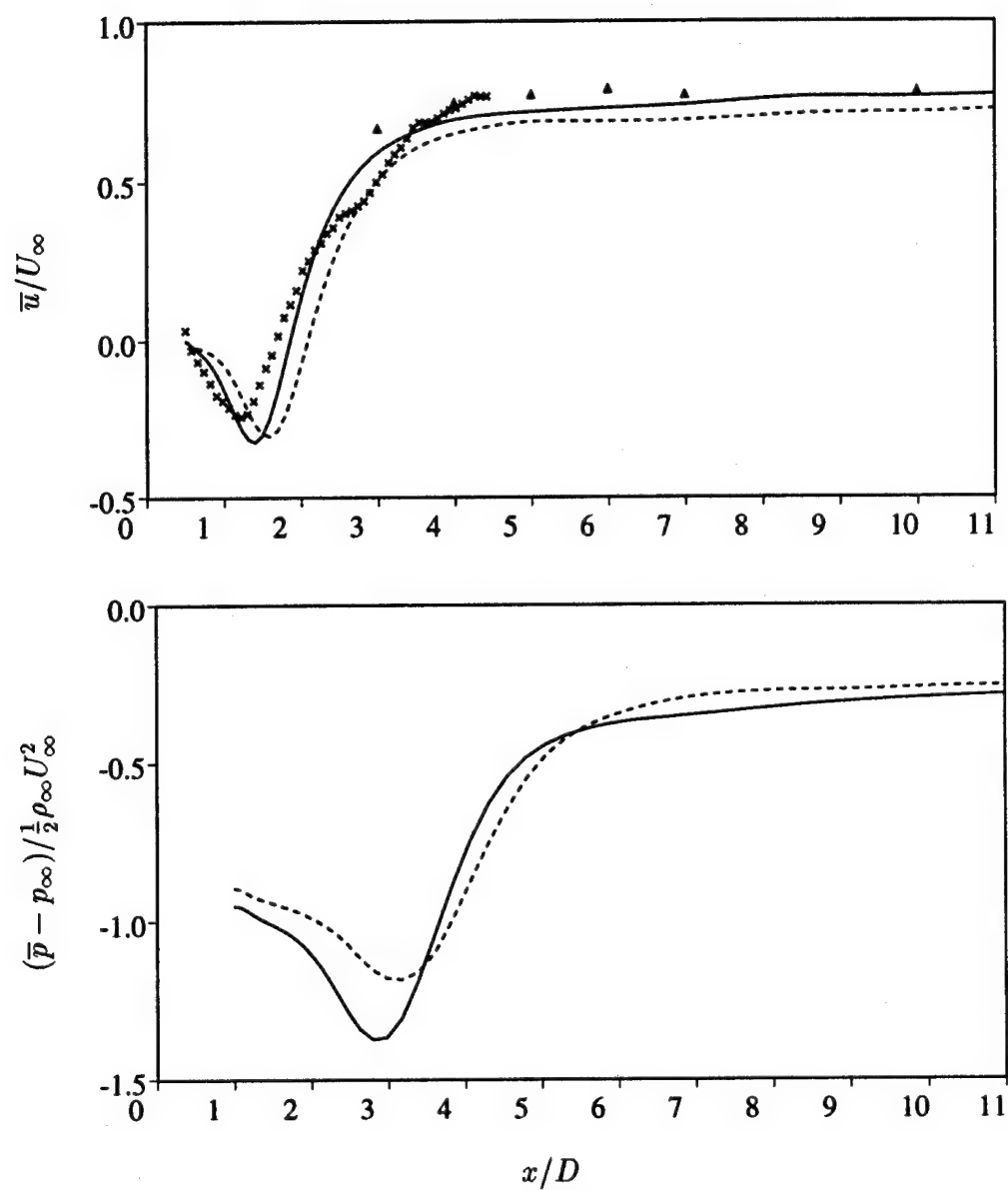
Figure 65: $Re = 3,900$; Centerline streamwise velocity and pressure coefficient
——— : 5^{th}order scheme; ---- : 7^{th}order scheme
× : Lourenco & Shih; △ : Ong & Wallace

119
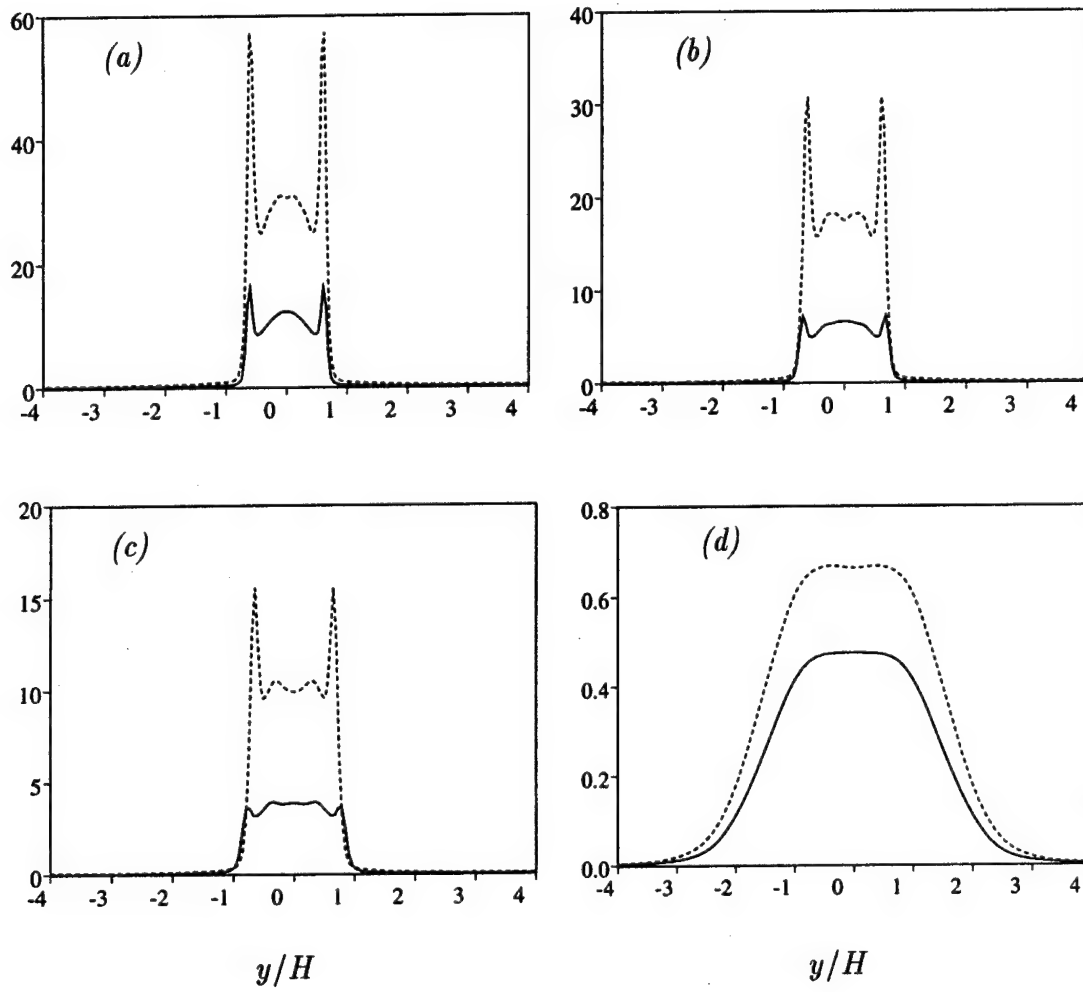
Figure 66: $Re = 3,900$; Formation zone total kinetic energy $(\overline{u'_k \, u'_k} + \overline{\tilde{u}_k \, \tilde{u}_k} + \overline{\tau}_{kk})/2u_c^2$
(a): $x/D = 0.8$; (b): $x/D = 0.9$; (c): $x/D = 1.0$; (d): $x/D = 3.0$
——— : 5^{th}order scheme; - - - - : 7^{th}order scheme
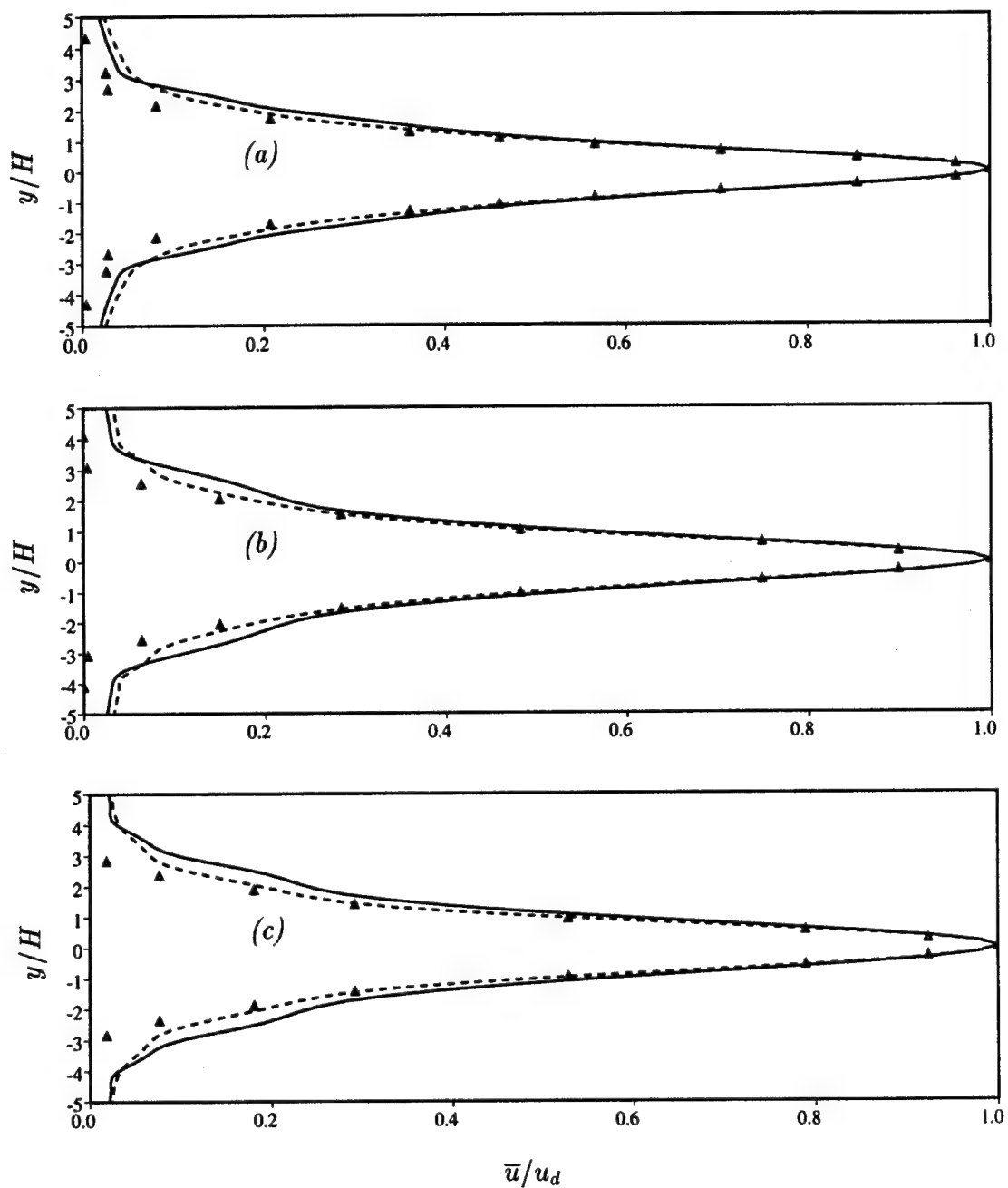
Figure 67: $Re = 3,900$; Streamwise velocity at $x/D = 5$ (a); 7 (b); 10 (c)
———— : 5th order scheme; ---- : 7th order scheme
$\triangle$: Ong & Wallace

121
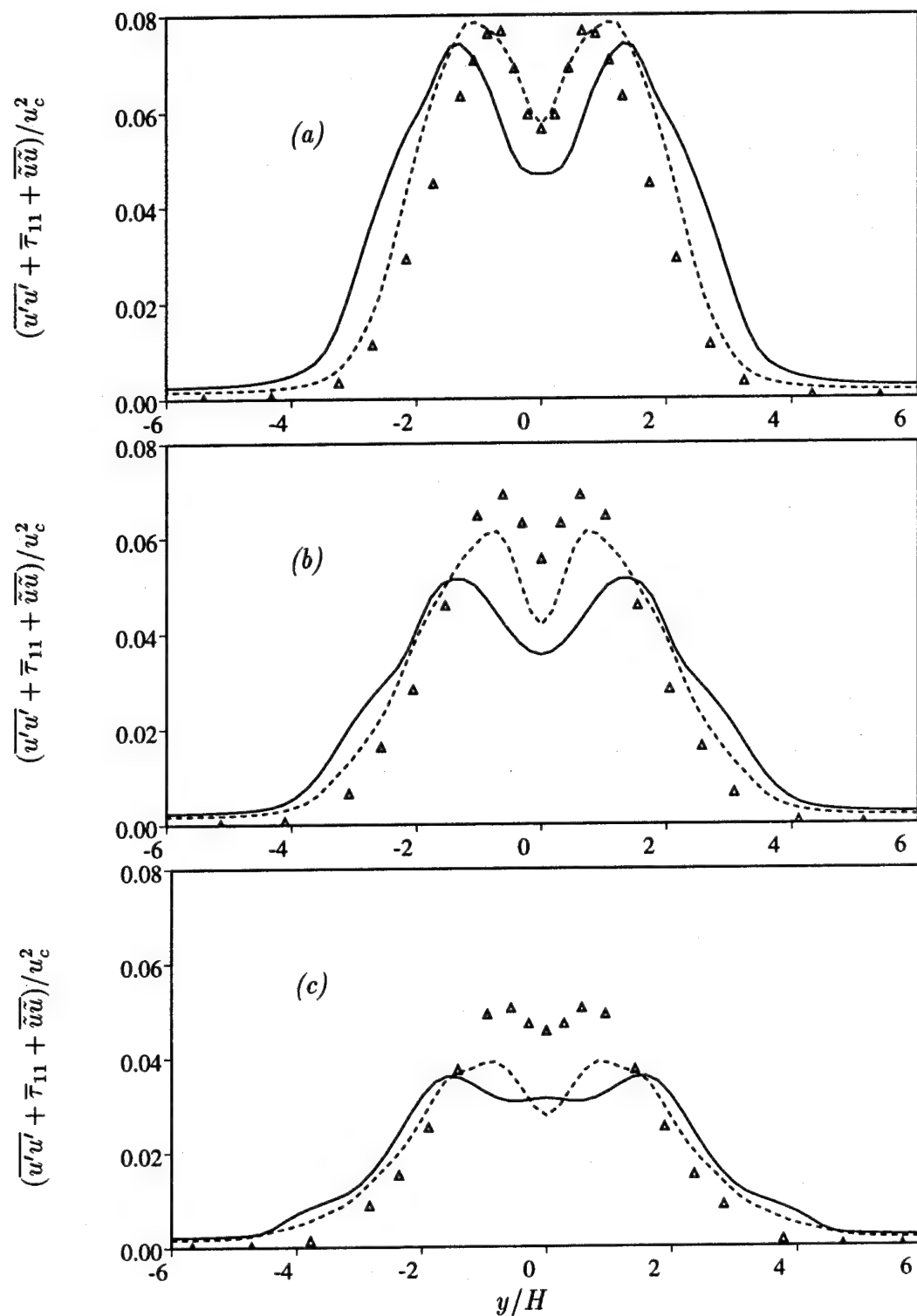
Figure 68: $Re = 3,900$; Streamwise Reynolds stresses at $x/D = 5$ (a); 7 (b); 10 (c)
———— : 5^{th}order scheme; ---- : 7^{th}order scheme; $\triangle$: Ong & Wallace
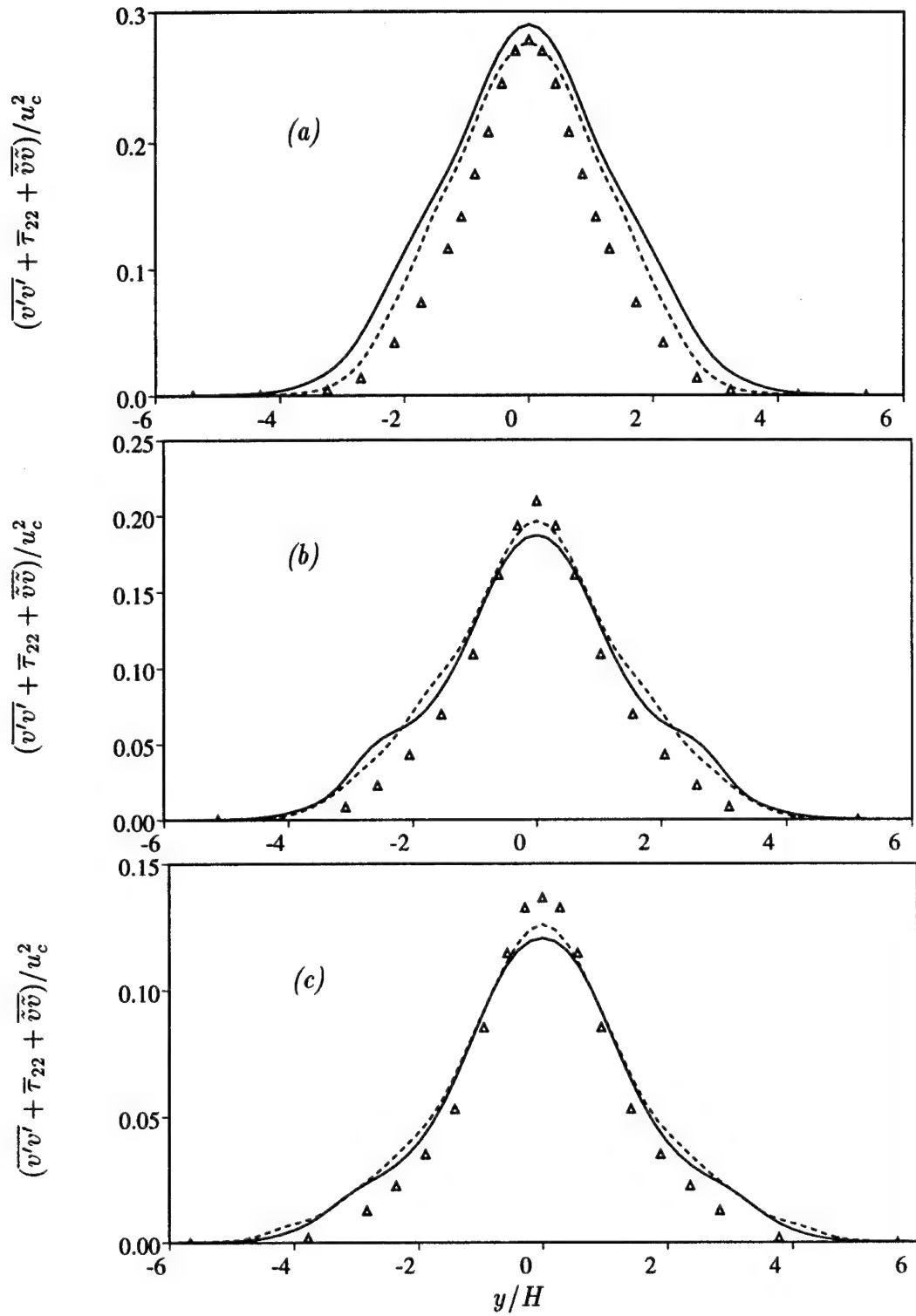
Figure 69: $Re = 3,900$; Vertical Reynolds stresses at $x/D = 5$ (a); 7 (b); 10 (c)
—— : 5^{th}order scheme; - - - - : 7^{th}order scheme; $\triangle$: Ong & Wallace

123
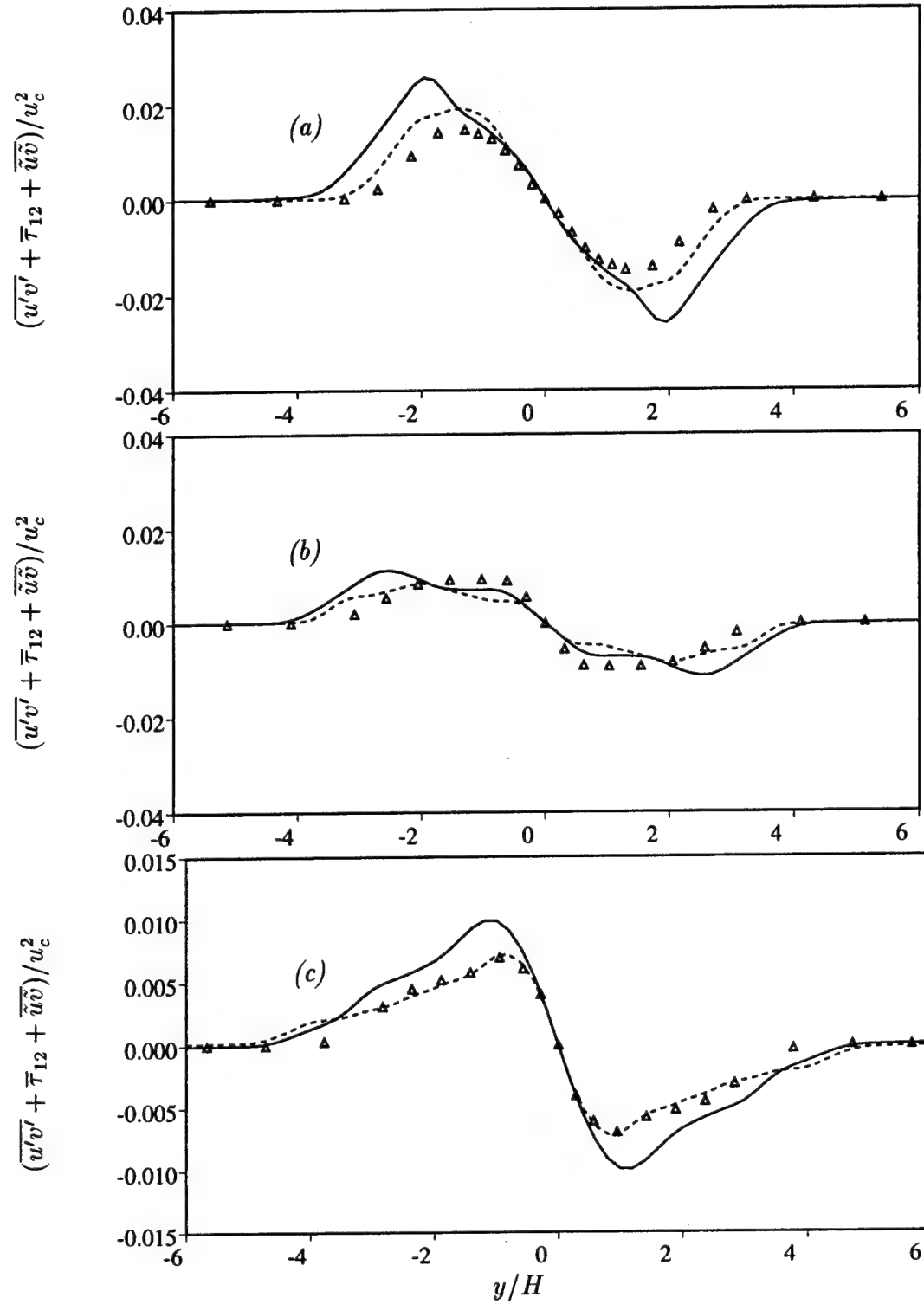
Figure 70: $Re = 3,900$; Reynolds shear stresses at $x/D = 5$ (a); 7 (b); 10 (c)
——— : 5^{th}order scheme; - - - - : 7^{th}order scheme; $\triangle$: Ong & Wallace

124

Chapter 6

Conclusions

Three large-eddy simulations of the flow around a circular cylinder at Reynolds number 3,900 were performed using the dynamic subgrid-scale model, a fixed-coefficient Smagorinsky model and no subgrid-scale model. The numerical method in these three simulations was based on a fifth-order accurate, upwind-biased finite-difference scheme for the convective terms, a sixth-order accurate central scheme for viscous terms, and a fully implicit, second-order accurate time integration technique. Two simulations using the dynamic subgrid-scale model on identical grids were further compared; one was based on the fifth-order accurate scheme described above, while the other one used a seventh-order accurate upwind-biased scheme for the convective derivatives. In this study we investigated the importance of three-dimensionality for the computed solution, the performance of the subgrid-scale turbulence models within the first ten diameters of the wake, and the impact of numerical dissipation generated by high-order accurate, upwind-biased numerical schemes. A summary of our findings is presented below.

Three-Dimensionality of the Near-Wake at Reynolds number 3,900

The near-wake appears to be strongly three-dimensional. In a two-dimensional simulation, the irregularity of the vortex shedding present in the three-dimensional solution and observed experimentally was greatly reduced. The three-dimensional near-wake contains counter-rotating streamwise vortices, the effect of which cannot

be reproduced in two dimensions: the mean two-dimensional velocity field does not reproduce the main recirculation region behind the cylinder which is present in the computed three-dimensional and in the experimental mean fields.

Performance of the Subgrid-Scale Turbulence Models

In three-dimensional calculations, mean wall statistics such as drag and pressure coefficients, wall shear stress and separation angles computed with the three subgrid-scale models were not significantly different from one another. In the vortex formation region, which includes first four diameters of the wake, the calculation with the dynamic model predicted more accurate mean velocities and Reynolds stresses than those without model or with the fixed-coefficient Smagorinsky model. Past the vortex formation region, differences between the solutions computed from the three simulations diminished with downstream distance, due to the numerical dissipation generated by the one-point upwinding in that region.

The dynamic model predicted a mean eddy viscosity distribution in better qualitative agreement with the physics of the flow relative to the fixed-coefficient Smagorinsky model: the maximum of the distribution occured in the turbulent near-wake, in the vicinity of the separated bubble closure point. With the fixed-coefficient model, the largest mean eddy viscosity was generated in the separated free shear layers, which are laminar at Reynolds number $3,900$.

Impact of Numerical Dissipation on the Computed Solution

The seventh-order accurate, upwind-biased scheme generated less numerical dissipation in the wake than the fifth-order accurate scheme. As a result, a comparison of the simulations using both schemes revealed that the magnitude of the subgrid-scale shear stresses in the wake increased by a factor of about 70%, and that the energy content of the velocity fluctuations was larger at higher frequencies than with the fifth-order accurate scheme. Instantaneous contours of the vorticity in the wake provided further evidence as to the presence of smaller-scale structures when using the seventh-order accurate scheme. Low-order statistics in the near-wake showed improvement with the higher-order scheme, although streamwise one-dimensional frequency spectra were damped by numerical dissipation over a significant portion of the resolvable

126

frequencies.

The fifth-order accurate, upwind biased scheme had shown potential for direct numerical simulations of flows in complex geometries (Rai & Moin 1991). Because of the numerical dissipation generated by the scheme on coarse meshes however, this method was found to be unsuitable for the large-eddy simulation of the wake behind a circular cylinder. In the near-wake region, where the mesh was coarse but yet fine enough to predict the mean velocity and Reynolds shear stresses within experimental uncertainty, numerical dissipation annihilated all contributions from the subgrid-scale eddy-viscosity models.

These observations suggest that the adequacy of numerical methods for large-eddy simulations cannot be extrapolated from conclusions drawn from direct numerical simulations. The pros and cons of numerical schemes to be used for large-eddy simulations should be investigated using large-eddy simulations.

Recommendations for Future Research

Within the context of large-eddy simulation, the comparative advantages of upwind-biased, highly accurate methods versus central schemes need to be assessed. The former control aliasing via numerical dissipation, while the latter can be formulated as energy conserving schemes. The performances of these methods on coarse, highly stretched grids such as those used in the present report need to be compared.

Using an appropriate numerical scheme, it is presumed that the large-eddy simulation of the flow around a circular cylinder at Reynolds number 1.4×10^5 (Cantwell & Coles 1983) would reveal substantial performance gaps between different subgrid-scale models in the near-wake, because of the presence of small-scales in that region.

Appendix A

Differencing Schemes and Generalized Fluxes

A.1 Differencing Schemes Near Boundaries

The differencing operators applied to convective and viscous fluxes were presented in Chapter 2 (equations 56 through 61) for periodic directions and wall-normal directions away from boundaries. Since the number of grid points available to differencing stencils is limited by the presence of domain boundaries in the generalized radial direction ξ, the order of accuracy of the corresponding differencing schemes decreases near the cylinder surface and far-field boundaries. The mesh spacing in computational space is set to $\Delta\xi = 1$. Along the ξ direction, grid points are ordered from 1 to N, the first point being located at the cylinder surface by convention. The following two Sections list the ξ-derivative operators applied to the convective and viscous terms near domain boundaries.

A.1.1 Convective Derivatives

The upwind and downwind derivative operators are denoted by $'+'$ and $'-'$ superscripts. The upwind scheme near boundaries is:

$$\left.\frac{\partial F^+}{\partial \xi}\right|_1 = -\frac{3}{2\Delta}F_1 + \frac{2}{\Delta}F_2 - \frac{1}{2\Delta}F_3 + \vartheta(\Delta^2) \qquad \left.\frac{\partial F^+}{\partial \xi}\right|_2 = \frac{1}{2\Delta}(F_3 - F_1) + \vartheta(\Delta^2)$$

$$\left.\frac{\partial F^+}{\partial \xi}\right|_3 = \frac{1}{6\Delta}F_1 - \frac{1}{\Delta}F_2 + \frac{1}{2\Delta}F_3 + \frac{1}{3\Delta}F_4 + \vartheta(\Delta^3)$$

$$\left.\frac{\partial F^+}{\partial \xi}\right|_{N-1} = \frac{1}{6\Delta}F_{N-3} - \frac{1}{\Delta}F_{N-2} + \frac{1}{2\Delta}F_{N-1} + \frac{1}{3\Delta}F_N + \vartheta(\Delta^3)$$

$$\left.\frac{\partial F^+}{\partial \xi}\right|_N = \frac{1}{2\Delta}F_{N-2} - \frac{2}{\Delta}F_{N-1} + \frac{3}{2\Delta}F_N + \vartheta(\Delta^2)$$

A second-order accurate central scheme is used at boundaries. Note that both upwind and downwind fluxes at boundaries are evaluated using identical central schemes, which is equivalent to not splitting the convective fluxes there. The downwind scheme is :

$$\left.\frac{\partial F^-}{\partial \xi}\right|_1 = -\frac{3}{2\Delta}F_1 + \frac{2}{\Delta}F_2 - \frac{1}{2\Delta}F_3 + \vartheta(\Delta^2), \qquad \left.\frac{\partial F^-}{\partial \xi}\right|_2 = -\frac{1}{3\Delta}F_1 - \frac{1}{2\Delta}F_2 + \frac{1}{\Delta}F_3 - \frac{1}{6\Delta}F_4 + \vartheta(\Delta^3)$$

$$\left.\frac{\partial F^-}{\partial \xi}\right|_{N-2} = -\frac{1}{3\Delta}F_{N-3} - \frac{1}{2\Delta}F_{N-2} + \frac{1}{\Delta}F_{N-1} - \frac{1}{6\Delta}F_N + \vartheta(\Delta^3)$$

$$\left.\frac{\partial F^-}{\partial \xi}\right|_{N-1} = \frac{1}{2\Delta}(F_N - F_{N-2}) + \vartheta(\Delta^2)$$

$$\left.\frac{\partial F^-}{\partial \xi}\right|_N = \frac{1}{2\Delta}F_{N-2} - \frac{2}{\Delta}F_{N-1} + \frac{3}{2\Delta}F_N + \vartheta(\Delta^2)$$

A.1.2 Viscous and Heat Flux Derivatives

Discretization of the viscous and heat fluxes requires first and second derivative operators. Second-order accuracy is retained at the boundaries in the corresponding numerical operators. First derivative schemes applied to viscous and heat flux terms are given as follows:

$$\left.\frac{\partial F}{\partial \xi}\right|_1 = -\frac{3}{2\Delta}F_1 + \frac{2}{\Delta}F_2 - \frac{1}{2\Delta}F_3 + \vartheta(\Delta^2), \qquad \left.\frac{\partial F}{\partial \xi}\right|_2 = \frac{1}{2\Delta}(F_3 - F_1) + \vartheta(\Delta^2)$$

$$\left.\frac{\partial F}{\partial \xi}\right|_3 = \frac{1}{12\Delta}(F_1 - F_5) + \frac{2}{3\Delta}(F_4 - F_2) + \vartheta(\Delta^4)$$

$$\frac{\partial F}{\partial \xi}\bigg|_{N-2} = \frac{1}{12\Delta}(F_{N-4} - F_N) + \frac{2}{3\Delta}(F_{N-1} - F_{N-3}) + \vartheta(\Delta^4)$$

$$\frac{\partial F}{\partial \xi}\bigg|_{N-1} = \frac{1}{2\Delta}(F_N - F_{N-2}) + \vartheta(\Delta^2), \quad \frac{\partial F}{\partial \xi}\bigg|_N = \frac{1}{2\Delta}F_{N-2} - \frac{2}{\Delta}F_{N-1} + \frac{3}{2\Delta}F_N + \vartheta(\Delta^2)$$

The second derivative schemes are:

$$\frac{\partial^2 F}{\partial \xi^2}\bigg|_1 = \frac{1}{\Delta}(2F_1 - 5F_2 + 4F_3 - F_4) + \vartheta(\Delta^2), \quad \frac{\partial^2 F}{\partial \xi^2}\bigg|_2 = \frac{1}{\Delta}(F_1 - 2F_2 + F_3) + \vartheta(\Delta^2)$$

$$\frac{\partial^2 F}{\partial \xi^2}\bigg|_3 = -\frac{1}{12\Delta}(F_1 + F_5) + \frac{4}{3\Delta}(F_2 + F_4) - \frac{5}{2\Delta}F_3 + \vartheta(\Delta^4)$$

$$\frac{\partial^2 F}{\partial \xi^2}\bigg|_{N-2} = -\frac{1}{12\Delta}(F_{N-4} + F_N) + \frac{4}{3\Delta}(F_{N-3} + F_{N-1}) - \frac{5}{2\Delta}F_{N-2} + \vartheta(\Delta^4)$$

$$\frac{\partial^2 F}{\partial \xi^2}\bigg|_{N-1} = \frac{1}{\Delta}(F_{N-2} - 2F_{N-1} + F_N) + \vartheta(\Delta^2)$$

$$\frac{\partial^2 F}{\partial \xi^2}\bigg|_N = \frac{1}{\Delta}(-F_{N-3} + 4F_{N-2} - 5F_{N-1} + 2F_N) + \vartheta(\Delta^2)$$

A.2   Inviscid Fluxes and Flux-Vector Splitting

The fluxes $\vec{F}_\xi$, $\vec{F}_\eta$ and $\vec{F}_z$ in directions ξ, η and z respectively are each the sum of inviscid, viscous and heat fluxes, $\vec{F}^e$, $\vec{F}^v$ and $\vec{F}^h$ respectively (see Chapter 2). The remainder of this Appendix details the expression for each component in terms of primitive variables. The notation in this section is identical to that of Beam & Warming (1978).

Inviscid fluxes in generalized coordinates are given by

$$\vec{F}_\xi^e = y_\eta \begin{pmatrix} \rho u \\ \rho u^2 + p \\ \rho u v \\ \rho u w \\ u(e + p) \end{pmatrix} - x_\eta \begin{pmatrix} \rho v \\ \rho u v \\ \rho u^2 + p \\ \rho v w \\ v(e + p) \end{pmatrix} \tag{104}$$

$$\vec{F}_\eta^e = -y_\xi \begin{pmatrix} \rho u \\ \rho u^2 + p \\ \rho uv \\ \rho uw \\ u(e+p) \end{pmatrix} + x_\xi \begin{pmatrix} \rho v \\ \rho uv \\ \rho u^2 + p \\ \rho vw \\ v(e+p) \end{pmatrix} \tag{105}$$

$$\vec{F}_z^e = J \begin{pmatrix} \rho w \\ \rho uw \\ \rho vw \\ \rho w^2 + p \\ w(e+p) \end{pmatrix}. \tag{106}$$

The split convective fluxes in all three directions can be written as one expression by introducing geometric coefficients k_1, k_2 and k_3. The general form of a split convective flux is

$$\vec{F}^\pm = \frac{\rho}{2\gamma} \begin{pmatrix} 2(\gamma-1)\widehat{\lambda}_1^\pm + \widehat{\lambda}_4^\pm + \widehat{\lambda}_5^\pm \\ 2(\gamma-1)\widehat{\lambda}_1^\pm u + \widehat{\lambda}_4^\pm (u + c\widehat{k}_1) + \widehat{\lambda}_5^\pm (u - c\widehat{k}_1) \\ 2(\gamma-1)\widehat{\lambda}_1^\pm v + \widehat{\lambda}_4^\pm (v + c\widehat{k}_2) + \widehat{\lambda}_5^\pm (v - c\widehat{k}_2) \\ 2(\gamma-1)\widehat{\lambda}_1^\pm w + \widehat{\lambda}_4^\pm (w + c\widehat{k}_3) + \widehat{\lambda}_5^\pm (w - c\widehat{k}_3) \\ \frac{\widehat{\lambda}_4^\pm}{2}((u + c\widehat{k}_1)^2 + (v + c\widehat{k}_2)^2 + (w + c\widehat{k}_3)^2) + x_1 \end{pmatrix} \tag{107}$$

where

$$\begin{aligned}
x_1 &= \frac{(3-\gamma)(\widehat{\lambda}_4^\pm + \widehat{\lambda}_5^\pm)c^2}{2(\gamma-1)} + 2\rho(\gamma-1)\widehat{\lambda}_1^\pm \widehat{k}_1(\widehat{k}_2 w - \widehat{k}_3 v) \\
&\quad + (\gamma-1)\widehat{\lambda}_1^\pm(u^2 + v^2 + w^2) + \frac{\widehat{\lambda}_5^\pm}{2}((u - c\widehat{k}_1)^2 + (v - c\widehat{k}_2)^2 + (w - c\widehat{k}_3)^2)
\end{aligned}$$

and where the superscript $\pm$ refers to the construction of the split eigenvalues λ_i discussed below. The total convective flux vector is the sum of its upwind and downwind components:

$$\vec{F}_\xi^e = \vec{F}_\xi^{e+} + \vec{F}_\xi^{e-}, \quad \vec{F}_\eta^e = \vec{F}_\eta^{e+} + \vec{F}_\eta^{e-}, \quad \vec{F}_z^e = \vec{F}_z^{e+} + \vec{F}_z^{e-}. \tag{108}$$

The geometric parameters k_i are displayed in table 7 for each spatial direction, and $\widehat{k}_i$ is defined by:

$$\widehat{k}_i = \frac{k_i}{\sqrt{k_1^2 + k_2^2 + k_3^2}}. \tag{109}$$

131

Direction	k_1	k_2	k_3
ξ	y_η	$-x_\eta$	0
η	$-y_\xi$	x_ξ	0
z	0	0	J

Table 7: Geometric coefficients

Direction	Λ_1	Λ_4	Λ_5
ξ	$y_\eta u - x_\eta v$	$\Lambda_1 + c\sqrt{x_\eta^2 + y_\eta^2}$	$\Lambda_1 - c\sqrt{x_\eta^2 + y_\eta^2}$
η	$-y_\xi u + x_\xi v$	$\Lambda_1 + c\sqrt{x_\xi^2 + y_\xi^2}$	$\Lambda_1 - c\sqrt{x_\xi^2 + y_\xi^2}$
z	Jw	$\Lambda_1 + Jc$	$\Lambda_1 - Jc$

Table 8: Generalized eigenvalues

The split eigenvalues $\widehat{\lambda}_i$ in each direction are:

$$\widehat{\lambda}_i^{\pm} = \frac{\Lambda_i \pm |\Lambda_i|}{2} \tag{110}$$

where the convective eigenvalues Λ_i are given in table 8. The split eigenvalues $\widehat{\lambda}_i$ defined in (110) do not have continuous derivatives in Λ_i at sonic and stagnation points (Van Leer 1982, Coirier & Van Leer 1991). This singularity leads to numerical oscillations near these points in the pressure and velocity fields, a problem which is circumvented by fitting $\widehat{\lambda}_i$ with a parabola in the vicinity of $\Lambda_i = 0$. Let δ_i be the threshold value of $|\Lambda_i|$ below which the split eigenvalue $\widehat{\lambda}_i$ is approximated by a parabola. The parabola is constructed in the $(\widehat{\lambda}_i^+, \Lambda_i)$ plane to be tangent to points $(-\delta_i, 0)$ and (δ_i, δ_i), and in the $(\widehat{\lambda}_i^-, \Lambda_i)$ plane to be tangent to points $(-\delta_i, -\delta_i)$ and $(\delta_i, 0)$. The modified split eigenvalues are then given by:

$$\widehat{\lambda}_i^+ = \Lambda_i \qquad \Lambda_i \geq \delta_i \tag{111}$$

$$\widehat{\lambda}_i^+ = \frac{\Lambda_i^2}{4\delta_i} + \frac{1}{2}\Lambda_i + \frac{1}{4}\delta_i \quad -\delta_i \leq \Lambda_i \leq \delta_i \tag{112}$$

$$\widehat{\lambda}_i^+ = 0 \qquad \Lambda_i \leq -\delta_i \tag{113}$$

and

$$\hat{\lambda}_i^- = 0 \qquad \Lambda_i \geq \delta_i \qquad (114)$$

$$\hat{\lambda}_i^- = -\frac{\Lambda_i^2}{4\delta_i} + \frac{1}{2}\Lambda_i - \frac{1}{4}\delta_i \quad -\delta_i \leq \Lambda_i \leq \delta_i \qquad (115)$$

$$\hat{\lambda}_i^- = \Lambda_i \qquad \Lambda_i \leq -\delta_i \qquad (116)$$

In a single formula, these expressions reduce to:

$$\hat{\lambda}_i^\pm = \frac{\Lambda_i \pm |\Lambda_i|}{2} \ \ |\Lambda_i| \geq \delta_i, \quad \hat{\lambda}_i^\pm = \frac{1}{2}\Lambda_i \pm \frac{1}{4}(\frac{\Lambda_i^2}{\delta_i} + \delta_i) \ \ |\Lambda_i| \leq \delta_i. \qquad (117)$$

In practice, we choose the threshold δ_i to be the largest magnitude of two eigenvalues Λ_i of opposite signs, which are neighbors along a grid line. Figure (71) displays the modified eigenvalues $\lambda^\pm$ in the vicinity of a singular point where $\Lambda = 0$. The corner formed by the solid lines corresponds to the singularity generated by flux-splitting. The eigenvalue magnitudes are referenced to the threshold δ, so that parabolic smoothing is applied in the range $-1 \leq |\Lambda|/\delta \leq 1$. A quartic smoothing function was also tested, and produced no visible differences in two-dimensional test calculations of the flow over a circular cylinder.

A.3 Iterative Time-Scheme Convective Jacobians

The factored iterative equations in the periodic azimuthal and spanwise directions (78 and 79) involve the diagonalized form of the convective flux:

$$\vec{F}_i^\pm = P_i \Lambda_i^\pm P_i^{-1} \vec{Q}. \qquad (118)$$

The three matrices the iterative scheme involves are P_η^{-1}, $(P_z^{-1} P_\eta)$ and P_z, which are given by Pulliam & Chaussee (1981) as:

$$P_\eta^{-1} = \frac{1}{\psi} \begin{pmatrix} -y_\xi(1 - (\gamma - 1)\Phi^2 c^{-2}) + x_\xi w\rho^{-1} & -y_\xi(\gamma - 1)uc^{-2} \\ x_\xi(1 - (\gamma - 1)\Phi^2 c^{-2}) + y_\xi w\rho^{-1} & x_\xi(\gamma - 1)uc^{-2} \\ \rho^{-1}(y_\xi v - x_\xi u) & x_\xi \rho^{-1} \\ \beta((\gamma - 1)\Phi^2\psi - c\theta) & \beta(-y_\xi c - (\gamma - 1)u\psi) \\ \beta((\gamma - 1)\Phi^2\psi + c\theta) & -\beta(-y_\xi c - (\gamma - 1)u\psi) \end{pmatrix}$$

$$
\left.
\begin{array}{ccc}
-y_\xi(\gamma-1)vc^{-2} & -x_\xi\rho^{-1}-y_\xi(\gamma-1)wc^{-2} & y_\xi(\gamma-1)c^{-2} \\
x_\xi(\gamma-1)vc^{-2} & -y_\xi\rho^{-1}+x_\xi(\gamma-1)wc^{-2} & -x_\xi(\gamma-1)c^{-2} \\
y_\xi\rho^{-1} & 0 & 0 \\
\beta(y_\xi c-(\gamma-1)v\psi) & -\beta\psi(\gamma-1)w & \beta\psi(\gamma-1) \\
-\beta(y_\xi c-(\gamma-1)v\psi) & \beta\psi(\gamma-1)w & \beta\psi(\gamma-1)
\end{array}
\right)
\qquad (119)
$$

$$
P_z^{-1}\,P_\eta = \frac{1}{\psi}
\begin{pmatrix}
0 & 0 & y_\xi & x_\xi/\sqrt{2} & -x_\xi/\sqrt{2} \\
0 & 0 & -x_\xi & y_\xi/\sqrt{2} & -y_\xi/\sqrt{2} \\
-y_\xi & x_\xi & 0 & 0 & 0 \\
-x_\xi/\sqrt{2} & -y_\xi/\sqrt{2} & 0 & \psi/2 & \psi/2 \\
x_\xi/\sqrt{2} & y_\xi/\sqrt{2} & 0 & \psi/2 & \psi/2
\end{pmatrix}
\qquad (120)
$$

and

$$
P_z =
\begin{pmatrix}
0 & 0 & 1 & \alpha & \alpha \\
0 & -\rho & u & \alpha u & \alpha u \\
\rho & 0 & v & \alpha v & \alpha v \\
0 & 0 & w & \alpha(w+c) & \alpha(w-c) \\
\rho v & -\rho u & \Phi^2 & \alpha(\Phi^2+\frac{c^2}{\gamma-1}+cw) & \alpha(\Phi^2+\frac{c^2}{\gamma-1}-cw)
\end{pmatrix}
\qquad (121)
$$

where

$$
\alpha = \frac{\rho}{\sqrt{2}c} \;;\quad \Phi^2 = \frac{1}{2}(u^2+v^2+w^2) \;;\quad \psi = \sqrt{x_\xi^2+y_\xi^2}
$$

$$
\theta = -y_\xi u + x_\xi v \;;\quad \beta = \frac{1}{\sqrt{2}\rho c}.
$$

A.4   Generalized Viscous and Heat Fluxes

Viscous and heat fluxes $\vec{F}_x^{v,h}$ along the x direction are decomposed into the contributions of derivatives of the primitive variables along each spatial direction, denoted as $\vec{F}_{\xi x}$, $\vec{F}_{\eta x}$ and $\vec{F}_{zx}$. This decomposition is presented in equations (50) through (52). Expressions for each of these fluxes are given below. In each vector, the symbol Σ represents the dot-product of the velocity with the three momentum components. This Section completes the description of the fluxes which appear in the governing equations of motion (55). The linearized viscous flux Jacobians in the left-hand side

of the factored equation corresponding to the wall-normal direction (80) are obtained from the viscous fluxes presented below by straight-forward differentiation. Viscous and heat fluxes are functions of the conservative variable vector $\vec{Q}$ and its spatial derivatives. In particular, $\vec{F}_{xx} = \vec{F}_{xx}(\vec{Q}, \vec{Q}_x)$. The Jacobian of this flux, appearing in the left-hand side of (80) is computed at time level $n+1$ from the Taylor expansion:

$$\Delta \vec{F}_{xx}(\vec{Q}^{n+1}, \vec{Q}_x^{n+1}) \simeq \left(\frac{\partial \vec{F}_{xx}}{\partial \vec{Q}}\right)^n \Delta \vec{Q}^{n+1} + \left(\frac{\partial \vec{F}_{xx}}{\partial \vec{Q}_x}\right)^n \Delta \vec{Q}_x^{n+1}. \tag{122}$$

The remainder of this Appendix lists the expressions for the viscous and heat fluxes along each coordinate direction.

Viscous fluxes along the ξ direction:

$$\vec{F}_{\xi\xi}^v = -\frac{1}{JRe} \begin{pmatrix} 0 \\ (\frac{4}{3}y_\eta^2 + x_\eta^2)u_\xi - \frac{1}{3}x_\eta y_\eta v_\xi \\ (\frac{4}{3}x_\eta^2 + y_\eta^2)v_\xi - \frac{1}{3}x_\eta y_\eta u_\xi \\ (x_\eta^2 + y_\eta^2)w_\xi \\ \Sigma \end{pmatrix} \tag{123}$$

$$\vec{F}_{\eta\xi}^v = -\frac{1}{JRe} \begin{pmatrix} 0 \\ -(\frac{4}{3}y_\eta y_\xi + x_\eta x_\xi)u_\eta + (x_\eta y_\xi - \frac{2}{3}y_\eta x_\xi)v_\eta \\ -(\frac{4}{3}x_\eta x_\xi + y_\eta y_\xi)v_\eta + (y_\eta x_\xi - \frac{2}{3}x_\eta y_\xi)u_\eta \\ -(x_\xi x_\eta + y_\eta y_\xi)w_\eta \\ \Sigma \end{pmatrix} \tag{124}$$

$$\vec{F}_{z\xi}^v = -\frac{1}{Re} \begin{pmatrix} 0 \\ -\frac{2}{3}y_\eta w_z \\ \frac{2}{3}x_\eta w_z \\ y_\eta u_z - x_\eta v_z \\ \Sigma \end{pmatrix} \tag{125}$$

Viscous fluxes along the η direction:

$$\vec{F}_{\xi\eta}^v = -\frac{1}{JRe} \begin{pmatrix} 0 \\ -(\frac{4}{3}y_\eta y_\xi + x_\eta x_\xi)u_\xi + (y_\eta x_\xi - \frac{2}{3}x_\eta y_\xi)v_\xi \\ -(\frac{4}{3}x_\eta x_\xi + y_\eta y_\xi)v_\xi + (x_\eta y_\xi - \frac{2}{3}y_\eta x_\xi)u_\xi \\ -(x_\xi x_\eta + y_\eta y_\xi)w_\xi \\ \Sigma \end{pmatrix} \tag{126}$$

135

$$\vec{F}_{\eta\eta}^{v} = -\frac{1}{JRe} \begin{pmatrix} 0 \\ (\frac{4}{3}y_{\xi}^{2} + x_{\xi}^{2})u_{\eta} - \frac{1}{3}x_{\xi}y_{\xi}v_{\eta} \\ (\frac{4}{3}x_{\xi}^{2} + y_{\xi}^{2})v_{\eta} - \frac{1}{3}x_{\xi}y_{\xi}u_{\eta} \\ (x_{\xi}^{2} + y_{\xi}^{2})w_{\eta} \\ \Sigma \end{pmatrix}, \quad \vec{F}_{z\eta}^{v} = -\frac{1}{Re} \begin{pmatrix} 0 \\ \frac{2}{3}y_{\xi}w_{z} \\ -\frac{2}{3}x_{\xi}w_{z} \\ -y_{\xi}u_{z} + x_{\xi}v_{z} \\ \Sigma \end{pmatrix} \quad (127)$$

Viscous fluxes along the z direction:

$$\vec{F}_{\xi z}^{v} = -\frac{1}{Re} \begin{pmatrix} 0 \\ y_{\eta}w_{\xi} \\ -x_{\eta}w_{\xi} \\ \frac{2}{3}(x_{\eta}v_{\xi} - y_{\eta}u_{\xi}) \\ \Sigma \end{pmatrix}, \quad \vec{F}_{\eta z}^{v} = -\frac{1}{Re} \begin{pmatrix} 0 \\ -y_{\xi}w_{\eta} \\ x_{\xi}w_{\eta} \\ \frac{2}{3}(y_{\xi}u_{\eta} - x_{\xi}v_{\eta}) \\ \Sigma \end{pmatrix} \quad (128)$$

$$\vec{F}_{zz}^{v} = -\frac{J}{Re} \begin{pmatrix} 0 \\ u_{z} \\ v_{z} \\ \frac{4}{3}w_{z} \\ \Sigma \end{pmatrix} \quad (129)$$

Heat fluxes along the ξ direction:

$$\vec{F}_{\xi\xi}^{h} = -\frac{\gamma}{(\gamma - 1)PrReJ}(x_{\eta}^{2} + y_{\eta}^{2})\frac{\partial T}{\partial \xi} \begin{pmatrix} 0 \\ 0 \\ 0 \\ 0 \\ 1 \end{pmatrix} \quad (130)$$

$$\vec{F}_{\eta\xi}^{h} = \frac{\gamma}{(\gamma - 1)PrReJ}(x_{\eta}x_{\xi} + y_{\eta}y_{\xi})\frac{\partial T}{\partial \eta} \begin{pmatrix} 0 \\ 0 \\ 0 \\ 0 \\ 1 \end{pmatrix} \quad (131)$$

Heat fluxes along the η direction:

$$\vec{F}^h_{\xi\eta} = \frac{\gamma}{(\gamma - 1)PrReJ}(x_\eta x_\xi + y_\eta y_\xi)\frac{\partial T}{\partial \xi}\begin{pmatrix} 0 \\ 0 \\ 0 \\ 0 \\ 1 \end{pmatrix} \tag{132}$$

$$\vec{F}^h_{\eta\eta} = -\frac{\gamma}{(\gamma - 1)PrReJ}(x_\xi^2 + y_\xi^2)\frac{\partial T}{\partial \eta}\begin{pmatrix} 0 \\ 0 \\ 0 \\ 0 \\ 1 \end{pmatrix} \tag{133}$$

Heat flux along the z direction:

$$\vec{F}^h_{zz} = -\frac{\gamma J}{(\gamma - 1)PrRe}\frac{\partial T}{\partial z}\begin{pmatrix} 0 \\ 0 \\ 0 \\ 0 \\ 1 \end{pmatrix} \tag{134}$$
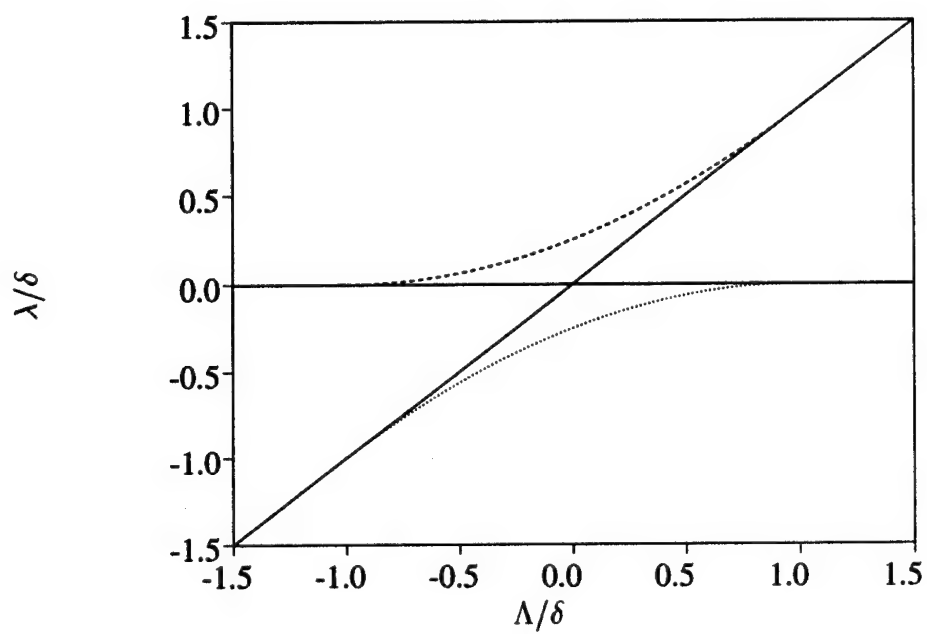
Figure 71: Eigenvalue smoothing near singular points
$$---- : \lambda^+/\delta; \quad \cdots : \lambda^-/\delta$$

138

Appendix B

Far-Field and Wall Boundary Conditions

B.1　Introduction

This Appendix details the conditions imposed explicitly and implicitly on the conservative variables at the wall and far-field boundaries. The generalized coordinates (ξ, η, z) correspond to the radial, azimuthal and spanwise directions respectively. Lines along the ξ direction extend from the cylinder surface to the outer boundary of the computational domain (figure 84, Appendix F), and are normal to the cylinder boundary surface by construction. Wall and far-field boundary conditions are required at the ξ boundaries. The azimuthal (η) and spanwise (z) directions are periodic, and the factored systems in these directions (equations 78 and 79) are solved with periodic boundary conditions.

B.2　Far-Field Boundary

Far-field surfaces are partitioned into potential and wake sub-regions, different sets of boundary conditions being appropriate for each. In potential regions, boundary conditions are based on Riemann invariants (Pulliam 1986b), while at wake boundaries the primitive variables are extrapolated with a first-order accurate scheme from

their values inside the computational domain. The locally-one-dimensional Riemann invariants R_1 and R_2 are defined as

$$R_1 = V_n - \frac{2c}{\gamma - 1}, \quad R_2 = V_n + \frac{2c}{\gamma - 1} \tag{135}$$

where c is the local sound speed and V_n the velocity normal to the boundary surface. Let V_t denote the velocity tangential to the surface. According to our axis convention, in which the η direction corresponds to the azimuthal direction and is positive as in the trigonometric convention, the normal and tangential components of the velocity are given by :

$$V_n = \frac{y_\eta u - x_\eta v}{\sqrt{x_\eta^2 + y_\eta^2}}, \quad V_t = \frac{x_\eta u + y_\eta v}{\sqrt{x_\eta^2 + y_\eta^2}}. \tag{136}$$

B.2.1 Potential Region : Explicit Formulation

In the following derivations, mesh points along the ξ axis have indices 1 through N, where ξ_1 and ξ_N lie respectively at the cylinder surface and outer boundary of the computational domain.

Inflow boundary conditions are chosen as:

$$\frac{p}{\rho^\gamma} = \left(\frac{p}{\rho^\gamma}\right)_\infty, \quad w = w_\infty, \quad V_t = V_{t\infty}, \quad R_1 = R_{1\infty}, \quad R_2 = R_{2N-1} \tag{137}$$

and those at outflow as

$$\frac{p}{\rho^\gamma} = \left(\frac{p}{\rho^\gamma}\right)_{N-1}, \quad w = w_{N-1}, \quad V_t = V_{tN-1}, \quad R_1 = R_{1\infty}, \quad R_2 = R_{2N-1}. \tag{138}$$

Using the definition of the conservative variable $\vec{Q}$ (equation 44, Chapter 2), these relations correspond to conditions on $\vec{Q}$ at the boundaries given at inflow by:

$$q_1 = J\left(\frac{\gamma - 1}{4}(R_{2N-1} - R_{1\infty})\right)^{\frac{2}{\gamma-1}} \tag{139}$$

$$q_2 = \frac{q_1}{\sqrt{x_\eta^2 + y_\eta^2}}\left(x_\eta V_{t\infty} + \frac{1}{2}y_\eta(R_{1\infty} + R_{2N-1})\right) \tag{140}$$

$$q_3 = \frac{q_1}{\sqrt{x_\eta^2 + y_\eta^2}}\left(y_\eta V_{t\infty} - \frac{1}{2}x_\eta(R_{1\infty} + R_{2N-1})\right) \tag{141}$$

$$q_4 = 0 \tag{142}$$

$$q_5 = \frac{q_1^\gamma}{\gamma(\gamma-1)J^{\gamma-1}} + \frac{q_2^2 + q_3^2 + q_4^2}{2q_1}. \tag{143}$$

while at the outflow:

$$q_1 = J\left(\frac{\rho_{N-1}^\gamma}{\gamma p_{N-1}}\left(\frac{\gamma-1}{4}\right)^2 (R_{2N-1} - R_{1\infty})^2\right)^{\frac{1}{\gamma-1}} \tag{144}$$

$$q_2 = \frac{q_1}{\sqrt{x_\eta^2 + y_\eta^2}}\left(x_\eta V_{tN-1} + \frac{1}{2}y_\eta(R_{1\infty} + R_{2N-1})\right) \tag{145}$$

$$q_3 = \frac{q_1}{\sqrt{x_\eta^2 + y_\eta^2}}\left(y_\eta V_{tN-1} - \frac{1}{2}x_\eta(R_{1\infty} + R_{2N-1})\right) \tag{146}$$

$$q_4 = q_1\left(\frac{q_4}{q_1}\right)_{N-1} \tag{147}$$

$$q_5 = \frac{q_1^\gamma p_{N-1}}{(\gamma-1)J^{\gamma-1}\rho_{N-1}^\gamma} + \frac{q_2^2 + q_3^2 + q_4^2}{2q_1}. \tag{148}$$

Conditions at infinity are found from the potential flow around a fixed circular cylinder:

$$u_\infty = M_\infty\left(1 - \frac{\cos 2\theta}{r^2}\right), \quad v_\infty = -M_\infty\frac{\sin 2\theta}{r^2}. \tag{149}$$

B.2.2   Potential Region : Implicit Formulation

The time scheme being written in delta-form (see equation 80), implicit boundary conditions are not applied to the conservative variables, but to their incremental change over one time-step $\Delta q_i = \Delta q_i^{n+1} = q_i^{n+1} - q_i^n$. Conservative variables at far-field boundaries are functions of the invariant R_2, the pressure p and the tangential velocity V_t, as described in the previous Section, so that their increments depend on ΔR_2, Δp and ΔV_t. By definition these increments are:

$$\Delta R_2 = \left(-\frac{c}{\gamma-1} + \frac{\gamma}{2cq_1^2}(q_2^2 + q_3^2 + q_4^2) - \frac{y_\eta q_2 - x_\eta q_3}{q_1\sqrt{x_\eta^2 + y_\eta^2}}\right)\frac{\Delta q_1}{q_1}$$

$$+ \left(\frac{y_\eta}{\sqrt{x_\eta^2 + y_\eta^2}} - \frac{\gamma q_2}{cq_1}\right)\frac{\Delta q_2}{q_1} - \left(\frac{x_\eta}{\sqrt{x_\eta^2 + y_\eta^2}} + \frac{\gamma q_3}{cq_1}\right)\frac{\Delta q_3}{q_1} - \frac{\gamma q_4}{cq_1^2}\Delta q_4 + \frac{\gamma}{cq_1}\Delta q_5$$

$$\Delta p = \frac{(\gamma - 1)}{J}\left(\frac{q_2^2 + q_3^2 + q_4^2}{2q_1^2}\Delta q_1 - \frac{q_2}{q_1}\Delta q_2 - \frac{q_3}{q_1}\Delta q_3 - \frac{q_4}{q_1}\Delta q_4 + \Delta q_5 \right)$$

$$\Delta V_t = \frac{1}{q_1\sqrt{x_\eta^2 + y_\eta^2}}\left(-\frac{1}{q_1}(x_\eta q_2 + y_\eta q_3)\Delta q_1 + x_\eta\Delta q_2 + y_\eta\Delta q_3 \right).$$

Substituting these into the explicit boundary conditions (139 through 148) leads to implicit conditions on the increments Δq_i. The resulting implicit inflow boundary conditions are:

$$\Delta q_1 = \frac{J}{2}\left(\frac{\gamma - 1}{4}(R_{2N-1} - R_{1\infty}) \right)^{\frac{3-\gamma}{\gamma-1}}\Delta R_{2N-1} \tag{150}$$

$$\Delta q_2 = \frac{\Delta q_1}{\sqrt{x_\eta^2 + y_\eta^2}}\left(x_\eta V_{t\infty} + \frac{1}{2}y_\eta(R_{1\infty} + R_{2N-1}) \right) + \frac{q_1 y_\eta}{2\sqrt{x_\eta^2 + y_\eta^2}}\Delta R_{2N-1} \tag{151}$$

$$\Delta q_3 = \frac{\Delta q_1}{\sqrt{x_\eta^2 + y_\eta^2}}\left(y_\eta V_{t\infty} - \frac{1}{2}x_\eta(R_{1\infty} + R_{2N-1}) \right) - \frac{q_1 x_\eta}{2\sqrt{x_\eta^2 + y_\eta^2}}\Delta R_{2N-1} \tag{152}$$

$$\Delta q_4 = 0 \tag{153}$$

$$\Delta q_5 = \left(\frac{q_1^{\gamma-1}}{(\gamma-1)J^{\gamma-1}} + \frac{q_2^2 + q_3^2 + q_4^2}{2q_1^2} \right)\Delta q_1 + \frac{q_2}{q_1}\Delta q_2 + \frac{q_3}{q_1}\Delta q_3 + \frac{q_4}{q_1}\Delta q_4 \tag{154}$$

while at the outflow boundary implicit conditions are given by:

$$\Delta q_1 = \Phi_1\left[\frac{2q_1^\gamma}{\gamma p J^\gamma}\Delta R_2 + (R_2 - R_{1\infty})\left(\frac{q_1^{\gamma-1}}{J^\gamma p}\Delta q_1 - \frac{q_1^\gamma}{\gamma J^\gamma p^2}\Delta p \right) \right]_{N-1} \tag{155}$$

$$\Delta q_2 = \frac{1}{\sqrt{x_\eta^2 + y_\eta^2}}\left(x_\eta V_{tN-1} + \frac{1}{2}y_\eta(R_{1\infty} + R_{2N-1}) \right)\Delta q_1$$
$$+ \frac{q_1}{\sqrt{x_\eta^2 + y_\eta^2}}\left(x_\eta\Delta V_{tN-1} + \frac{1}{2}y_\eta\Delta R_{2N-1} \right) \tag{156}$$

$$\Delta q_3 = \frac{1}{\sqrt{x_\eta^2 + y_\eta^2}}\left(y_\eta V_{tN-1} - \frac{1}{2}x_\eta(R_{1\infty} + R_{2N-1}) \right)\Delta q_1$$
$$+ \frac{q_1}{\sqrt{x_\eta^2 + y_\eta^2}}\left(y_\eta\Delta V_{tN-1} - \frac{1}{2}x_\eta\Delta R_{2N-1} \right) \tag{157}$$

$$\Delta q_4 = \left(\frac{q_4}{q_1} \right)_{N-1}\Delta q_1 + \frac{q_1}{(q_1)_{N-1}}\Delta(q_4)_{N-1} - \frac{q_1(q_4)_{N-1}}{(q_1^2)_{N-1}}\Delta(q_1)_{N-1} \tag{158}$$

$$\Delta q_5 = \Phi_5 \Delta q_1 + \frac{q_2}{q_1}\Delta q_2 + \frac{q_3}{q_1}\Delta q_3 + \frac{q_4}{q_1}\Delta q_4$$
$$+ \frac{q_1^\gamma}{J^{\gamma-1}\rho_{N-1}^\gamma(\gamma-1)}\Delta p_{N-1} - \frac{\gamma q_1^\gamma p_{N-1}}{J^{\gamma-1}(\gamma-1)\rho_{N-1}^{\gamma+1}J_{N-1}}\Delta(q_1)_{N-1} \quad (159)$$

where the parameters Φ_1 and Φ_5 are defined by

$$\Phi_1 = \frac{J(\gamma-1)}{16}(R_{2N-1} - R_{1\infty})\left((\frac{\rho^\gamma}{\gamma p})_{N-1}(\frac{\gamma-1}{4})^2(R_{2N-1} - R_{1\infty})^2\right)^{\frac{2-\gamma}{\gamma-1}}$$

and

$$\Phi_5 = \frac{\gamma q_1^{\gamma-1} p_{N-1}}{J^{\gamma-1}\rho_{N-1}^\gamma(\gamma-1)} - \frac{q_2^2 + q_3^2 + q_4^2}{2q_1^2}.$$

B.2.3 Wake Region : Explicit Formulation

The edge of the wake layer at the outflow boundary is defined by a boundary-layer criterion

$$u \leq 0.99\, u_\infty. \quad (160)$$

Physically realistic boundary conditions within the wake region should consist of 4 constraints on the conservative variables and take the viscous stress into account (Poinsot & Lele 1989, 1992). In the present simulations, outflow conditions are simplified, and the region of interest in the computation is shielded from the errors generated by inaccuracies at the boundaries by a long region in which the mesh is highly stretched, allowing numerical dissipation to damp all scales of motion. At the wake boundary, all primitive variables ρ, u, v, w, p are extrapolated, and the explicit conditions are

$$u = u_{N-1}, \quad v = v_{N-1}, \quad w = w_{N-1}, \quad p = p_{N-1}, \quad \rho = \rho_{N-1}. \quad (161)$$

B.2.4 Wake Region : Implicit Formulation

The implicit boundary conditions corresponding to a first-order extrapolation of the primitive variables are:

$$J_{N-1}\Delta q_1 = J\Delta(q_1)_{N-1} \quad (162)$$

$$\Delta q_2 = \Delta q_1 \left(\frac{q_2}{q_1} \right)_{N-1} + \frac{q_1}{(q_1)_{N-1}} \Delta (q_2)_{N-1} - \frac{q_1 (q_2)_{N-1}}{(q_1)^2_{N-1}} \Delta (q_1)_{N-1} \qquad (163)$$

$$\Delta q_3 = \Delta q_1 \left(\frac{q_3}{q_1} \right)_{N-1} + \frac{q_1}{(q_1)_{N-1}} \Delta (q_3)_{N-1} - \frac{q_1 (q_3)_{N-1}}{(q_1)^2_{N-1}} \Delta (q_1)_{N-1} \qquad (164)$$

$$\Delta q_4 = \Delta q_1 \left(\frac{q_4}{q_1} \right)_{N-1} + \frac{q_1}{(q_1)_{N-1}} \Delta (q_4)_{N-1} - \frac{q_1 (q_4)_{N-1}}{(q_1)^2_{N-1}} \Delta (q_1)_{N-1} \qquad (165)$$

$$\Delta p = \Delta p_{N-1} \qquad (166)$$

B.3   Solid Walls

B.3.1   Explicit Formulation

At solid surfaces, no-slip conditions are imposed, $q_2 = q_3 = q_4 = 0$. The surface is constrained to be adiabatic $(\partial (q_5/q_1)/\partial \xi = 0)$, and the wall pressure derivative is found from the normal momentum equation. The normal momentum equation is found by projecting the ξ and η momentum equations onto the normal direction vector at the surface

$$\hat{n} = \frac{1}{\sqrt{y_\eta^2 + x_\eta^2}} (y_\eta \vec{i} - x_\eta \vec{j}), \qquad (167)$$

where $\vec{i}$ and $\vec{j}$ are the direction vectors in the x and y directions respectively. The grid is normal to the cylinder surface by construction, so that an equation governing the wall pressure gradient $\partial p/\partial \xi = \partial (q_5/J)/\partial \xi$ is necessary. Since the time scheme is in factored form, the equation defining this pressure gradient should only involve derivatives in the ξ direction. The appropriate momentum equation is obtained by manipulation of both the normal and tangential momentum equations, and reduces to:

$$\alpha_1 \frac{\partial p}{\partial \xi} + \alpha_2 \frac{\partial^2 u}{\partial \xi^2} + \alpha_3 \frac{\partial^2 v}{\partial \xi^2} + \alpha_4 \frac{\partial u}{\partial \xi} + \alpha_5 \frac{\partial v}{\partial \xi} + \alpha_6 \frac{\partial^2 u}{\partial \xi \partial \eta} + \alpha_7 \frac{\partial^2 v}{\partial \xi \partial \eta} = 0 \qquad (168)$$

with the coefficients:

$$\alpha_1 = x_\eta^2 + y_\eta^2, \quad \alpha_2 = -\frac{4}{3} \frac{y_\eta}{JRe} (x_\eta^2 + y_\eta^2), \quad \alpha_3 = \frac{4}{3} \frac{x_\eta}{JRe} (x_\eta^2 + y_\eta^2)$$

$$\alpha_4 = -y_\eta \left[\frac{1}{JRe} \left(\frac{4}{3} y_\eta^2 + x_\eta^2 \right) \right]_\xi - \frac{1}{3} x_\eta \left(\frac{1}{JRe} x_\eta y_\eta \right)_\xi$$
$$+ y_\eta \left[\frac{1}{JRe} \left(\frac{4}{3} y_\xi y_\eta + x_\xi x_\eta \right) \right]_\eta + x_\eta \left[\frac{1}{JRe} \left(y_\xi x_\eta - \frac{2}{3} x_\xi y_\eta \right) \right]_\eta$$

$$\alpha_5 = x_\eta \left[\frac{1}{JRe} \left(\frac{4}{3} x_\eta^2 + y_\eta^2 \right) \right]_\xi + \frac{1}{3} y_\eta \left(\frac{1}{JRe} x_\eta y_\eta \right)_\xi$$
$$- y_\eta \left[\frac{1}{JRe} \left(-\frac{2}{3} x_\xi y_\eta + y_\xi x_\eta \right) \right]_\eta - x_\eta \left[\frac{1}{JRe} \left(y_\xi y_\eta + \frac{4}{3} x_\xi x_\eta \right) \right]_\eta$$

$$\alpha_6 = \frac{1}{3ReJ} (8 y_\xi y_\eta^2 + y_\xi x_\eta^2 + 7 x_\eta x_\xi y_\eta), \quad \alpha_7 = -\frac{1}{3ReJ} (8 x_\xi x_\eta^2 + x_\xi y_\eta^2 + 7 x_\eta y_\xi y_\eta).$$

Spatial derivatives of the pressure and temperature at the wall are evaluated with first-order accurate schemes.

B.3.2 Implicit Formulation

The no-slip conditions on the velocity field at the wall hold for all times, so that

$$\Delta q_2 = 0, \quad \Delta q_3 = 0, \quad \Delta q_4 = 0. \tag{169}$$

The implicit boundary condition on pressure at each sub-iteration neglects the change in viscous stresses between iterations; the implicit adiabatic wall condition is obtained directly from its explicit counterpart:

$$\Delta \frac{\partial}{\partial \xi} \frac{q_5}{J} = 0, \quad \Delta \frac{\partial}{\partial \xi} \frac{q_5}{q_1} = 0. \tag{170}$$

The boundary condition on the pressure is updated after each time-step, so that neglecting the viscous stresses at each sub-iteration does not affect the accuracy of the solution.

B.4 A Three-Dimensional Example

Figures (72) through (76) display the five conservative variables at a given instant in time in a large-eddy simulation of the turbulent flow around a circular cylinder using

the dynamic subgrid-scale model. The Reynolds number is $3,900$ based on cylinder diameter and free-stream velocity. The grid contains $144 \times 136 \times 48$ points in the radial, azimuthal and spanwise directions respectively.

The figures show the instantaneous fields in the entire domain (top picture on each page), with the outer boundary of the computational domain marked by a limiting circle, and in the vicinity of the cylinder surface (bottom picture). The solution near the inflow and outflow boundaries does not exhibit undesirable numerical oscillation in any of the conservative variables. From the contours of the streamwise and vertical velocities, the numerical dissipation in the far wake of the large scales of motion is clearly evident.

Figure 72: $Re = 3,900$; Instantaneous density (ρ)
$144 \times 136 \times 48$ Dynamic model simulation
top : whole grid; bottom : cylinder vicinity

147
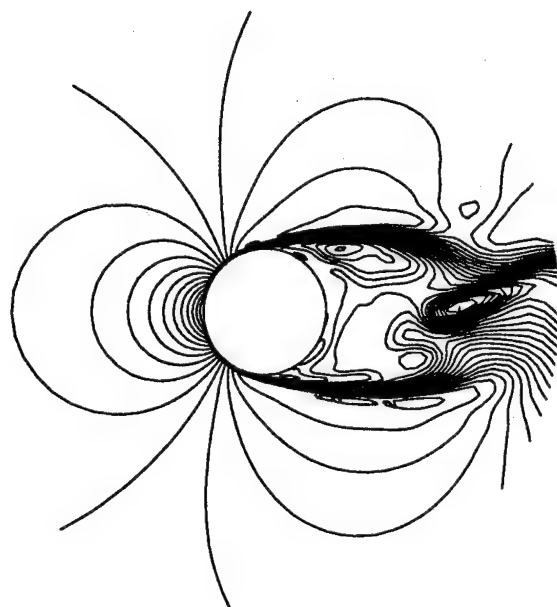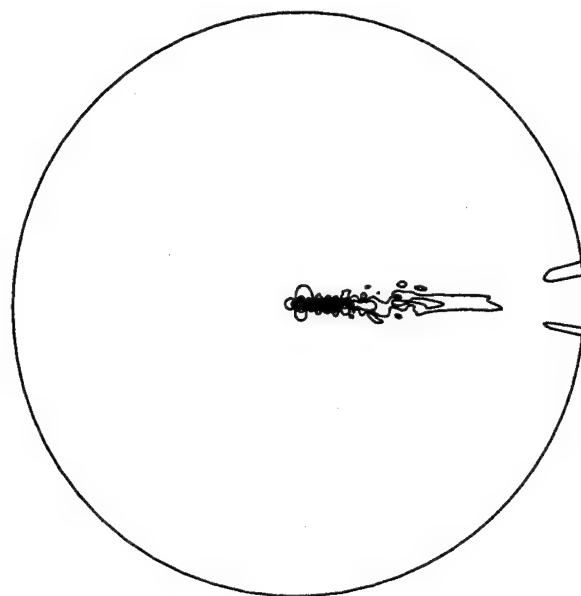
Figure 73: $Re = 3,900$; Instantaneous streamwise velocity (ρu)
$144 \times 136 \times 48$ Dynamic model simulation
top : whole grid; bottom : cylinder vicinity
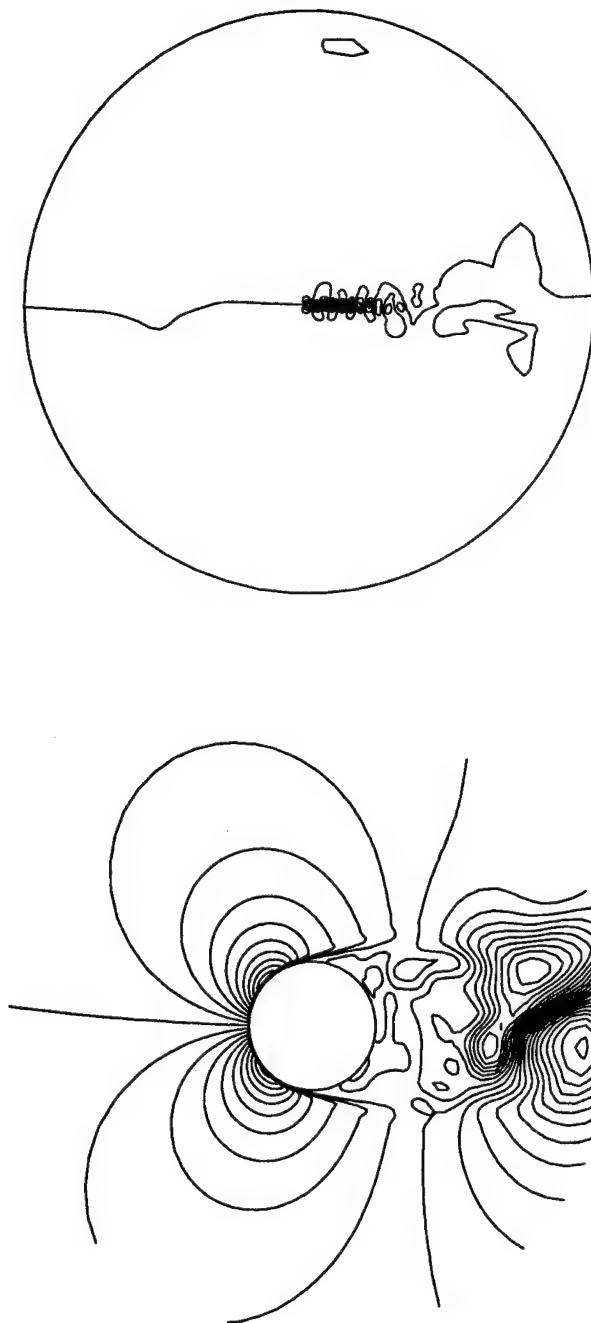
Figure 74: $Re = 3,900$; Instantaneous vertical velocity (ρv)
$144 \times 136 \times 48$ Dynamic model simulation
top : whole grid; bottom : cylinder vicinity
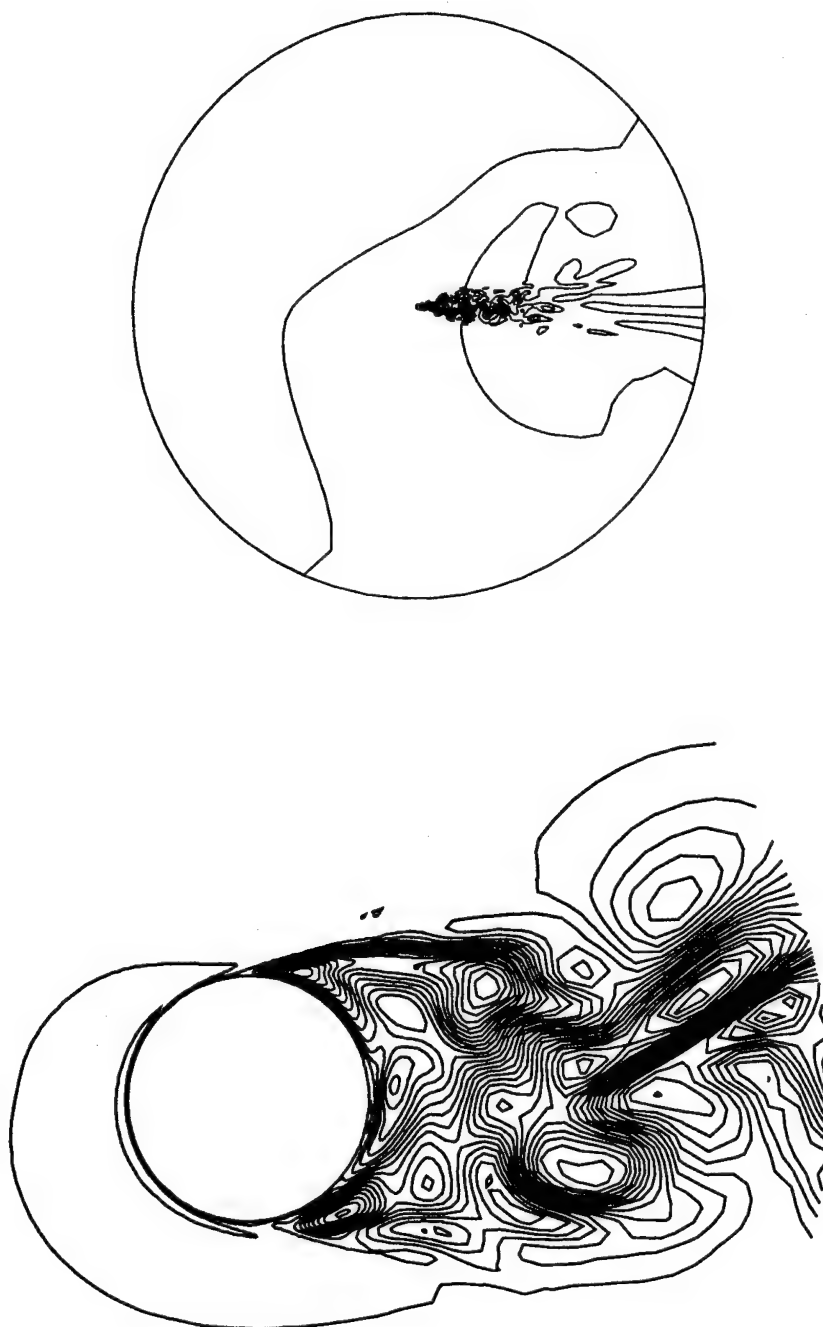
Figure 75: $Re = 3,900$; Instantaneous spanwise velocity (ρw)
$144 \times 136 \times 48$ Dynamic model simulation
top : whole grid; bottom : cylinder vicinity
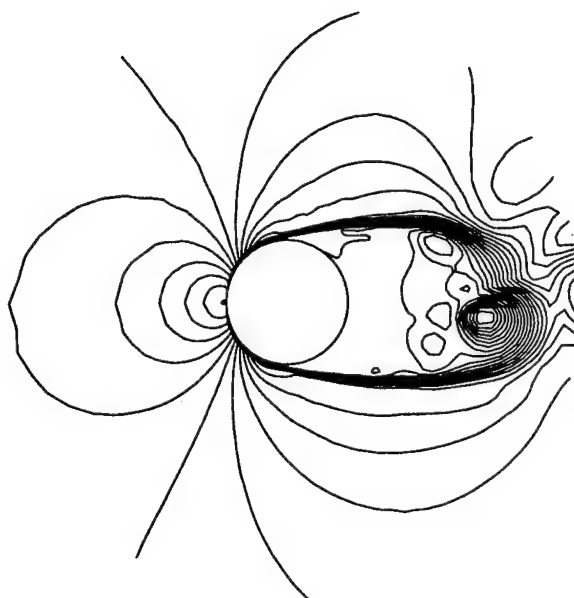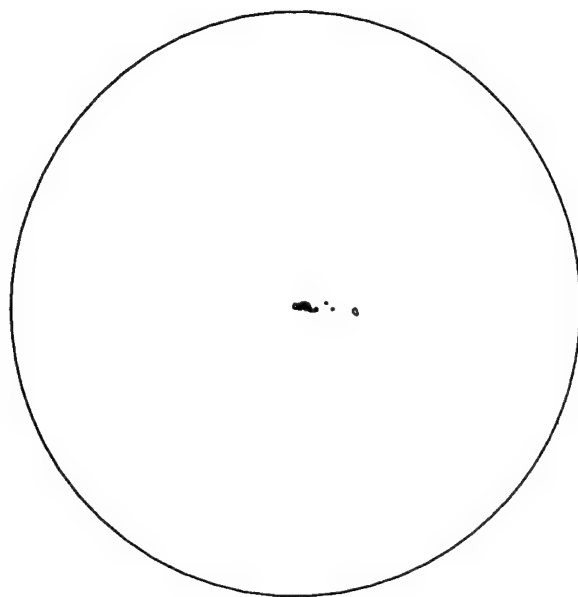
Figure 76: $Re = 3,900$; Instantaneous total energy (e)
$144 \times 136 \times 48$ Dynamic model simulation
top : whole grid; bottom : cylinder vicinity

Appendix C

Cylinder Grid Generation Technique

C.1   Introduction

In all simulations, the computational domain is an annulus of outer radius $R_D R_c$ and spanwise length $L_z R_c$, where R_c is the cylinder radius, spanned by $(N_\xi \times N_\eta \times N_z)$ points in the radial, azimuthal and spanwise directions respectively. All grids share the following properties: they are constrained to be symmetric in the upper and lower half (ξ, η) planes; generalized radial grid-lines $(\eta = \text{constant}, z = \text{constant})$ are normal to the cylinder surface by construction; three-dimensional grids are generated by aligning N_z identical two-dimensional meshes in the spanwise direction; spanwise points are equispaced; azimuthal points are distributed in the (ξ, η)-plane on circles of constant radius $(\xi = \text{constant})$.

Given these characteristics, the grid is fully described by the location of each of these circles, *i.e.* the distribution of radial points $r(\xi)$, and the layout of azimuthal points along each circle $\theta(\eta)$. This Appendix describes these distributions, which differ for laminar and turbulent simulations. The following two sections treat these regimes separately. Figure (77) displays the nomenclature used throughout this report to represent the features of the near-wake flow structure. The locations of the laminar surface boundary layer, separated shear layers, recirculation and potential zones are

illustrated using contours of instantaneous streamwise velocity extracted from the $(116 \times 136 \times 48)$ mesh simulation at Reynolds number $3,900$ presented in Appendix F.

C.2 Grids for Laminar Simulations at Reynolds Numbers $20, 80$ and 100

C.2.1 Radial Point Distribution

All laminar simulations use an identical family of grids, described in this Section. In the radial direction, the mapping from physical to computational space is:

$$r(\xi) = a - (1+a)e^{\xi \ln s_r} \tag{171}$$

where a is a constant equal to $1 + (R_D - 1)/(1 - s_r^{N_\xi - 1})$. The coefficient s_r represents the stretching factor of the grid. Points in computational space are equispaced and given by:

$$\xi_i = i - 1 \quad i = 1, \ldots, N_\xi \tag{172}$$

The mapping $r(\xi)$ can equivalently be written as:

$$r(\xi) = 1 + (R_D - 1)\frac{1 - s_r^{\xi}}{1 - s_r^{N_\xi - 1}}. \tag{173}$$

Substituting the expression for ξ_i, it follows that $r_{i+1} - r_i = \Delta r_{i+1} = (1+a)(1-s_r)s_r^{i-1}$. The discrete grid stretching is thus defined by the geometric series $\Delta r_{i+1} = s_r \Delta r_i$ when s_r is constant. Note that the Jacobian of the mapping $r(\xi)$ is a smooth function:

$$\frac{\partial r}{\partial \xi} = \frac{1 - R_D}{1 - s_r^{N_\xi - 1}}s_r^{\xi} \ln s_r. \tag{174}$$

The stretching factor s_r is fixed at a value of 1.03 in the steady flow computations at $Re = 20$. In laminar vortex shedding simulations, the coefficient s_r is itself a geometrically increasing function of downstream radial distance:

$$s_r(i) = s_1 + (s_2 - s_1)\frac{1 - s_1^{i-1}}{1 - s_1^{N_\xi - 1}} \quad i = 1, \ldots, N_\xi. \tag{175}$$

This formulation allows for slow stretching near the cylinder boundary characterized by s_1. The stretching continuously increases in the wake and reaches a value of s_2 near the outflow boundary. Values for s_1 and s_2 are given in tables 9, 10 and 11.

C.2.2   Azimuthal Point Distribution

Azimuthal points in the steady simulations are equispaced:

$$\theta(\eta) = 2\pi \frac{\eta}{N_\eta} \tag{176}$$

with

$$\eta_j = j - 1 \quad j = 1, \ldots, N_\eta. \tag{177}$$

In the shedding cases, grid points are selectively distributed in two separate zones representing the potential region and the wake layer. The grid boundary, or envelope, of the wake layer in the plane of mean motion (x, y) is defined analytically by a line extending from the cylinder surface to the domain outer boundary, parametrized as $(x(t), y(t))$ where t is a positive continuous parameter. This line is normal to the cylinder surface at position $(\cos\theta_0, \sin\theta_0)$, and reaches the outer boundary at $(R_D \cos\theta_1, R_D \sin\theta_1)$, where R_D is the computational domain radius, θ_0 and θ_1 are free parameters. The wake-layer half width at each radial position is $y(t)$. Within the wake layer, a given number $N_{\eta\,\mathrm{wake}}$ of azimuthal points are equispaced.

Expressions for $x(t)$ and $y(t)$ are derived by considering a particle traveling in space and subjected to an acceleration. At time $t = 0$, its position and velocity are $(\cos\theta_0, \sin\theta_0)$ and $(U_0, U_0 \tan\theta_0)$ respectively. The location of this particle as a function of time is:

$$\begin{cases} x(t) = (R_D \cos\theta_1 - \cos\theta_0 + U_0)t^2 - U_0 t + \cos\theta_0 \\ y(t) = (R_D \sin\theta_1 - \sin\theta_0 + U_0 \tan\theta_0)t^2 - U_0 \tan(\theta_0)t + \sin\theta_0 \end{cases} \tag{178}$$

Although this envelope could be used to define the wake layer, its growth downstream of the cylinder $(y(t))$ is only proportional to t^2. However, a desirable property of the grid is rapid stretching in all spatial directions, which enhances the numerical dissipation of the energetic scales of motion, downstream of the part of the wake which

is resolved in the computation. The downstream radial distance up to which the wake is resolved is denoted by R_{wake} in the following. The width of the wake envelope can be made to grow exponentially fast provided the t^2 term appearing in the expression for $y(t)$ is replaced by $(e^{bt} - 1 - bt)/(e^b - 1 - b)$ where b is a free parameter which, together with U_0, controls the width and growth-rate of the envelope. The resulting expression for $y(t)$ is

$$y(t) = (R_D \sin \theta_1 - \sin \theta_0 + U_0 \tan \theta_0)\frac{e^{bt} - 1 - bt}{e^b - 1 - b} - U_0 \tan(\theta_0)t + \sin \theta_0. \qquad (179)$$

The grid generation parameters used at Reynolds numbers 80 and 100 are displayed in tables (9) and (10). In simulations at Reynolds number 80, the envelope equations (178) were used exclusively. This is the reason for which no values of the parameter b are indicated in table (9). The exponential growth of the wake envelope is a feature used in the simulations at Reynolds number 100.

Figure (78) displays the wake envelope in a grid constructed with parameters $U_0 = -2$, $b = 10$, $\theta_0 = 85$ and $\theta_1 = 20$. The same envelope in the near-wake region is shown in figure (79). The wake width grows as the square root of radial distance in the vicinity of the cylinder, and exponentially fast in the downstream wake.

C.3 Grids for Turbulent Simulations

C.3.1 Azimuthal Point Distribution

The construction of computational grids for the turbulent simulations presented in Chapter 4 and Appendix F is based on the 'wake envelope' described in the previous section. The grid is equispaced within the envelope. The one exception to this approach is the $(174 \times 128 \times 48)$ mesh described below. In that grid, the azimuthal resolution was increased by 50% in the separated shear layer regions ($40^o \leq |\theta| \leq 80^o$).

C.3.2　Radial Point Distribution

In the radial direction, points are distributed according to (171), in which s_r is a function of radial distance, defined separately in three regions. Matching at the region interfaces ensures that the mapping from physical to computational space has smooth Jacobians. These three regions are defined by 5 parameters: fixed stretching ratios at the cylinder surface and outer computational domain boundary, (s_1) and (s_2) respectively, a prescribed maximum grid spacing (Δ_{wake}) which cannot be exceeded within (R_{wake}) radii downstream, and the grid-spacing at the cylinder surface (Δr_{wall}).

In the first zone, the grid spacing Δr grows geometrically from its wall value Δr_{wall} to a level close to its wake value Δ_{wake} at a rate imposed by the stretching s_1. The grid then becomes equispaced in the second zone, for $r \leq R_{\text{wake}}$. In the outflow, or third zone, the grid spacing increases geometrically from Δ_{wake}, with a stretching ratio which increases with radial distance from 1 to s_2. The radius of the computational domain is determined by the total number of radial points available.

The radial increment distribution $\Delta r(r)$ is displayed in figure (80) for the mesh containing 116 radial points with the corresponding stretching ratio distribution:

$$s_r(r_i) = \frac{\Delta r_{i+1}}{\Delta r_i} \quad i = 1, \cdots, N_\xi - 1 \tag{180}$$

in the near-wake. The grid spacing is $\Delta r_{\text{wall}} = 0.005 R_c$ at the wall and first increases geometrically with a stretching factor $s_1 = 1.1$. In the resolved wake region extending to $R_{\text{wake}} = 10 R_c$, the increment Δr is close to the prescribed maximum value of $\Delta_{\text{wake}} = 0.25 R_c$ at locations past 2 cylinder diameters downstream. Beyond the resolved region, at distances $r \geq R_{\text{wake}}$, the grid stretches geometrically with a stretching factor increasing from $s_1 = 1$ to a maximum of $s_2 = 1.22$. In this example, the unresolved outflow region, extending from 5 diameters downstream to the outer boundary at $r = 198.62 R_c$, contains 26% of the total number of grid points.

C.3.3　Grid Configuration Summary

This section describes the geometric layout of each mesh used for turbulent simulations. The relationship between grid characteristics and physical flow features is

examined in the subsequent Section.

The wake envelope and near-wake parameters defining the grids used in turbulent simulations are listed in tables (11) and (12).

The mesh refinement study presented in Appendix F involves grids containing $(88 \times 90 \times 32)$, $(88 \times 90 \times 48)$, $(116 \times 136 \times 48)$ and $(174 \times 128 \times 48)$ points in the radial, azimuthal and spanwise directions respectively. The spanwise box size is $L_z = 2\pi R_c$ in all cases. The corresponding grid configurations in the near wake are displayed in figures (81) through (83). The exponential growth of the wake envelope is illustrated in the case of the $(116 \times 136 \times 48)$ mesh, shown for the entire computational (ξ, η) plane in figure (84).

The $(116 \times 136 \times 48)$ mesh features a 50% uniform increase in azimuthal resolution and a 100% increase in the radial resolution of the cylinder boundary layer and resolved near-wake over the $(88 \times 90 \times 48)$ mesh. The mean boundary-layer velocity distribution on the upstream side of the cylinder is found to be identical for both simulations on meshes with 90 and 136 azimuthal points, as discussed in Appendix F. The finest $(174 \times 128 \times 48)$ mesh is thus constructed with the same azimuthal point distribution in the potential region, outside the 'wake envelope', as that used on the $(88 \times 90 \times 48)$ point mesh, while the azimuthal resolution is increased by 50% in the separated shear-layer regions. In the cylinder boundary-layer and the downstream recirculation region, the radial resolution is increased by 100%. The resolved wake region is extended by 40% to 7 diameters downstream, and its radial resolution is 50 percent finer than on the $(116 \times 136 \times 48)$ mesh. Since the spatial differencing scheme is globally fifth-order accurate, mesh refinements by 50% and 100% in a spatial direction represent decreases of the corresponding leading truncation error by factors of 7.6 and 32 respectively.

Section F.4.1 of Appendix F discusses a test carried out to evaluate the impact which stretching the grid radially in the resolved wake region has on the mean velocities and eddy viscosity. The $(106 \times 136 \times 48)$ grid used for this test is identical to the $(116 \times 136 \times 48)$ mesh described above, except that between 1 and 5 diameters downstream of the cylinder, the grid stretches geometrically with a factor of 1.02 in the radial direction. Radial increment distributions $\Delta r(r)$ for the unstretched and

stretched test-meshes are presented in figure (85) with the corresponding stretching ratio distributions $s_r(r)$.

The final grid selected for large-eddy simulations contains $(144 \times 136 \times 48)$ radial, azimuthal and spanwise points. This grid in the (ξ, η) plane is displayed in figure (86).

C.3.4   Physical Flow Features and Grid Selection

The features of all grids used in turbulence simulations are governed by four principal length scales: the cylinder boundary-layer thickness, the free shear-layer thickness, the size of the vortices shed from the cylinder and the downstream growth of the wake layer.

The boundary-layer thickness on the upstream side of the cylinder is measured by the thickness of the vorticity layer δ_ω. On a radial line ($\theta = $ constant), δ_ω is defined as the distance from the wall at which the vorticity magnitude, denoted by Ω_z, equals 1% of its maximum value:

$$\Omega_z(r = \delta_\omega) = 0.01 \max_{1 \le r \le R_D} \Omega_z(r). \tag{181}$$

Because the surface boundary-layer separations and the downstream wake have a substantial impact on the pressure distribution on the cylinder surface, simplified momentum integral techniques cannot provide accurate estimates of the vorticity thickness distribution. Approximate values of δ_ω are thus obtained from the most accurate simulation, performed on the $(174 \times 136 \times 48)$ mesh. Although the wake turbulence is not fully resolved in that simulation, the mean velocity distribution on the upstream face of the cylinder is found to be grid independent. Table (13) lists the vorticity thickness, as well as the number of radial points in each grid within the vorticity layer, at several azimuthal positions. The angle θ in that table has its origin at the downstream mean stagnation point ($x = R_c, y = 0$) and is positive in the anti-clockwise direction. The final grid selected $(144 \times 136 \times 48)$ has 30 radial points in the boundary layer at the top of the cylinder ($\theta = 90°$), and about 14 points across the layer at the forward stagnation point.

158

Cardell (1993) experimentally documented the width of the free shear layers at Reynolds numbers 4,800 and 9,500. The mean width δ_s and vertical position y_s of the shear layers are roughly identical close to the cylinder at both Reynolds numbers. At $(x = 0.5D, y_s \simeq 0.6D)$, $\delta_s \simeq 0.15D$. At $x \simeq 2D$ and $Re = 4,800$, the boundaries of the shear layers emerging from the top and bottom halves of the cylinder meet at the wake center and $\delta_s \simeq 0.8D$. At $Re = 9,500$ the shear-layer edges meet at $x \simeq 1.6D$, and the local δ_s is also about $0.8D$. These data lead us to expect that at $Re = 3,900$, the shear layers grow from about $\delta_s \simeq 0.15D$ at $(x = 0.5D, y_s \simeq 0.6D)$ to $\delta_s \simeq 0.8D$ near the bubble closure point. Interpolating Cardell's data, the closure point lay at $x/D = 1.83 \pm 0.2$ at $Re = 3,900$. Table (14) lists the number of vertical grid points across the shear layers at $x/D = 0.5$ and $x/D = 2$. The $(144 \times 136 \times 48)$ mesh contains 9 and 16 points across the shear layers at these respective locations.

The number of grid points per cylinder diameter in all three directions in the wake is listed in table (15). In the (ξ, η) plane of mean motion, the numbers shown represent grid-point densities at the radial limit of the resolved wake region $(r = R_{\text{wake}})$. The azimuthal resolution at that location is the coarsest within the resolved region, since the wake-grid grows with the wake layer.

At Reynolds number 3,900, the Kolmogorov length scale (l_K) at locations $x/D = 5$, 7 and 10 are displayed in table 16. The grid spacing in Kolmogorov units ten diameters downstream for the final grid selected is 27.2, 8.7 and 6.5 in the streamwise, vertical and spanwise directions respectively.

The wake-grid, discussed in Section C.2.2, grows downstream with the square-root of radial distance. The adequacy of the chosen wake-envelope growth was confirmed by visual inspection of the flow field. Figure (87) displays the instantaneous spanwise-averaged streamwise, vertical and spanwise intensity contours, obtained from the $(174 \times 128 \times 48)$ simulation. These contours are superposed onto the (ξ, η) grid and the wake envelope is clearly seen to encompass the volume of active turbulence.
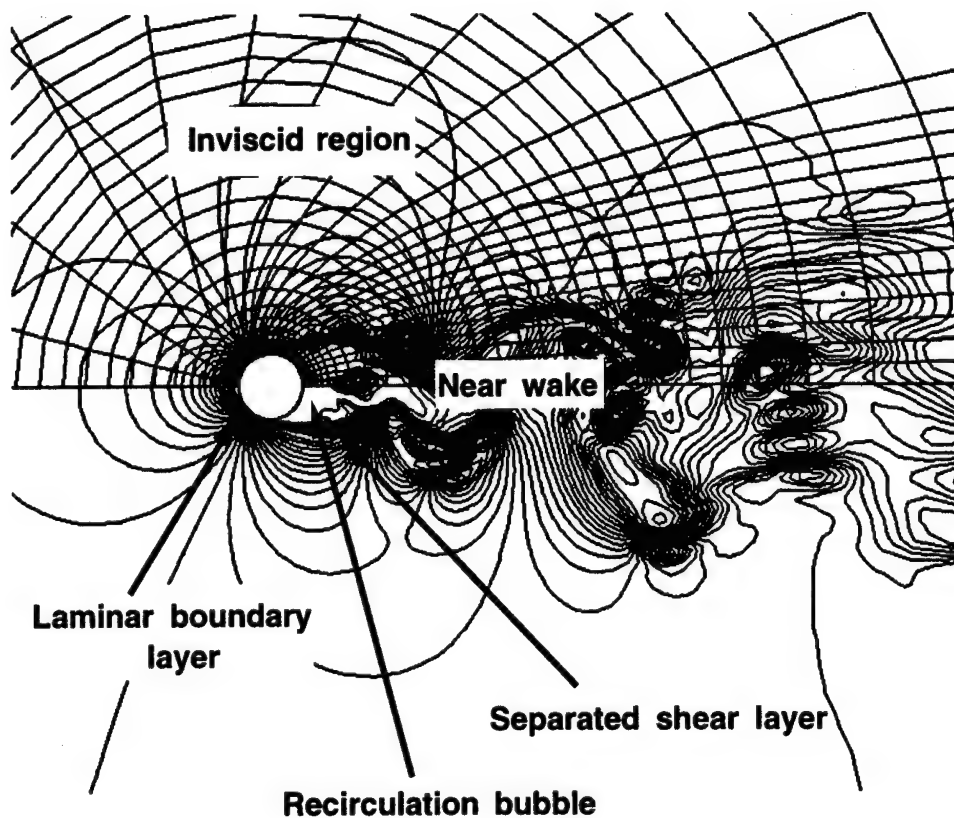
Figure 77: Diagram of near-wake structure
Snapshot of streamwise velocity contours at a given instant in time
from $116 \times 136 \times 48$ simulation at $Re = 3,900$.
Top half of (ξ, η) grid is shown with skipped grid-lines in radial and azimuthal directions.

160

Grid	Mesh size (r,θ)	s_1	s_2	U_0	θ_0	θ_1	$N_{\eta_{\text{wake}}}$	$\Delta r_{\text{wall}}/R_c$
1	65×65							1.5930
2	129×65							0.2087
3	200×65						32	0.0251
4	256×65	1.03	1.03	0	90	90		0.0048
5	320×65							
6	320×97		1.1				48	0.00072
7	320×127		1.03				64	
8	320×122		1.1	-20	75	6	94	

Table 9: Grid construction parameters at Re= 80

Grid	Mesh size (r,θ)	s_1	s_2	U_0	b	θ_0	θ_1	$N_{\eta_{\text{wake}}}$	$\Delta r_{\text{wall}}/R_{\text{c}}$
1	129×81							40	
2	129×121						7	80	0.2078
3	129×141	1.03	1.1	-5	10	85			
4	200×141						30	100	0.0250
5	256×141								0.0048
6	300×171							130	0.0013

Table 10: Grid construction parameters at Re= 100
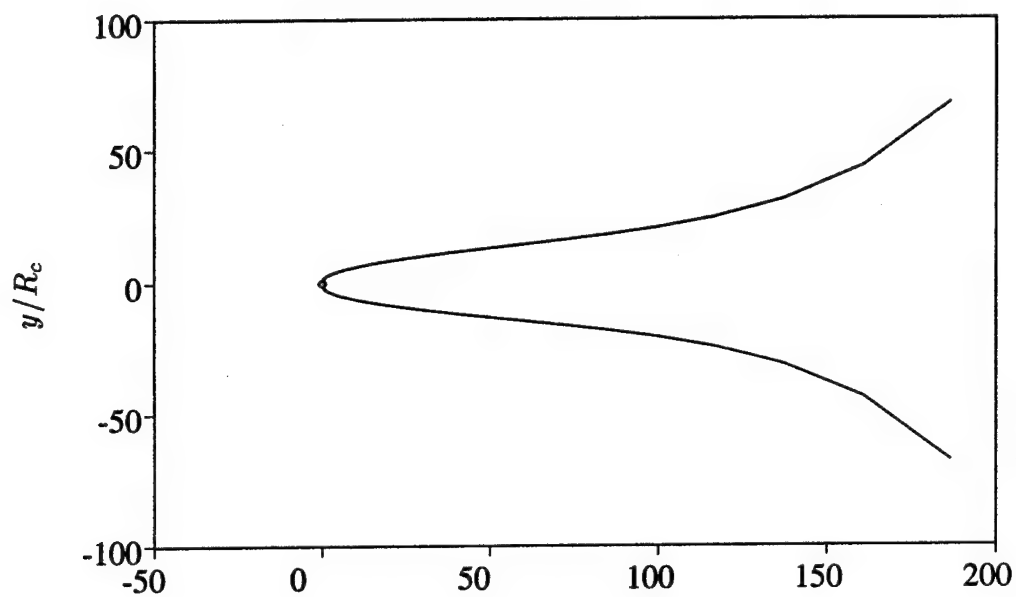
Figure 78: Wake envelope configuration
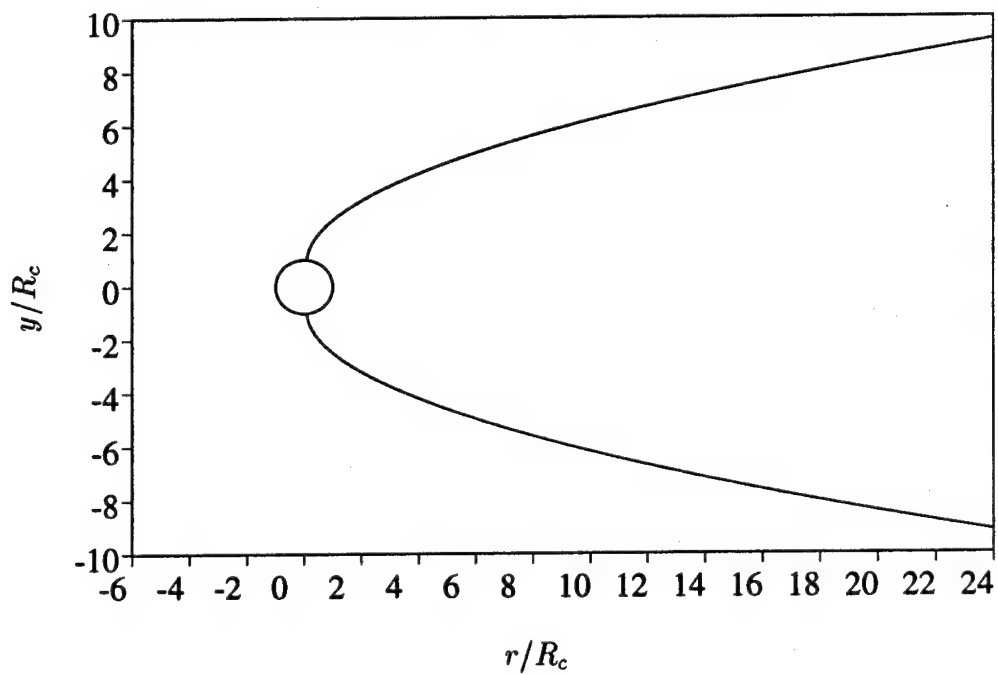
Figure 79: Near-wake envelope
Construction parameters: $U_0 = -2$, $b = 10$, $\theta_0 = 85$, $\theta_1 = 20$

163
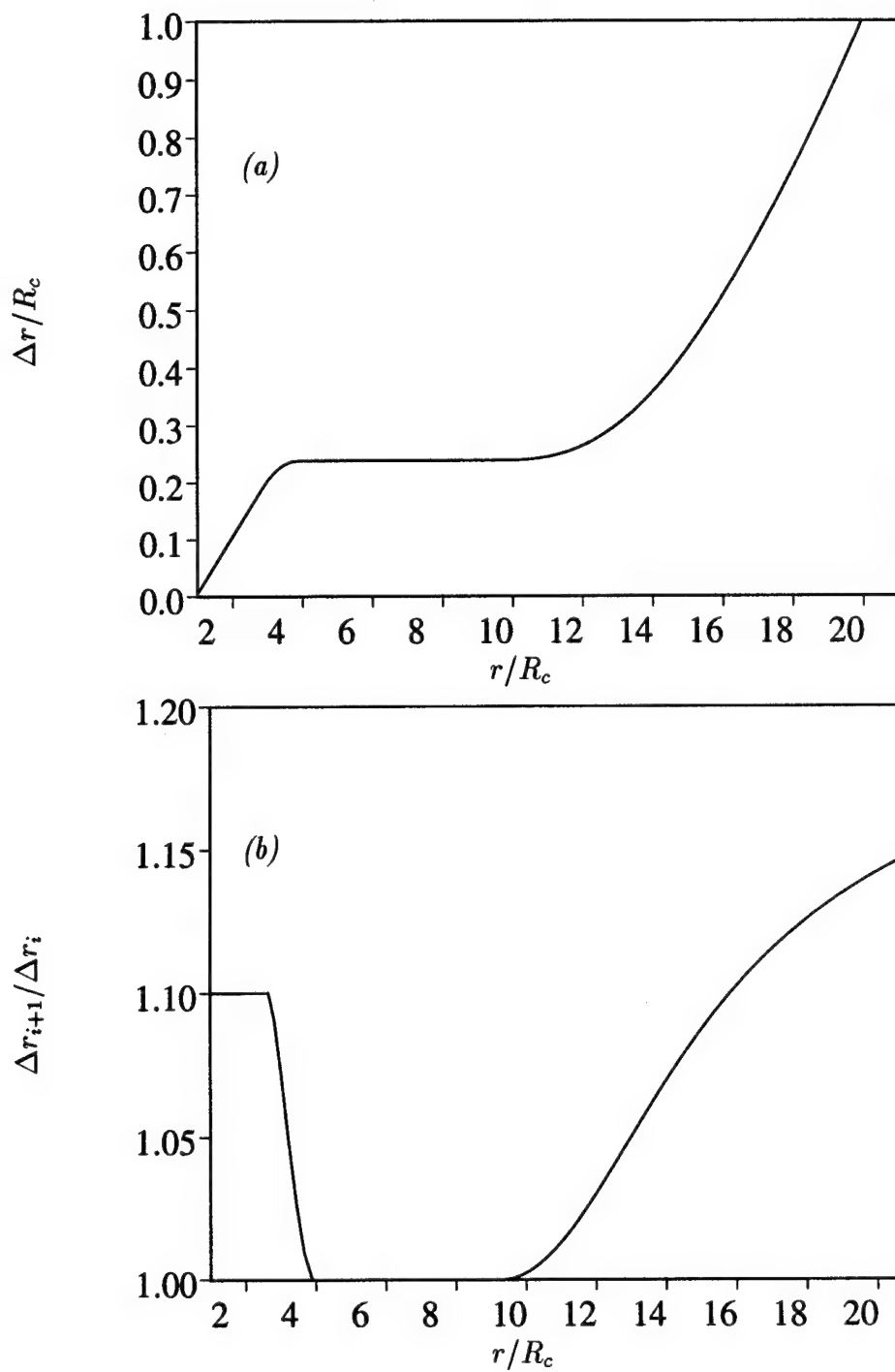
Figure 80: Near-wake radial spacing (a) and stretching ratio (b) distributions for the 116 × 136 planar mesh

Grid		Mesh size (r, θ)	U_0	b	θ_0	θ_1	s_1	s_2	R_D/R_c
Purpose	Number								
Grid refinement study	1,2	88×90	-2	10	85	20	1.1	1.22	139.06
	3	116×136	-2	10	85	20	1.1	1.22	198.62
	4	174×128	1.5	10	100	20	1.05	1.20	65.27
Test impact of radial grid stretching in wake		106×136	-2	10	85	20	1.1	1.22	176.07
Final grid selected		144×136	-2	10	85	20	1.1	1.22	127.41

Table 11: Grid parameters for wake envelope construction
(Turbulent simulations)

Mesh size (r, θ, z)	$N_{\eta_{\text{wake}}}$	$\Delta r_{\text{wall}}/R_c$	R_{wake}/R_c	Δ_{wake}/R_c
$88 \times 90 \times 32$ and $88 \times 90 \times 48$	50	0.01	10	0.5
$106 \times 136 \times 48$ and $116 \times 136 \times 48$	75	0.005	10	0.25
$174 \times 128 \times 48$	90	0.0025	14	0.17
$144 \times 136 \times 48$	75	0.0025	21	0.25

Table 12: Parameters defining the resolved wake region
(Turbulent simulations)
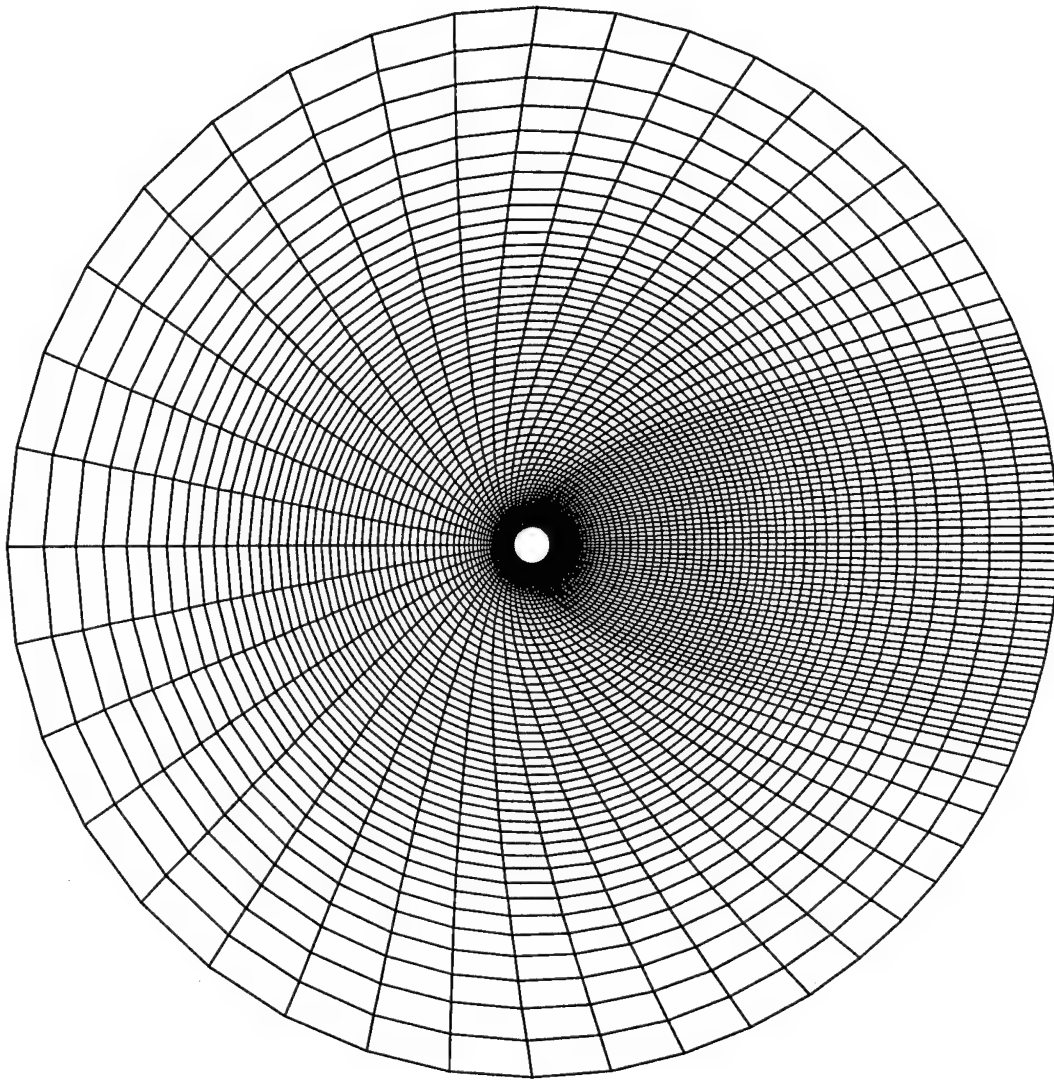
Figure 81: $88 \times 90 \times 32$ and $88 \times 90 \times 48$ meshes within $13D$ of the cylinder
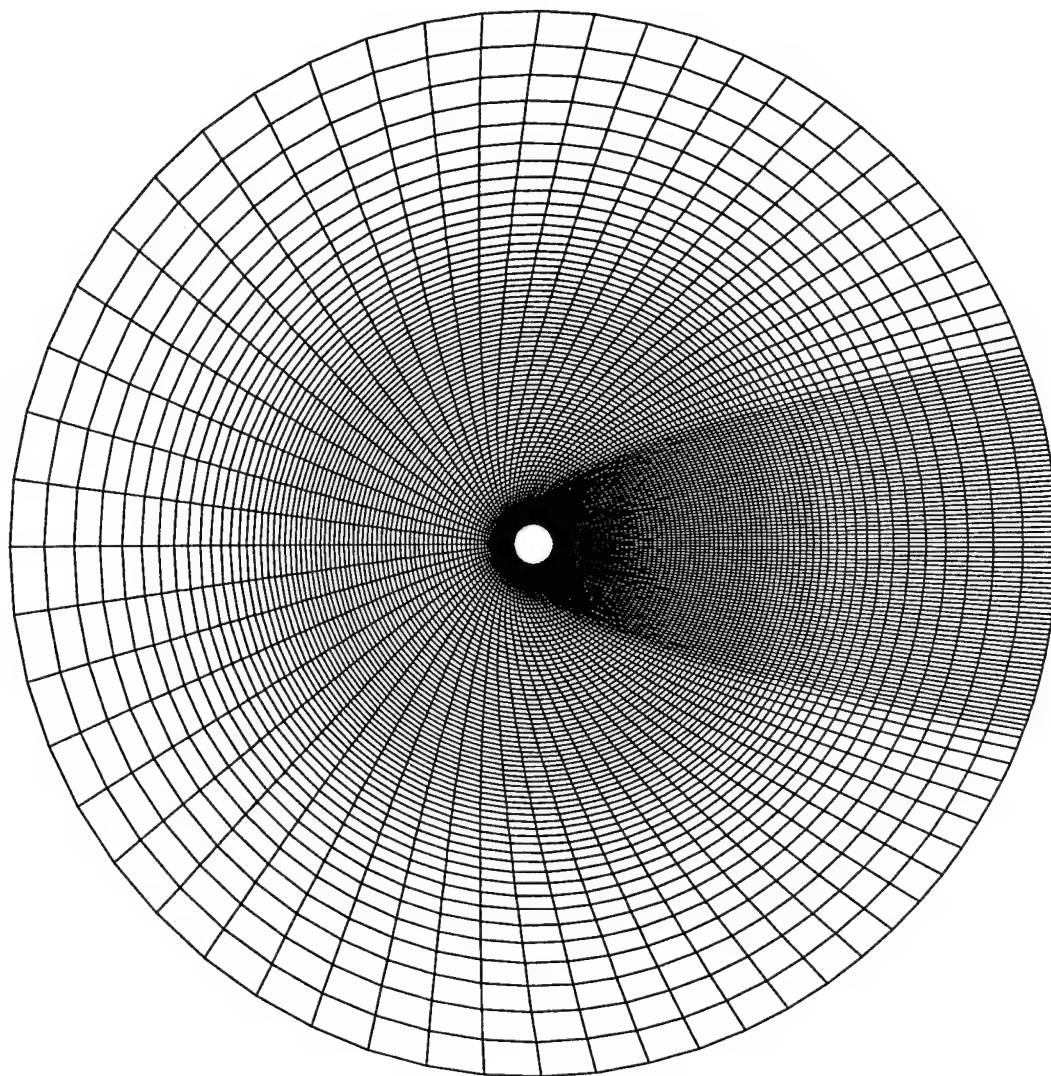
Figure 82: $116 \times 136 \times 48$ mesh within $13D$ of the cylinder
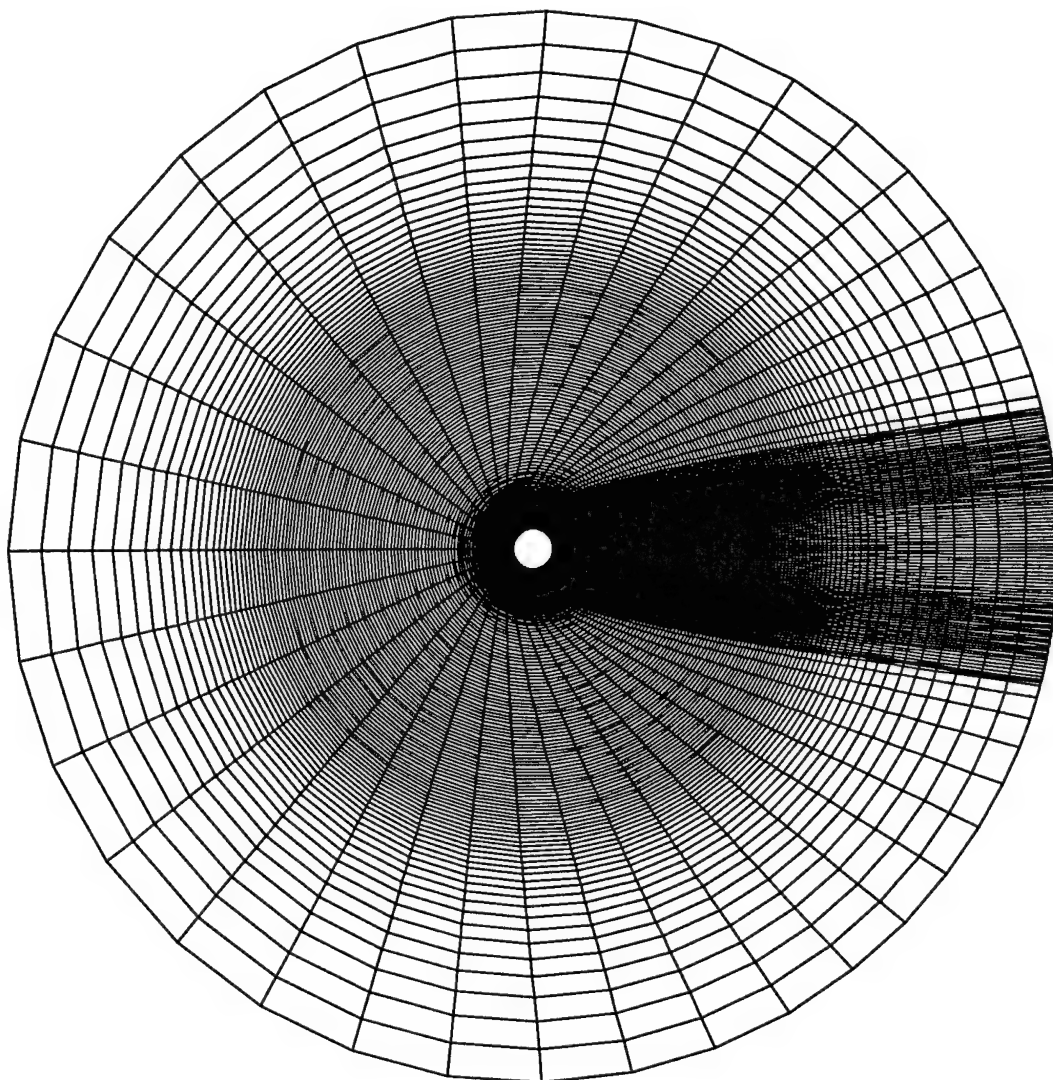
Figure 83: $174 \times 128 \times 48$ planar grid within $13D$ of the cylinder
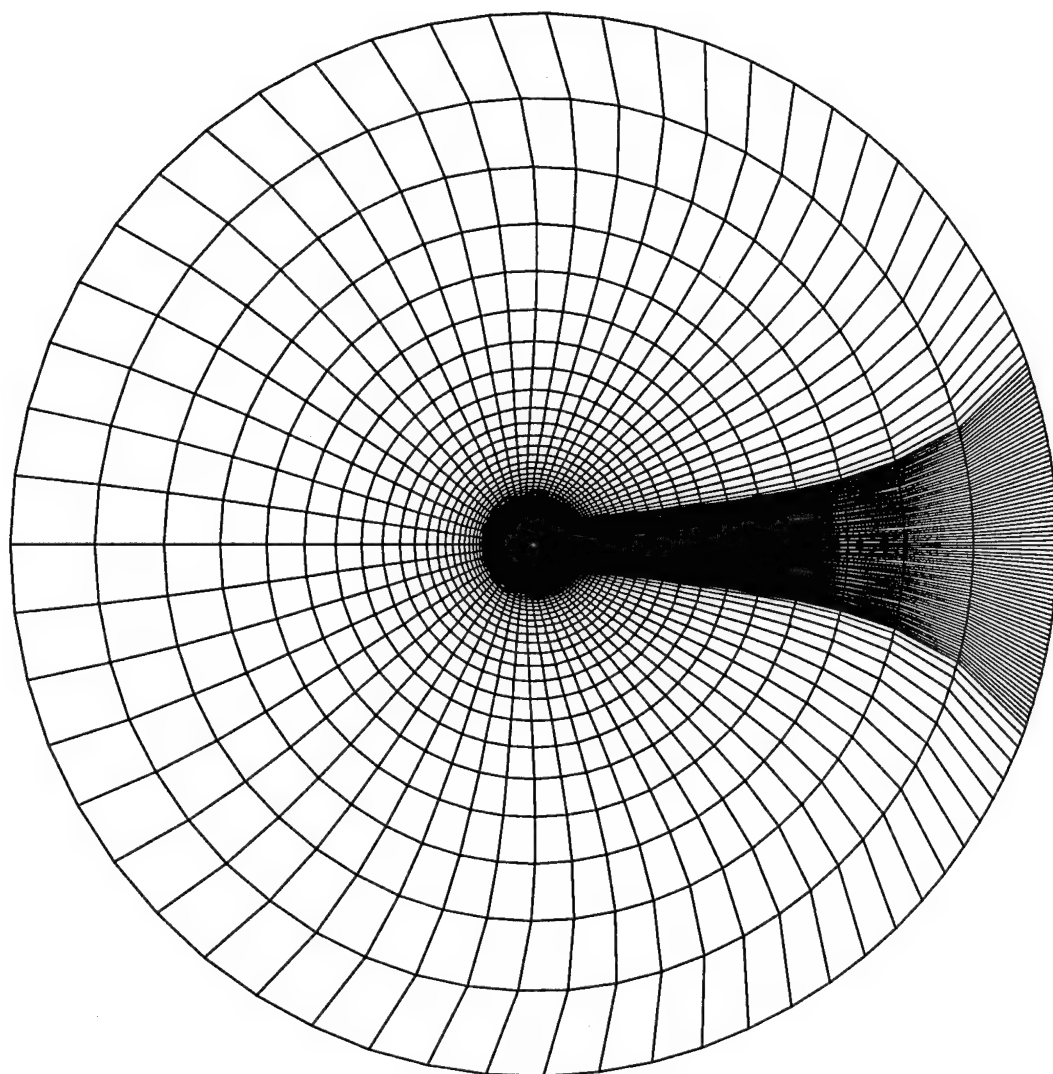
Figure 84: 116×136 mesh on the entire domain
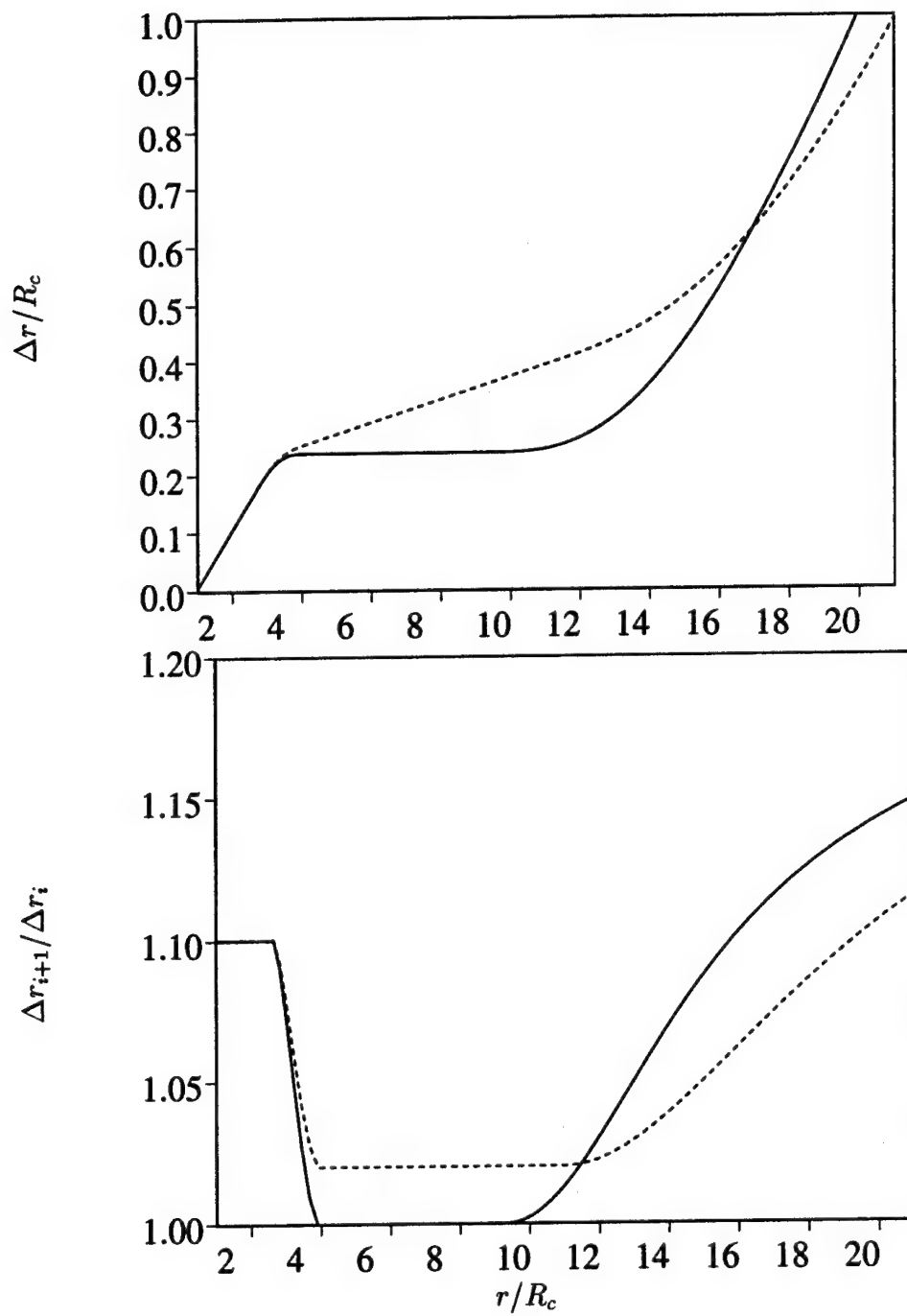
Figure 85: Near-wake radial spacing (top) and stretching ratio (bottom) distributions for stretched and unstretched meshes in the wake

—— : No stretching ($116 \times 136 \times 48$); ---- : stretched ($106 \times 136 \times 48$)
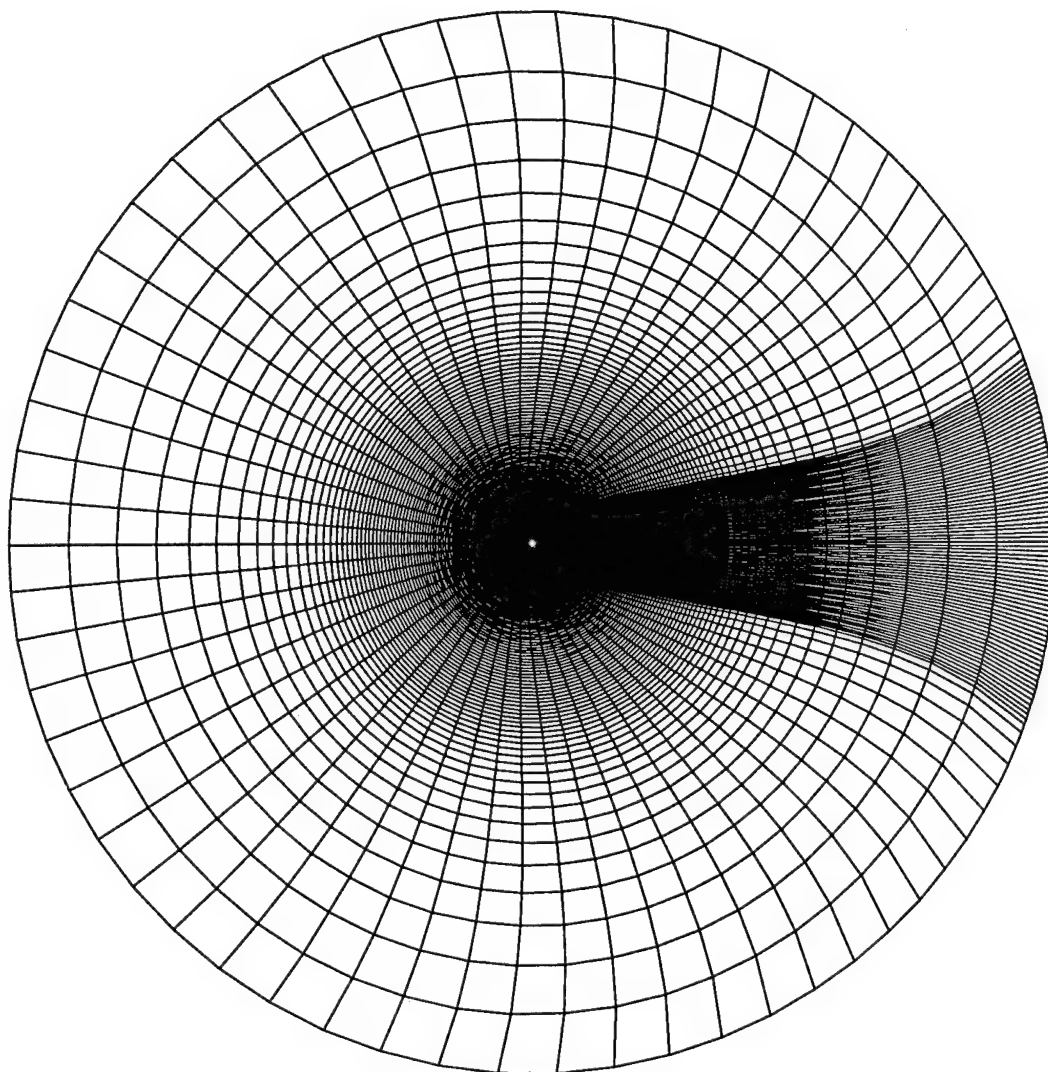
Figure 86: $144 \times 136 \times 48$ grid on the entire domain

Angle	Vorticity thickness	Grid size (r, θ)		
θ (deg.)	$\delta_\omega \times 100/R_c$	88×90	$(116, 106) \times 136$	174×128 & 144×136
90	16.0	11	16	30
110	9.0	8	12	22
130	6.1	6	9	17
150	5.3	5	8	16
170	4.6	5	7	14

Table 13: Radial grid points in surface boundary layer

Location	Layer thickness	Grid size (r, θ)		
x/D	δ_s/D	88×90	$(116, 106, 144) \times 136$	174×128
0.5	0.15	5	9	13
2.0	0.8	10	16	21

Table 14: Vertical grid points across free shear layers

| Grid size	Grid-point density at $r = R_\text{wake}$		
(r, θ, z)	radial	azimuthal	spanwise
$88 \times 90 \times 32$	4	7	10
$88 \times 90 \times 48$	4	7	15
$116 \times 136 \times 48$	8	12	15
$174 \times 128 \times 48$	12	16	15
$106 \times 136 \times 48$	6	12	15
$144 \times 136 \times 48$	4	12	15

Table 15: Grid-point density in the near wake

x/D	$10^3 \times l_K/D$	$\Delta x/l_K$	$\Delta y/l_K$	$\Delta z/l_K$
5	8.81	20.4	6.4	7.4
7	9.11	24.1	7.8	7.2
10	10.1	27.2	8.7	6.5

Table 16: Grid spacing, in Kolmogorov units, in the final grid selected

173
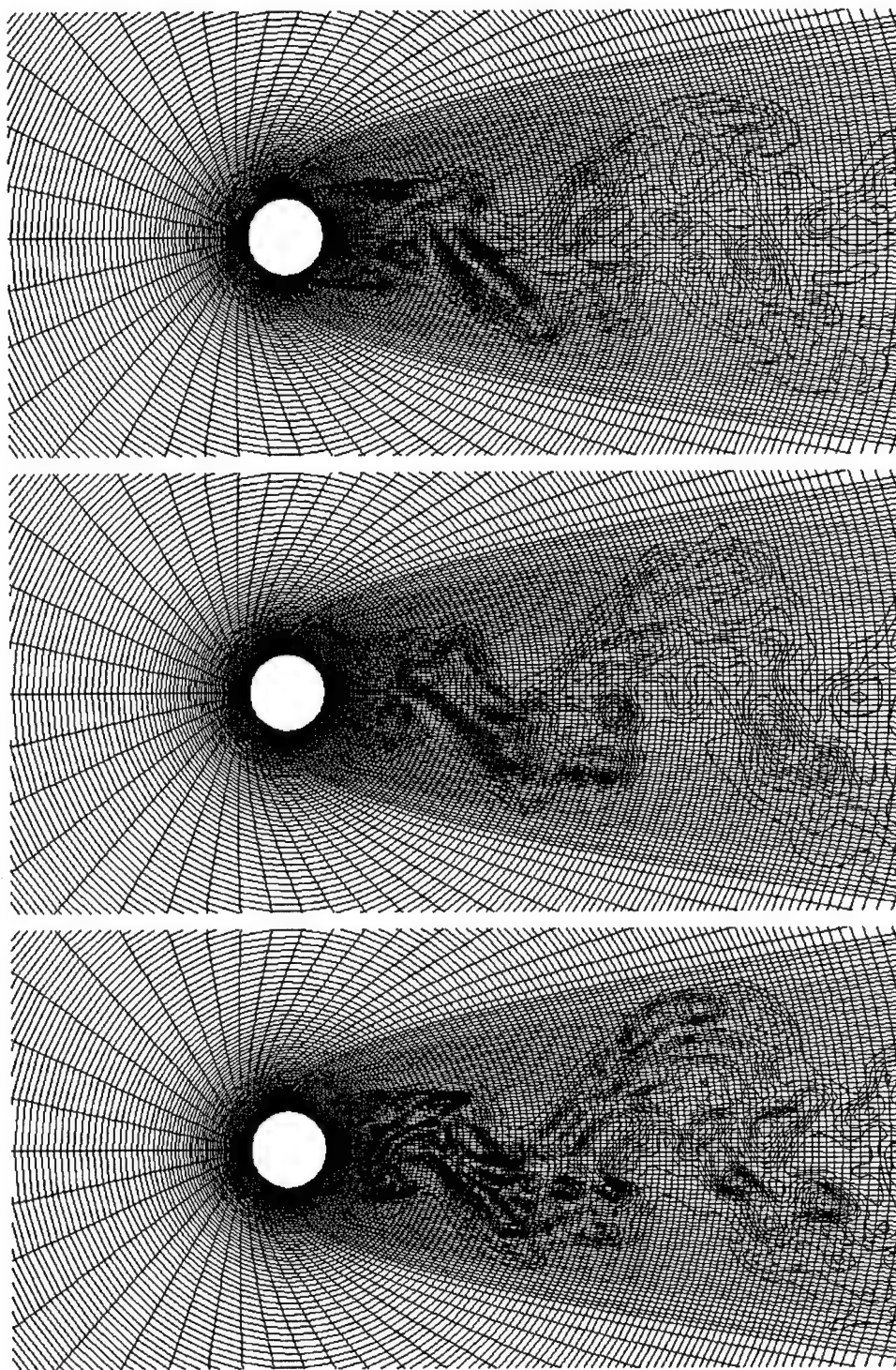
Figure 87: Instantaneous spanwise-averaged intensities at $Re = 3,900$
Illustration of the wake envelope adequacy using the $(174 \times 128 \times 48)$ simulation data
top: Streamwise; center: Vertical; bottom: Spanwise

174

Appendix D

Laminar Cylinder Flow Validations

D.1 Definitions

This section defines aerodynamic coefficients and numerical parameters of relevance in cylinder simulations. The pressure and viscous components of the drag coefficient are denoted by C_{D_p} and C_{D_v} respectively, and those of the lift coefficient as C_{L_p} and C_{L_v}. The total, spanwise-averaged lift and drag coefficients are the sum of these two contributions:

$$C_L = \frac{\text{Lift}}{\frac{1}{2}\rho_\infty U_\infty^2 2R_c L_z} = C_{L_p} + C_{L_v}, \quad C_D = \frac{\text{Drag}}{\frac{1}{2}\rho_\infty U_\infty^2 2R_c L_z} = C_{D_p} + C_{D_v} \quad (182)$$

with

$$C_{L_p} = -\frac{1}{M_\infty^2 L_z} \int_0^{L_z} \int_0^{2\pi} p \sin\theta \ \partial\theta\partial z$$

$$C_{L_v} = \frac{1}{Re M_\infty^2 L_z} \int_0^{L_z} \int_0^{2\pi} \left(\frac{4}{3}(u_\xi \cos\theta + v_\xi \sin\theta)\sin\theta + \Omega_{z_0}\cos\theta \right)\partial\theta\partial z$$

$$C_{D_p} = -\frac{1}{M_\infty^2 L_z} \int_0^{L_z} \int_0^{2\pi} p \cos\theta \ \partial\theta\partial z$$

$$C_{D_v} = \frac{1}{ReM_\infty^2 L_z} \int_0^{L_z} \int_0^{2\pi} \left(\frac{4}{3}(u_\xi \cos\theta + v_\xi \sin\theta)\cos\theta - \Omega_{z_0}\sin\theta\right)\partial\theta\partial z$$

where $\Omega_{z_0} = y_\eta v_\xi + x_\eta u_\xi$ is the vorticity at the wall and L_z is the spanwise box size. The Mach number M_∞ appears in these definitions because the reference velocity was chosen as the sound speed c_∞ (Chapter 2).

The Courant numbers used in this report are based on free-stream velocity ($CFL(U_\infty)$) or sound speed ($CFL(c_\infty)$) and are defined as:

$$CFL(c_\infty) = \max_{(x,y,z)} \left[\frac{|u|+c}{\Delta x} + \frac{|v|+c}{\Delta y} + \frac{|w|+c}{\Delta z}\right]\Delta t \qquad (183)$$

$$CFL(U_\infty) = \max_{(x,y,z)} \left[\frac{|u|}{\Delta x} + \frac{|v|}{\Delta y} + \frac{|w|}{\Delta z}\right]\Delta t \qquad (184)$$

where the 'max' operator extracts the maximum value of its argument in the entire computational domain.

D.2   Steady Flow at $Re = 20$

At Reynolds number 20, the flow around a circular cylinder is steady, and a pair of vortices is attached to the downstream side of the cylinder. This Section presents a study of the impact of domain size on the steady solution. It is shown that a small computational domain does not affect the velocity field in the vicinity of the cylinder, but that the pressure in the wake region is sensitive to the position of the outflow computational boundary. An appropriate domain radius for which the near-wake pressure and velocity are not affected by the boundary conditions is found to be about 300 cylinder radii. The steady solution on that domain is compared to experimental results in Chapter 3.

D.2.1   Effect of Computational Domain Size

The computational domain is a circle of radius R_D. In all simulations, the radial grid distribution stretches geometrically from the cylinder surface to the outer boundary with a stretching factor fixed at 1.03, while azimuthal grid points are equispaced.

176

Asymptotically far downstream of the cylinder the velocity defect on the wake centerline decreases as

$$u \sim \frac{1}{\sqrt{r}}. \qquad \qquad \cdot \qquad (185)$$

The effect of the body is thus felt at large distances downstream, so that extending the computational domain to distances where the influence of the cylinder is negligible is not practical. Since one cannot impose exact outflow boundary conditions in the wake region, the mismatch between flow physics and numerical constraints creates spurious pressure waves. However the mesh stretching near the outer boundary increases numerical dissipation, dampening these perturbations. The influence of the boundary conditions on the near wake is demonstrated on three different domains of size $R_D = 60R_c$, $120R_c$ and $300R_c$. The solutions are grid independent on each domain studied. For instance on the larger domain, simulations are performed with mesh sizes containing (129×104), (200×200) and (256×300) points in the radial and azimuthal directions respectively, to establish the grid-independence of the solution.

Figures (88) through (90) display several flow quantities computed on the different domains. The pressure coefficient and vorticity distribution at the wall (figures 88 and 89), which together determine the total drag on the cylinder, differ on the upstream side of the cylinder by a pointwise maximum of 2% on the $120R_c$ and $300R_c$ domains. Downstream of the separation point ($\theta \geq 0.75\pi$), on the portion of the cylinder wall facing the wake, both wall pressure coefficient and vorticity are independent of computational domain size.

The streamwise velocity on the rear flow symmetry axis (figure 90), is influenced by the domain size in a region extending from approximatly 10 diameters downstream to the outer domain boundary. In the near wake however, the velocity distributions obtained on the three domains are identical. The pressure coefficient on the rear flow axis, shown in the same figure, is the quantity most sensitive to domain size. On the smaller domain, the pressure overshoots and increases above its stagnation value. As the domain size increases, the overshoot diminishes and has disappeared on the larger domain. Based on these results, the domain chosen for all steady and unsteady laminar computations is a circle of radius $R_D = 300R_c$.

D.3 Laminar Vortex Shedding at $Re = 80, 100$

Two-dimensional computations at Reynolds numbers 80 and 100 are performed to establish the temporal accuracy of the numerical method. These simulations further test the far-field boundary condition performance in unsteady flow by examining whether the only energetic frequency is the primary wake frequency. Inaccuracies in outflow boundary conditions can generate modulating frequencies in the flow response (Don 1989).

Appendix C describes the family of grids on which all cylinder computations are performed. Simulation results at Reynolds numbers 80 and 100 are presented in Sections D.3.1 and D.3.2 respectively. It is shown that the Strouhal frequency converges, with grid refinement, to the experimental results of Williamson (1991) for two-dimensional vortex shedding. The performance of the iterative solver is evaluated in Section D.3.3 using the case of laminar vortex shedding at Reynolds number 100. The iterative scheme is shown to have good convergence properties in this case.

D.3.1 Vortex Shedding at Reynolds Number 80

Table (9) in Appendix C describes the grids used in the simulations at Reynolds number 80. Radial and azimuthal directions are refined separately in this study, while the computational domain radius is set to $300R_c$. Radial grid refinements are performed on 5 successive meshes. On these, the radial wall spacing decreases from $1.59R_c$ to $7.2 \times 10^{-4} R_c$, the stretching factors s_1 and s_2 are equal and fixed at 1.03, and the 65 total azimuthal points are equispaced. The angles defining both end points of the wake envelop are equal and set at 90 degrees, resulting in standard polar mesh configurations.

Azimuthal refinements of the wake envelop region are done on 3 additional grids, which contain respectively 48, 64 and 94 points across the wake layer. The last grid features a wake envelop similar to that presented in figure (78). It further uses a variable radial grid stretching ranging between 1.03 at the cylinder surface and 1.1 at the outer domain boundary.

Grid Number	CFL (U_∞)	CFL (c_∞)	$U_\infty\Delta t/R_c$	St
1		13	0.254	0.
2		6	0.118	0.137
3		12	0.060	0.148
4	1	39	0.037	0.149
5		225	0.033	0.150
6		178	0.026	0.152
7		154	0.022	
	0.5	72	0.010	0.152
8	1	154	0.022	

Table 17: Computed Strouhal number at Re= 80

CFL numbers and time-steps used on each grid are listed in table (17). The time step in each simulation was chosen to correspond to a velocity-based CFL number of 1. A time-step refinement performed on grid 7 compares solutions computed with CFL numbers of 1 and 0.5. It is worthwhile to note that in these two-dimensional simulations, the implicit time-marching scheme is stable and accurate for CFL numbers as high as 225.

On the coarsest mesh (65×65), no vortex shedding can be sustained ($St = 0$). As the grid-density increases at the cylinder surface, the Strouhal number reaches a value of 0.152. Figure 94 displays the evolution of the Strouhal number with grid refinement. It indicates that the value $St = 0.152$ is closely grid-independent. This result is in agreement with the experimental frequency of 0.153 documented by Williamson (1991).

On the densest mesh with (320×127) points, a reduction of the time-step by a factor of 2 does not affect the value of the computed Strouhal number. The simulation on the mesh (8) with the wake envelop shown in figure (78), accurately predicts the Strouhal frequency, demonstrating that selectively refining the wake layer, while maintaining the resolution in the potential region, does not affect the accuracy of the vortex shedding frequency at this Reynolds number.

The least-squares curve-fit of the lift coefficient (C_L) with a sine function is shown

Grid Number	CFL (U_∞)	CFL (c_∞)	$U_\infty\Delta t/R_c$	St
1		5	0.0782	0.153
2		6	0.0458	0.156
3	1	6	0.0364	0.157
4		5	0.0262	0.163
5		21	0.0201	0.164
6		61	0.0159	0.164

Table 18: Computed Strouhal number at Re= 100

in figure (93). The maximum pointwise error between C_L and the fitted curve is on the order of 10^{-4} smaller than the lift amplitude, indicating that no energetic mode other than the primary vortex shedding one is present. Modulation of the lift coefficient response by frequencies lower than the Strouhal frequency is a numerical problem which can arise because of inaccuracies in far-field boundary conditions (Don 1989).

Lift and drag coefficient decompositions into viscous and pressure components are shown in figures (91) and (92). At this Reynolds number, the skin-friction contributes appreciably to the total lift, and accounts for about one-third of the total drag.

D.3.2 Vortex Shedding at Reynolds Number 100

The grids used at Reynolds number 100 are described in table (10) (Appendix C). All feature an azimuthal wake envelop as well as variable radial grid stretching. The cylinder surface and outer boundary stretching factors are fixed at $s_1 = 1.03$ and $s_2 = 1.1$ respectively. Azimuthal refinements of the wake envelop are performed on grids containing 40, 80, 100 and 130 points across the wake layer. The radial spacing at the cylinder surface varies on the 6 grids from $0.2078R_c$ to $0.0013R_c$. The computational domain radius is fixed in all cases at $300R_c$.

The CFL numbers on each grid are summarized in table (18). Velocity-based CFL

Re	S_t	max C_{L_p}	max C_{L_v}	max C_{D_p}	max C_{D_v}
80	0.152	0.215	0.037	0.976	0.378
100	0.164	0.297	0.045	1.021	0.344

Table 19: Lift and drag maxima

numbers, fixed at 1 in each simulation, define the associated time-steps and sound-speed-based CFL numbers. The evolution of the Strouhal number with grid refinement is displayed in figure (98). In the most accurate simulation, the Strouhal frequency stands at 0.164, in agreement with the experimental value of 0.164 (Williamson 1991). Lift and drag coefficients are shown in figures (95) through (97). The contribution of the shear stress to both coefficients (table 19) is smaller at Reynolds number 100 than at Reynolds number 80. The maximum lift due to viscosity is 13% of the total lift at Reynolds number 100, and 15% at Reynolds number 80. The maximum skin-friction accounts in these same cases for respectively 25% and 28% of the total drag.

Figure (97) demonstrates, as in the case of Reynolds number 80, the fit of the lift coefficient response with a sinusoidal curve, and the absence of energetic low frequency modes.

D.3.3   Iterative Solver Performance

The performance of the iterative solver is tested in the computation of the Strouhal number at Reynolds number 100. The fourth grid described in table (10) is used to demonstrate the behavior of the residuals with two different time-steps. In both computations, the number of sub-iterations per time-step is set to 3. The two time-steps correspond to velocity-based Courant numbers of 1 and 0.5, or sound-speed Courant numbers of 5 and 2.5 respectively. A measure of convergence error in the solution at time-level n and sub-iteration p is the L_1 norm of the residual error $\|R^{n,p}\|_1$

(equation 73, Chapter 2), defined by:

$$\|R^{n,p}\|_1 = \int_0^{L_z} \int_0^{2\pi} \int_1^{R_D} |R^{n,p}| \, \partial r \partial \theta \partial z \qquad (186)$$

The decrease in this residual error at a given time level, expressed by the ratio of residual norms at the first and last iterations $\|R^{n,1}\|_1/\|R^{n,3}\|_1$, is an indicator of the performance of the iterative solver. Time evolutions of this ratio are displayed in figures (99) and (100) for each CFL number. Convergence at each sub-iteration is better for smaller time-steps, the norm of the residuals dropping faster than linearly with decreasing time-step. At CFL number of 5, all residuals drop by a factor of about $1,000$ in three iterations. At half the CFL number, the residuals drop by an additional factor of approximately 4.

The iterative method with three sub-iterations per time-step is approximately three times faster than a direct inversion method. Because of the modifications made to simplify the linearizing Jacobians (Chapter 2), the standard proof of quadratic convergence for a Newton scheme does not hold. Empirically, this scheme is found to be robust. The accuracy of mean surface quantities, including Strouhal number, drag and lift coefficients, does not seem unduly affected by fixing the number of iterations at 3, incurring at each time-step a finite residual error.
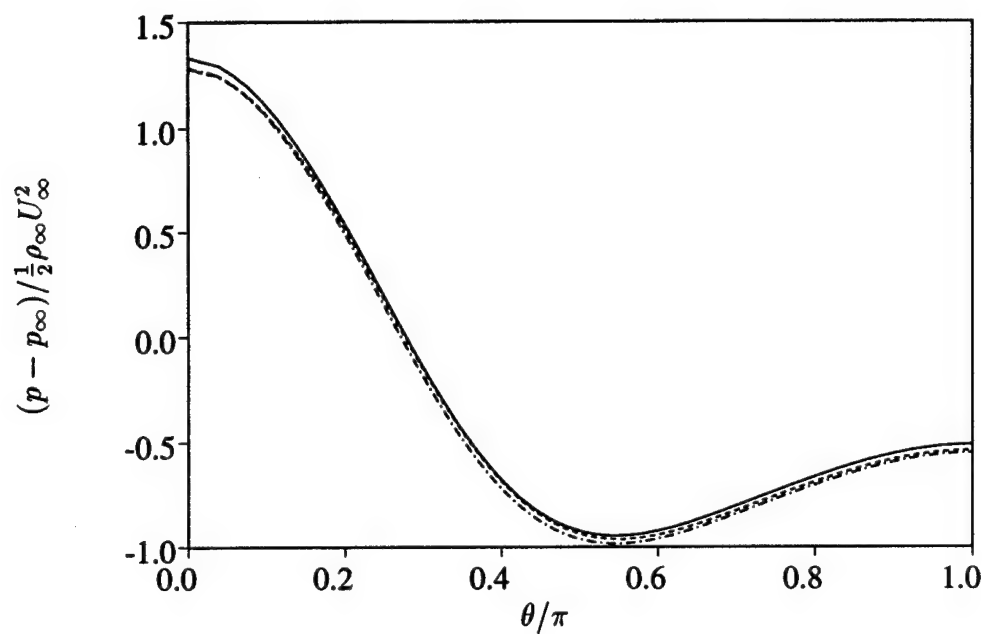
Figure 88: Re=20; Wall pressure coefficient

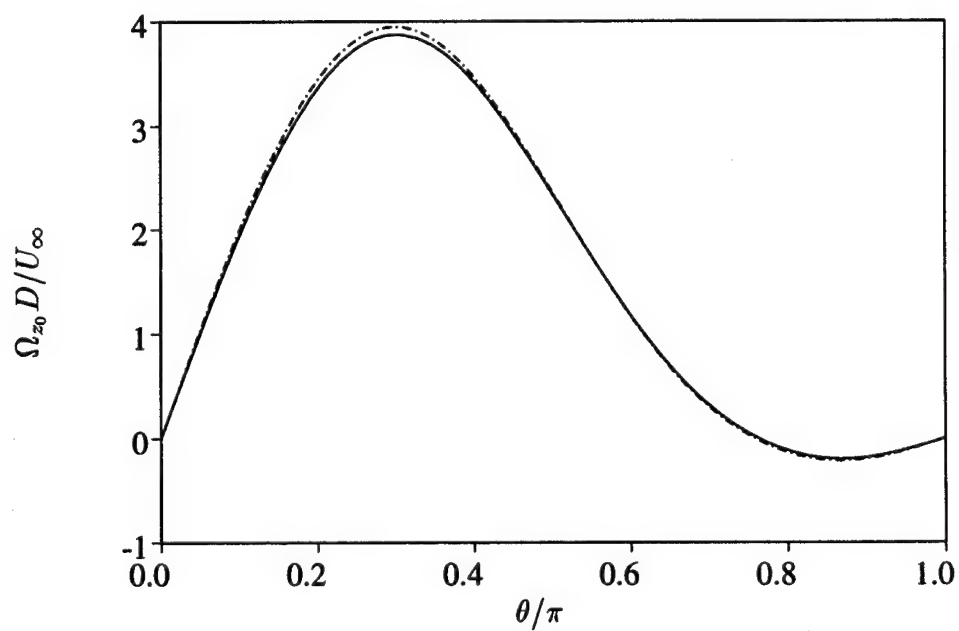Figure 89: Re=20; Wall vorticity

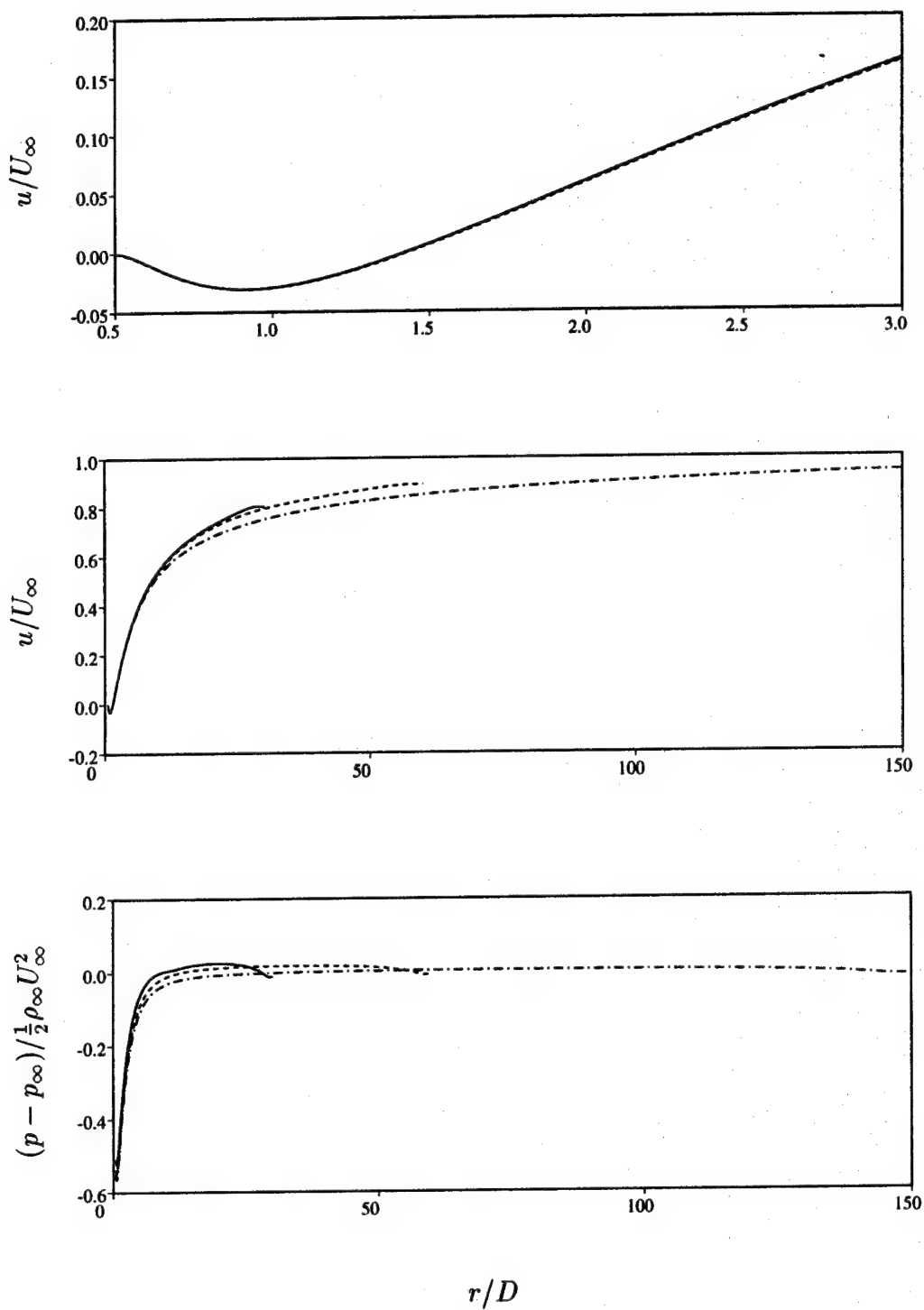——— : $R_D/R_c = 60$; ---- : $R_D/R_c = 120$; —·— : $R_D/R_c = 300$

Figure 90: Re=20; Rear axis streamwise velocity and pressure coefficient
——— : $R_D/R_c = 60$; - - - - : $R_D/R_c = 120$; —·— : $R_D/R_c = 300$

184

Figure 91: Re=80; Lift coefficient

---- : Pressure lift; $\cdots$: Viscous lift; —— : Total lift

Figure 92: Re=80; Drag coefficient

---- : Form drag; $\cdots$: Skin friction; —— : Total drag

185

Figure 93: Re=80; Strouhal frequency evaluation
—— : Computation; ● : Best sinusoidal fit
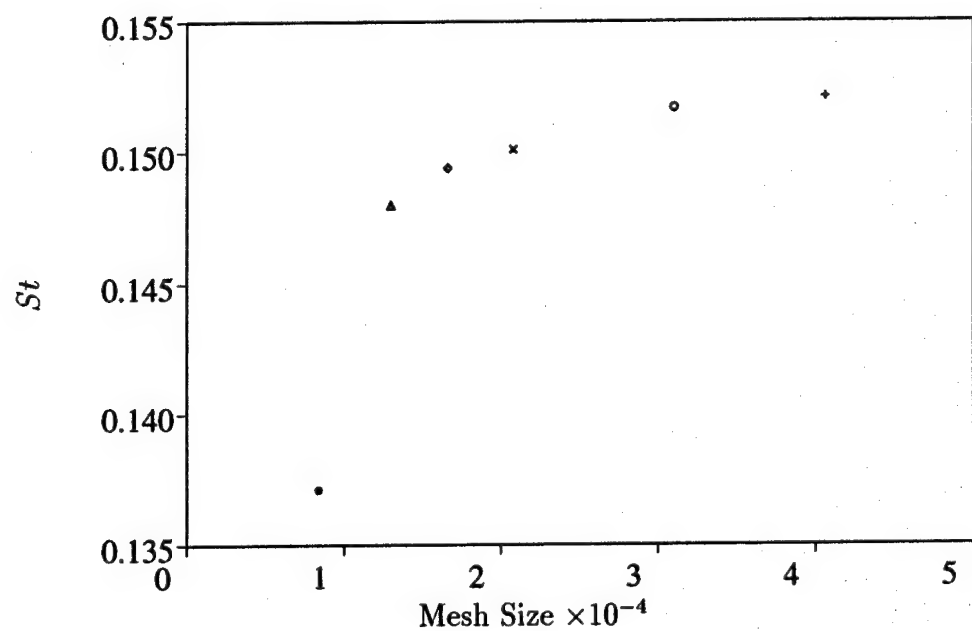
Figure 94: Re=80; Strouhal frequency convergence
● : 129 × 65; △ : 200 × 65; ◇ : 256 × 65
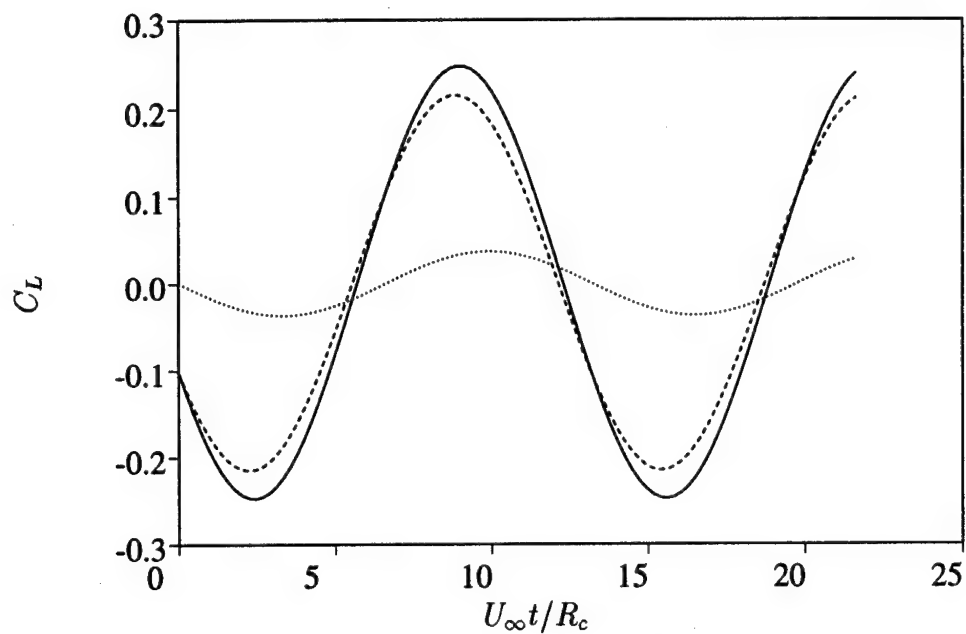× : 320 × 65; o : 320 × 97; + : 320 × 127
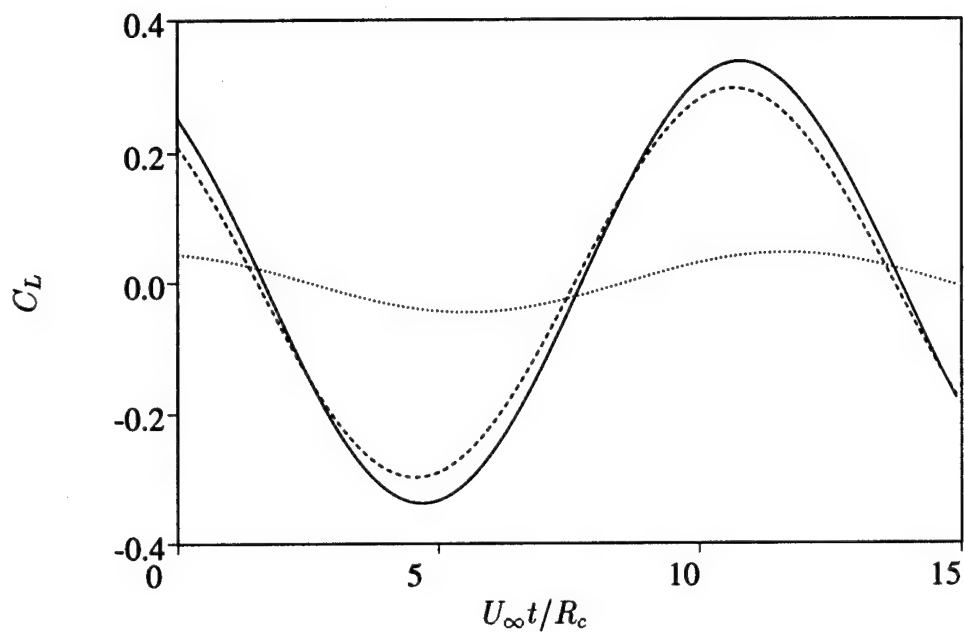
Figure 95: Re=100; Lift coefficient
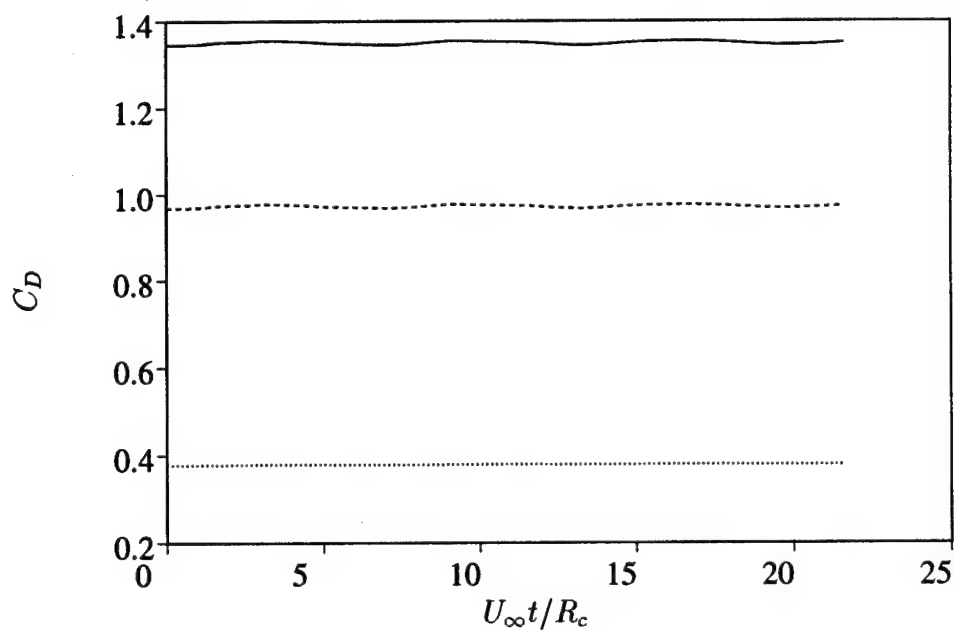---- : Pressure lift; ⋯ : Viscous lift; —— : Total lift
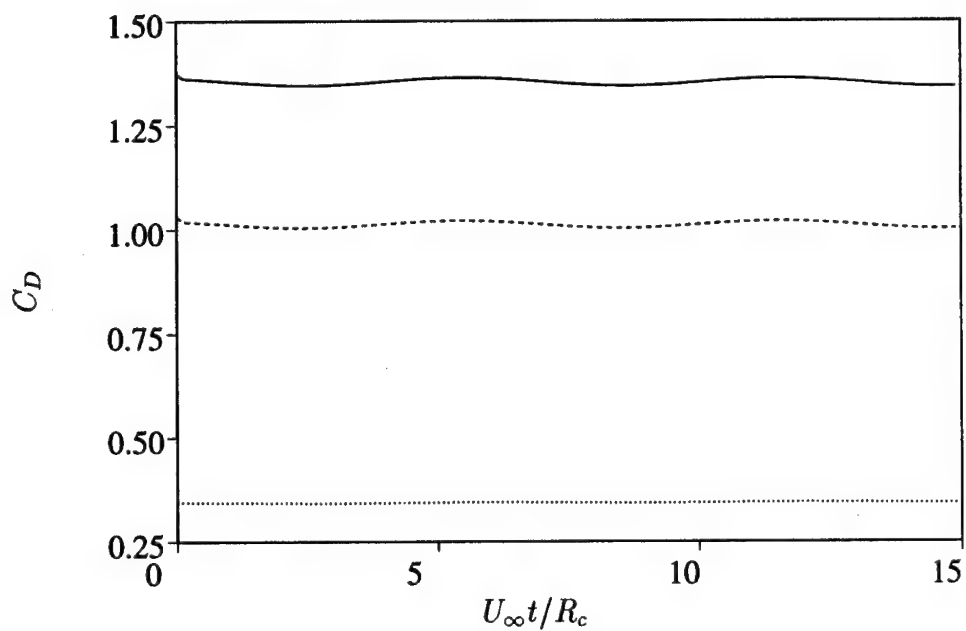
Figure 96: Re=100; Drag coefficient
---- : Form drag; ⋯ : Skin friction; —— : Total drag
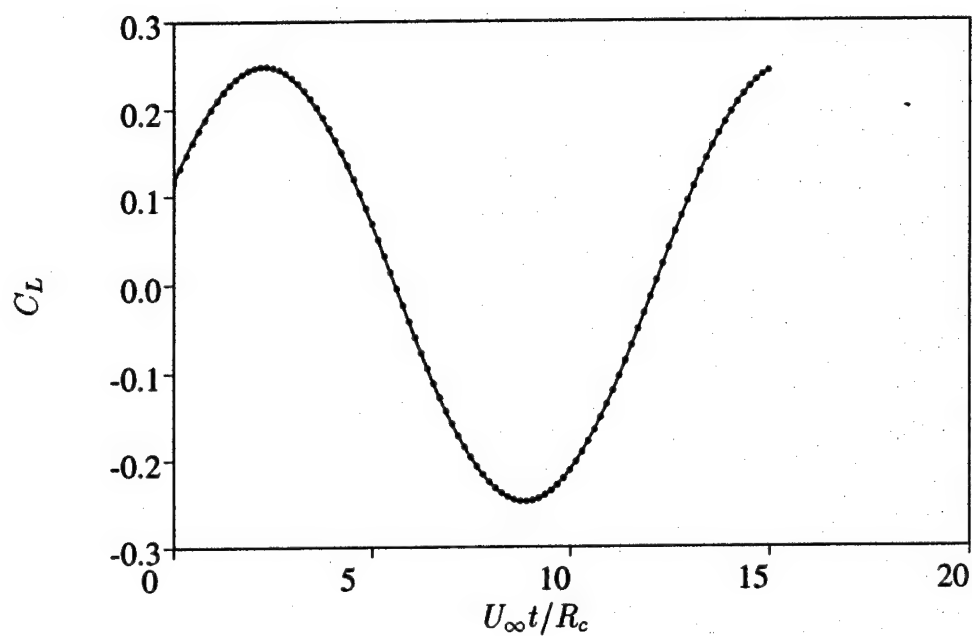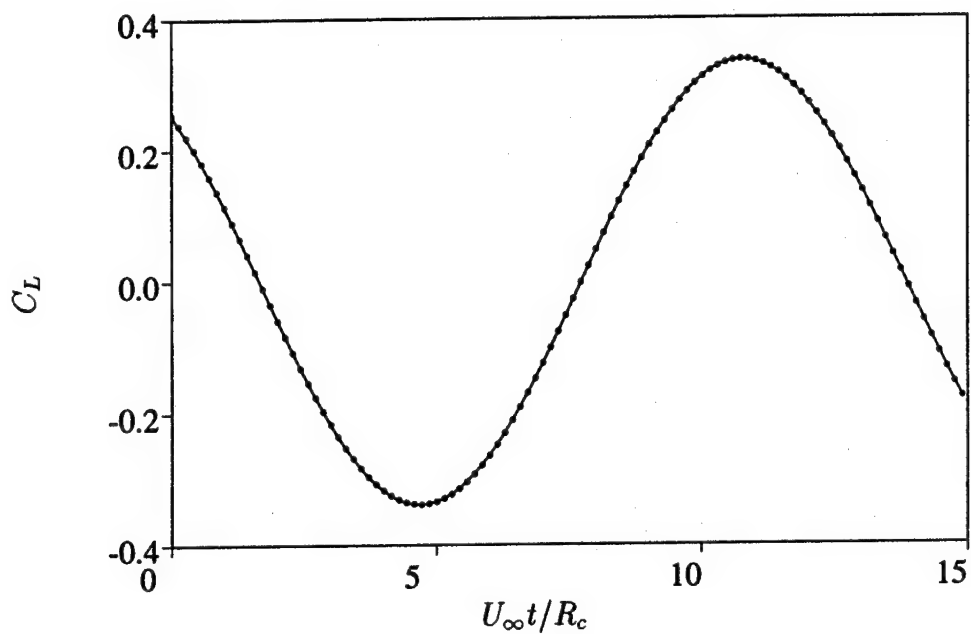
Figure 97: Re=100; Strouhal frequency evaluation
——— : Computation; • : Best sinusoidal fit
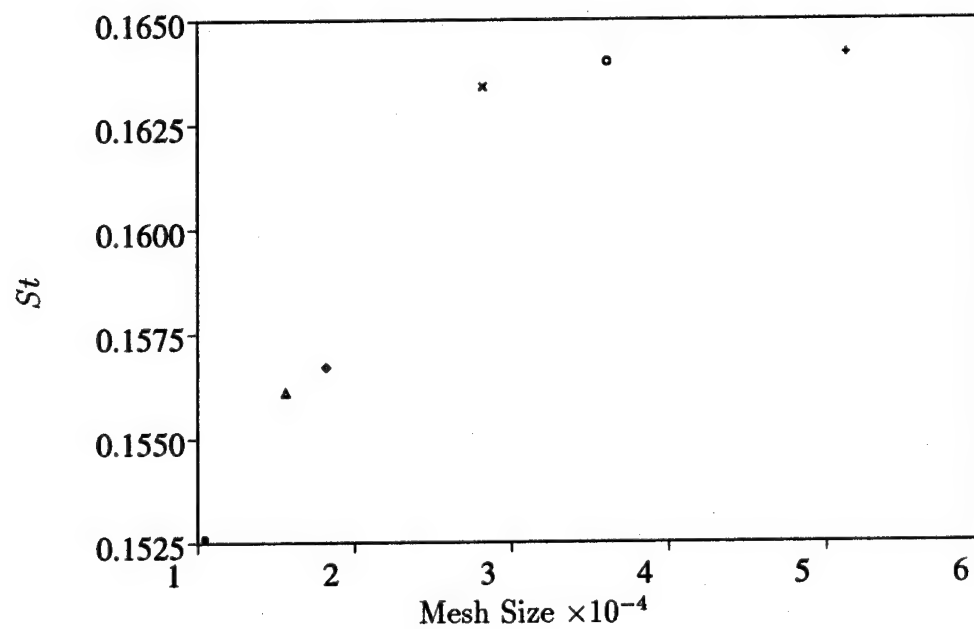
Figure 98: Re=100; Strouhal frequency convergence;
• : 129 × 81; △ : 129 × 121; ◇ : 129 × 141
× : 200 × 141; o : 256 × 141; + : 300 × 171
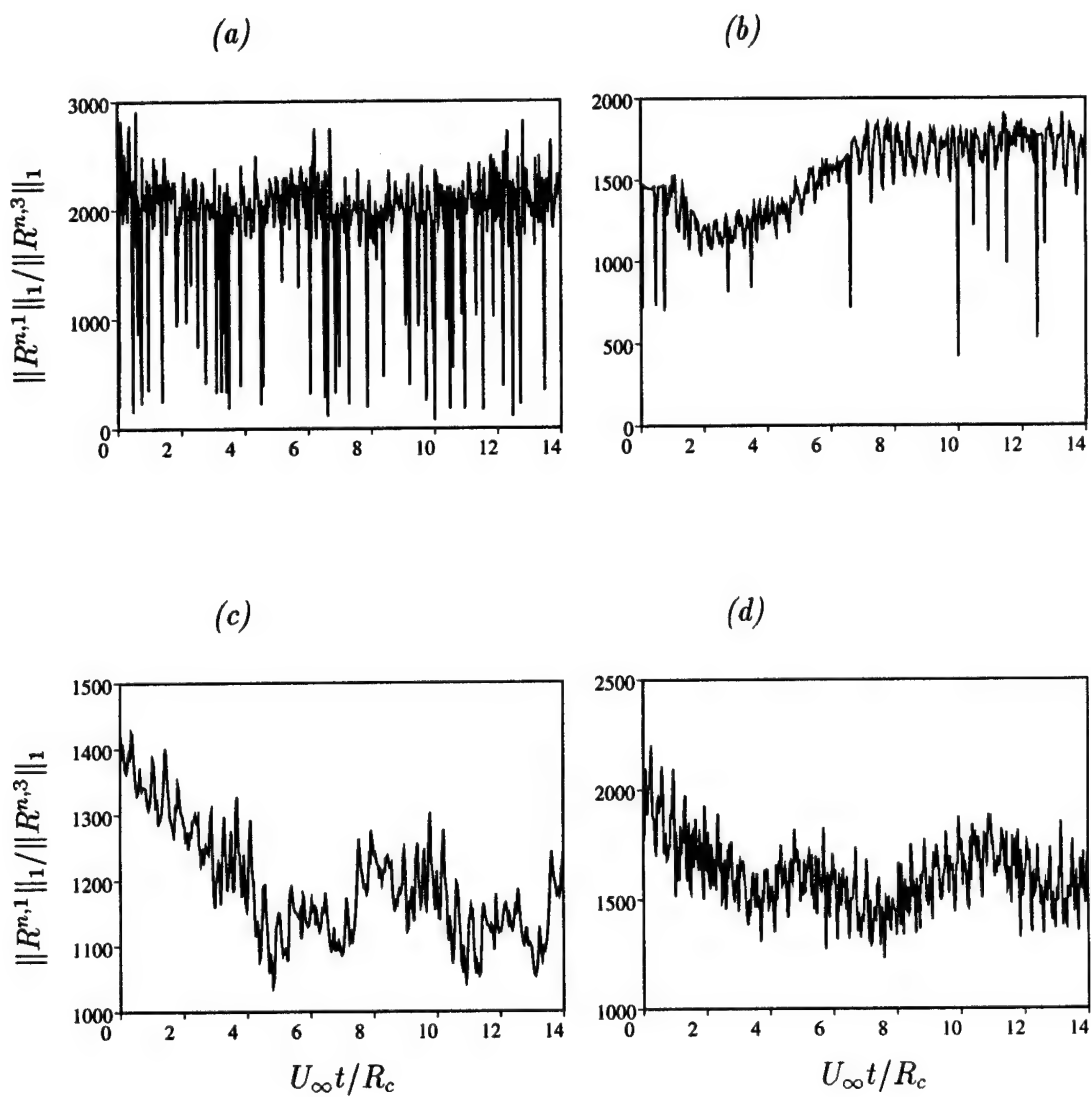
Figure 99: Re=100; CFL=5; Sub-iteration convergence factor time history
continuity (a) , streamwise momentum (b)
vertical momentum (c), energy (d)
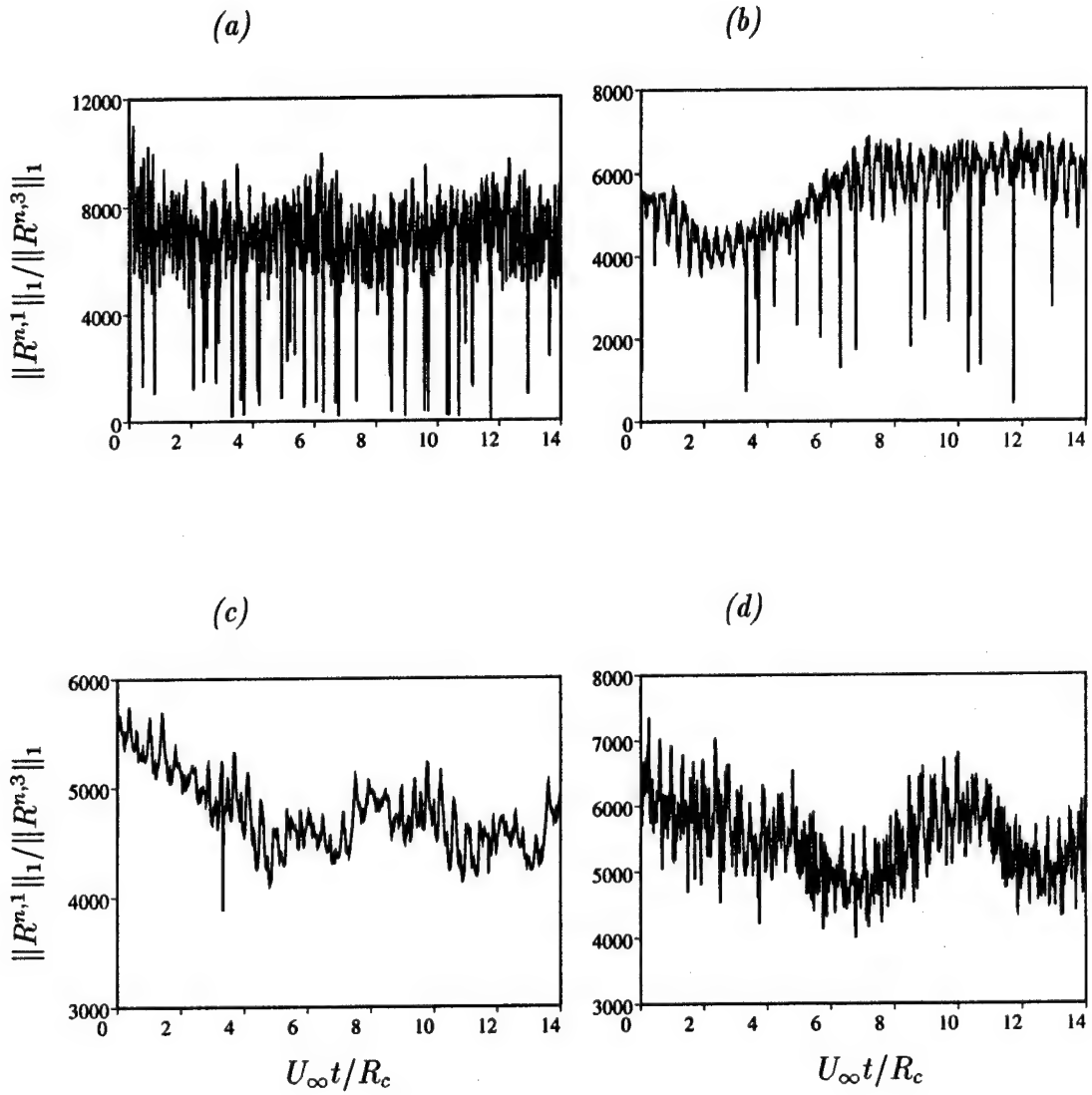
Figure 100: Re=100; CFL=2.5; Sub-iteration convergence factor time history
continuity (a) , streamwise momentum (b)
vertical momentum (c), energy (d)

190

Appendix E

Linear Stability of a Forced Channel Flow

E.1 Formulation of the Problem

The accuracy of the numerical treatment of the convective acceleration is tested in a periodic channel using linear stability analysis. The work necessary to drive the fluid through the channel is provided by an external periodic force. The streamwise direction in the channel is denoted by y, and x is the cross-channel direction.

In steady-state incompressible Poiseuille flow, the maximum streamwise velocity is denoted $v = U_\infty$, and is related to the the pressure gradient across the channel by:

$$\frac{\partial p}{\partial y} = -\frac{2}{h^2}\mu U_\infty, \tag{187}$$

where h is the channel half-width and μ the viscosity. The quantity

$$-\frac{1}{\rho_\infty}\frac{\partial p}{\partial y} = \frac{2}{\rho_\infty h^2}\mu U_\infty \tag{188}$$

is a constant streamwise force per unit mass, and represents the source of momentum necessary for the flow to achieve the steady-state velocity $v = U_\infty$ on the channel centerline.

The thermodynamic pressure distribution obtained by integrating (188) is linear in y. It is thus not a solution to the boundary-value problem describing the compressible flow in a periodic channel. To circumvent this difficulty, an external forcing is introduced to drive the flow, in the form of a momentum and energy flux calibrated to match the magnitude of the force given in (188). The external force imposed in the streamwise momentum equation is a constant denoted by Λ. Corresponding to this momentum source, an energy source, equal in magnitude to the product of Λ and the streamwise velocity v, appears in the energy equation. The flux that must be imposed as an external source term in the Navier-Stokes equations written in conservative form is then

$$\vec{\Gamma} = \Lambda \begin{pmatrix} 0 \\ 0 \\ 1 \\ 0 \\ v \end{pmatrix}. \tag{189}$$

The constant Λ is defined by:

$$\Lambda = \frac{2JM_\infty}{Re} \tag{190}$$

where the reference velocity is the sound speed c_∞. The symbol J refers to the Jacobian of the transformation from physical to computational space (equation 42, Chapter 2). Upon introduction of the external forcing, the governing equations (equation 45, Chapter 2) become:

$$\frac{\partial}{\partial t}\vec{Q} + \frac{\partial}{\partial \xi}\vec{F}_\xi + \frac{\partial}{\partial \eta}\vec{F}_\eta + \frac{\partial}{\partial z}\vec{F}_z = \vec{\Gamma}. \tag{191}$$

The vector $\vec{Q}$ represents the conservative variables (equation 44, Chapter 2). Its definition is restated here for clarity:

$$\vec{Q} = \begin{pmatrix} q_1 \\ q_2 \\ q_3 \\ q_4 \\ q_5 \end{pmatrix} = J \begin{pmatrix} \rho \\ \rho u \\ \rho v \\ \rho w \\ e \end{pmatrix} \tag{192}$$

It is worth noting that although the external force Λ itself is known and constant, the external energy source involves the streamwise component of momentum (v). The time integration of the equations above thus involves both explicit and implicit contributions by the external forcing. The corresponding implicit Jacobian of the forcing term is described in the next Section.

E.2   Numerical Implementation

The modifications to the time-marching schemes arising because of the forcing $\vec{\Gamma}$ are derived by considering the time-marching scheme given by (73) in Chapter 2:

$$\Delta\vec{Q}^{n+1} - c_3\frac{\partial}{\partial t}\Delta\vec{Q}^{n+1} = (c_1 - 1)\vec{Q}^n + c_2\vec{Q}^{n-1} + c_3\frac{\partial}{\partial t}\vec{Q}^n \qquad (193)$$

where n represents the time level, $\Delta\vec{Q}^{n+1} = \vec{Q}^{n+1} - \vec{Q}^n$, and the coefficients c_1 through c_3 are functions of the time step. Adding the forcing flux $\vec{\Gamma}$ to the right-hand side of the Navier-Stokes equations results in equation (191), which substituted into (193) leads to:

$$\Delta\vec{Q}^{n+1} + c_3\Delta\left(\frac{\partial}{\partial\xi}\vec{F}_\xi + \frac{\partial}{\partial\eta}\vec{F}_\eta + \frac{\partial}{\partial z}\vec{F}_z\right)^{n+1} - \underbrace{c_3\Delta\vec{\Gamma}^{n+1}}_{\text{implicit contribution}} =$$

$$(c_1 - 1)\vec{Q}^n + c_2\vec{Q}^{n-1} - c_3\left(\frac{\partial}{\partial\xi}\vec{F}_\xi + \frac{\partial}{\partial\eta}\vec{F}_\eta + \frac{\partial}{\partial z}\vec{F}_z\right)^n + \underbrace{c_3\vec{\Gamma}^n}_{\text{explicit contribution}} \qquad (194)$$

The implicit contribution $\Delta\vec{\Gamma}$ of the forcing flux is a new term which must be expressed as a function of the solution vector $\Delta\vec{Q}$. It is linearized in time using a Taylor series expansion:

$$\Delta\vec{\Gamma}^{n+1} = \left(\frac{\partial\vec{\Gamma}}{\partial\vec{Q}}\right)^n \Delta\vec{Q}^{n+1} + \vartheta(\Delta t^{n+1})^2 \qquad (195)$$

where the flux Jacobian is obtained directly from the definition of $\vec{\Gamma}(\vec{Q})$ given in (189)

as:

$$\frac{\partial \vec{\Gamma}}{\partial \vec{Q}} = \Lambda \begin{pmatrix} 0 & 0 & 0 & 0 & 0 \\ 0 & 0 & 0 & 0 & 0 \\ 0 & 0 & 0 & 0 & 0 \\ 0 & 0 & 0 & 0 & 0 \\ -q_3/q_1^2 & 0 & 1/q_1 & 0 & 0 \end{pmatrix} \qquad (196)$$

This expression for the Jacobian of the forcing completes the definition of the additional terms appearing in the time-marching scheme. The non-linear system of equations is inverted using the iterative technique outlined in Chapter 2.

E.3   Steady One-Dimensional Solution

The governing steady-state one-dimensional compressible equations in physical space are obtained from (191) as:

$$\frac{\partial}{\partial t}\vec{Q} + \frac{\partial}{\partial x}\vec{F_x} = \vec{\Gamma} \qquad (197)$$

with $J = 1$ and $u(x) = w(x) = 0$. In terms of the primitive variables, the equations reduce to:

$$\frac{\partial}{\partial x}\begin{pmatrix} (\gamma-1)(e - \rho v^2/2) \\ -v_x/Re \\ -\frac{1}{Re}(vv_x + \gamma T_x/Pr(\gamma-1)) \end{pmatrix} = \Lambda \begin{pmatrix} 0 \\ 1 \\ v \end{pmatrix}. \qquad (198)$$

Channel walls are located at $x = \pm 1$, where the boundary conditions are:

$$u = v = w = 0, \quad T = T_w = \frac{1}{\gamma}. \qquad (199)$$

Substituting the definition of Λ (equation 190), the solution of this boundary-value problem is:

$$v(x) = M_\infty(1 - x^2) \qquad (200)$$

$$\rho(x) = \frac{3}{PrM_\infty^2(\gamma-1)(1 - x^4) + 3\gamma T_w} \qquad (201)$$

$$e(x) = \frac{1}{\gamma(\gamma-1)} + \frac{1}{2}\rho v^2. \qquad (202)$$

194

In this solution, the pressure is constant, $p = 1/\gamma$, the streamwise velocity is formally identical to the incompressible Poiseuille solution, and the temperature is

$$T(x) = \frac{1}{\gamma\rho(x)} = T_w + \frac{Pr}{3\gamma}M_\infty^2(\gamma - 1)(1 - x^4). \qquad (203)$$

In the limiting case of zero Mach number, the density becomes constant and the solution is well behaved. The governing equations generate this solution because the molecular viscosity is assumed independent of temperature, and because the forcing (Λ) is per unit volume instead of per unit mass.

E.4   Small-Disturbance Equations

Substituting perturbed primitive variables into the conservative form of the Navier-Stokes equations (191) written in cartesian coordinates, and neglecting all products of perturbation fields, leads to the three-dimensional small-disturbance equations,

$$\frac{\partial}{\partial t}\begin{pmatrix} \rho' \\ \rho u' \\ \rho v' + \rho' v \\ \rho w' \\ e' \end{pmatrix} +$$

$$+\frac{\partial}{\partial x}\begin{pmatrix} \rho u' \\ p' \\ \rho v u' \\ 0 \\ u'(e + p) \end{pmatrix} + \frac{\partial}{\partial y}\begin{pmatrix} \rho v' + \rho' v \\ \rho v u' \\ 2\rho v v' + \rho' v^2 + p' \\ \rho v w' \\ v(e' + p') + v'(e + p) \end{pmatrix} + \frac{\partial}{\partial z}\begin{pmatrix} \rho w' \\ 0 \\ \rho v w' \\ p' \\ w'(e + p) \end{pmatrix} -$$

$$-\frac{1}{Re}\frac{\partial}{\partial x}\begin{pmatrix} 0 \\ \frac{4}{3}u'_x - \frac{2}{3}(v'_y + w'_z) \\ v'_x + u'_y \\ w'_x + u'_z \\ vv'_x + v'v_x + vu'_y \end{pmatrix} - \frac{1}{Re}\frac{\partial}{\partial y}\begin{pmatrix} 0 \\ v'_x + u'_y \\ -\frac{2}{3}(u'_x + w'_z) + \frac{4}{3}v'_y \\ w'_y + v'_z \\ u'v_x - \frac{2}{3}v(u'_x + w'_z) + \frac{4}{3}vv'_y \end{pmatrix} -$$

$$-\frac{1}{Re}\frac{\partial}{\partial z}\begin{pmatrix} 0 \\ w'_x + u'_z \\ w'_y + v'_z \\ -\frac{2}{3}(u'_x + v'_y) + \frac{4}{3}w'_z \\ v(w'_y + v'_z) \end{pmatrix} - \frac{\gamma}{(\gamma-1)RePr}\begin{pmatrix} 0 \\ 0 \\ 0 \\ 0 \\ T'_{xx} + T'_{yy} + T'_{zz} \end{pmatrix} = \Lambda\begin{pmatrix} 0 \\ 0 \\ 0 \\ 0 \\ v' \end{pmatrix}.$$

where the perturbation pressure and temperature are:

$$p' = e' - \rho v'v - \frac{1}{2}\rho'v^2 \tag{204}$$

and

$$T' = \frac{1}{\rho}\left(p' - \frac{\rho'}{\gamma\rho}\right). \tag{205}$$

At the solid wall, we impose

$$u' = v' = w' = 0, \quad T' = 0. \tag{206}$$

These are the only physical boundary conditions required, since the normal momentum equation at the wall defines the normal gradient of pressure at the wall. The channel geometry is periodic in the streamwise (y) and spanwise (z) directions, and disturbances are decomposed in Fourier modes along these directions. Considering a generic Fourier mode, we seek solutions to the small-disturbance equations of the form

$$\begin{pmatrix} \rho' \\ u' \\ v' \\ w' \\ e' \end{pmatrix}(x,y,z,t) = \begin{pmatrix} \hat{\rho}(x) \\ \hat{u}(x) \\ \hat{v}(x) \\ \hat{w}(x) \\ \hat{e}(x) \end{pmatrix} e^{i\alpha(y+\beta z-ct)}. \tag{207}$$

Substitution into the small-disturbance equations yields an eigenvalue-eigenvector problem for c,

$$L_2\frac{\partial^2}{\partial x^2}\vec{\Psi} + L_1\frac{\partial}{\partial x}\vec{\Psi} + L_0\vec{\Psi} = c\vec{\Psi} \tag{208}$$

196

where $\vec{\Psi}$ is the solution eigenvector

$$\vec{\Psi} = \begin{pmatrix} \hat{u} \\ \hat{v} \\ \hat{w} \\ \hat{p} \\ \hat{T} \end{pmatrix} . \tag{209}$$

The matrix L_0 is proportional to the product of two matrices M_1 and M_2:

$$L_0 = -\frac{i}{\alpha\rho} M_1 M_2 \tag{210}$$

where M_1 and M_2 are given by

$$M_1 = \begin{pmatrix} 0 & 1 & 0 & 0 & 0 \\ -v & 0 & 0 & 1 & 0 \\ 0 & 0 & 0 & 1 & 0 \\ \rho\frac{v^2}{2}(\gamma-1) & 0 & \rho v(1-\gamma) & 0 & \rho(\gamma-1) \\ -\frac{1}{\gamma\rho} + \frac{v^2}{2}(\gamma-1) & 0 & v(1-\gamma) & 0 & (\gamma-1) \end{pmatrix}$$

$$M_2 = \begin{pmatrix} \rho_x & i\alpha\rho & i\alpha\beta\rho & i\alpha\rho\gamma v & -i\alpha\rho^2\gamma v \\ i\alpha\rho v + \frac{\alpha^2}{Re}(1+\beta^2) & 0 & 0 & 0 & 0 \\ (\rho v)_x & 2i\alpha\rho v + \frac{\alpha^2}{Re}(\frac{4}{3}+\beta^2) & i\alpha\beta\rho v + \frac{\alpha^2\beta}{3Re} & i\alpha(1+\gamma\rho v^2) & -i\alpha\gamma\rho^2 v^2 \\ 0 & \frac{\alpha^2\beta}{3Re} & i\alpha\rho v + \frac{\alpha^2}{Re}(1+\frac{4}{3}\beta^2) & i\alpha\beta & 0 \\ e_x - 2\frac{i\alpha}{Re}v_x & \phi_1 & i\alpha\beta(e+p) + v\frac{\alpha^2\beta}{3Re} & i\gamma\alpha v(\frac{1}{\gamma-1} + \rho\frac{v^2}{2}) & \phi_2 \end{pmatrix},$$

with

$$\phi_1 = -\Lambda - \frac{v_{xx}}{Re} + i\alpha(e+p) + \frac{\alpha^2 v}{Re}(\frac{4}{3} + \beta^2) + i\alpha\rho v^2,$$

and

$$\phi_2 = \frac{\gamma}{(\gamma-1)RePr}\alpha^2(1-\beta^2) - \frac{1}{2}i\alpha\gamma\rho^2 v^3.$$

Matrices L_1 and L_2 are given by

$$L_1 = - \begin{pmatrix} 0 & \frac{1}{3\rho Re} & \frac{\beta}{3\rho Re} & \frac{i}{\alpha\rho} & 0 \\ \frac{1}{3\rho Re} & 0 & 0 & 0 & 0 \\ \frac{\beta}{3\rho Re} & 0 & 0 & 0 & 0 \\ \frac{i}{\alpha} & -2i(\gamma-1)\frac{v_x}{\alpha Re} & 0 & 0 & 0 \\ \frac{i(\gamma-1)}{\alpha\rho\gamma} & -2i(\gamma-1)\frac{v_x}{\alpha\rho Re} & 0 & 0 & 0 \end{pmatrix} \tag{211}$$

and

$$L_2 = \frac{i}{\alpha Re} \begin{pmatrix} 4/3\rho & 0 & 0 & 0 & 0 \\ 0 & 1/\rho & 0 & 0 & 0 \\ 0 & 0 & 1/\rho & 0 & 0 \\ 0 & 0 & 0 & 0 & \gamma/Pr \\ 0 & 0 & 0 & 0 & \gamma/\rho Pr \end{pmatrix}. \tag{212}$$

For given wave-numbers α and β, the solution of this eigenvalue problem yields the eigenfunctions $(\hat{u}, \hat{v}, \hat{w}, \hat{p}, \hat{T})$ and the complex frequency c. The perturbation energy is defined as

$$E(t) = \int_0^{L_z} \int_0^{L_y} \int_{-1}^1 (u'^2 + v'^2 + w'^2)\partial x \partial y \partial z. \tag{213}$$

Its evolution in time is exponential,

$$E(t) = E(0)e^{2c_i t} \tag{214}$$

where c_i is the imaginary part of the eigenvalue c. The objective of the linear-stability simulations is to test the code accuracy in predicting the energy growth-rate $(2c_i)$.

E.5   Three-Dimensional Eigenfunctions

The oblique mode $\alpha = \beta = 1$ is selected for three-dimensional simulations. The equations do not admit growing modes in this case, and the slowest decaying Orr-Sommerfeld mode is chosen as the perturbation. The corresponding frequency is $c = 0.02962395 - i0.00220154$ at Reynolds number $7,500$ and Mach number 0.1.

Scaling Factor	Real Part	Imaginary Part
$|\hat{u}|_{\mathbf{max}}$	0.08143	0.07145
$|\hat{v}|_{\mathbf{max}}$	0.9964	0.5974
$|\hat{w}|_{\mathbf{max}}$	0.81796	0.7994
$|\hat{P}|_{\mathbf{max}}$	0.00274	0.00283
$|\hat{T}|_{\mathbf{max}}$	0.01504	0.01606

Table 20: Scaling factors of 3-D eigenvalues

The corresponding incompressible solution gives as the slowest decaying mode $c = 0.02963201 - i0.00219390$, a difference in norm of 0.025%.

The real and imaginary parts of the eigenfunctions are shown in figures (101) and (102). These functions are scaled on their respective maxima across the channel, which are listed in table (20). The results of the simulations performed are described in Chapter 2. In all simulations, the point distribution across the channel is given by a hyperbolic tangent with a stretching factor α:

$$x = \frac{\tanh(\alpha x i)}{\tanh(\alpha)} \tag{215}$$

$$\xi_i = -1 + 2\frac{i-1}{N-1} \quad i = 1, \cdots, N \tag{216}$$

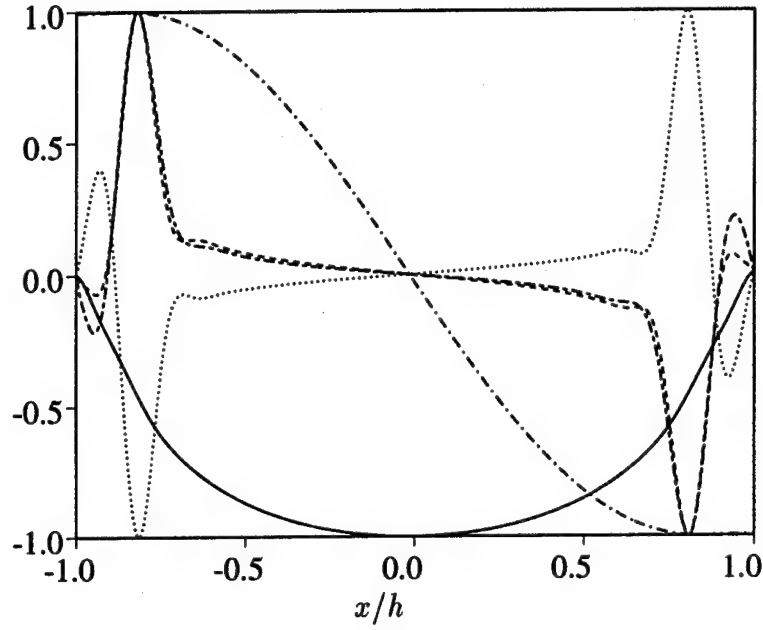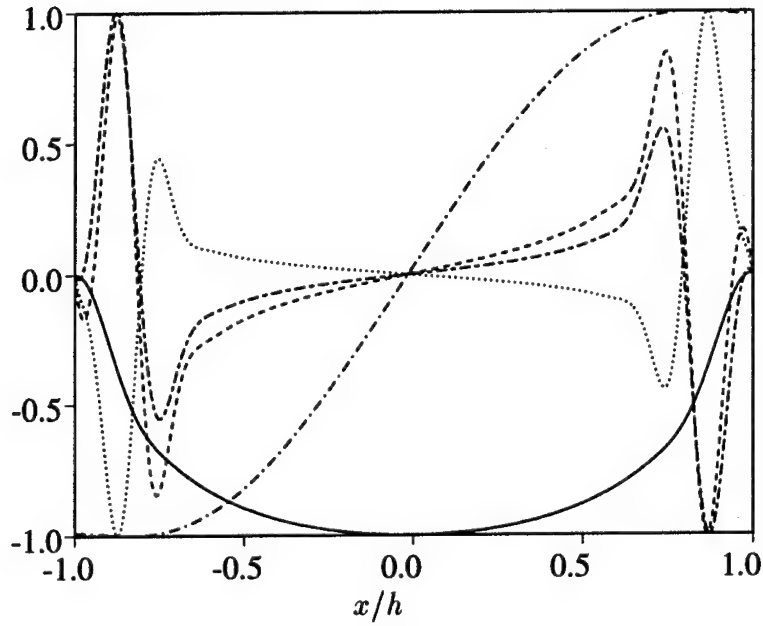Figure 101: Real part of 3-D eigenfunctions

Figure 102: Imaginary part of 3-D eigenfunctions

—— : $\hat{u}/\hat{u}_{\max}$; ---- : $\hat{v}/\hat{v}_{\max}$; $\cdots$: $\hat{w}/\hat{w}_{\max}$; —·— : $\hat{P}/\hat{P}_{\max}$; —–— : $\hat{T}/\hat{T}_{\max}$
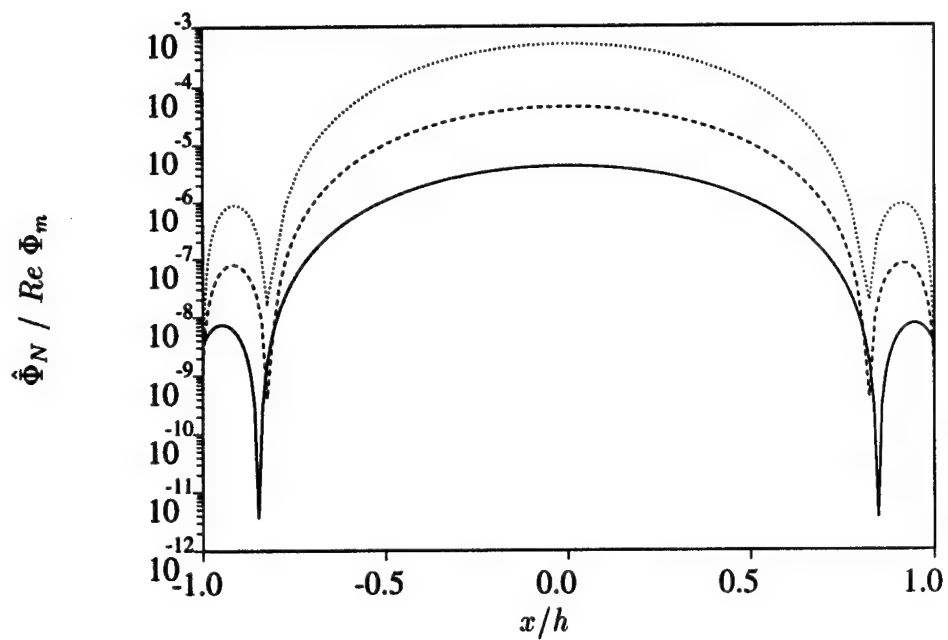
Figure 103: Numerical dissipation in steady channel flow solution
Stretching factors:—— : $\alpha = 2$; ---- : $\alpha = 3$; $\cdots$: $\alpha = 4.5$

Appendix F

Numerical Aspects of LES

F.1 Introduction

Large-eddy simulations are based on the division of turbulent flows into large and small-scale motions. The energetics of the large scales are computed directly, whereas the effect of the small scales on the large scales is modeled. The performance of this division of labor between the filtered, large-scale equations and the subgrid-scale model hinges partially on the ability of the mesh, given a numerical method, to accurately resolve the dynamically important motion. This appendix summarizes the large-eddy grid-refinement study performed at a Reynolds number of $3,900$ based on free-stream velocity and cylinder diameter. The objective is to select a grid on which comparisons between simulations using different subgrid-scale eddy-viscosity models can be established. All calculations presented in this appendix were performed with the fifth-order accurate, upwind-biased scheme for the convective derivatives.

The subgrid-scale eddy viscosity, given by (30) in Chapter 2, is of the form $\nu_t = C\Delta^2\overline{\rho}\,|\overline{S^*}|$, where C is a function of space depending on the Leonard stress tensor, density and rate of strain fields. The convergence properties of the subgrid-scale Reynolds stresses as the grid is refined have not been thoroughly investigated. The purpose of the present study is thus to examine the variations of the mean quantities in the wake and at the cylinder surface as grid resolution increases. Most velocity and resolvable Reynolds shear stress statistics near the wake centerline are found

to oscillate with grid refinement, indicating that the finer meshes capture the main statistical flow features.

The following section discusses three-dimensional initial conditions. Grid and time-step refinement studies are presented in section F.3. The final mesh selected for large-eddy simulations is described in section F.4.

F.2 Three-Dimensional Initial Conditions

Three-dimensional calculations are initialized with planes of data obtained from preliminary two-dimensional simulations, each plane corresponding to the flow-field at a different phase of the vortex shedding cycle. The resulting initial fields numerically satisfy the continuity equation, and the three-dimensional motions are generated by a spanwise force imbalance. This technique is used to generate turbulent fields only once for each spanwise box-size. Simulations performed on computational domains having identical spanwise lengths but different grids are initialized with fields interpolated from solutions computed on coarser meshes to minimize the perturbation of the large scales.

In the present simulations, no external perturbations are imposed upstream of the cylinder. In the absence of external perturbations, the three-dimensionality of the flow was found to be numerically self-sustained for spanwise grid spacings smaller than $\Delta z = 0.4R_c$, corresponding to 5 spanwise points per cylinder diameter. For coarser spanwise resolutions the flow reverts to a two-dimensional state after a transient of 1 to 2 vortex shedding cycles.

Grid size (r, θ, z)	$U_\infty \Delta t / R_c$	$CFL(U_\infty)$	$CFL(c_\infty)$
$88 \times 90 \times 32$	0.03	1.2	15
$88 \times 90 \times 48$	0.01	0.4	5
$116 \times 136 \times 48$	0.005	0.3	6
$174 \times 128 \times 48$	0.005	0.7	13

Table 21: Time integration parameters

F.3   Spatial and Time Resolution Study

F.3.1   Grid Sizes

The selection of a box-size in the spanwise direction (z) is such that the two-point correlation function of velocity component u_i

$$R_{ii}(0, 0, r) = \overline{u_i(z, y, z, t)\, u_i(x, y, z + r, t)} - \frac{1}{T} \int_0^T u_{i_{2D}}^2(x, y, t)\partial t - \overline{u}_i^2(x, y) \quad (217)$$

is close to zero at the box center. The bar over a quantity in that expression denotes an average over time and spanwise distance. The two-dimensional component of the velocity $u_{i_{2D}}$ is by definition independent of the spanwise direction (chapter 2, section 2.8). This relation assumes that the random and two-dimensional components of the flow are uncorrelated (Cantwell & Coles 1983). Recent experiments have investigated the size and nature of the structures present in the intermediate-wake behind the cylinder. These large-scale three-dimensional structures are pairs of counter-rotating streamwise vortices (Hayakawa & Hussain 1989). Between Reynolds numbers 330 and 21,000, the mean spanwise spacing of these structures is constant at about one pair per diameter (Bays-Muchmore & Ahmed 1993). The correlation functions $R_{ii}(0, 0, r)$ were however not documented in these experiments.

The only location where experimental measurements are available to evaluate spanwise two-point correlations is three diameters downstream of the cylinder. Ong & Wallace (1994) computed the spanwise two-point correlation of the hot-wire voltage E at that location at Reynolds number 3,900, using a single-wire probe. The effects of both streamwise and vertical velocities are thus included in these correlations. The measurements, taken on the wake centerline $(y = 0)$, are shown in figure 104. They

204

represent the sum of the correlation function and the squared periodic component of the voltage fluctuation:

$$R_{EE}^*(0,0,r) = R_{EE}(0,0,r) + \frac{1}{T}\int_0^T E_{2D}^2(x,y,t)\partial t \qquad (218)$$

The two-dimensional component of the voltage fluctuations is not available experimentally. To derive the most pessimistic estimate of the location at which the correlation R_{EE} is zero, we assume that the voltage function $E(t)$ is defined uniquely by the streamwise velocity $u(t)$, and that the periodic component is the net two-dimensional component of the flow. At $x/D = 3$, the experimental value of $u_{2D}^2/R_{uu}^*(0,0,0)$ is about 0.1. The correlation function $R_{uu}(0,0,r)$ at three diameters downstream is thus zero at approximately $r/D = 1.5$. In all the simulations documented in this report, the spanwise box-size is set to twice this distance, at $L_z = \pi D$.

The layouts of the meshes used in this resolution study are discussed in section C.3 of Appendix C. To establish that the final mesh selected resolves the main features of the flow, mean velocities and Reynolds shear stresses are presented below on 4 grids containing $(88 \times 90 \times 32)$, $(88 \times 90 \times 48)$, $(116 \times 136 \times 48)$ and $(174 \times 128 \times 48)$ points in the radial, azimuthal and spanwise directions respectively.

F.3.2 Time Stepping and Iteration Residuals

The time-steps and CFL numbers corresponding to each calculation are displayed in table (21). Statistics are compiled in each simulation over 60 to 65 time units based on cylinder radius and free-stream velocity, corresponding to approximately 6 vortex shedding cycles. The convergence of the iteration residuals, illustrated in the case of the $(88 \times 90 \times 48)$ simulation, is shown in figure (105). This figure displays time histories of the residual errors in each governing equation, defined in section D.3 of Appendix D, over approximately half a vortex shedding cycle. The number of sub-iterations per time-step is fixed at 3. Residuals drop on the average by a factor of 10^3 at each time-step, with extrema in all five equations of motion as low 20 and as high as 10^4. Although convergence histories at Reynolds number $3,900$ are noisier than those at Reynolds number 100 (figures 99 and 100, Appendix D), the level of mean convergence is comparable in both cases.

F.3.3   Mean Convergence with Time of Integration

The convergence of mean flow statistics with time of integration is examined in the case of the $(116 \times 136 \times 48)$ simulation. Table (23) summarizes the evolution of the main near-wake features integrated over 6 vortex shedding cycles. Figures (106) and (107) display the wall pressure coefficient and shear stress, as well as velocity profiles inside and downstream of the recirculation bubble at different times of integration. Total drag, skin-friction, upstream separation angle and back-pressure are close to their final values after two shedding cycles. Other quantities, including secondary separation angles, bubble length, wall stress and wake velocities require up to 5 shedding cycles for convergence, corresponding to integrations over approximately $50R_c/U_\infty$ time units.

F.3.4   Effect of Refinement on Mean Wake Quantities

Statistics obtained from each simulation are summarized in table (24) and figures (108) through (116). Table (24) lists mean quantities of interest at the cylinder surface and in the main recirculation bubble. These parameters are observed to either oscillate, or decrease, reach a minimum and increase, or undergo the reverse trend, as the grid is refined. In particular, the oscillatory behavior of the back-pressure coefficient and separation angles can be observed in figure (108), which displays pressure coefficient and vorticity around the cylinder circumference for each simulation.

Three of the most important wall quantities are the back-pressure coefficient, the upstream separation location of the boundary layer and the total drag coefficient. These all lay within experimental error in the two most resolved simulations. The back-pressure coefficients are equal and stand at $\overline{C}_{P_b} = -0.94$ in these simulations, while the upstream separation angle, equal to $\overline{\theta}_1 = 86.2^o$ in the most accurate case, differs by about 1% from is value on the $116 \times 136 \times 48$ mesh. The experimental value of the drag coefficient is $C_D = 0.98 \pm 0.05$ at Reynolds number $3,900$. The most accurate simulation predicts a drag coefficient of $\overline{C}_D = 0.98$. The Strouhal frequency however is underestimated on all meshes, and stands on the finest one at 0.20, 5%

206

below the experimental bound of 0.215 ± 0.003 (Cardell 1993). On the upstream face of the cylinder, the laminar boundary-layer velocity profiles $v_\theta(r)$ are shown in figure (109) at angles $\theta = 90, 120$ and 150 degrees. Although the boundary-layer velocities are underestimated on the mesh with 32 spanwise points, they are well resolved in the 48-spanwise-point simulations.

One of the most significant near-wake statistics is the length of the recirculation bubble downstream of the cylinder. It equals $1.18 \pm 0.05D$ according to Lourenco's PIV experiment (1993), and 1.33 ± 0.2 based on Cardell's hot-wire investigation (1993). Its computed values, illustrated by bubble-velocity and pressure distributions in figure (110), in the two most accurate simulations are $1.36D$ and $1.44D$, which is within Cardell's error range but higher than the PIV estimates. Mean velocity and Reynolds shear stress profiles across the wake are displayed in figures (111) through (116) at several locations downstream. Reynolds shear stress and velocity local extrema, oscillate as resolution increases. Streamwise velocities exhibit $\pm 5\%$ oscillations of their maximum norms based on local centerline velocity deficit. Peak values of Reynolds shear stress vary in a 10% band in the $(88 \times 90 \times 48)$ and $(174 \times 128 \times 48)$-simulations.

F.4   Final Grid Selected

These results indicate that on the $(116 \times 136 \times 48)$-point mesh, near-wake mean velocities and Reynolds stresses are resolved within uncertainty bounds of 5% and 10% respectively. This mesh is thus appropriate for turbulence simulations. However in two computations with and without the dynamic subgrid scale model, differences in mean velocities were small and confined to the first 2 diameters of the wake. To enhance the impact of the subgrid scale model, the final mesh selected is similar to the $(116 \times 136 \times 48)$ grid with three modifications: (1) the radial resolution at the cylinder surface is chosen to match that of the $(174 \times 128 \times 48)$ mesh; (2) the resolved wake region is extended from 5 to 10 diameters downstream; (3) downstream of the bubble closure point, the mesh is stretched geometrically in the radial direction. The next section demonstrates that this stretching has a minimal effect on the mean velocity,

while the eddy viscosity increases locally by up to 40 percent. These three modifications translate into a mesh containing $(144 \times 136 \times 48)$ points in the radial, azimuthal and spanwise directions respectively. Its physical characteristics are documented in Appendix C. The grid layout is displayed in figure (86).

F.4.1   Impact of Radial Grid Stretching Past the Bubble Closure

In the resolved wake downstream of the recirculation bubble ($L \leq r \leq R_w$), meshes used in the refinement study above have a constant radial spacing, (figure 80). In the final grid selected described above, the mesh stretches radially downstream of the recirculation bubble in order to enhance the contribution of the turbulence model within the resolved wake region. The objective of this section is to demonstrate that this radial coarsening of the mesh increases the turbulent eddy viscosity relative to the molecular viscosity without unduly affecting the accuracy of the solution.

The impact of radial grid stretching for $r \leq R_w$ is demonstrated using the $(116 \times 136 \times 48)$ simulation described in tables (11) and (12) as a base case. Geometric stretching in the radial direction between 1 and 5 diameters downstream with a factor of 1.02 results in a $(106 \times 136 \times 48)$-point mesh. Stretched and uniform radial grid-spacing distributions are displayed in figure (85). Azimuthal and spanwise grid construction parameters are identical to those of the unstretched $(116 \times 136 \times 48)$-point mesh. On both grids, the initial condition is a fully developed field. Statistics are averaged over $11.4 R_c/U_\infty$ time units, corresponding to approximately 1 vortex shedding cycle. The time-step is $0.005 R_c/U_\infty$, which translates into velocity and sound-speed based CFL numbers of 0.3 and 6 respectively.

Table (22) lists mean quantities of interest at the cylinder surface computed on both grids. Total drag ($\overline{C}_D = 0.98$) and skin-friction ($\overline{C}_f = 0.90 \times 10^{-2}$) are identical in both cases. Differences in back-pressure coefficient and upstream separation angles stand at 1% and 0.1% respectively.

Mean eddy viscosity and velocities at various locations in the wake are displayed in figures (117) and (118). The maximum difference in mean velocity occurs 3.5

208

Wake mesh	$\overline{C_{P_b}}$	$\overline{C_D}$	$\overline{C_f} \times 100$	$\overline{\theta_1}$
Unstretched	−0.90	0.98	0.90	84.6
Stretched	−0.91	0.98	0.90	84.5

Table 22: Aerodynamic coefficients on stretched and unstreched meshes

diameters downstream, where the streamwise velocity difference is approximately 3% of the centerline velocity deficit. On the stretched mesh, the eddy viscosity peaks up to 40% higher than on the uniform wake grid, indicating that the radial stretching and coarsening of the grid have the targeted property of enhancing subgrid-scale dissipation while having little effect on the mean flow.
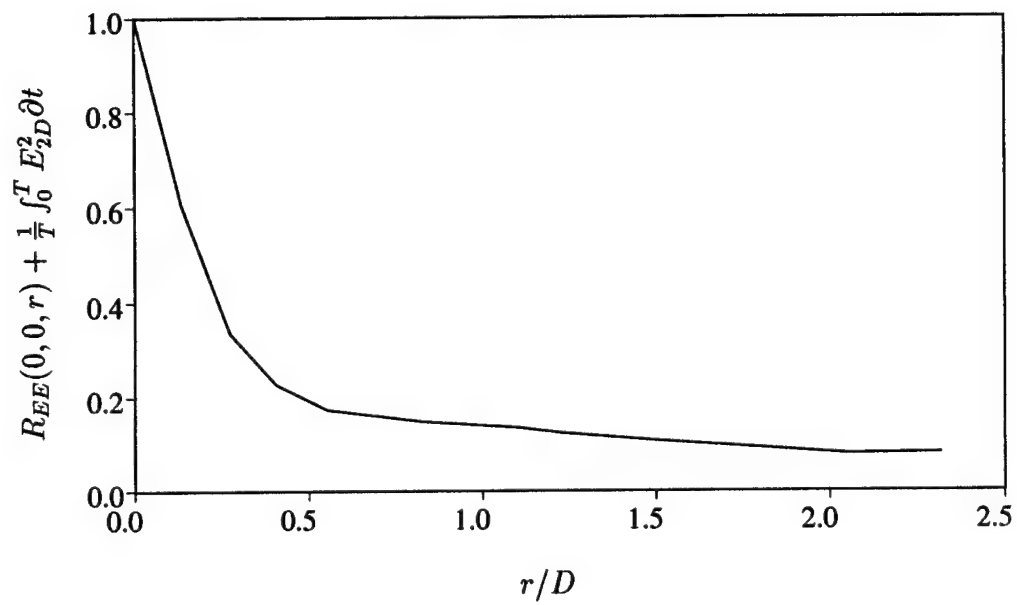
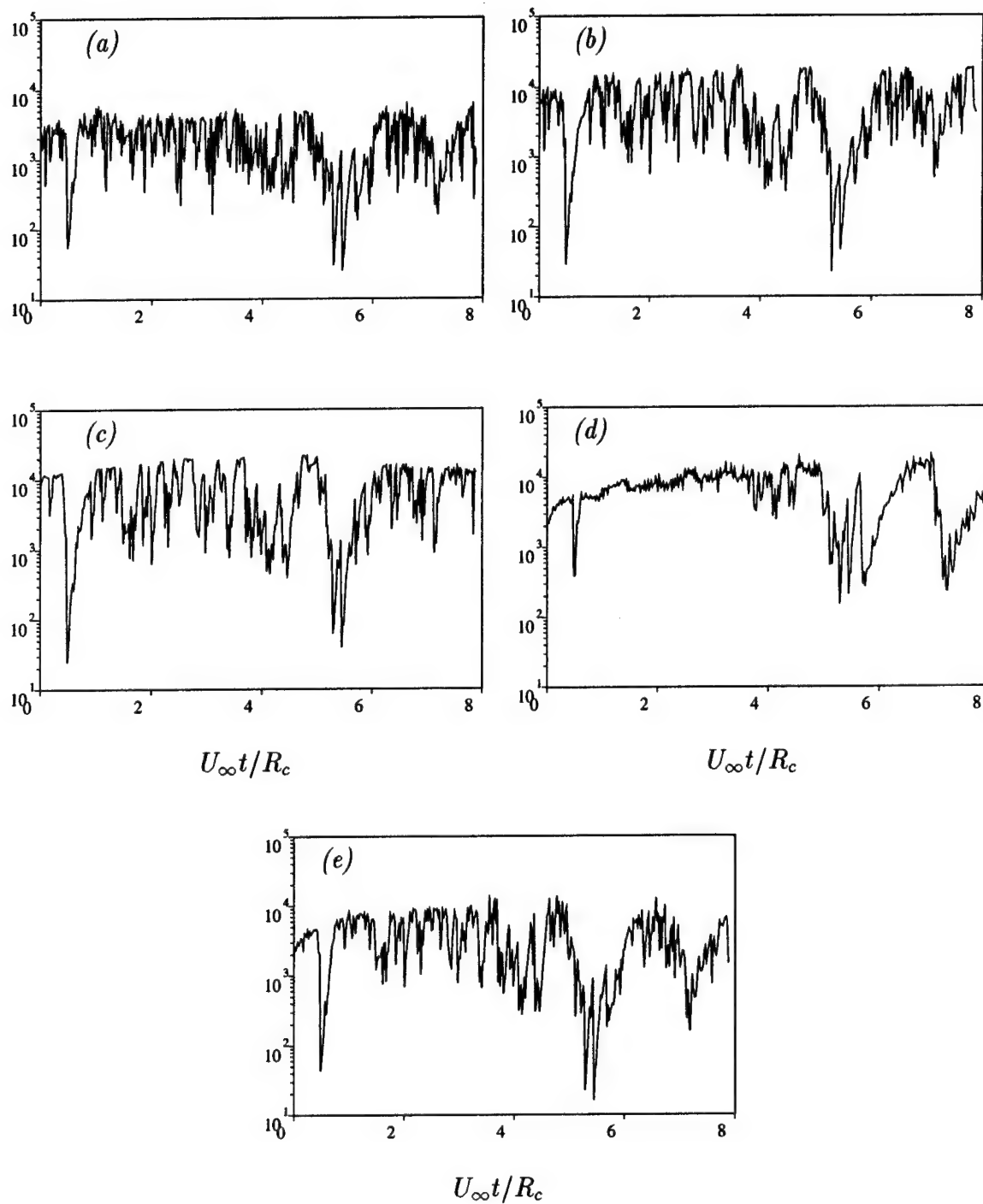Figure 104: Experimental spanwise two-point correlations of hot-wire voltage $x/D = 3$; Ong & Wallace (1994)

Figure 105: Sub-iteration convergence factor ($\|R^{n,1}\|_1/\|R^{n,3}\|_1$) time history
(88 × 90 × 48) Simulation; Continuity (a); Streamwise Momentum (b)
Vertical Momentum (c); Spanwise Momentum (d); Energy (e)

211

		Shedding cycles					
		1	2	3	4	5	6
Sampling time	$U_\infty t/R_c$	10.20	18.11	30.82	43.41	52.67	62.44
Back pressure	$\overline{C}_{P_b}$	-1.05	-0.93	-0.95	-0.94	-0.95	-0.94
Total drag	$\overline{C}_D$	1.12	1.02	1.02	1.02	1.02	1.01
Skin friction	$\overline{C}_f \times 100$	0.95	0.91	0.91	0.91	0.91	0.91
	$\bar{\theta}_1$	88.6	85.0	84.8	84.9	84.9	84.8
Separations	$\bar{\theta}_2$	107.1	108.1	106.5	107.7	108.1	108.4
	$\bar{\theta}_3$	141.2	150.7	148.3	148.6	153.7	154.1
Bubble length	L/D	1.05	1.23	1.55	1.37	1.35	1.36

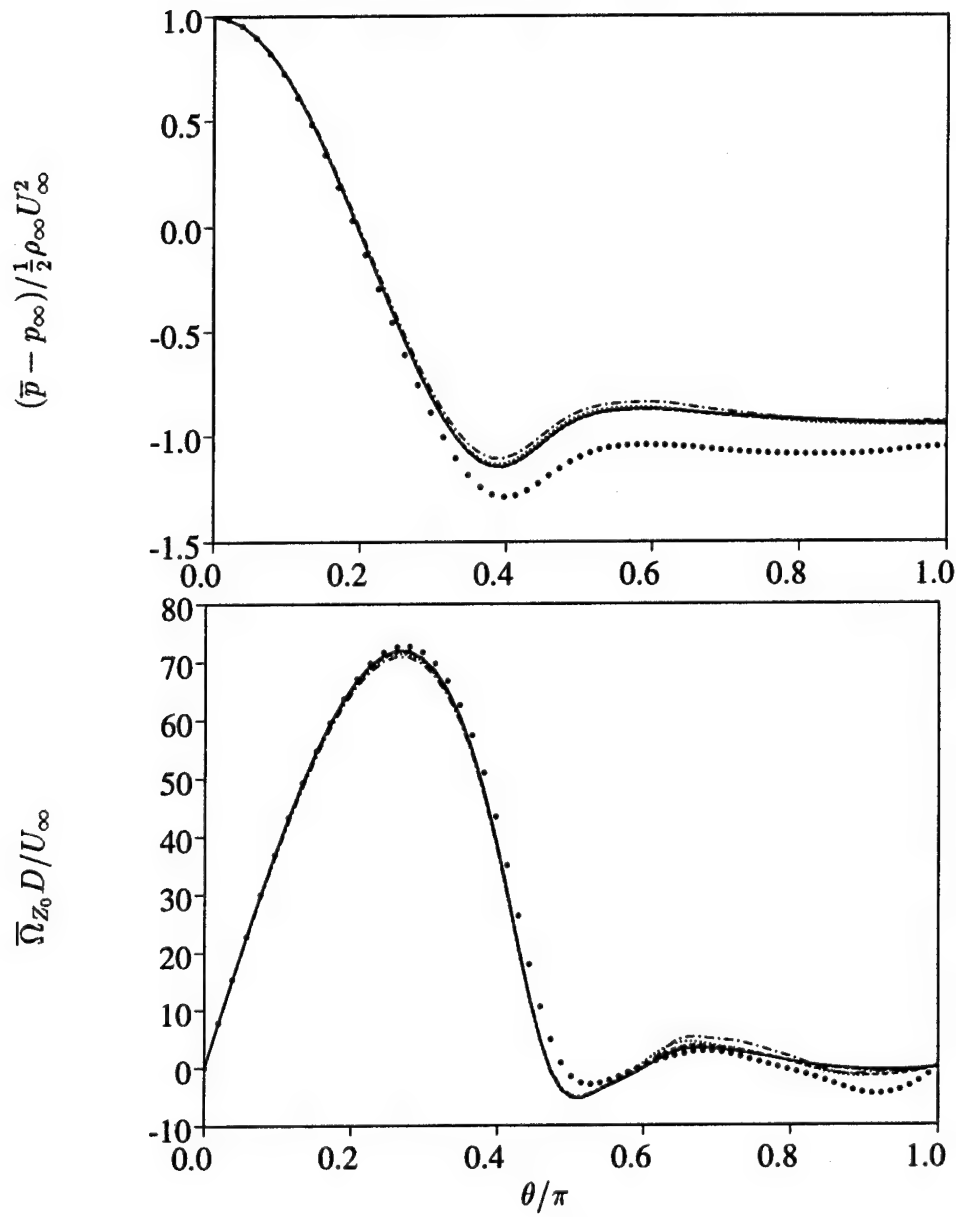Table 23: Sampling error analysis; $(116 \times 136 \times 48)$ simulation

Figure 106: Wall pressure and vorticity convergence
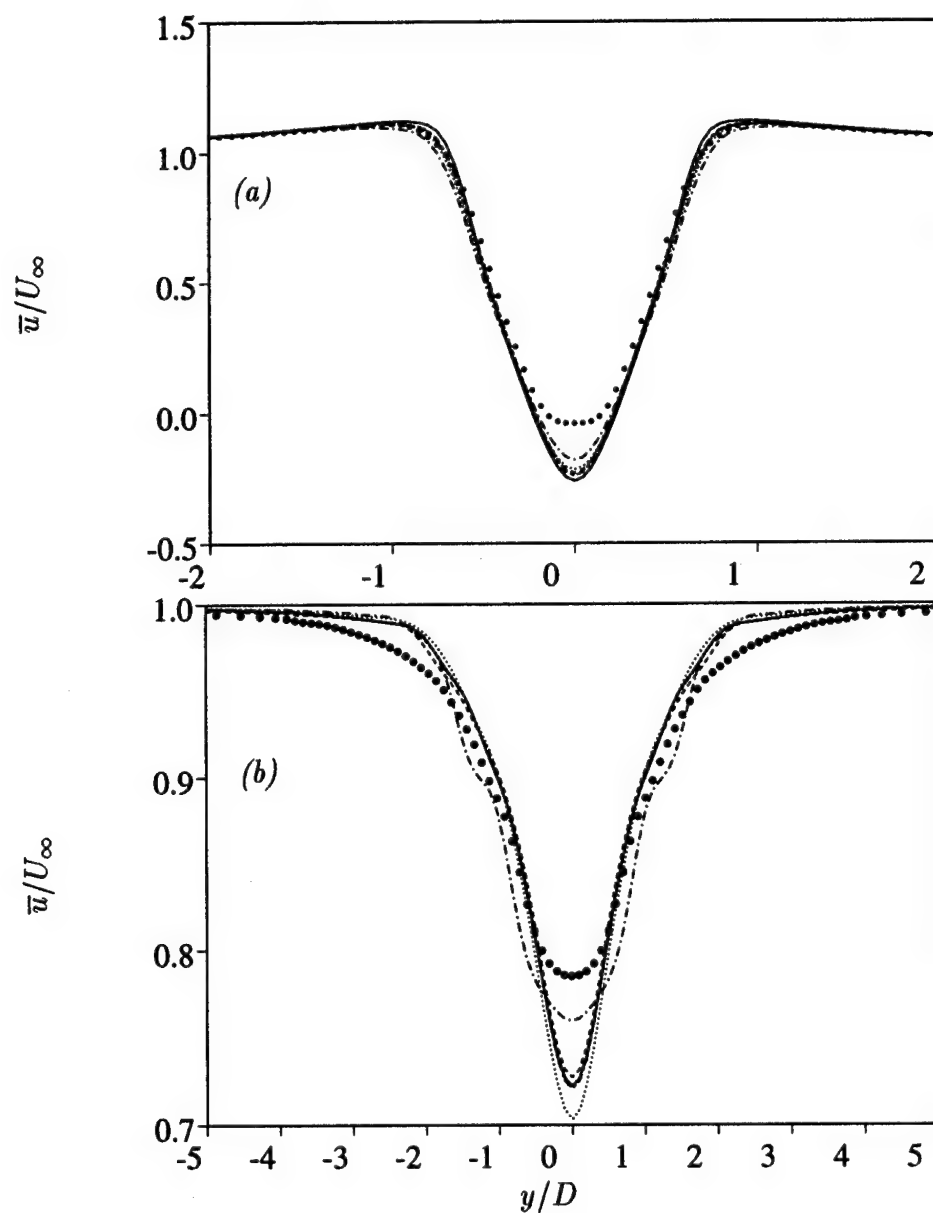Shedding cycles: ● : 1; —·— : 2; ··· : 3; ---- : 4; —-— : 5; —— : 6

213

Figure 107: Streamwise velocity convergence at $x/D = 1.5$ (a), $x/D = 5.0$ (b)
Shedding cycles: ● : 1; —·— : 2; ··· : 3; ---- : 4; —-— : 5; —— : 6

|	Grid size (r, θ, z)				
	88×90 $\times 32$	88×90 $\times 48$	116×136 $\times 48$	174×128 $\times 48$	Experiments $(Re = 3{,}900)$
St Strouhal	0.19	0.20	0.19	0.20	0.215 ± 0.005 (Ong 1994)
$\overline{C}_{P_b}$ Back pressure	-0.96	-0.99	-0.94	-0.94	-0.90 ± 0.05 (Norberg 1987)
$\overline{C}_D$ Total drag	1.03	1.07	1.01	0.98	0.98 ± 0.05 (Norber 1987)
$\overline{C}_f \times 100$ Skin-friction	0.86	0.87	0.91	0.90	$\cdots$
$\overline{\theta}_1$ Separation	87.8	87.3	84.8	86.2	85 ± 2 (Son 1969)
$\overline{\theta}_2$ Separation	107.5	105.2	108.4	112.2	$\cdots$
$\overline{\theta}_3$ Separation	——	147.4	154.1	152.6	$\cdots$
L/D Bubble length	1.55	1.47	1.36	1.44	1.18 ± 0.05 (Lourenco 1993)
$\overline{u}_{\min}/U_\infty$ in bubble	-0.33	-0.31	-0.31	-0.31	-0.24 ± 0.1 (Lourenco 1993)
$r_{\min}/D$ $\overline{u}_{\min}$ location	0.99	0.90	0.84	0.91	0.72 ± 0.1 (Lourenco 1993)

Table 24: Near-wake result summary
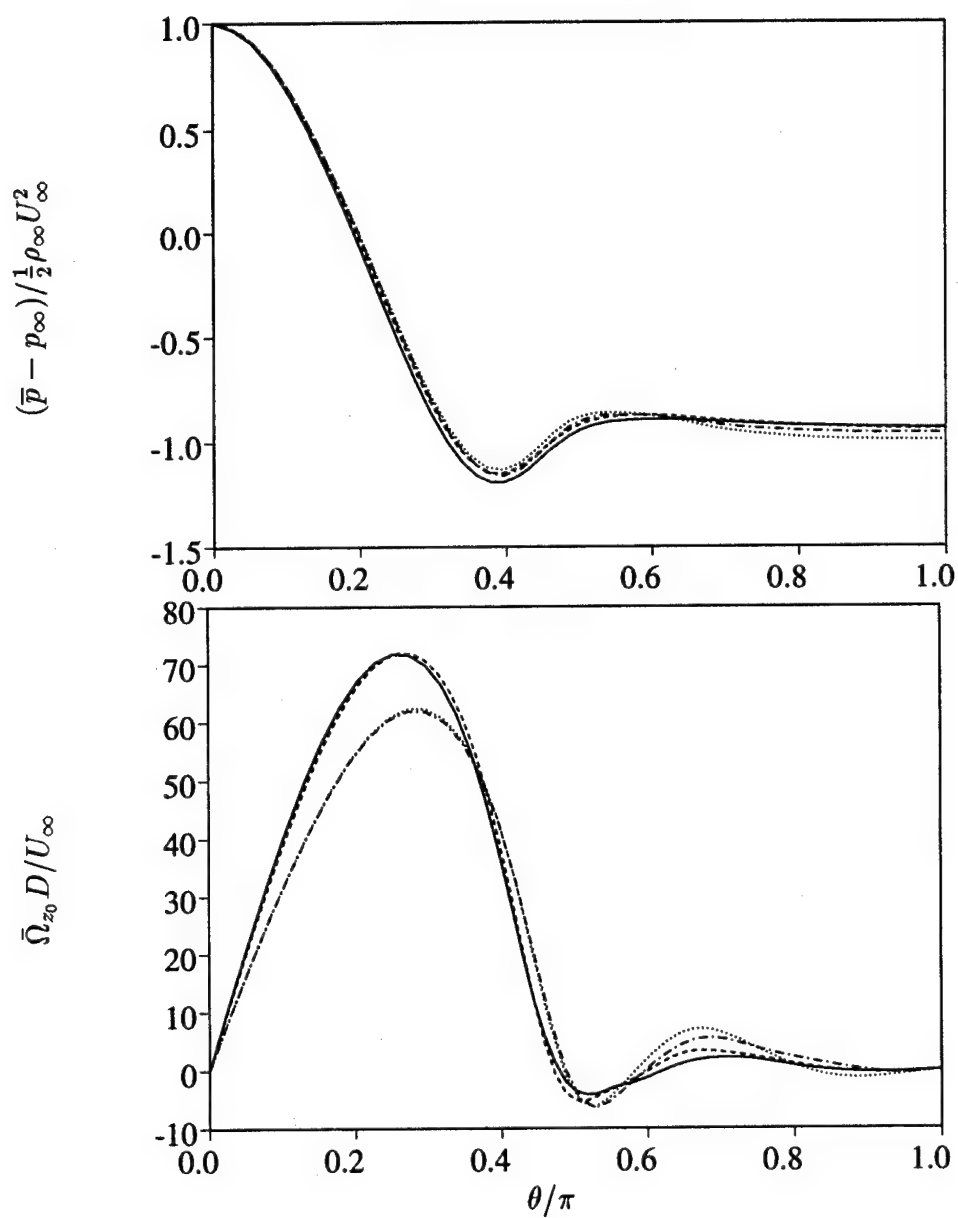
Figure 108: Wall pressure and vorticity
—·— : $88 \times 90 \times 32$; $\cdots$: $88 \times 90 \times 48$
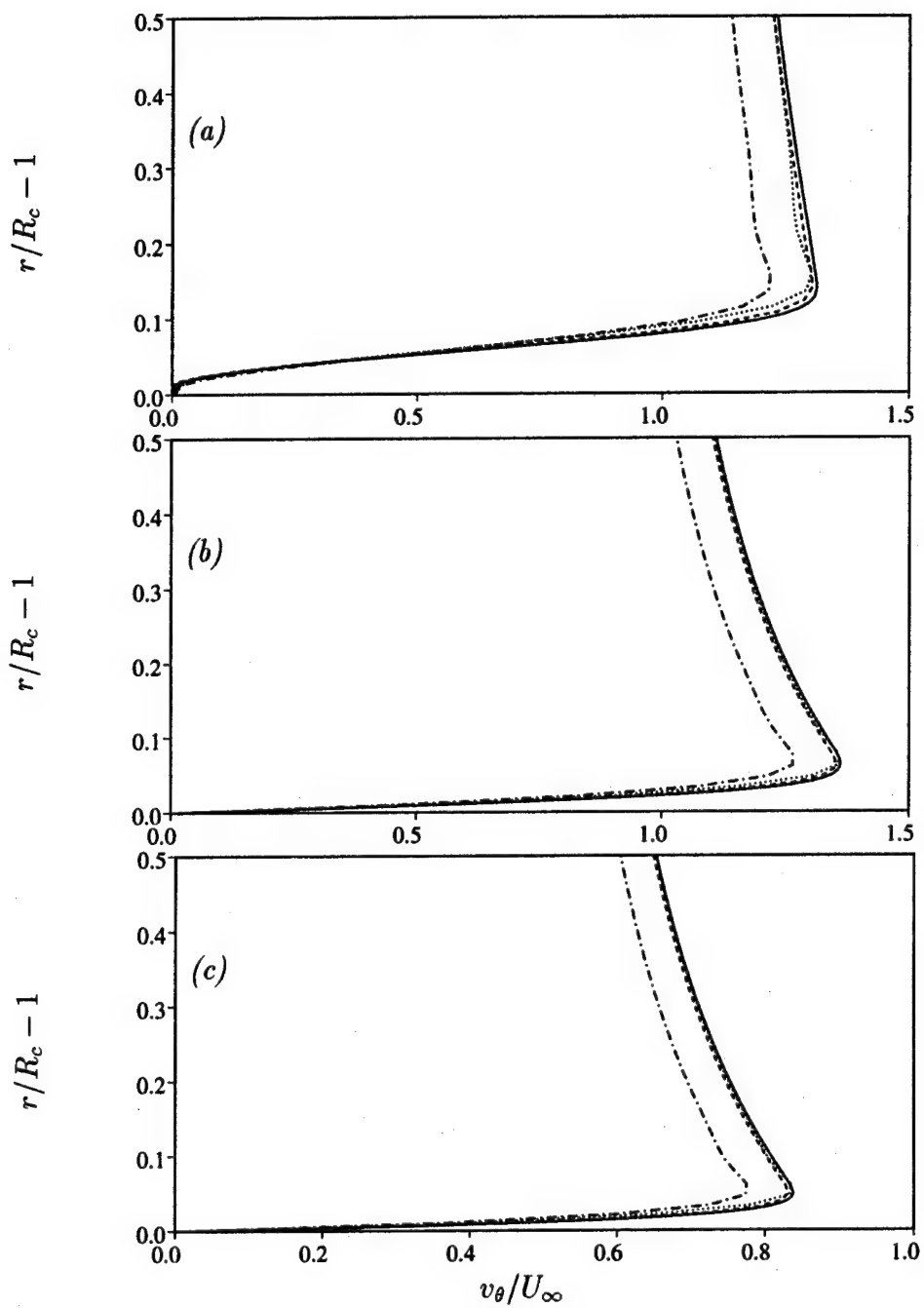---- : $116 \times 136 \times 48$; —— : $174 \times 128 \times 48$

Figure 109: Tangential velocity radial profiles at the cylinder surface
—·— : $88 \times 90 \times 32$; $\cdots$: $88 \times 90 \times 48$; ---- : $116 \times 136 \times 48$
—— : $174 \times 128 \times 48$ (a) : $\theta = 90^o$; (b) : $\theta = 120^o$; (c) : $\theta = 150^o$
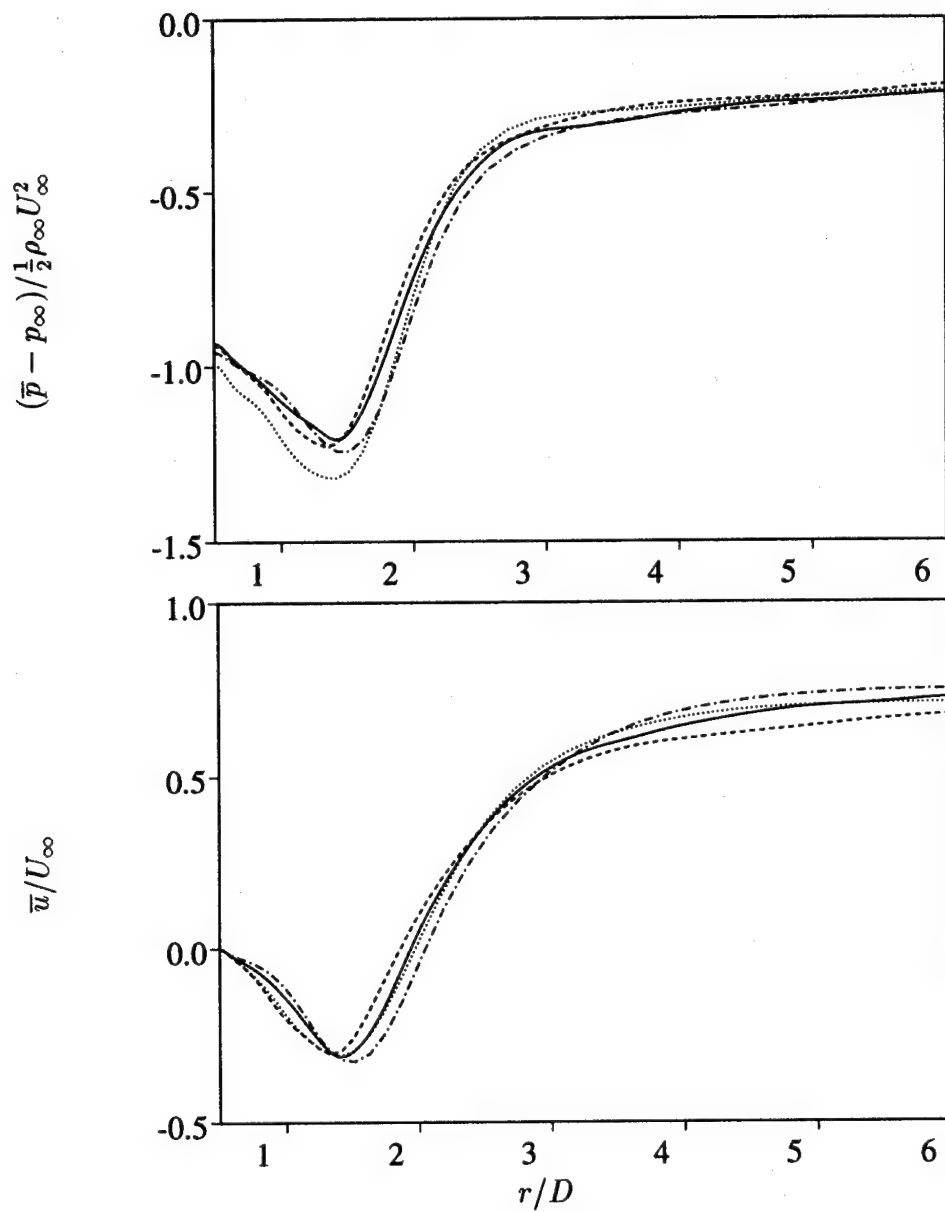
Figure 110: Rear axis pressure coefficient and streamwise velocity
——·— : $88 \times 90 \times 32$; · · · : $88 \times 90 \times 48$
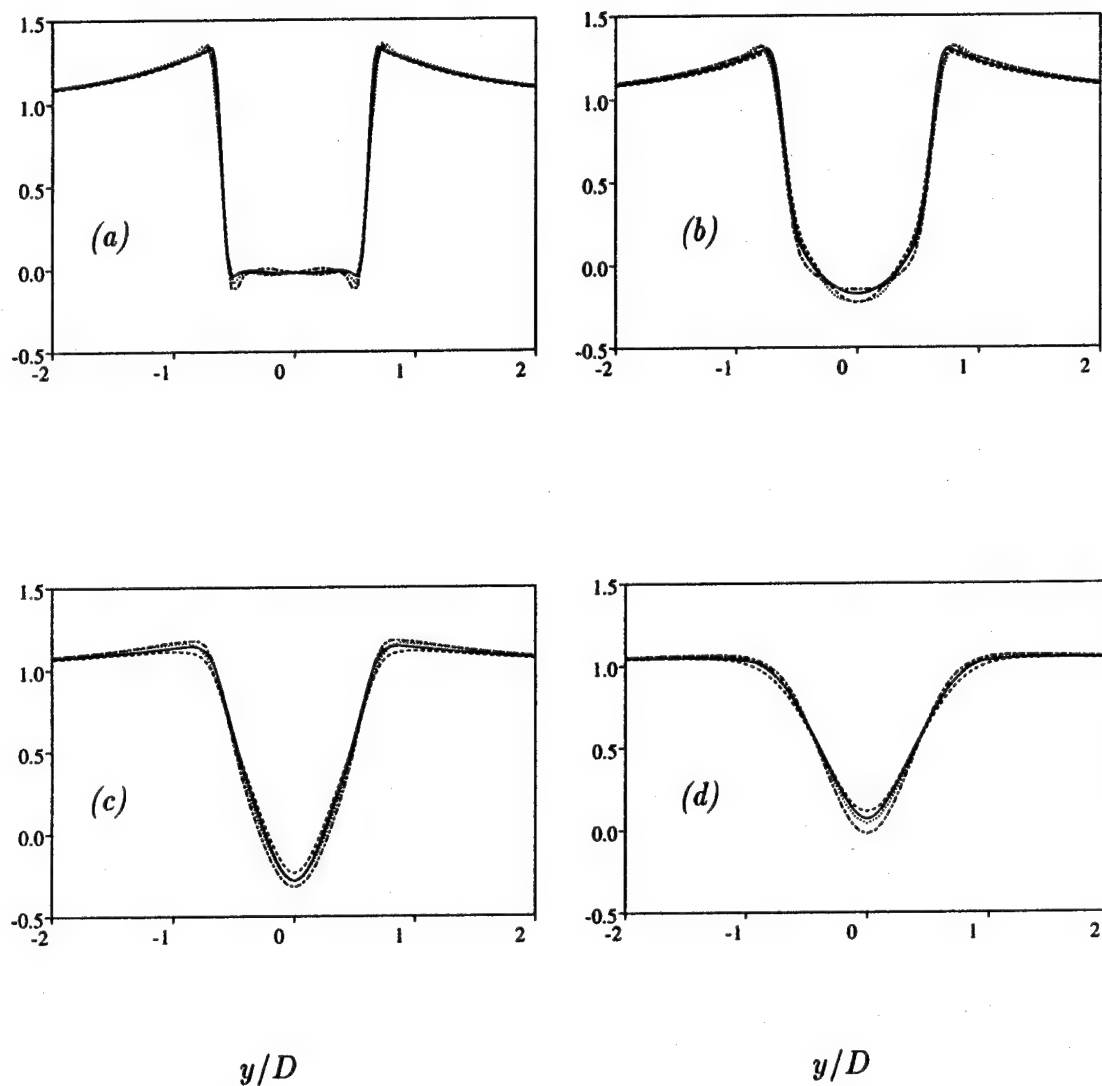- - - - : $116 \times 136 \times 48$; —— : $174 \times 128 \times 48$

Figure 111: Streamwise velocity $\overline{u}/U_\infty$ at $x/D = 0.58$ (a), 1.06 (b), 1.54 (c), 2.02 (d)
—·— : $88 \times 90 \times 32$; ··· : $88 \times 90 \times 48$; ---- : $116 \times 136 \times 48$
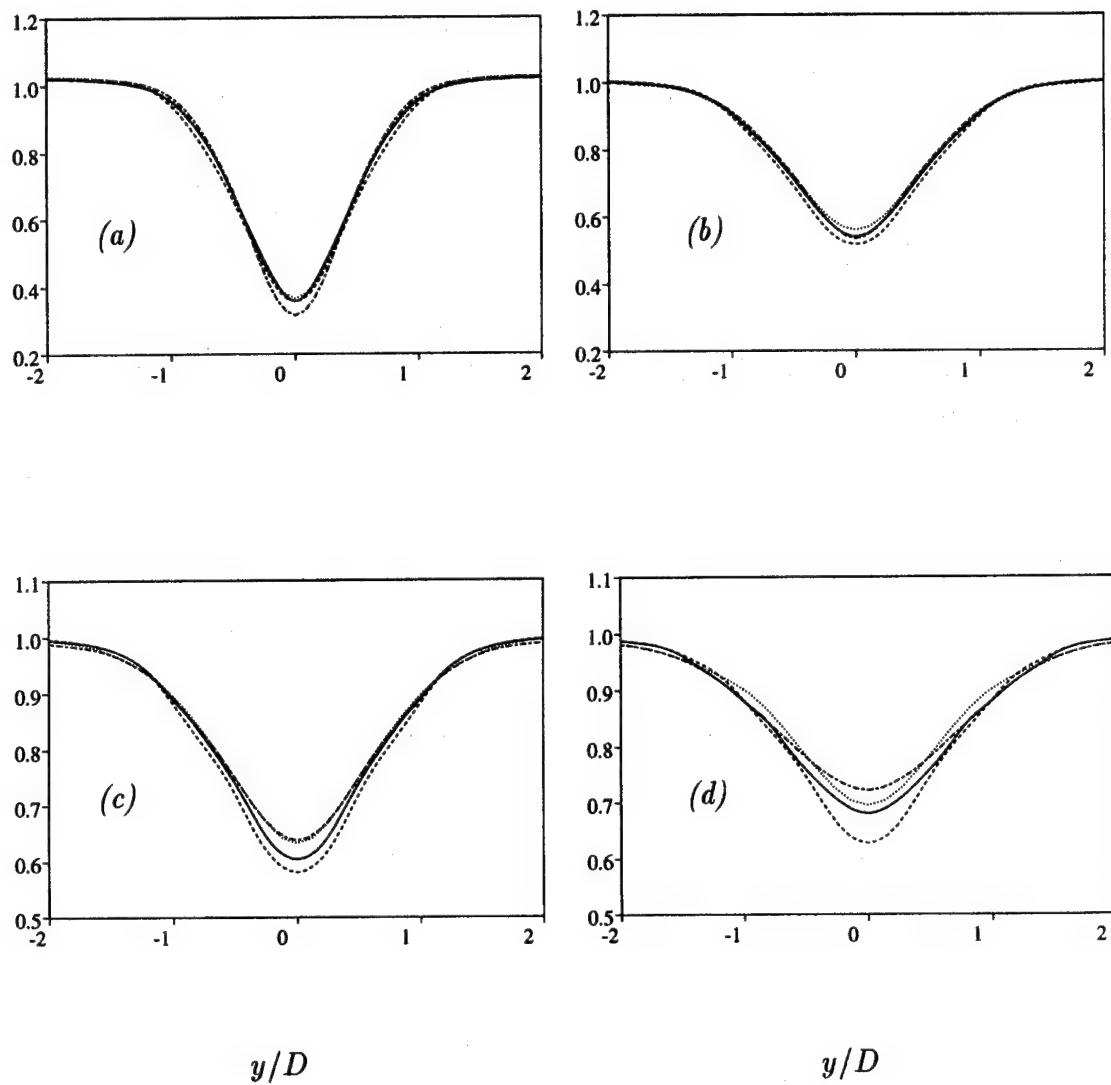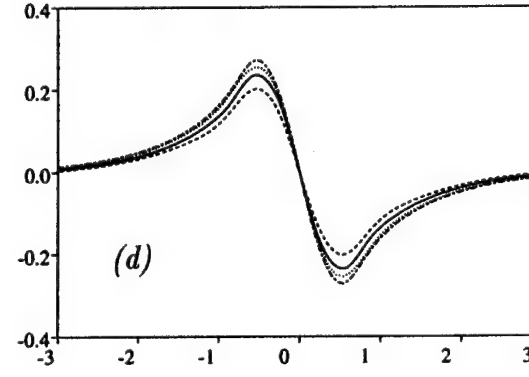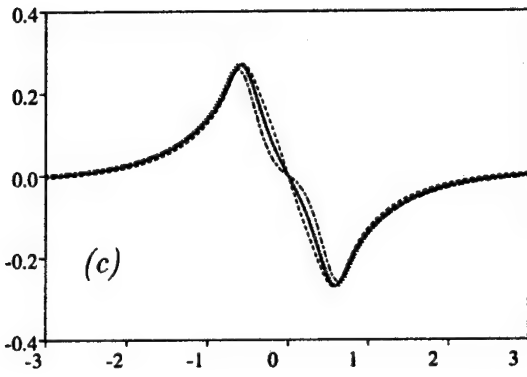—— : $174 \times 128 \times 48$

219

Figure 112: Streamwise velocity $\overline{u}/U_\infty$ at $x/D = 2.50$ (a), 3.06 (b), 3.54 (c), 4.50 (d)
—·— : $88 \times 90 \times 32$; $\cdots$: $88 \times 90 \times 48$; - - - - : $116 \times 136 \times 48$
——— : $174 \times 128 \times 48$

Figure 113: Vertical velocity $\overline{v}/U_\infty$ at $x/D = 0.58$ (a), 1.06 (b), 1.54 (c), 2.02 (d)
—·— : $88 \times 90 \times 32$; $\cdots$: $88 \times 90 \times 48$; ---- : $116 \times 136 \times 48$
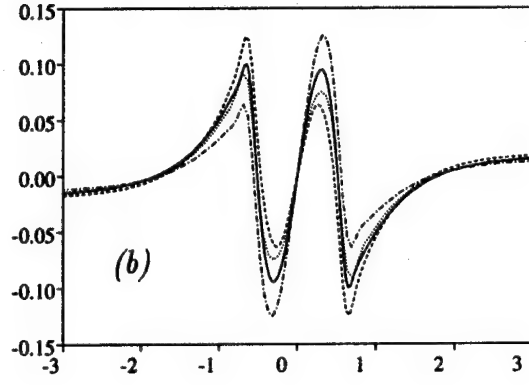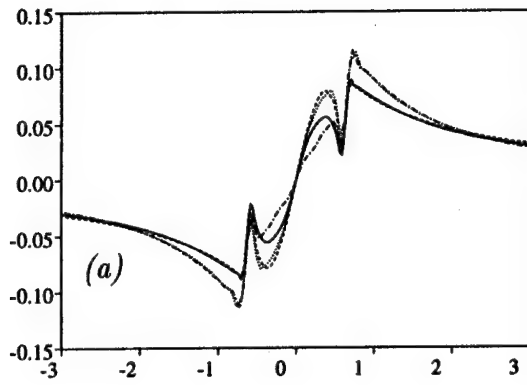——— : $174 \times 128 \times 48$

221

y/D y/D

Figure 114: Vertical velocity $\bar{v}/U_\infty$ at $x/D = 2.50$ (a), 3.06 (b), 3.54 (c), 4.50 (d)
—·— : $88 \times 90 \times 32$; $\cdots$: $88 \times 90 \times 48$
---- : $116 \times 136 \times 48$; —— : $174 \times 128 \times 48$

222
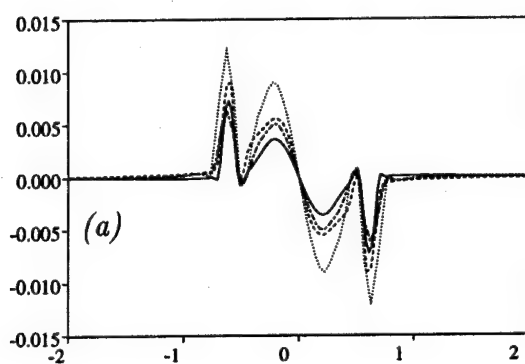
Figure 115: Total Reynolds shear stress in the formation zone
$x/D = 0.58$ (a), 1.06 (b), 1.54 (c), 2.02 (d)
—·— : $88 \times 90 \times 32$; · · · : $88 \times 90 \times 48$; - - - - : $116 \times 136 \times 48$
——— : $174 \times 128 \times 48$

223
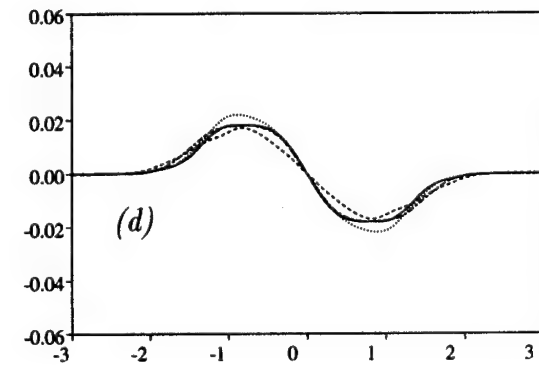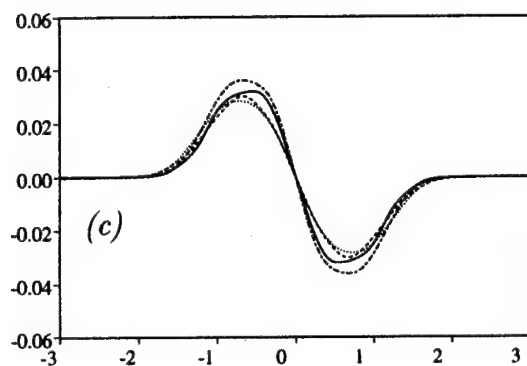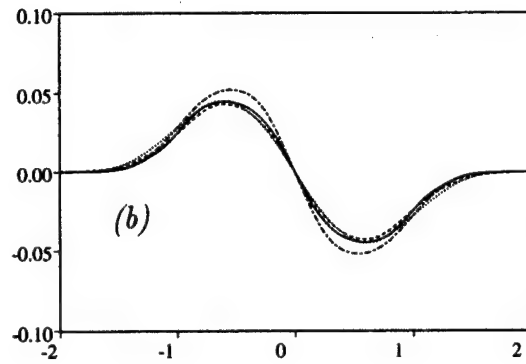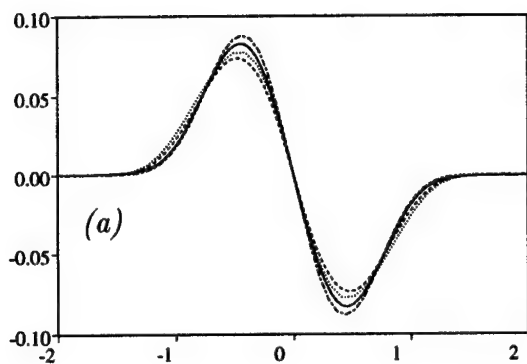
y/D y/D

Figure 116: Total Reynolds shear stress in the near-wake
$x/D = 2.50$ (a), 3.06 (b), 3.54 (c), 4.50 (d)
—·— : $88 \times 90 \times 32$; · · · : $88 \times 90 \times 48$; ---- : $116 \times 136 \times 48$
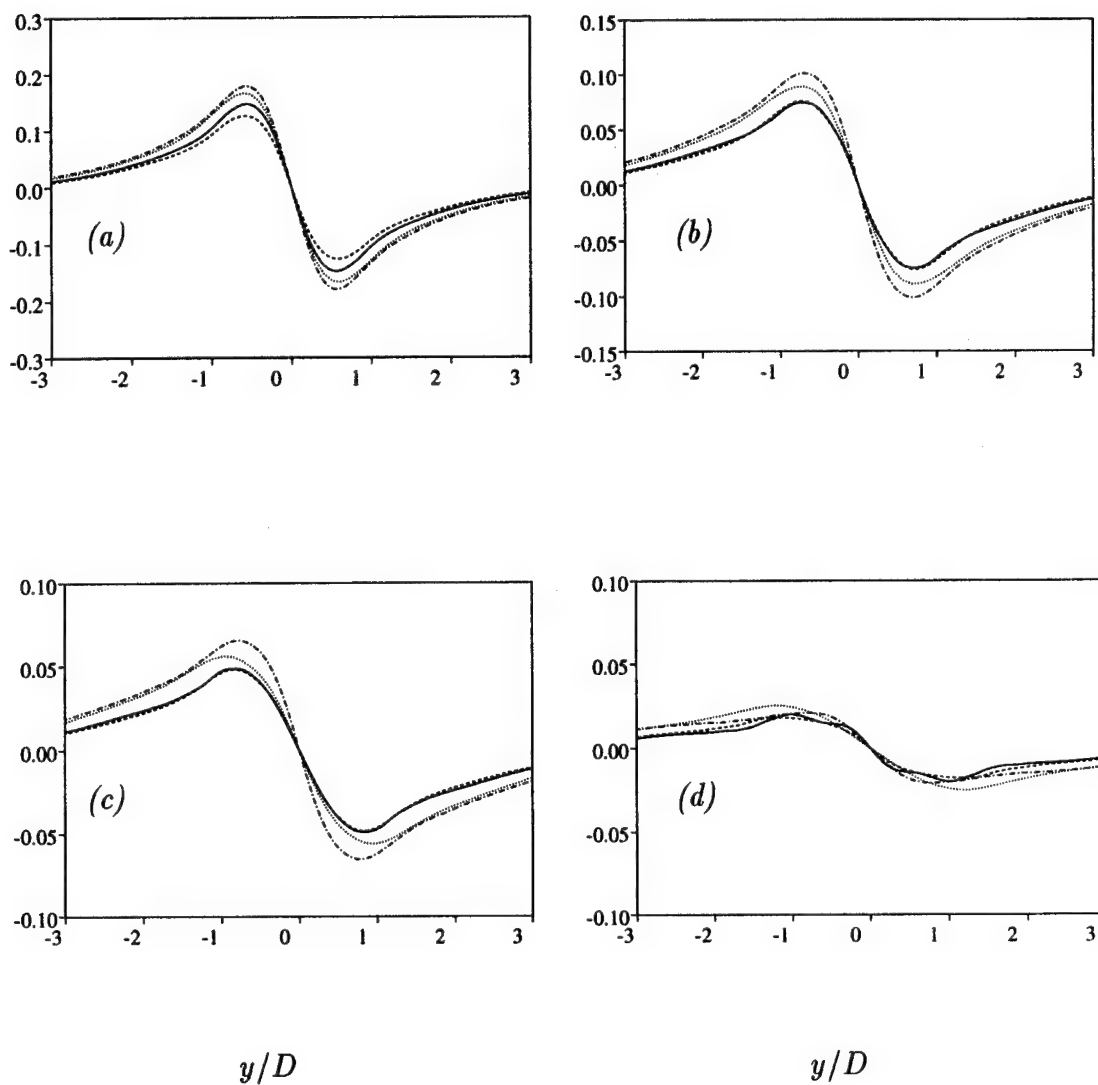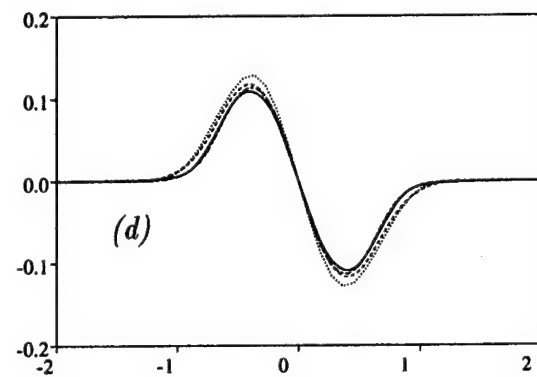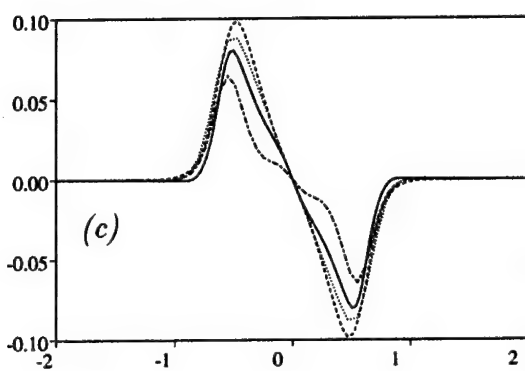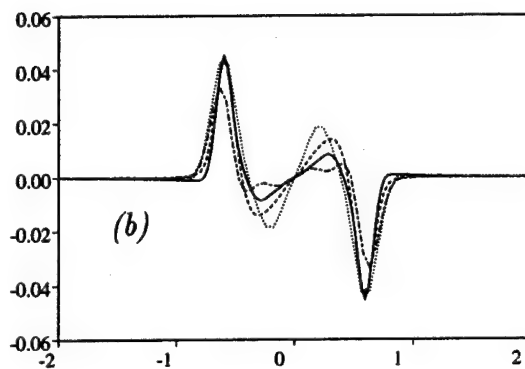——— : $174 \times 128 \times 48$

224
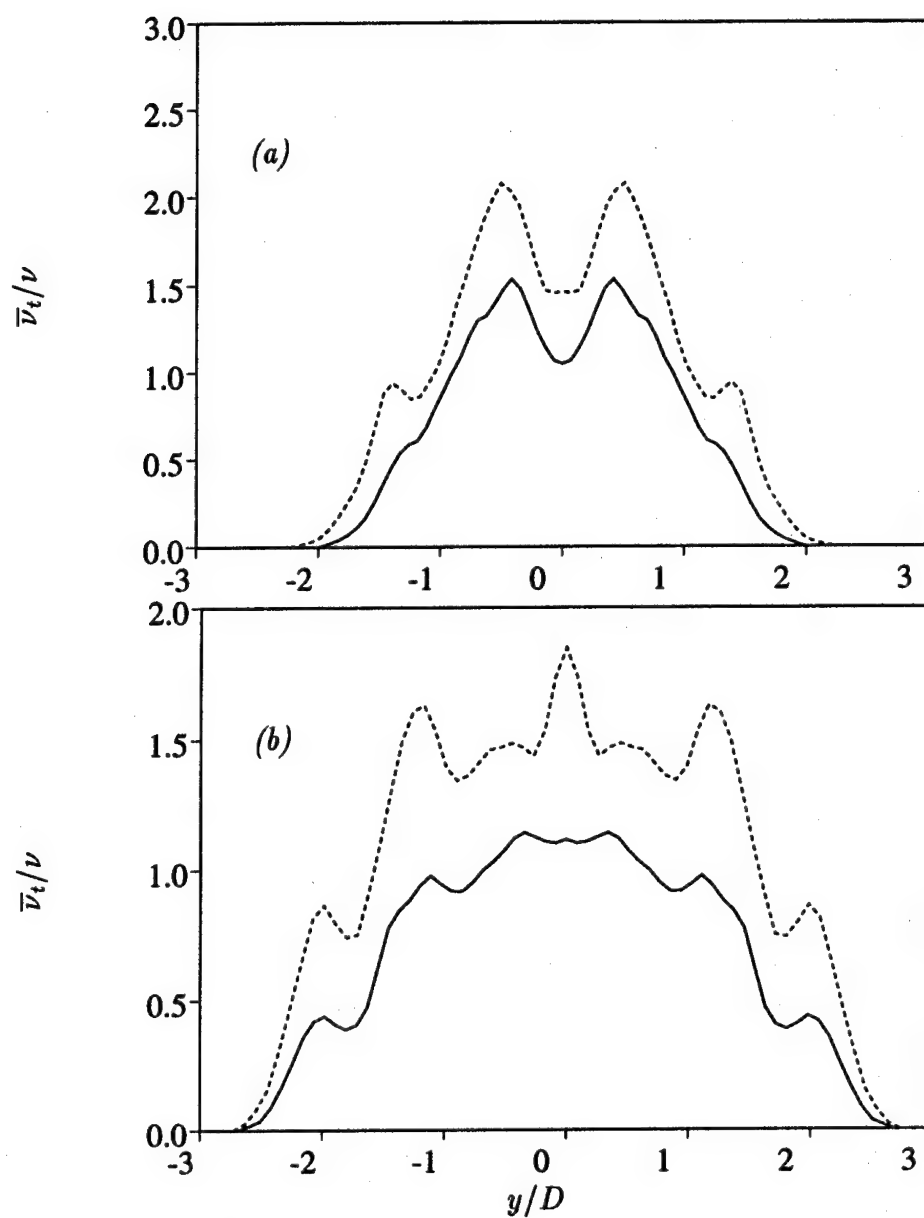
Figure 117: Eddy viscosity averaged over 1 shedding cycle
——— : No stretching; ---- : Stretched mesh
$x/D = 3.5$ (a), 5.5 (b)
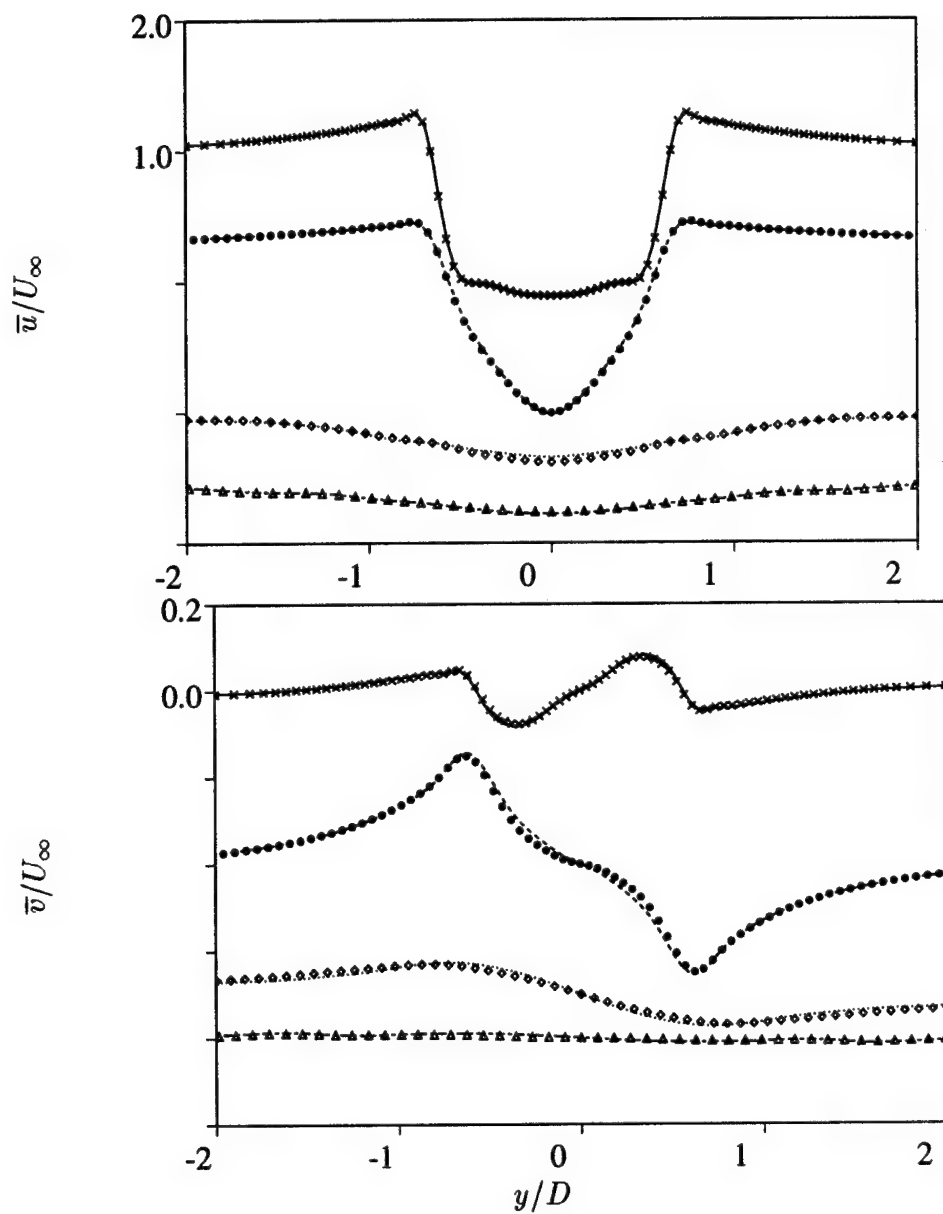
Figure 118: Effect of grid stretching on streamwise and vertical velocities
Lines: No stretching; Symbols : Stretched mesh
x/D : $\times$: 1; $\bullet$: 1.5; $\diamond$: 3.5; $\triangle$: 5.5

Bibliography

[1] ACHENBACH, E. 1968 Distribution of local pressure and skin friction around a circular cylinder in cross-flow up to $Re = 5 \times 10^6$. *J. Fluid Mech.* **34,** 625-639.

[2] ACHENBACH, E. 1971 Influence of surface roughness on the cross-flow around a circular cylinder. *J. Fluid Mech.* **46,** 321-335.

[3] ACRIVOS, A., SNOWDEN, D.D., GROVE, A.S. & PETERSEN E.E. 1965 The steady separated flow past a circular cylinder at large Reynolds numbers. *J. Fluid Mech.* **21,** 737-760.

[4] AHMED, A., KHAN, M.J. & BAYS-MUCHMORE,B. 1992 Experimental investigation of a three-dimensional bluff body wake. Presented at AIAA 30rd Aerospace Sciences Meeting, Reno, Nevada. AIAA Paper No. 92-0429.

[5] AKSELVOLL, K. & MOIN, P. 1993a In *Engineering Turbulence Modelling and Experiments 2,* W. Rodi & Martelli eds. Elsevier Science Publishers B. V.

[6] AKSELVOLL, K. & MOIN, P. 1993b ASME Fluids Engineering Conference, Washington, D.C., June 21-24, 1993.

[7] ANTONIA, R.A. & BROWNE, L.W.B. 1987 Average wavelength of organised structures in the turbulent far wake of a cylinder. *Exper. in Fluids* **5,** 298-304.

[8] ANTONIA, R.A., BROWNE, L.W.B., BISSET, D.K. & FULACHIER, L. 1987 A description of the organized motion in the turbulent far wake of a cylinder at low Reynolds number. *J. Fluid Mech.* **184,** 423-444.

[9] BARDINA, J., FERZIGER, J.H. & REYNOLDS, W.C. 1980 Improved subgrid-scale models for large-eddy simulations. *AIAA Paper No. 80-1357.*

[10] BAYS-MUCHMORE B. & AHMED, A. 1993 On streamwise vortices in turbulent wakes of cylinders. *Phys. Fluids A* **5** (2), 387-392.

[11] BEAM, R.M., WARMING, R.F. 1978 An implicit factored scheme for the compressible Navier-Stokes equations. *AIAA J.* **16,** *No.* 4, 393.

[12] BERGER, E. & WILLE, R. 1972 Periodic flow phenomena. Ann. Rev. Fluid Mech. **4,** 313-340.

[13] BLAISDELL, G. A, MANSOUR, N. N. & REYNOLDS, W. C. 1990 Numerical simulations of compressible homogeneous turbulence. *Report No. TF-50.* Thermosciences Division, Department of Mechanical Engineering, Stanford University, Stanford, CA.

[14] BLOOR, M.S. 1964 The transition to turbulence in the wake of a circular cylinder. *J. Fluid Mech.* **19,** 290-304.

[15] BLOOR, M.S. & GERRARD, J.H. 1966 Measurements on turbulent vortices in a cylinder wake. *Proc. Roy. Soc.* A **294,** 319-342.

[16] BOHNERT, M. & FERZIGER, J.H. 1993 In *Engineering Turbulence Modelling and Experiments 2,* W. Rodi & Martelli eds. Elsevier Science Publishers B. V.

[17] BOUARD, R. & COUTANCEAU, M. 1980 The early stage of development of the wake behind an impulsively started cylinder for $40 \leq \text{Re} \leq 10^4$. *J. Fluid Mech.* **101,** 583-607.

228

[18] BRAZA, M. CHASSAING, P. & HA MINH, H. 1986 Numerical study and physical analysis of the pressure and velocity fields in the near wake of a circular cylinder. *J. Fluid Mech.* **165,** 79-130.

[19] BRAZA, M., CHASSAING, P. & HA MINH, H. 1990 Prediction of large-scale transition features in the wake of a circular cylinder. *Phys. Fluids* A **2,** 1461-1471.

[20] CABOT, W. 1993 *Annual Research Briefs - 1992* Center for Turbulence Research, Stanford University/NASA Ames, 45-60.

[21] CABOT, W. & MOIN, P. 1991 Large eddy simulation of scalar transport with the dynamic subgrid-scale model. *Center for Turbulent Research, Stanford Univ., Manuscript* **128.**

[22] CANTWELL, B. & COLES, D. 1983 An experimental study of entrainment and transport in the turbulent near wake of a circular cylinder. *J. Fluid Mech.* **136,** 321-374.

[23] CARDELL, G.S. 1993 Flow past a circular cylinder with a permeable splitter plate. *Ph.D. Thesis,* Graduate Aeronautical Laboratories, California Institute of Technology.

[24] CHOI, H. & MOIN, P. 1990 On the space-time characteristics of wall-pressure fluctuations. *Phys. Fluids* A **2** (8), 1450-1460.

[25] CHOLLET, J.P., LESIEUR, M. 1981 Parametrization of small scales of three-dimensional isotropic turbulence utilizing spectral closures. *J. Atmos. Sci.* **38,** 2747-2757.

[26] CHOMAZ, J.M., HUERRE, P. & REDEKOPP, L.T. 1988 Bifurcations to local and global modes in spatially developing flows. *Phys. Rev. Lett.* **60,** 25-28.

[27] CIMBALA, J.M., NAGIB, H.M. & ROSHKO, A. 1988 Large Structure in the far wake of two-dimensional bluff bodies. *J. Fluid Mech.* **190,** 265-298.

[28] COIRIER, W.J. & VAN LEER, B. 1991 Numerical flux formulas for the Euler and Navier-Stokes equations: II. Progress in flux-vector splitting. AIAA Paper No. 91-1566-CP.

[29] COUTANCEAU, M. & BOUARD, R. 1977 Experimental determination of the main features of the viscous flow in the wake of a circular cylinder in uniform translation. Part 1. Steady Flow. *J. Fluid Mech.* **79,** 231-256.

[30] DELANEY, N. K. & SORENSEN, N. E. 1953 Low speed drag of cylinders of various shapes. NACA Tech. Note 3038.

[31] DENNIS, S.C.R. & CHANG, G. 1970 Numerical solution for steady flow past a circular cylinder at Reynolds numbers up to 100. *J. Fluid Mech.* **42,** 471-489.

[32] DON, W.S. 1989 Theory and application of speectral methods for the unsteady compressible wake flow past a two-dimensional circular cylinder. Ph.D. Thesis, Brown University.

[33] FABRIS, G. 1979 Conditional Sampling study of the turbulent wake of a cylinder. Part 1. *J. Fluid Mech.* **94,** 673-709.

[34] FARELL, C. & BLESSMANN, J. 1983 On critical flow around smooth circular cylinders. *J. Fluid Mech.* **136,** 375-391.

[35] FEIEREISEN, W. J., REYNOLDS, W. C. & FERZIGER, J. H. 1981 Numerical simulations of a compressible, homogeneous, turbulent shear flow. *Report No. TF-13.* Thermosciences Division, Department of Mechanical Engineering, Stanford University, Stanford, CA.

[36] FERRE, J. A., MUMFORD, J.C., SAVILL, A.M. & FRANCESC, G. 1990 Three-dimensional large-eddy motions and fine-scale activity in a plane turbulent wake. cylinders. *J. Fluid Mech.* **210,** 371-414.

[37] FORNBERG, B. 1980 A numerical study of steady viscous flow past a circular cylinder. *J. Fluid Mech.* **98,** 819-855.

[38] FRANKE, R. & RODI, W. 1991 Calculation of vortex shedding past a square cylinder with various turbulence models. 8th *Symp. on Turb. Shear Flows*, Munich.

[39] FRANKE, R. & RODI, W. & SCHÖNUNG, B. 1989 Analysis of experimental vortex shedding data with respect to turbulence modelling. 7th *Symp. on Turb. Shear Flows*, Stanford Univ.

[40] FRANKE, R. & RODI, W. & SCHÖNUNG, B. 1990 Numerical Calculation of Laminar Vortex Shedding Flow Past Cylinders *J. Wind Eng. & Ind. Aero.* **35,** 237-257.

[41] GERMANO, M. 1990 Average invariance of turbulent equations and similar subgrid scale modeling. *CTR Manuscript 116,* Center for Turbulence Research, Stanford Univ. and NASA-Ames.

[42] GERMANO, M., PIOMELLI, U., MOIN, P. & CABOT, W. 1991 A dynamic subgrid-scale eddy viscosity model. *Phys. of Fluids*, **A, 3,** No. 7, 1760-1765.

[43] GERRARD, J.H. 1965 A disturbance-sensitive Reynolds number range of the flow past a circular cylinder. *J. Fluid Mech.* **22,** 187-196.

[44] GHOSAL, S., LUND, T.S. & MOIN, P. 1992 *Annual Research Briefs* Center for Turbulence Research, Stanford Univ. and NASA-ames, 3-25.

[45] HAYAKAWA, M. & HUSSAIN, F. 1989 Three-dimensionality of organized structures in a plane turbulent wake. *J. Fluid Mech.* **206,** 375-404.

[46] HO, C.M. & HUERRE, P. 1984 Perturbed free-shear layers. *Ann. Rev. Fluid Mech.* **16,** 365-424.

[47] HOMMAN, F. 1936 Forsch. Geb. IngWes. **7,** 1.

[48] HUSSAIN, A. K. M. F. 1983 Coherent structures-reality and myth. *Phys. Fluids,* **26,** 2816.

[49] HUSSAIN, A. K. M. F. 1986 Coherent structures and turbulence. *J. Fluid Mech.* **173,** 303.

[50] IMAI, I. 1951 On the asymptotic behaviour of viscous fluid flow at a great distance from a cylindrical body, with special reference to Filon's paradox. *Proc. Roy. Soc.* A **208,** 487.

[51] KARNIADAKIS, G.E. & TRIANTAFYLLOU, G.S. 1992 Three-dimensional dynamics and transition to turbulence in the wake of bluff objects. *J. Fluid Mech.* **238,** 1.

[52] KATO, C. & IKEGAWA, M. 1991 Large Eddy Simulation of the unsteady turbulent wake of a circular cylinder using the finite element method. Presented at the 1st. ASME/JSME Fluids Engng. Conf., June 23rd-27th, Portland, USA.

[53] KIYA, M., & MATSUMURA, M. 1988 Incoherent turbulence structure in the near wake of a normal plate. *J. Fluid Mech.* **190,** 343-356.

[54] KOURTA, A., BOISSON, H.C., CHASSAING, P. & HA MINH, H. 1987 Nonlinear interaction and the transition to turbulence in the wake of a circular cylinder. *J. Fluid Mech.* **181,** 141-161.

[55] KOVASZNAY, L.S.G. 1949 Hot wire investigation of the wake behind cylinders at low Reynolds numbers. *Proc. Roy. Soc.* A **198,** 174-190.

[56] KRAICHNAN, RH 1976 Eddy viscosity in two and three dimensions. *J. Atmos. Sci.* **33,** 1521-1536.

[57] LEE, S., MOIN, P. & LELE, S. K. 1992 Interaction of isotropic turbulence with a shock wave. *Report No. TF-52.* Thermosciences Division, Department of Mechanical Engineering, Stanford University, Stanford, CA.

[58] LILLY, D. 1992 A proposed modification of the Germano subgrid-scale closure method. *Phys. Fluids*, A, **4 (3)**, 633-635.

232

[59] LIU, J. & PIOMELLI, U. 1993 ASME Fluids Engineering Conference, Washington, D.C., June 21-23.

[60] LOURENCO, L. M. & KROTHAPALLI, A. 1988 Application of PIDV to the study of the temporal evolution of the flow past a circular cylinder. *Laser Anemometry in Fluid Mech.*, Publ. Ladoan-Instituto Superior Tecnico 1096 Lisbon Codex-Portugal, 161-177.

[61] LOURENCO, L. M. & SHIH, C. 1993 Characteristics of the plane turbulent near wake of a circular cylinder. A particle image velocimetry study. (Private Communication).

[62] MAJUMDAR, S. & RODI, W. 1985 Numerical calculation of turbulent flow past circular cylinders. Paper presented at third Symposium on Numerical and Physical Aspects of Aerodynamic Flows, Long Beach, CA.

[63] MALIK, M.R., ZANG, T.A. & HUSSAINI, M.Y. 1985 A spectral collocation method for the Navier-Stokes equations. *J. Comput. Phys.* **61**, 64.

[64] MANSY, H., YANG, P. & WILLIAMS, D.R 1994 Quantitative measurements of three-dimensional structures in the wake of a circular cylinder. *J. Fluid Mech.* **270**, 277-296.

[65] MATSUMURA, M. & ANTONIA, R.A. 1993 Momentum and heat transport in the turbulent intermediate wake of a circular cylinder. *J. Fluid Mech.* **250**, 651-668.

[66] METAIS, O. & LESIEUR, M. 1992 Spectral large-eddy simulation of isotropic and stably stratified turbulence. *J. Fluid Mech.* **239**, 157-194.

[67] MOIN, P. & JIMENEZ, J. 1993 Large-eddy simulation of complex turbulent flows. Presented at AIAA 24th Fluid Dynamics Conference, Orlando, Florida. AIAA paper No. 93-3099.

[68] MOIN, P., SQUIRES, K., CABOT, W. & LEE, S. 1991 A dynamic subgrid-scale model for compressible turbulence and scalar transport. *Phys. Fluids A,* **3:** 2746-2757.

[69] MONKEWITZ, P.A 1988 The absolute and convective nature of instability in two-dimensional wakes at low Reynolds numbers. *Phys. Fluids,* **31,** 999-1006.

[70] MORKOVIN, M.V. 1964 Flow around a circular cylinder. A kaleidoscope of challenging fluid phenomena. *ASME Symp. on Fully Separated Flows, Philadelphia, Pa.,* 102-119.

[71] MOSER, R.D & ROGERS, M.M 1994 Direct simulation of a self-similar plane wake. *AGARD Symposium on Application of Direct and Large Eddy Simulation,* Chania, Crete, Greece, April 18-21, 1994.

[72] MURAKAMI, S. 1990 Computational wind engineering. *J. Wind Eng. and Indus. Aero.* **36,** 517-538.

[73] MURAKAMI, S., MOCHIDA, A., HAYASHI, Y. & SAKAMOTO, S. 1991 Numerical study on velocity-pressure field and wind forces for bluff bodies by $k - \epsilon$, ASM and LES. 8th *Intl. Conf. on Wind Engng.,* London, Canada.

[74] NIEUWSTADT, F. & KELLER, H.B. 1973 Viscous flow past circular cylinders. *Computers & Fluids* **1,** 59-71.

[75] NISHIOKA, M. & SATO, H. 1974 Measurements of velocity distributions in the wake of a circular cylinder at low Reynolds numbers. *J. Fluid Mech.* **65,** 97-112.

[76] NISI H. & PORTER, A. W. 1923 On eddies in air. *Phil. Mag.* (6), **46,** 754.

[77] NORBERG, C. 1987 Effects of Reynolds number and a low-intensity free-stream turbulence on the flow around a circular cylinder. Publication No. 87/2, Department of Applied Thermodynamics and Fluid Mechanics, Chalmer University of Technology, Gothenburg, Sweden.

234

[78] ONG, L. & WALLACE, J. 1994 Private Communication.

[79] PAPAILIOU D.D. & LYKOUDIS P.S. 1974 Turbulent vortex streets and the entrainment mechanism of the turbulent wake. *J. Fluid Mech.* **62,** 11-31.

[80] PERRY, A.E. & LIM, T.T. 1978 Coherent structures in coflowing jets and wakes. *J. Fluid Mech.* **88,** 451-463.

[81] PERRY, A.E. & WATMUFF, J.H. 1981 The phase-averaged large-scale structures in three-dimensional turbulent wakes. *J. Fluid Mech.* **103,** 33-51.

[82] PIOMELLI, U., FERZIGER, J. & MOIN, P. 1989 New approximate boundary conditions for large eddy simulations of wall bounded flow. *Phys. Fluids* **1,** 1061.

[83] PIOMELLI, U., ZANG, T.A., SPEZIALE, C.G. & LUND, T. 1990 In *Stability and Transition*, M.Y. Hussaini and R.G. Voit eds. Springer-Verlag.

[84] POINSOT, T.J. & LELE, S.K. 1989 Boundary conditions for direct simulations of compressible viscous reacting flows. *Center for Turb. Research Manuscript* 102, Stanford University.

[85] POINSOT, T.J. & LELE, S.K. 1992 Boundary conditions for direct simulations of compressible viscous reacting flows. *J. Comp. Phys.* **101,** No. 1, 104-129.

[86] PULLIAM, T.H. 1986a Efficient solution methods for the navier-Stokes equations. Lecture Notes for the Von Karman Institute for Fluid Dynamics Lecture Series: Numerical Techniques for Viscous Flow Computation in Turbomachinery Bladings, January 20-24, Brussels, Belgium.

[87] PULLIAM, T.H. 1986b Implicit solution methods in computational fluid dynamics. *Applied Num. Math.* **2,** 441.

[88] PULLIAM, T.H. & CHAUSSEE D.S. 1981 A diagonal form of an implicit approximate factorization algorithm. *J. Comp. Phys.* **39**, 347.

[89] RAI, M.M. 1985 An implicit, conservative, zonal-boundary scheme for Euler equation calculations. Presented at AIAA 23rd Aerospace Sciences Meeting, Reno, Nevada. AIAA Paper No. 85-0488.

[90] RAI, M.M. 1986a A conservative treatment of zonal boundaries for Euler equation calculations. *J. Comp. Phys.* **62**, 472-503.

[91] RAI, M.M. 1986b A relaxation approach to patched-grid calculations with the Euler equation. *J. Comp. Phys.* **66**, 99-131.

[92] RAI, M.M. & MOIN, P. 1993 Direct numerical simulation of transition and turbulence in a spatially evolving boundary layer. *J. Comp. Phys.* **109**, No. 2, 169-192.

[93] RAI, M.M. & MOIN, P. 1991 Direct simulations of turbulent flow using finite-difference schemes. *J. Comp. Phys.* **96**, No. 1, 15-53.

[94] REYNOLDS, W.C. & HUSSAIN, A.K.M.F. 1972 The mechanics of an organized wave in turbulent shear flow. Part3. Theoretical models and comparisons with experiments. *J. Fluid Mech.* **54**, 263-288.

[95] ROSHKO, A. 1954a On the development of turbulent wakes from vortex streets. NACA *Rep.* 1191.

[96] ROSHKO, A. 1954b On the drag and shedding frequency of two-dimensional bluff bodies. NACA *Rep.* 3169.

[97] ROSHKO, A. 1961 Experiments on the flow past a circular cylinder at very high Reynolds number. *J. Fluid Mech.* **10**, 345-356.

[98] ROSHKO, A. & FISZDON, W. 1969 On the persistence of Transition in the Near-Wake. *SIAM* 606-616.

[99] SCHEWE, G. 1983 On the force fluctuations acting on a circular cylinder in crossflow from subcritical up to transcritical Reynolds numbers. *J. Fluid Mech.* **133**, 265-285.

[100] SCHEWE, G. 1986 Sensitivity of transition phenomena to small perturbations in the flow around a circular cylinder. *J. Fluid Mech.* **172**, 33-46.

[101] SHIH, W.C.L., WANG, C., COLES, D. & ROSHKO, A. 1992 Experiments on flow past rough circular cylinders at large Reynolds numbers. Presented at the Second International Colloquium on Bluff Body Aerodynamics and Applications, Melbourne Australia, December 7-10.

[102] SON, J. & HANRATTY T.J. 1969 Velocity gradients at the wall for flow around a cylinder at Reynolds numbers from 5×10^3 to 10^5. *J. Fluid Mech.* **35**, 353-368.

[103] SQUIRES, K.D. & PIOMELLI, U. 1993 *Proceedings of the Ninth Int. Symp. on Turbulent Shear Flows*, Kyoto, Japan.

[104] STEGER, J.L. & WARMING, R.F. 1981 Flux vector splitting of the inviscid gasdynamics equations with application to finite difference methods. *J. Comp. Phys.* **40**, 263.

[105] SUGAVANAM, A. & WU, J.C. 1982 Numerical study of separated turbulent flow over airfoils *AIAA J.* **20**, 464.

[106] TAKAMI, H. & KELLER, H.B. 1969 Steady two-dimensional flow of an incompressible fluid past a circular cylinder. *Phys. Fluids Supp.* **II**, 51-56.

[107] TAMURA, T., OHTA, I. & KUWAHARA, K. 1990 On the reliability of two-dimensional simulation for unsteady flows around a circular-type structure. *J. Wind Eng.* **35**, 275-298.

[108] TANEDA, S. 1956 Experimental investigation of the wakes behind cylinders and plates at low Reynolds numbers. *J. Phys. Soc. Japan* **11**, 302.

[109] THOM, A. 1933 The flow past circular cylinders at low speeds. *Proc. Roy. Soc.* **A 141,** 651.

[110] TOWNSEND, A.A. 1949 Momentum and energy diffusion in the turbulent wake of a cylinder. *Proc. Roy. Soc.* A **197,** 124-140.

[111] TRITTON, J.D. 1959 Experiments on the flow past a circular cylinder at low Reynolds numbers. *J. Fluid Mech.* **6,** 547-567.

[112] TRITTON, J.D. 1971 A note on vortex streets behind circular cylinders at low Reynolds numbers. *J. Fluid Mech.* **45,** 203.

[113] UBEROI, M.S. & FREYMUTH, P. 1969 Spectra of turbulence in wakes behind circular cylinders. *Phys. of Fluids* **12,** No. 7, 1359-1363.

[114] UNAL, M.F. & ROCKWELL, D. 1988 On vortex formation from a cylinder: Part 1. The initial instability, Part 2. Control by a splitter plate interference. *J. Fluid Mech.* **190,** 491-529.

[115] VAN DYKE, M. 1982 *An album of fluid motion,* The Parabolic Press, Stanford, California.

[116] VAN LEER, B. 1982 Flux-vector splitting for the Euler equations. ICASE *Report No.* 82-30.

[117] WEI, T. & SMITH, C.R. 1986 Secondary vortices in the wake of circular cylinders *J. Fluid Mech.* **169,** 513-533.

[118] WEST, G.S. & 1990 Measurements of fluctuating effects on a circular cylinder in a uniform flow at subcritical Reynolds number. Part 1. Queensland Univ., Brisbane (Australia). Dept. of Civil Engng. RR-CE-109.

[119] WEST, G.S. & 1990 Measurements of fluctuating effects on a circular cylinder in a uniform flow at subcritical Reynolds number. Part 2. Queensland Univ., Brisbane (Australia). Dept. of Civil Engng. RR-CE-110.

[120] WILLIAMSON, C.H.K 1989 Oblique and parallel modes of vortex shedding in the wake of a cylinder at low Reynolds numbers. *J. Fluid Mech.* **206,** 579.

[121] WILLIAMSON, C.H.K. 1991a Three-dimensional aspects and transition of the wake of a circular cylinder. *Seventh Symp. on Turb. Shear Flows, Stanford Univ.,* 173-194.

[122] WILLIAMSON, C.H.K. 1991b The natural and forced formation of spot-like Λ structures caused by vortex dislocations in a wake. it 8th Symp. Turb. Shear Flows, Munich, Sept. 9-11, 1991.

[123] WYGNANSKY, I., CHAMPAGNE, F. & MARASLI, B. 1986 On the large scale structures in two-dimensional, small deficit wakes. *J. Fluid Mech.* **168,** 31-71.

[124] YAKHOT, A., ORSZAG, S.A. 1986 *J. Sci. Comp.* **11,** 3-51.

[125] ZANG, Y., STREET, R.L. & KOSEFF, J.R. 1993 *Annual Research Briefs - 1992* Center for Turbulence Research, Stanford University/NASA Ames, 85-95.

[126] ZHOU, Y. & ANTONIA, R.A. 1992 Convection velocity measurements in a cylinder wake *Exp. in Fluids* **13,** 63-70.